


UNIVERSITY OF
OXFORD

# Electrode Materials for Stable Perovskite Solar Cells

**Tino Lukas**

A thesis submitted for the degree of Doctor of Philosophy in Condensed Matter Physics at the University of Oxford

Department of Physics

Keble College

**March 2025**

# Acknowledgements

First and foremost, I thank my supervisor, Prof Henry Snaith, for giving me the opportunity to do my PhD in his group, for supervising me, and for all his fruitful ideas I was able to benefit from during my PhD. Recognizing also the EPSRC Programme Grant ATIP (Application Targeted and Integrated Photovoltaics) (EP/T028513/1) for partly funding my degree. Especially, I thank Dr Markus Kohlstädt and Dr Uli Würfel for supervising me during my stay as an academic visitor at the Fraunhofer ISE. Enormous gratitude as well to Dr Lukas Wagner for being the best long-term mentor I could wish for and an amazing human being and friend. Profound thanks to the Perovskite Thin Film PV group at the Fraunhofer ISE that I was visiting during my PhD for welcoming me so kindly. Also, I convey my gratitude to Dr Seongrok Seo and Dr Philippe Holzhey for mentoring me over the past years in the Snaith group. Likewise, I thank the Perovskite solar cells with graphite electrodes: Advanced interfaces for highest performance and stability (PeroGAIN) project by Deutsche Forschungsgemeinschaft (DFG, SPP2196) for the good collaborative environment to progress with my carbon-related research. Especially grateful to Dr Salma Zouhair for showing me how to make carbon-based perovskite solar cells. Support from the EPSRC National Thin Film Facility for Advanced Functional Materials (NTCF), hosted by the Department of Physics at the University of Oxford, is also acknowledged. Truly, most importantly, I thank you, Jin, for helping me so much at the NTCF! Incredible support from so many people has made this possible. Needless to say, I am deeply grateful for every bit of guidance and kindness I received. Everyone mentioned here has left a lasting impact on my academic and personal growth.

Fantastic collaborations with brilliant scientists around the world have made this journey incredibly rewarding. Countless thanks to Hadi Mohammadzadeh, Dr Lukas Wagner, Clemens Baretzky, Dr Markus Kohlstädt, Dr Katie Stewart, Charlie Henderson, Dr Abhay Shivayogimath, Dr Matthias Diethelm, Dr Robert Hoye, Dr Dave Beynon, Dr Trystan Watson, Dr Amit Kumar, Ali Reza Nazari Pour, Georgios Loukeris, Dr Luke Sutherland, Dr Joseph Asare, and Dr Alexey Tsapenko. Kind appreciation to all my friends, and the volunteer crew at the Duque Nest in Tenerife, where I wrote most of this document; muchas gracias, it was a blast! Amazing times, especially with Katia Abdellaoui and Nico Sestito! Forever grateful to the people in the group who see me for who I truly

am, especially Shaoni Kar, Jake Drysdale, Nicky Evans, and Amit Kumar. Daily life was made so much better by my past and present housemates, especially thank you May, Kasra, and Catrin.

Most importantly, deepest appreciation to the people most significant in my life who have supported me tremendously throughout this very difficult part of my life: my best friends back home in Germany, my new good friends in Oxford, and my Family. Thanks, especially to my parents, grandparents, Betriska, and Thies Lukas. Vielen, vielen Dank Mama, Papa, Oma und Opa! Enxhi Sharxhi, thank you so much for all the beautiful memories, always being on my side, and supporting me so much on this journey! Thank you so, so much to my best friends Alejandro Gómez de las Heras, May Chemais, Sewin Tariverdian, Janina Thiel, Joshua Nielsen, Mara and Sina Montag. You all are the best! I love you.

# Statement of Authorship

The work presented in this thesis is entirely based on my own research unless otherwise indicated in the text. No part of this work has been submitted for a degree or qualification at the University of Oxford or any other University if not stated otherwise in the text.

Tino Lukas, 24 June 2025

# Table of Contents


**1 INTRODUCTION ..... 21**

1.1 Climate Emergency ..... 21
1.2 Photovoltaics ..... 23
1.2.1 Silicon Photovoltaics ..... 25
1.2.2 Other Absorber Materials ..... 28
1.2.2.1 Thin Film Technologies ..... 29
1.2.2.2 Perovskite Single Junctions ..... 29

**2 BACKGROUND ..... 31**

2.1 Semiconductor Physics ..... 31
2.1.1 Energy States and Bands ..... 31
2.1.2 Indirect vs Direct Band Gap ..... 33
2.1.3 Fermi Level ..... 34
2.1.4 Doping ..... 36
2.1.5 Work function ..... 37
2.1.6 Contact Potential ..... 37
2.1.7 Recombination Processes ..... 40
2.1.7.1 Radiative ..... 40
2.1.7.2 Trap Assisted ..... 40
2.1.7.3 Auger ..... 41
2.2 Photovoltaic Effect ..... 42
2.2.1 Light ..... 42
2.2.2 Photo Absorption ..... 43
2.3 Solar Cell Working Principles ..... 43
2.3.1 Charge Separation ..... 44
2.3.2 Device Structures ..... 44
2.3.3 Current Density-Voltage Behaviour ..... 46
2.3.4 Series and Shunt Resistance ..... 48
2.3.5 Hysteresis ..... 49
2.4 Perovskite Solar Cells ..... 51
2.4.1 Perovskite Crystal Structure ..... 52
2.4.2 Mixed Ion Perovskites ..... 55
2.4.3 Defect Tolerance ..... 55
2.4.4 Solvent Processing ..... 56
2.4.5 Tunable Band Gap ..... 57
2.5 Stability Challenges ..... 58
2.5.1 Perovskite Instabilities ..... 59

2.5.1.1 Heat Stability ..... 59
2.5.1.2 Light Stability ..... 62
2.5.2 Electrode Materials and Stability Issues ..... 64
2.5.2.1 Metal Halide Formation ..... 64
2.5.2.2 Metal Ion Diffusion ..... 66
2.5.2.3 Metal Oxide Instabilities ..... 67
2.5.3 Carbon-Based Electrodes ..... 69
2.5.3.1 Carbon Allotropes and their Properties ..... 69
2.5.3.2 Advantageous Properties of Carbon-Based Materials ..... 71
2.5.3.3 Carbon-Based Electrode Preparation Types ..... 75
**3 METHODS ..... 81**
3.1 Device Fabrication ..... 81
3.1.1 Materials ..... 81
3.1.2 Substrate Preparation ..... 82
3.1.3 Precursor Solution Preparation ..... 82
3.1.4 Thin Film Deposition ..... 82
3.1.4.1 Spin-Coating ..... 82
3.1.4.2 Blade-Coating ..... 84
3.1.4.3 Thermal Evaporation ..... 84
3.1.4.4 Atomic Layer Deposition ..... 85
3.1.5 Wetting Agent ..... 85
3.1.6 Perovskite Layer ..... 86
3.1.7 Electron Transport Layer ..... 86
3.1.7.1 PCBM ..... 86
3.1.7.2 C60 ..... 86
3.1.7.3 BCP ..... 86
3.1.7.4 Tin Oxide Atomic Layer Deposition ..... 87
3.1.7.5 Interlayers ..... 87
3.1.7.6 Graphene ..... 87
3.1.8 Electrode ..... 88
3.1.8.1 Cr Interlayer ..... 88
3.1.8.2 Metals ..... 89
3.1.8.3 Carbon Blade-Coating ..... 89
3.1.8.4 Carbon Lamination ..... 90
3.1.9 Hole Transport Layer ..... 90
3.2 Ageing ..... 91
3.2.1 Encapsulation ..... 91
3.2.2 Outdoor Ageing ..... 91

3.2.3 Accelerated Ageing ..... 91
3.2.3.1 "Freiburg" box ..... 92
3.2.3.2 Atlas boxes (65 and 85 °C light ageing) ..... 92
3.2.3.3 Nitrogen heat-light ageing ..... 93
3.2.3.4 Light ambient ageing ..... 93
3.2.3.5 Nitrogen heat ageing ..... 94
3.3 Characterisation ..... 94
3.3.1 Solar Simulator ..... 94
3.3.2 Scanning Electron Microscopy ..... 96
3.3.3 Four Point Probe Measurements ..... 96
3.3.4 Photoluminescence Quantum Yield ..... 97
3.3.5 Time-Resolved Photoluminescence ..... 97
3.3.6 X-Ray Diffraction ..... 98
3.3.7 Kelvin Probe ..... 98
3.3.8 Ambient-pressure Photoemission Spectroscopy ..... 98
3.3.9 External Quantum Efficiency ..... 99
3.3.10 Time of Flight Secondary Ion Mass spectrometry ..... 99
3.3.11 Atomic Force Microscopy ..... 100
**4 INTERFACIAL LAYERS FOR P-I-N PEROVSKITE SOLAR CELLS WITH CARBON ELECTRODES ..... 101**
4.1 Motivation ..... 101
4.2 Introduction ..... 102
4.3 Results ..... 104
4.3.1 Solvent Damage-Related Issues of Carbon Electrodes ..... 104
4.3.2 Solution-Processed Buffer Layers ..... 110
4.3.3 Atomic Layer Deposited Tin Oxide ($SnO_2$) as a Buffer Layer ..... 114
4.3.4 A PH1000 Interface Layer ..... 115
4.4 Discussion ..... 120
4.5 Conclusion ..... 122
**5 STABILITY ENHANCEMENTS THROUGH THE USE OF CARBON-BASED MATERIALS ..... 124**
5.1 Carbon Film Lamination for Inverted Perovskite Solar Cells ..... 124
5.1.1 Results ..... 125
5.1.1.1 Stability Challenges ..... 125
5.1.1.2 Adhesion of Laminated Carbon Films ..... 139
5.1.2 Discussion ..... 150
5.1.3 Conclusion ..... 157
5.2 Graphene Diffusion Barriers ..... 158

5.2.1 Increased Film Stability ..... 159
5.2.2 Implementation of Devices ..... 166
**6 SUSTAINABLE ELECTRODE MATERIALS ..... 175**
6.1 Motivation ..... 175
6.2 Introduction ..... 177
6.3 Results ..... 178
6.3.1 Stability of Cr/Ag Electrodes ..... 178
6.3.2 General Stability of Cr Metal Bilayers ..... 182
6.3.3 ITO and FTO Transparent Electrodes ..... 191
6.3.4 Perovskite Devices with Improved Long-term Stability ..... 203
6.4 Discussion ..... 206
6.5 Conclusion ..... 210
**7 CONCLUSION AND OUTLOOK ..... 212**
**8 REFERENCES ..... 215**

# Abstract

Countering climate change requires a shift to renewable energy, with perovskite solar cells (PSCs) bound to play a crucial role. Ensuring the longevity of PSCs is important to enable their sustainable and reliable use. Research into improving PSC stability has primarily focused on the perovskite active layer, while the role of electrode materials and their interfaces remains underexplored. This thesis investigates the impact of different electrode materials on PSC stability, providing insights into interfacial energetics and material compatibilities, enabling future device design.

Firstly, I examined the interface energetics between carbon-based electrodes and the electron transport layer (ETL) in p-i-n PSCs. I reveal that blade-coated carbon electrodes exhibit unexpected semiconducting behaviour at the ETL interface, leading to preferential hole extraction. These findings explain the common use of carbon electrodes for hole-, rather than electron-, extraction. Additionally, I identify fundamental incompatibilities with commonly used ETLs. Based on this, I developed the first p-i-n PSCs without evaporated layers, incorporating atomic layer deposition (ALD) of $SnO_2$ and a conductive polymer interface modifier to improve ETL/carbon contact. I further demonstrate the first p-i-n PSCs with laminated carbon electrodes, achieving strongly enhanced stability compared to blade-coated counterparts. Additionally, I show that laminated graphene encapsulation enhances perovskite thin film stability by orders of magnitude compared to films without graphene.

Subsequently, I present the first direct comparison between indium tin oxide (ITO) and fluorine-doped tin oxide (FTO) transparent electrodes, revealing a significant advantage of FTO in long-term device stability. In a systematic study, I identify indium ion leaching from ITO into the perovskite layer as a probable factor accelerating light- and heat-induced degradation. Finally, I examine the stability of metal electrodes (gold, silver, aluminium, and copper), with and without a chromium interlayer. A chromium-aluminium bilayer electrode improves device stability beyond gold while reducing raw material costs by five orders of magnitude.

These findings deepen the understanding of electrode-induced degradation in PSCs and provide practical design strategies to enhance device stability while reducing material and deposition costs.

# List of Abbreviations

| Abbreviation | Meaning |
|---|---|
| $Al_2O_3$ np | Alumina Nanoparticles |
| ALD | Atomic Laser Deposition |
| AM1.5 | Air Mass 1.5 |
| APS | Atmosphericpressure Photospectroscopy |
| AZO | Aluminium Zinc Oxide |
| BC | Blade-Coated |
| BCP | Bathocuproine |
| BMP | 1-butyl-1-methylpiperidinium |
| BOS | Balance of System |
| C60 | Buckminsterfullerene |
| CapEx | Capital Expenditure |
| CB | Chlorobenzene |
| CBM | Conduction Band Minimum |
| CIGS | Copper Indium Gallium Selenide |
| CNT | Carbon Nano Tube |
| C-PSC | Carbon-based Perovskite Solar Cells |
| CSIRO | Commonwealth Scientific and Industrial Research Organisation |
| CVD | Chemical Vapour Deposition |
| DCB | di-chlorobenzene |
| DI | deionised |
| DMF | N, N-Dimethylformamide |
| DMSO | Dimethyl Sulfoxide |
| DTU | Technical University of Denmark |
| EPSRC | Engineering and Physical Sciences Research Council |
| EQE | External Quantum Efficiency |
| ETL | Electron-Transporting Layer |

| | |
|---|---|
| F4TCNQ | 2,3,5,6-Tetrafluor-7,7,8,8-tetracyanochindimethan |
| FA | Formamidinium |
| FAI | Formamidinium Iodide |
| FF | Fill Factor |
| FTO | Fluorine-Doped Tin Oxide |
| Fraunhofer ISE | Fraunhofer Institute for Solar Energy Systems |
| GHG | Greenhouse Gas |
| HOMO | Highest Occupied Molecular Orbital |
| HTL | Hole-Transporting Layer |
| IEEE | Institute of Electrical and Electronics Engineers |
| IPA | Iso-Propyl-2-Alcohol |
| IPCC | Intergovernmental Panel on Climate Change |
| ITO | Indium Tin Oxide |
| J | Current Density |
| $J_{sc}$ | Short Circuit Current Density |
| JV | Current Density-Voltage |
| KP | Kelvin Probe |
| LED | Light Emitting Diode |
| LTC | Low-temperature Carbon |
| LUMO | Lowest Unoccupied Molecular Orbital |
| MA | Methylammonium |
| MAI | Methylammonium Iodide |
| MPP or mpp | Maximum Power Point |
| MPPT | Maximum Power Point Tracking or Maximum Power Point Tracked |
| NOAA | Intergovernmental Panel on Climate Change |
| NDC | Nationally Determined Contributions |
| np | Nanoparticles |
| oc | Open Circuit |
| PCBM | [6,6] Phenyl-C61-Butyric Acid Methyl Ester |

| | |
|---|---|
| PCE | Power Conversion Efficiency |
| PDMS | Polydimethylsiloxane |
| PEDOT | Poly(3,4-ethylenedioxythiophene) |
| PEI | Polyethyleneimine |
| PEIE | Polyethyleneimine Ethoxylated |
| PL | Photoluminescence |
| PLQY | Photoluminescence Quantum Yield |
| PMMA | Poly(methyl methacrylate) |
| polyTPD | Poly(N,N'-bis-4-butylphenyl-N,N'-bisphenyl)benzidine |
| PSC | Perovskite Solar Cell |
| PSS | Polystyrene Sulfonate |
| PTFE | Polytetrafluoroethylene |
| PV | Photovoltaic |
| PVA | Polyvinyl Alcohol |
| QCM | Quartz Crystal Microbalance |
| QE | Quantum Efficiency |
| QFLS | Quasi-Fermi-Level-Splitting |
| QY | Quantum Yield |
| RT | Room Temperature |
| SAM | Self-Assembled Monolayer |
| sc | Short Circuit |
| SEM | Scanning Electron Microscopy or Scanning Electron Microscopy |
| SJ | Single Junction |
| SPO | Stabilised Power Output |
| ss | Stabilised |
| TCO | Transparent Conducting Oxides |
| TGA | Thermogravimetric Analysis |
| TOF-SIMS | Time-of-Flight Secondary Ion Mass Spectrometry |
| UVvis | Ultraviolet-Visible Spectroscopy |

| | |
|---|---|
| TRPL | Time-Resolved Photoluminescence |
| UK | United Kingdom (of Great Britain and Northern Ireland) |
| UN | United Nations |
| US | United States (of America) |
| VB | Valence Band |
| VBM | Valence Band Maximum |
| $V_{oc}$ | Open Circuit Voltage |
| XRD | X-Ray Diffraction (Analysis) |
| ZrAcac | Zirconium(IV)acetylacetonate,Tetracids(2,4-pentandionato)zirconium(IV) |
| $\Delta G$ | Gibbs Free Energy |

# Table of Figures

Figure 1.1 Annual Global Surface Temperature Increase ..... 21

Figure 1.2 Atmospheric Carbon Dioxide Concentrations ..... 22

Figure 1.3 Global Greenhouse Gas Emission Pathways for Different Warming Scenarios ..... 23

Figure 1.4 Available Energy Source on the Earth's Surface ..... 24

Figure 1.5 Schematics of a Solar Cell ..... 25

Figure 1.6 Growth in Photovoltaics ..... 26

Figure 1.7 National Renewable Energies Laboratory Chart of the best Research-Cell Efficiencies 28

Figure 2.1 Electronic Properties of Materials ..... 33

Figure 2.2 Direct and Indirect Band Gap Semiconductor ..... 34

Figure 2.3 Junctions ..... 39

Figure 2.4 Absorption and Recombination ..... 42

Figure 2.5 The n-i-p and p-i-n Structures ..... 45

Figure 2.6 Example of Current Density-Voltage Scans ..... 47

Figure 2.7 Equivalent Circuit of a Solar Cell ..... 49

Figure 2.8 Current Density-Voltage Scan Hysteresis ..... 51

Figure 2.9 Applications for Perovskite Solar Cells ..... 51

Figure 2.10 Perovskite Crystal Structure ..... 52

Figure 2.11 Ionic Radii ..... 53

Figure 2.12 Globularity Factor of Organic Cations in a Perovskite Lattice ..... 54

Figure 2.13 Defect Level in Methylammonium Lead Halide Perovskites ..... 56

Figure 2.14 Adjustable Band Gap of Perovskite Material by Ion Replacement ..... 58

Figure 2.15 Improved Thermal Stability by introducing Cs Cations ..... 61

Figure 2.16 Lead-Iodide Light Instability and Excess ..... 63

Figure 2.17 Effects of Metal-Induced Perovskite Solar Cell Degradation ..... 65

Figure 2.18 Carbon Perovskite Solar Cell Scanning Electron Microscopy Cross-Section ..... 70

Figure 2.19 Material Costs Common Laboratory Perovskite Solar Cell as Module ..... 72

Figure 2.20 Carbon Electrode Advantages ..... 73

Figure 2.21 Stability advantages of a Carbon PSC ..... 74

Figure 2.22 High-temperature Carbon Treatment - Triple Mesoporous Structure ..... 76

Figure 2.23 Blade-Coating Process Schematics ..... 78

Figure 2.24 Press transfer of a Carbon Electrode ..... 79

Figure 3.1 Perovskite Spin-Coating with Antisolvent Quench ..... 83

Figure 3.2 Electrode Design ..... 88

Figure 3.3 Blade-Coating Setup ..... 90

Figure 3.4 Ageing chamber Cr/metal study ..... 92

Figure 3.5 Atlas Ageing Box ..... 93

Figure 3.6 Ambient 25 °C ageing setup ..... 94

Figure 3.7 Solar Simulator Operation ..... 95

Figure 3.8 Four Probe Measurement ..... 97

Figure 4.1 Advantages of a PH1000 Layer at the Carbon $SnO_2$ Interface ..... 101

Figure 4.2 Carbon Paste Dissolving Fullerene-Based Layers ..... 105

Figure 4.3 *JV* of Devices with Different Electron Transport Layer Thicknesses ..... 106

Figure 4.4 Gold and Carbon Devices with 70 nm Evaporated $C_{60}$ ..... 106

Figure 4.5 PCBM Carbon Device Cross-Sections ..... 107

Figure 4.6 Carbon Paste Curing Methods ..... 108

Figure 4.7 Buffer Layers for Carbon Perovskite Solar Cells ..... 109

Figure 4.8 Half-Stack polarity of PCBM/Carbon Devices ..... 110

Figure 4.9 Alternative Solution-Processed Buffer Layers ..... 112

Figure 4.10 $SnO_2$ Nanoparticle Carbon Device Scanning Electron Microscope Cross-Section ..... 113

Figure 4.11 Carbon Devices with and without a Buffer Layer ..... 113

Figure 4.12 Stability of $SnO_2$ Buffer Compared with Cr ..... 115

Figure 4.13 ALD $SnO_2$/Carbon ..... 116

Figure 4.14 Atomic Force Microscopy Results ..... 117

Figure 4.15 Ambient-Pressure Photoemission Spectroscopy Results ..... 118

Figure 4.16 Transferability of PH1000 Treatment of $SnO_2$ ..... 119

Figure 4.17 Multiple Batch Statistics of $SnO_2$/Carbon with and without PH1000 ..... 120

Figure 5.1 $SnO_2$/PH1000/Carbon Stability ..... 125

Figure 5.2 Carbon Encapsulation ..... 126

Figure 5.3 Stability of $SnO_2$ compared with $SnO_2$/PH1000 Buffer ..... 127

Figure 5.4 Gold Carbon Ageing Comparison ..... 128

Figure 5.5 Carbon versus Metal Stability ..... 129

Figure 5.6 BCP versus $SnO_2$/Au Ageing Behaviour ..... 130

Figure 5.7 $SnO_2$/Carbon Outdoor Stability ..... 131

Figure 5.8 Influence of Heat Gun Annealing Times on Stability ..... 133

Figure 5.9 Device Performance with Different Carbon Pastes ..... 134

Figure 5.10 Conductivity for Number of Carbon Coatings ..... 136

Figure 5.11 Device Performance for Number of Carbon Coatings ..... 137

Figure 5.12 Thermogravimetric Analysis of Carbon Paste ..... 138

Figure 5.13 Influence of 30 Minutes Anneal on Carbon Device Performance and Stability ..... 139

Figure 5.14 Data First Lamination Experiments ..... 141

Figure 5.15 First p-i-n Carbon Lamination ..... 144

Figure 5.16 Substrates and Laboratory Comparison of Carbon Electrodes ..... 145

Figure 5.17 Comparison of Blade-Coated and Laminated Carbon Electrodes ..... 146

Figure 5.18 Efficiency of Single and Double-Laminated ..... 147

Figure 5.19 Stability Comparison: Blade-Coated and Laminated..... 149

Figure 5.20 Proposed Equivalent Circuit ..... 150

Figure 5.21 Proposed Working Principle of a Graphene Diffusion Barrier in a p-i-n Device ..... 158

Figure 5.22 Graphene-Encapsulated Films Ageing ..... 160

Figure 5.23 Influence of Holes in Graphene on Film Ageing..... 161

Figure 5.24 Full-spectrum X-ray Diffraction of Aged Graphene Samples ..... 162

Figure 5.25 X-ray Diffraction Graphene Ageing ..... 163

Figure 5.26 Relation between Diffraction Signal and Peak Position ..... 165

Figure 5.27 Lateral Shunting Issues in Graphene Devices..... 169

Figure 5.28 Device Parameters First Batch Graphene ..... 171

Figure 5.29 Performance of Devices on each Substrate - First Batch Graphene ..... 172

Figure 5.30 Polymer Residues and Atomic Force Microscopy..... 174

Figure 6.1 Overview Sustainable Electrodes ..... 175

Figure 6.2 Initial Cr/Ag stability results..... 179

Figure 6.3 Cr Metal Devices aged in Nitrogen ..... 180

Figure 6.4 Pre-Ageing Behaviour of Different Metal Electrodes ..... 182

Figure 6.5 *JV* scans Cr/metal ageing ..... 183

Figure 6.6 Hysteresis Index..... 184

Figure 6.7 Shunting Statistics..... 185

Figure 6.8 Cr Shunt Ageing ..... 186

Figure 6.9 Cr/metal Ageing Study ..... 187

Figure 6.10 Silver Paste Application ..... 188

Figure 6.11 Champion PCEs ..... 189

Figure 6.12 Overview Cr/metal PCE ..... 191

Figure 6.13 Hole Transport Layers for FTO and ITO ..... 192

Figure 6.14 Hole transport layer ageing comparison ..... 193

Figure 6.15 Ageing Behaviour Transparent Electrodes at 65 °C ..... 194

Figure 6.16 ITO vs FTO Ageing Study at 25 °C ..... 195

Figure 6.17 X-ray Diffraction Spectra of Aged Devices on ITO and FTO ..... 196

Figure 6.18 Time of flight secondary ion mass spectrometry results ..... 197

Figure 6.19 Stability of Devices on ITO and FTO ..... 198

Figure 6.20 Full Data Photoluminescence Quantum Yield Ageing Study ..... 199

Figure 6.21 Time-Resolved Photoluminescence of Transparent Electrodes ..... 200

Figure 6.22 Influence of added Indium (III) Iodide ..... 202

Figure 6.23 Cr/Al Trial in a Different Evaporator ..... 204

Figure 6.24 Ageing Behaviour of Different Metal Electrodes on Different Transparent Conductive Oxides ..... 205

# 1 INTRODUCTION

## 1.1 Climate Emergency

Climate change is one of humanity's biggest challenges.[1,2] The last year, 2024, was the hottest year on record, as well as the first one breaching the important threshold of a 1.5 °C warming above the pre-industrial level (Figure 1.1a).[3] Crossing the 1.5 °C threshold permanently will have severe implications for humans and other life on Earth, including a near-total extinction of the global coral reef population.[4]

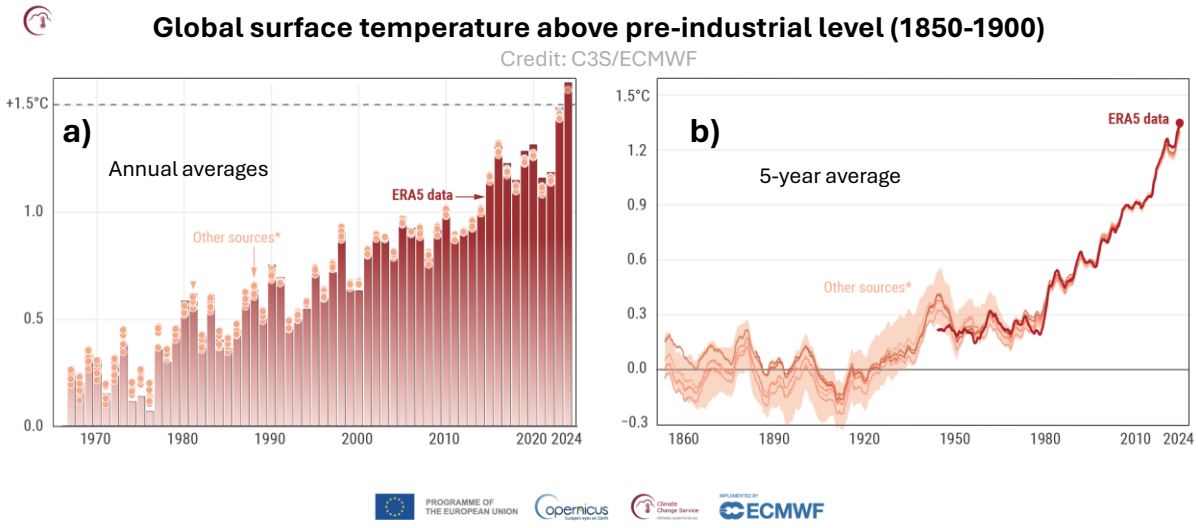



**Figure 1.1 Annual Global Surface Temperature Increase**

(a) Yearly average global surface temperatures from 1967 to 2024 relative to the pre-industrial reference period of 1850 to 1900. ERA5 data from Copernicus are indicated in a box chart and other sources as points. (b) 5-year average data from 1850 to 2024. *Other sources include JRA-30, GISTEMPv4, NOAAGlobalTempv6, Berkeley Earth, and HadCRUT5 ensemble mean. Shading in (b) indicates the range of HadCRUT5. Figure adapted from Copernicus Climate Change Service.[3]

Direct measurements of carbon dioxide ($CO_2$) show a steady increase in concentration from around 315 ppm in 1958 to above 420 ppm at the end of 2024 (Figure 1.2a).[5] Secondary data obtained from ice core drillings show that both the level as well as the rate of the increase of $CO_2$ have been unprecedented for at least the last 800,000 years (Figure 1.2b).[6-10] The data further suggests a strong link between atmospheric $CO_2$ levels and atmospheric temperature.[11] The vast majority of the increase is caused by human activity.[12-14]

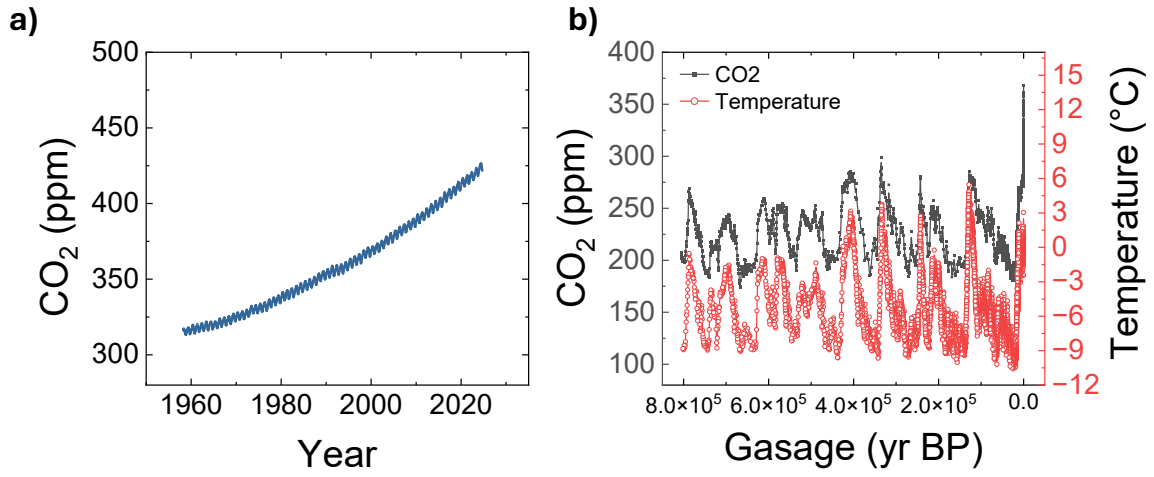



**Figure 1.2 Atmospheric Carbon Dioxide Concentrations**

(a) The longest continuous direct measurement of carbon dioxide ($CO_2$) concentrations in the Earth's atmosphere at the Mauna Loa Observatory in Hawaii.[5] (b) Paleoclimatic temperature values (red circles) and $CO_2$ concentrations (black squares) are based on a composition of ice core data sets.[6-10]

The rising amount of greenhouse gases (GHG), including $CO_2$, causes increased radiative forcing in the Earth's atmosphere.[15] This, in turn, pushes the Earth to a higher-energy equilibrium with higher temperatures and larger amounts of water in the atmosphere. The number of natural disasters and extreme weather events like droughts, heavy rainfall, heat, flooding, and storms increases. Sea levels are currently rising at an accelerating rate of more than 3 mm each year due to the thermal expansion of water and the melting of land ice.[16,17] This is threatening 600 million people (about 10% of the world's population) living in coastal areas less than 10 m above the current sea level.[17] Extreme weather events are occurring with rising frequency globally, but are disproportionately affecting people of weaker socio-economic communities, especially in lower-income countries in the global south.[18,19]

To mitigate the adverse effects of climate change, humanity must urgently reduce the emissions of greenhouse gases. Projections show the need for a radical change in the trajectory of GHG emissions to keep within the 2.0 °C target to avoid catastrophic effects on the human population (Figure 1.3). A change in energy provision is vital to achieve this. Today, over 80% of the primary energy demand is still met by burning fossil fuels.[20] This, in turn, is responsible for almost three-quarters of the global GHG emissions.[20] Therefore, a rapid switch to renewable energy sources is necessary. Systems based on renewable energies do not emit GHG during energy provision and are significantly less harmful to the environment over their lifetime than fossil-fuel-based systems.[21,22]

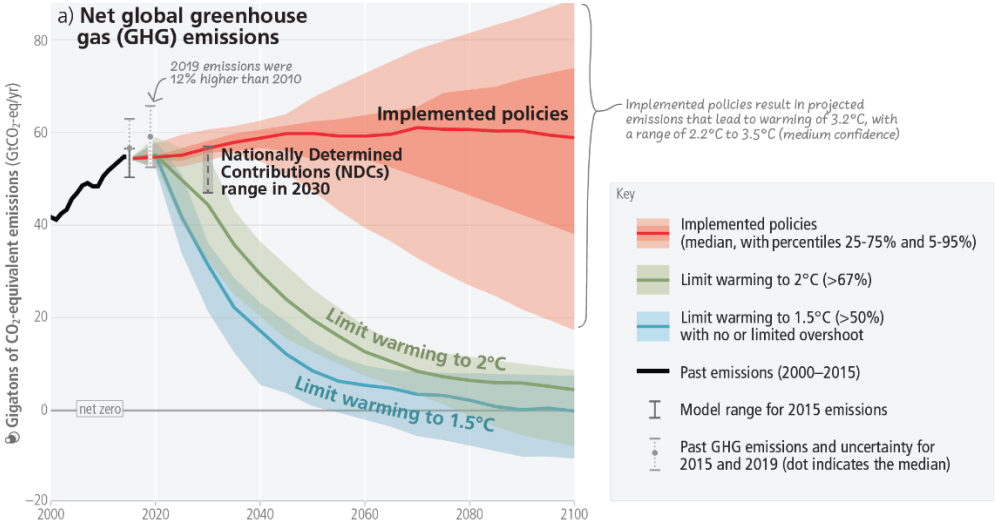



**Figure 1.3 Global Greenhouse Gas Emission Pathways for Different Warming Scenarios**

Greenhouse gas emission global modelled pathways for certain probabilities to reach different limitations of global warming compared to policies implemented in 2020. The shaded area around the lines indicates the 5th to 95th percentile across the pathways. Emissions for 2015 and 2019 are indicated with a median as a black dot and uncertainties with black whiskers. Figure from Calvin et al.[4]

## 1.2 Photovoltaics

To meet the growing energy needs of the world's population, humanity needs to use multiple sources of renewable energy in combination. The most widely available source in terms of quantity and spatial distribution is solar radiation (Figure 1.4). It could provide more than a thousand times the equivalent of the current world energy demand.[23] On a global scale, photovoltaics (PV) have the highest relative growth in installed generation capacity of all renewable energy sources. It is expected to replace wind as the biggest renewable source in terms of generation capacity within this decade.[24]

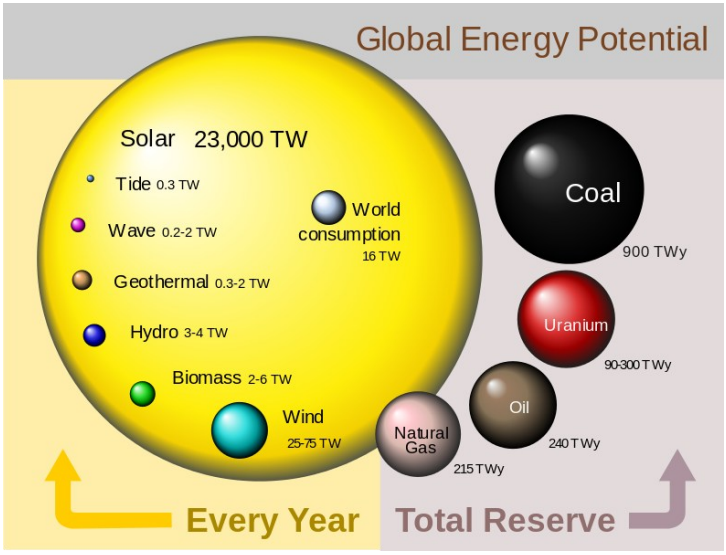



**Figure 1.4 Available Energy Source on the Earth's Surface**

On the left side is the average power in terawatt (TW) provided to the Earth's surface by different renewable sources over one year. The right side displays the energy in TWy of all the reserves of conventional energy sources. Solar energy is the largest renewable source with 23,000 TW. Over one year, solar energy reaching Earth has been higher than the energy from all conventional reserves. Solar power is more than 1,000 times the average world power demand. Figure and data from Perez et al.[25,26]

PV directly converts incoming light into electricity. This direct conversion makes PV systems simpler to operate and install than thermal power plants, such as biomass, geothermal, or solar-thermal. Furthermore, PV systems usually contain no moving parts, making them significantly less maintenance-intensive than all other power plants. PV systems can be easily adapted to varying local demands, with their power output and area adjustable by modifying the number of modules fielded. The deployment and operation of PV systems are undemanding, enabling their use in remote locations and by private individuals. They are well suited to decentralised energy provision and stand-alone systems, which is difficult using other power sources. PV during operation is free from noise and other emissions and can hence be installed directly into human settlements. Furthermore, solar power is available in the daytime, coincidentally being the peak time of human awake hours and power demand.[27,28] While PV will be a major part of the future world's energy mix, it must be combined with other sources. This will be necessary to ensure a reliable energy supply at night-time and in places further away from the equator.

A semiconductor material is used for the light absorption process in PV (see 2.1 Semiconductor Physics). In semiconductors, there is a discontinuity in the energy states that can be occupied by electrons within them. This continuity is called the band gap. When a photon with energy larger than

the band gap hits the material, the photon can be absorbed, exciting an electron from an energy state below the band gap to one above it (see Figure 1.5 b). This creates an unoccupied state below the band gap with a net positive charge (see Photovoltaic Effect). This empty state can be treated as a quasi-particle and is called a “hole”. By separating these opposingly charged carriers - the hole and the electron - and extracting them from the absorber at different electrodes, a voltage can be obtained and electric energy can be drawn from the PV device (for more detail see Solar Cell Working Principles).

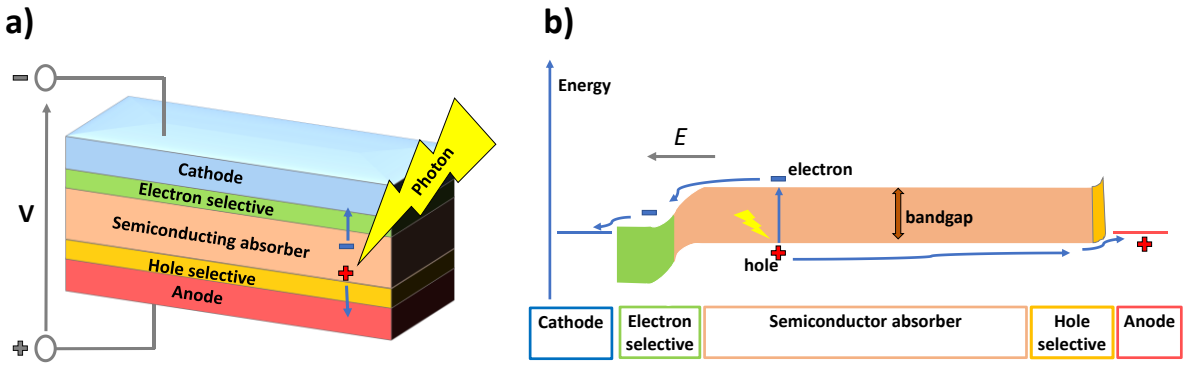



**Figure 1.5 Schematics of a Solar Cell**

a) Simplified device architecture of a solar cell and b) simplified relative alignment of energetic states as well as light absorption and charge extraction process with an n-p junction to the left and a $p^+$ hole selective layer to the right.

### 1.2.1 Silicon Photovoltaics

The currently most used absorber in PV is crystalline silicon (Figure 1.6a). Silicon has been used for PV applications for decades, dating as far back as 1941. In over half a century of research and real-world application, the technology has progressed greatly.[29] With the production of silicon-based modules increasing exponentially, prices decreased exponentially (Figure 1.6b).[30,31] Silicon PV has also benefited from shared production processes and supply chains with the integrated circuit industry. The rapid decline in module prices has lowered the price of electricity generated by PV systems below all types of fossil energy carriers (Figure 1.6d).[30–32] The International Energy Agency concludes in its 2020 World Energy Report that solar PV is already the cheapest electricity source in all the major markets today. In addition, it is also cheaper than any other source in the history of electric energy.[33]

The stability of silicon PV technology is relatively high, with some producers offering warranties for silicon panels to retain more than 90% of their initial power output after 25 years of operation.[34] These warranties on stability are a result of decades of production and application experience and optimisation. The combination of these warranties and ever-lower module prices facilitates the implementation of silicon PV today. As a result, silicon technology makes up over 97% of all PV modules produced globally in 2023 (Figure 1.6a).[30]

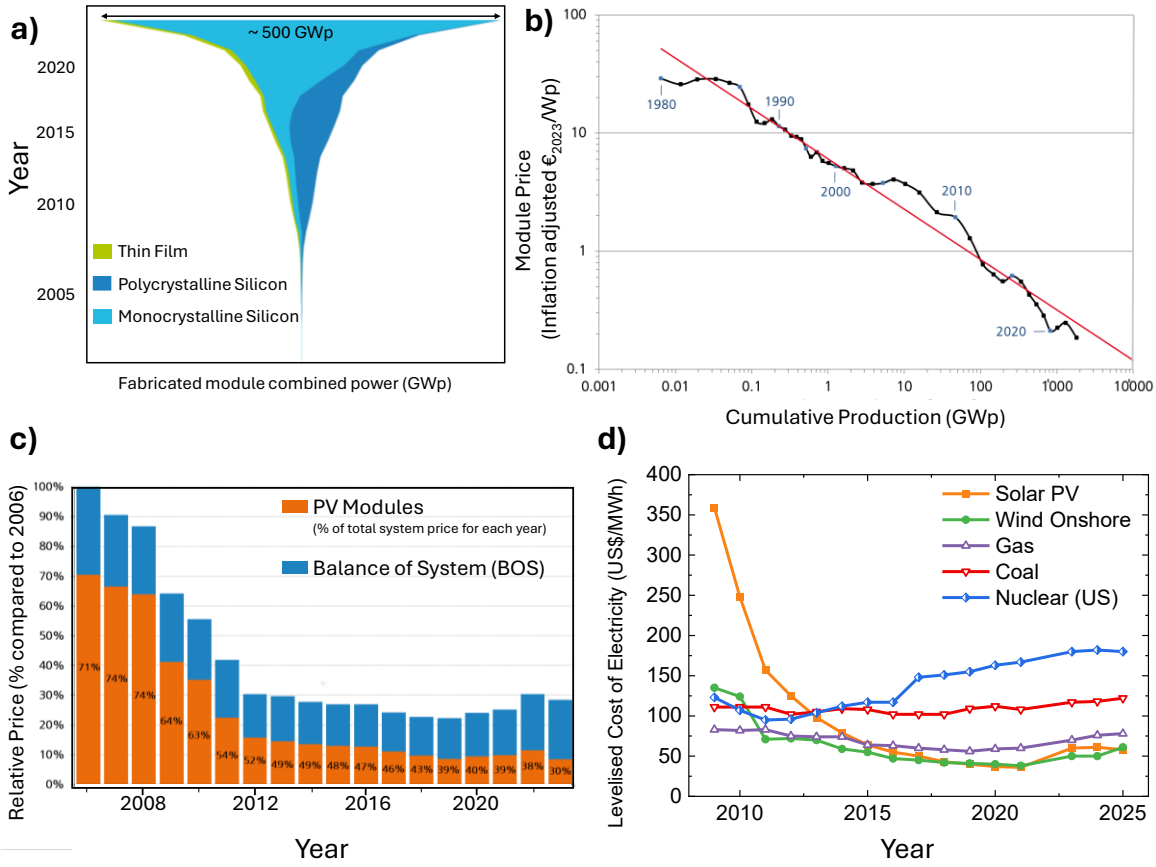



**Figure 1.6 Growth in Photovoltaics**

(a) Contributions of different technologies to the increased total PV module produced in GWp up until ~500 GWp in 2023. (b) Historical development of PV module prices in € per Wp adjusted to 2023 prices against the cumulative production of PV modules in GWp. A learning curve was fitted to the logarithmic data. (c) Relative price development of PV systems in Germany compared to 2006 prices. Dark blue represents the fraction of the system other than the cost of the modules (Balance of System Costs - BOS), and light orange is the fraction of the cost of the modules. The latter one is denoted as a percentage for each year in the column. (d) Levelised Cost of Electricity of new energy systems of different technologies installed in the United States of America for each year in US$/MWh over the system's lifetime. For 2025 solar PV is with 58 US$/MWh the cheapest source of electricity and nuclear with 180 US$/MWh the most expensive. (a) - (c) adapted from Fraunhofer ISE Photovoltaics report[30] and (d) data from Lazard.[32]

Given the successful history of silicon PV technology, it is worth noting that the physical properties of crystalline silicon are not particularly well suited for absorbing sunlight. It has a relatively low absorption coefficient of between $10^5$ and $10^3$ $cm^{-1}$ and an indirect band gap of about 1.1 eV.[35] The size of this band gap is slightly lower than the optimum for single absorbers of the solar spectrum. For the higher energetic part of the spectrum, the energy of the photons is lost when they thermalise back to the conduction band edge (see 2.2.2 Photo Absorption). The indirect band gap lowers the overall absorption probability (see 2.1.2 Indirect vs Direct Band Gap).

To ensure sufficient absorption given the unfavourable absorption properties, the absorber layer in silicon solar cells needs to be relatively thick in the order of about 200 µm. Therefore, photogenerated charge carriers need to travel relatively long distances inside a silicon solar cell. To enable efficient charge extraction, a long diffusion length and minimal recombination must be ensured. Passivation of surfaces and interfaces has led to significant improvements in reducing recombination centres. But besides that, it is still necessary to have highly pure (>99.9999%)[36] and highly crystalline bulk material in silicon solar cells. This is achieved with the complex processing of silicon material. The processing involves first a chemical treatment for purification. Subsequently, long, very high-temperature (1,373 K) processes are applied for further purification.[36,37]

Since PV do not emit any GHG directly during operation, the GHG during production needs to be carefully considered to assess the environmental impact of each technology. Of all PV technologies, silicon, due to the mentioned purification, has a high energy demand and emission of GHG during production. Because of the comparatively thick layer and complex processing of silicon, solar cells comprise relatively high intrinsic energy expenditure during production.[30]

Because of successful and advanced research on silicon, research solar cells are already close to the maximum possible efficiencies for a single absorber of its band gap (see Photo Absorption). These high efficiencies must be scaled from laboratory devices to full-size modules. Silicon photovoltaic module prices are already highly competitive. All costs of a PV power system other than the costs of PV modules, like the costs of installation and real estate, are usually summarised as Balance of System Costs (BOS). In industrialised countries, the BOS has surpassed the costs of modules. For example, in Germany, the module costs made up 30% of the total PV system's cost in 2023, down

from 71% in 2006 (Figure 1.6c).[30] Even on a global average, the cost of the modules accounts for only 31% of the total cost of the system.[30] Because of the already low price of modules, a promising strategy to further lower the Levelised Cost of Energy (LCoE) is to increase the power output of modules. This way, a higher-energy output per area and per installed module over the system lifetime is combined with equal BOS costs for module installation. Since silicon PV is already close to the thermodynamic limit for single absorber efficiencies, it is desirable to also implement other PV technologies to achieve this.

### 1.2.2 Other Absorber Materials

Several other materials that could be used as a light absorber besides silicon. The National Renewable Energy Laboratory in the US maintains a chart comparing the efficiency developments of several different researched technologies. This chart starts with the year 1976 and is frequently updated with new certified record efficiencies achieved by research cells of the different PV technologies. Because I focus on recent technology development, I plot an excerpt of the chart data from 2000 to 2025 below in Figure 1.7. The currently highest-performing silicon technology is plotted with blue dots. Other plotted single junction (SJ) absorber materials are introduced in this chapter.

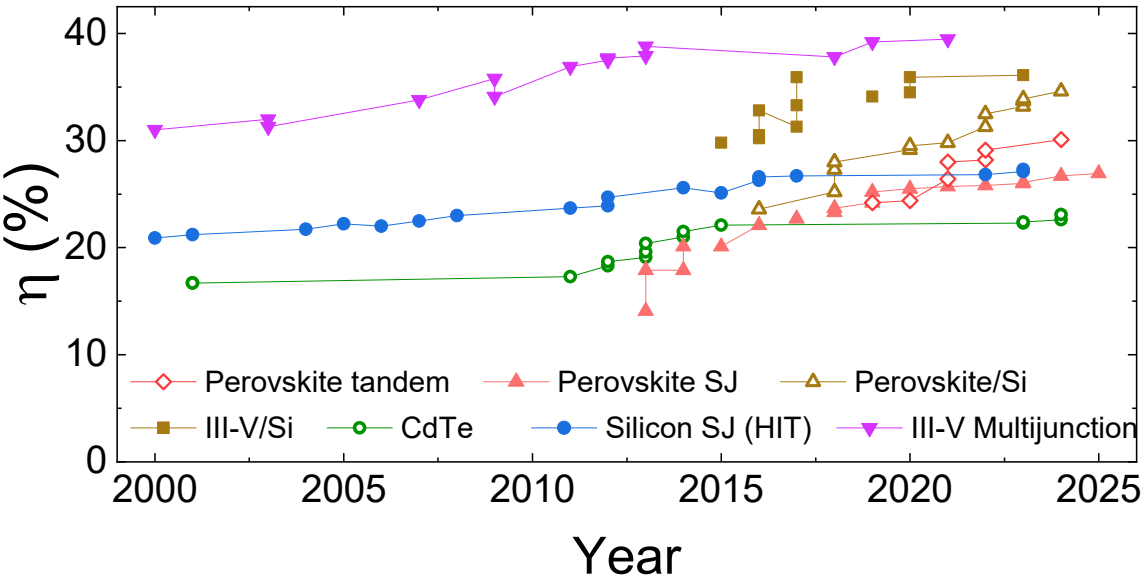



**Figure 1.7 National Renewable Energies Laboratory Chart of the best Research-Cell Efficiencies**

The table shows the development in yearly record efficiencies of laboratory cells of different relevant PV single junction (SJ) and multijunction technologies. Technologies included are perovskite-based SJ and multi junctions including perovskite-silicon tandems (Perovskite/Si), cadmium telluride (CdTe) and silicon

heterojunction SJ, and III-V semiconductors—data from the National Renewable Energies Laboratory.[28]

#### 1.2.2.1 Thin Film Technologies

Thin film PV is an early alternative to crystalline silicon technologies, using materials such as amorphous silicon, copper-indium-gallium-selenide (CIGS), and cadmium telluride (CdTe). A major advantage of thin film materials lies in their much stronger light attenuation coefficients compared to crystalline silicon. This enables the use of significantly thinner absorber layers (hundreds of nm instead of hundreds of µm), reducing both material consumption and energy requirements during production. However, thin film technologies consistently lag behind crystalline silicon in terms of efficiency. For example, CdTe cells (green in Figure 1.7) reach only 23.1% while Silicon Photovoltaics single junction (Heterostructures - blue in Figure 1.7) perform at 27.3%.

Thin film technologies have been extensively researched and successfully commercialised over several decades. At their peak in 2009, the thin film technologies collectively held more than 16% of the global PV market share. Since then, however, amorphous silicon and CIGS have almost disappeared from the market.[30] CIGS and CdTe technologies use critical materials like the rare indium and gallium, and the highly toxic cadmium. Concerns about materials' criticality and toxicity made many producers abandon their thin film ambitions.[38] CdTe, however, has continued to grow, increasing production from approximately 2 GWp in 2017 to over 12 GWp in 2023. This growth has, however, been far outpaced by silicon photovoltaics, reducing CdTe's market share to about 2.5% (Figure 1.6b).[30]

CdTe cells are mainly installed at a utility scale on large free areas. For this application, the land and installation costs per module are smaller, making module prices more important. Therefore, thin film cells can exploit their lower module costs and achieve a price advantage per installed output for large solar farm applications.

#### 1.2.2.2 Perovskite Single Junctions

In the last 15 years, organic-inorganic hybrid lead halide perovskite-based absorbers have emerged as another promising material class. In the following, they will be addressed as "perovskite" for simplicity. PV devices using this material class showed a quick increase in efficiencies, reaching or even surpassing long-established technologies like Silicon Photovoltaics and Thin Film

Technologies (Figure 1.7). This quick success was enabled by favourable material properties like its Defect Tolerance, Tunable Band Gap, and the possibility of Solvent Processing, which will all be examined in separate chapters. I research this technology because it bears great potential to revolutionise PV. Important for translating the laboratory success of this material class to commercial application are their long-term stability under operational conditions and the use of expensive raw materials. These challenges will be addressed by research presented in this thesis, focusing on overlooked contributors to device instabilities.

# 2 BACKGROUND

This chapter outlines the knowledge needed to understand the presented research on perovskite solar cells (PSC). Since solar cells use semiconductors for charge absorption and charge separation, the fundamentals of semiconductors are explained in the subsequent section. This section is partly based on the course "MS2018: Electronic and Magnetic Properties of Materials" by Professor Wang Junling I received at Nanyang Technological University, Singapore. Following the introduction, the background of semiconductors, the Photovoltaic effect, and the working principles of solar cells are described. The latter draws partly from the lecture series "Fundamentals and Technology of Solar Cells" by Professor Wolfram Jägermann and Professor Jan Philipp Hofmann, which I followed at Technical University Darmstadt.

Ensuing, PSCs are explained in more detail, including the unique properties of hybrid organic-inorganic-lead halide-perovskite semiconductors and the stability challenges PSCs face. This chapter further expands on my MSc thesis "Carbon-based electrode materials for stable perovskite solar cells", submitted to obtain my Energy Science and Engineering degree at Technological University Darmstadt.

## 2.1 Semiconductor Physics

Photovoltaic devices, as mentioned, use semiconducting materials to absorb electromagnetic light and to separate light-generated charges. Therefore, semiconductors' fundamental principles are crucial to understanding the research presented. These principles are discussed in this section. The light absorption is treated in the subsequent Chapter 2.2 Photovoltaic Effect and how semiconductors are used to fabricate functional devices is shown in Chapter 2.3.2 Device Structures.

### 2.1.1 Energy States and Bands

In the matter around us, positively charged nuclei are surrounded by shells of negatively charged electrons. The probability distribution of electrons, where the electrons are around the nuclei, also leads to a charge distribution. In isolated atoms, this probability distribution forms discrete orbitals.

Each electron needs to be unique in its energy level and momentum. Because of this, each orbital can host a maximum of two electrons of opposite spin angular momentum.

In solid-state materials, the periodic arrangement of nuclei in a crystal lattice generates a Coulomb potential variation that extends throughout the material, as well periodically. Due to the proximity of the nuclei, the orbitals of neighbouring atoms overlap, causing the probability distribution of electrons to extend across the material. As a result, the discrete energy levels of individual atoms merge to form continuous energy bands. Within these bands, electrons can occupy a continuous range of allowed energies. Certain energy ranges remain forbidden, forming band gaps limiting the bands of allowed states.

The highest occupied energy band at 0 K is called the valence band ($E_v$), and the lowest unoccupied band at 0 K is the conduction band ($E_c$). The energy difference between these bands is the band gap ($E_g$). Metals or conductors have partially filled bands at 0 K, allowing electrons to move freely (Figure 2.1a). Semiconductors, in contrast, have either fully occupied or empty bands at 0 K, with a small $E_g$ that enables limited conduction at higher temperatures. Insulators differ from semiconductors by having a large $E_g$, restricting electron flow under typical conditions.

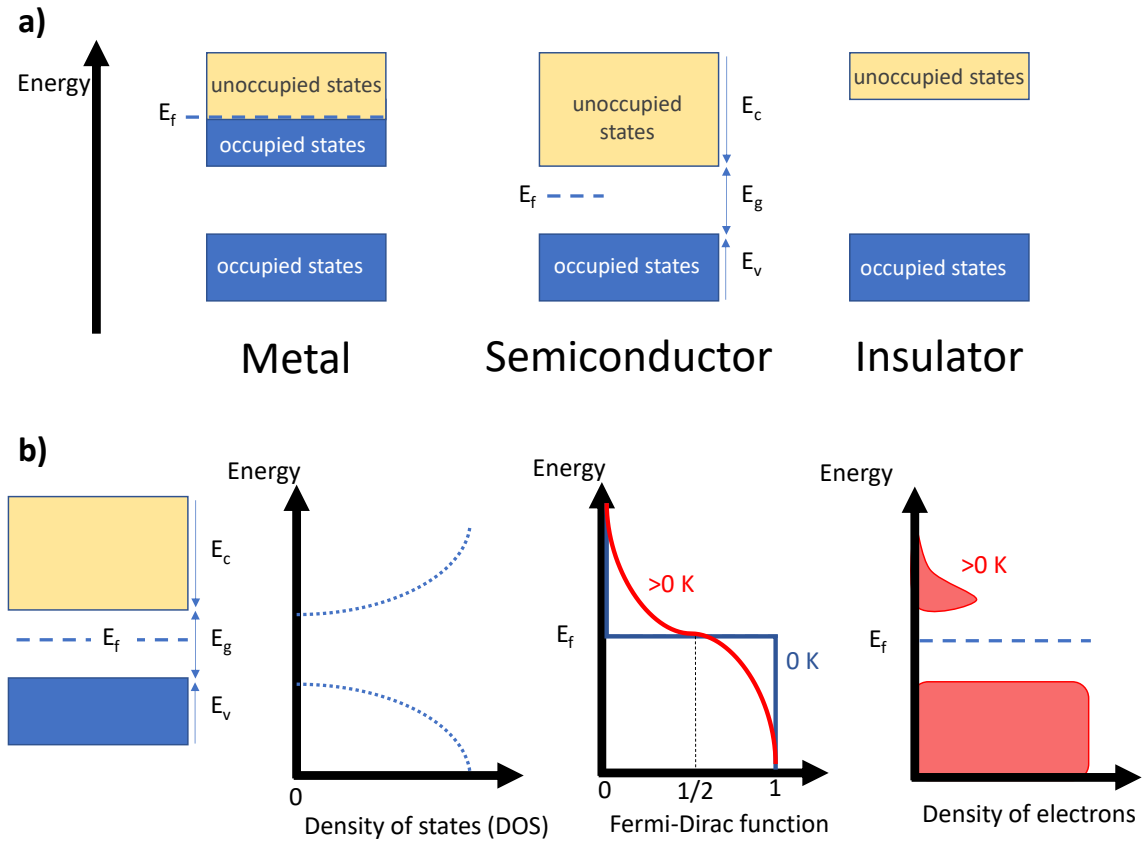



**Figure 2.1 Electronic Properties of Materials**

(a) The occupation of energy bands and energy levels (including the conduction and valence bands $E_c$ and $E_v$) in metals/conductors, semiconductors, and insulators. (b) From left to right schematics of the density of states (DOS), Fermi-Dirac probability function (probability of occupancy of a state), and density of electrons present for different energy levels in a semiconductor relative to the fermi level ($E_f$) and the band gap ($E_g$). The number of electrons is given by the product of DOS and occupation probability. Because the DOS is zero inside the band gap there are no electrons present inside the gap.

### 2.1.2 Indirect vs Direct Band Gap

In real semiconductors, the band structure is more complex than sketched in Energy States and Bands above. The real band edges are not flat as sketched in Figure 2.1a, but show local minima and maxima at different wave vectors k in momentum space. The band gap is between the valence band maximum (VBM) and the conduction band minimum (CBM). The VBM and CBM do not necessarily lie at the same position inside the momentum space. If they do not, the material is called an "indirect band gap semiconductor". If both VBM and CBM are at the same vector k, typically at Γ-point, the material is referred to as a "direct band gap semiconductor."

In direct band gap semiconductors, the alignment of CBM and VBM enables efficient electron transitions between the bands without a need for a change in momentum space (Figure 2.2).

Examples of direct semiconductors are III-V semiconductors and perovskite semiconductors. Because of the direct band gap, these materials are particularly suitable for light absorption and emission and can be used for PV and light-emitting diode applications.

In indirect band gap semiconductors, an electron transfer between the bands requires a change in momentum space. These transitions are phonon-assisted (Figure 2.2). This reduces the efficiency of light absorption and emission, complicating their use in optoelectronics. This explains the need for relatively thick absorber layers in the indirect band gap semiconductor silicon (~150 - 200 µm) as compared to the absorber thickness in the direct band gap semiconductor perovskite (~0.5 - 1 µm).

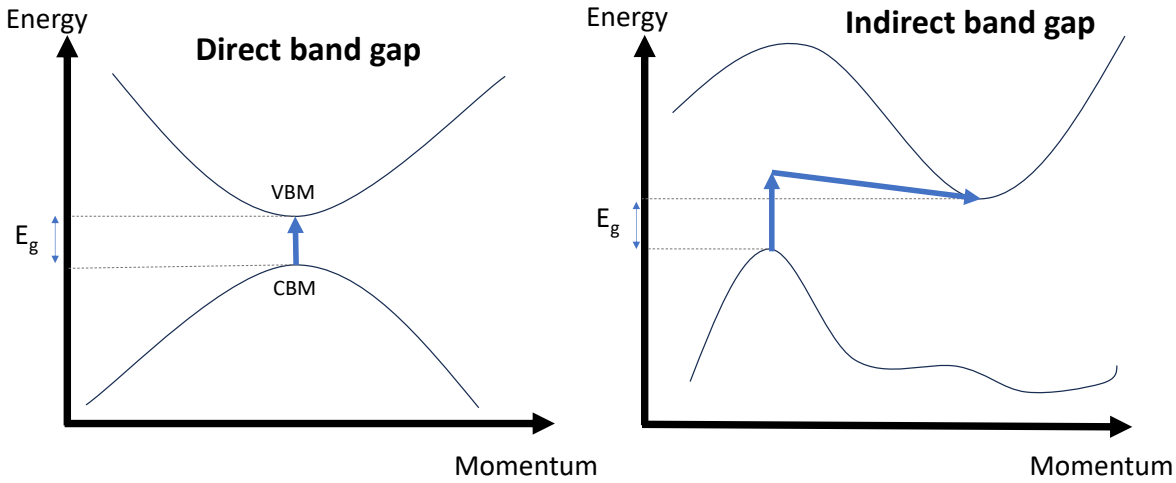



**Figure 2.2 Direct and Indirect Band Gap Semiconductor**

An example of a direct (left-hand side) and indirect (right-hand side) band gap band structure. Transitions for an electron from the conduction to the valence band for both cases (blue arrows).

### 2.1.3 Fermi Level

At absolute zero temperature (0 K), electrons occupy the lowest available energy states, filling them up to a maximum energy known as the Fermi level ($E_f$). This makes Ef the highest occupied energy level at 0 K. When thermal energy is introduced to the system (e.g., via phonons), electrons can be excited to higher energy states, leaving some lower-energy states unoccupied (Figure 2.1b). The number of electrons at certain energy levels equals the density of states g(E) at this energy level times their occupation probability (f) (Figure 2.1b). The occupation probability f of a state in a material, for a given energy E and temperature T, is given by the Fermi-Dirac distribution as follows:

$$f(E) = \left( e^{\frac{E - E_f}{k_B T}} + 1 \right)^{-1} \qquad 2.1$$

Where $k_B$ is the Boltzmann constant ($1.380649 \cdot 10^{-23}$ J/K). For $E - E_f \gg k_B T$, this can be simplified with the Boltzmann approximation to:

$$f(E) \approx e^{-\frac{E - E_f}{k_B T}} \qquad 2.2$$

The Fermi Level ($E_f$) for materials at 0 K is an important material property. It is defined by the highest occupied energy state at this temperature. At temperatures higher than 0 K, the occupation probability shifts more gradually from 1 to 0 (Figure 2.1b). The occupation probability at $E_f$ is defined as ½ in the Fermi-Dirac distribution. However, in semiconductors, $E_f$ is within the band gap where the density of states is zero. A finite occupation probability within the band gap, hence, does not indicate the presence of electrons at the given energy. The number of electrons n is given by the product of g and f:

$$n_0\,(T) = g(E) \cdot f(E) \qquad 2.3$$

The Fermi-Dirac distribution only indicates an actual occupation probability for energies with a non-zero g (available states for the given energy). Within the band gap of an ideal semiconductor, available states are absent ($g(E) = 0$ for $E_V < E < E_C$). Therefore, the Fermi level in a semiconductor does not indicate the presence of electrons but the chemical potential of the electrons at thermal equilibrium.

Electrons excited from the valence band to higher states leave unoccupied available states behind. These unoccupied electron states can be treated as positively charged quasi-particles called “holes”. This simplifies carrier transport analysis in a partially filled valence band. The probability of such a vacancy is one minus the electron occupation probability. Therefore, the number of holes (p) at a certain energy level E is given by:

$$p_0(T) = g(E) \cdot \big(1 - f(E)\big) \qquad 2.4$$

To determine the number of free electrons inside a semiconductor, we need to calculate the integrated n inside the CB. For the thermal equilibrium case, this equates to:

$$n = \int_{E_c}^{\infty} g(E)f(E)dE = N_C \cdot e^{-\frac{E_C - E_f}{k_B T}} \quad 2.5$$

with $N_C$ being:

$$N_C = 2 \cdot \left(\frac{2\pi m_e^* k_B T}{h^2}\right)^{3/2} \quad 2.6$$

Extending for the total charge carrier concentration, taking the holes in the valence band into account we get:

$$p = \int_0^{E_V} g(E)\big(1 - f(E)\big)dE = N_V \cdot e^{-\frac{E_f - E_V}{k_B T}} \quad 2.7$$

with $N_v$ being:

$$N_V = 2 * \left(\frac{2\pi m_h^* k_B T}{h^2}\right)^{3/2} \quad 2.8$$

And the total charge carrier concentration:

$$np = N_V N_C \cdot e^{-\frac{E_g}{k_B T}} \quad 2.9$$

A shift in the Fermi level within the band gap can indicate a relative change in the number of electrons present in the conduction band compared to the number of holes in the valence band. The position of $E_f$ in semiconductors shifts if electrons are removed or added to the material. The $E_f$ is approximately the middle of the $E_g$ in intrinsic semiconductors, but deviates due to different effective masses of holes and electrons. The position of $E_f$ depends on the ratio of $N_V$ to $N_C$ or the ratio of electron to hole effective mass:

$$E_f = \frac{1}{2}(E_v + E_c) + \frac{3}{4}k_B T ln\left(\frac{N_V}{N_C}\right) = \frac{1}{2}(E_v + E_c) + \frac{3}{4}k_B T ln\left(\frac{m_h^*}{m_e^*}\right) \quad 2.10$$

### 2.1.4 Doping

It is possible to introduce small amounts of impurities, for example, foreign atoms or molecules, into an intrinsic semiconductor material. Doping is a process where this is done purposefully to modify its electrical properties. Impurities that introduce extra electrons to the material are called donor impurities, and impurities depleting the material of electrons are called acceptor impurities. Depleting a semiconductor of electrons increases the number of holes. Adding donor or acceptor materials, the number of free charge carriers in the semiconductor increases, making it more

conductive. Additionally, the doping changes the majority charge carrier to be either electrons or holes, making the semiconductor's properties be dominated by either of them. A semiconductor with increased free electron concentration is called negative type (n-type), and a semiconductor with increased hole concentration is called positive type (p-type). In n-type semiconductors, the Fermi Level is shifted within the band gap closer to $E_c$, whereas in p-type material, it is shifted closer to $E_v$. This controlled manipulation of the Fermi Level enables precise control of the semiconductor's behaviour in its affinity to accept or donate electrons to other materials, its Contact Potential (see below) with other materials, and its ability to conduct electrons and holes. Changing a semiconductor's electronic characteristics enables a wide range of applications. Among others, it is crucial to enable charge extraction in solar cell devices.

### 2.1.5 Work function

The work function Φ is the minimum energy required to extract an electron from the Fermi level of a material to the vacuum level just outside its surface. Unlike intrinsic bulk properties, the work function is strongly surface-dependent. It varies not only with the type of material and its temperature, but also with surface characteristics such as crystallographic orientation, surface termination, and cleanliness. Even for the same type of material, different crystal facets can exhibit different work function values. In this work, I determined the work functions of selected materials using Kelvin probe measurements.

### 2.1.6 Contact Potential

When two materials with different energetic properties are brought into contact, a contact potential forms due to the difference in their respective Fermi Level ($E_f$). This contact potential affects the distribution of charge carriers and the energy levels at the interfaces. The two Fermi Levels of the two materials align while an electron transfer occurs across the interface (Figure 2.3). This exchange leads to a potential difference at the interface, proportional to their difference in work functions. When two metals with different $E_f$ come in contact, the contact potential forms, but no band-bending occurs (Figure 2.3a).

When a metal is brought into contact with a semiconductor, a so-called Schottky Junction forms. At this interface, the behaviour depends again on the relative work functions of the two materials. If the metal has a deeper $E_f$ than the semiconductor, electrons transfer from the semiconductor to the metal, causing the bands in the semiconductor to bend up at the interface, presenting a barrier for electrons (Figure 2.3b). We assume such contact is formed at the interface between the carbon electrode and the $SnO_2$ ETL of devices presented in Chapter 4. If the metal's $E_f$ is shallower, it transfers electrons into the semiconductor, which displays a band-bending upwards, forming a barrier for electrons at the interface. In the first-mentioned case, the transfer of electrons from the metal into the semiconductor is blocked, and in the second case, the transfer of electrons from the semiconductor into the metal is blocked.

When two semiconductors are brought into contact, the alignment of their Fermi levels leads to band-bending within each material. The degree of this bending depends on the charge carrier concentrations of the semiconductors. If one semiconductor is brought in contact with a material with a shallower (higher up) $E_f$ the contact causes the bands to bend down at the contact area because electrons are transferred into this material. The area of the bend-down bands is depleted of electrons and is hence called the depletion zone. In turn, if the other material has a deeper (further down) $E_f$ electrons are transferred from this material into the semiconductor, causing the bands to bend up to shallower levels (Figure 2.3c). This creates a depletion region at the junction, where charge carrier concentrations are significantly lower, and causes an internal electric field.

These kinds of junctions (semiconductor-semiconductor and Schottky) are used for many semiconductor devices, including diodes, because they control the flow of charge carriers under biases, blocking charge transfer in one direction and allowing it in the other. They display a rectifying behaviour, forming a diode. If the energy alignment between the materials results in no preferential direction of charge transfer across the interface with minimal resistance and no significant barrier, we speak of an ohmic contact. Diodes are crucial for charge separation inside a solar cell. Ohmic contacts are critical for the extraction of charge carriers from the solar cell after they have been separated.

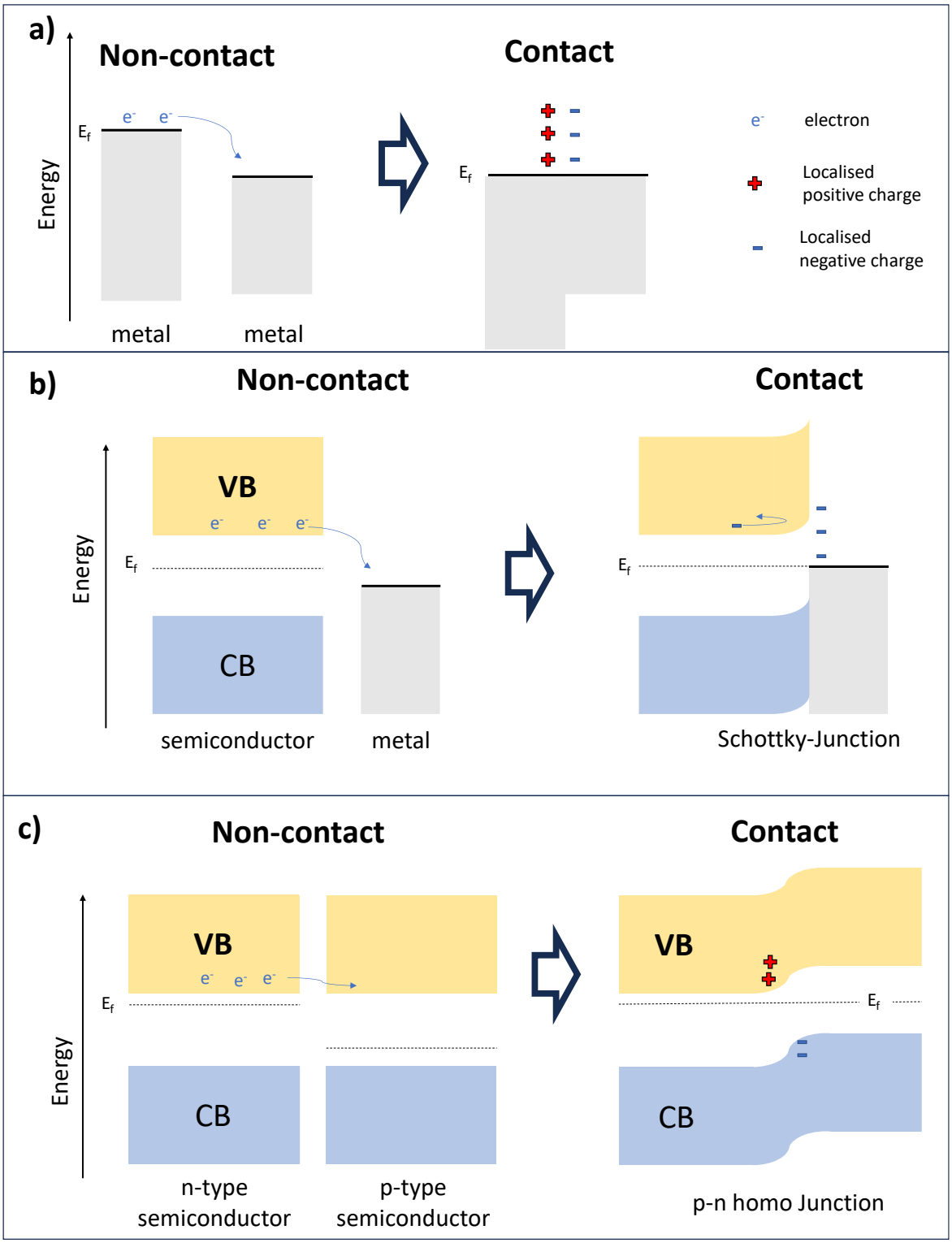



**Figure 2.3 Junctions**

Different junctions formed for materials with different fermi levels $E_f$ brought into contact. (a) a metal-metal contact with indicated contact potential, (b) an example of a metal-semiconductor contact forming a Schottky junction, and (c) an example of a semiconductor-semiconductor junction forming when an n- and a p-doped material of the same band gap is brought in contact forming a p-n homo junction.

### 2.1.7 Recombination Processes

When two opposing charge carriers are generated in the same material without being extracted, they will recombine. There are three different pathways for this electron-hole recombination, which will be explained here.

#### 2.1.7.1 Radiative

Radiative, or band-to-band recombination, is when an electron from the conduction band recombines directly with a hole in the valence band. The energy difference is emitted as a photon with the energy corresponding to the material's $E_g$. This process is exactly the reverse process of light absorption and happens analogue to the light absorption more efficiently in direct band gap semiconductors like perovskites. This recombination process is generally unavoidable in semiconductors by material engineering. It is a two-particle process because only an electron and a hole are involved.

#### 2.1.7.2 Trap Assisted

For trap-assisted recombination to occur, there need to be energy states within the band gap. These energy states arise from defects in the crystal lattice, like vacancies (unoccupied sites) and interstitials (ions between regular lattice sites). Charge carriers transfer from the bands into these isolated states and get trapped in them. From the trapped state, the charge carrier can recombine. Traps with energy states close to the band edges are called shallow traps. Charge carriers can de-trap out of them and remobilise (electrons back into the $E_c$ and holes into $E_v$). Traps further towards the middle of the band gap are called deep traps (or midgap if they are in the centre). Charge carriers trapped in deep traps are less likely to de-trap and more likely to recombine across the band (Figure 2.4b). This process is undesirable because these charge carriers in deep traps are lost and cannot be extracted from the device. An important property of perovskite absorbers is their relatively large Defect Tolerance described below.

A major strategy to improve solar cells in general, and PSCs in particular, is to reduce the number of deep traps inside the device. Avoiding the formation of defects during the processing is difficult. Another strategy to reduce the impact of these defects is their passivation by employing a material that selectively occupies the defect locations inside the lattice without causing states inside the band gap. Passivation strategies are distinguished by locations in the device where they are applied. Inside

the absorber layer (perovskite layer), they are referred to as bulk passivation and on the interfaces to adjacent layers (ETL and HTL) as interface passivation. Throughout this thesis, a perovskite bulk passivation is achieved by adding a small quantity of a passivating molecule into the perovskite layer (see Perovskite Layer below).

A method to investigate the impact of trap-assisted recombination is photoluminescence, including time-resolved photoluminescence (TRPL) and photoluminescence quantum yield (PLQY). In both these methods charge carriers are generated inside the absorber layer by controlled photoexcitation. The light emitted as a consequence is measured to analyse the extent of radiative and trap-assisted recombination and at what speed the two processes occur in the semiconductor (for more details, see Photoluminescence Quantum Yield and Time-Resolved Photoluminescence in the Methods section). Both methods are employed throughout this work, especially to analyse the degradation of perovskite films in Chapter 6.

#### 2.1.7.3 Auger

In Auger recombination, an electron recombines with a hole across the band gap, similar to the process of radiative recombination. But instead of emitting the energy difference as a photon, the recombining electron transfers the energy to another electron in the conduction band (Figure 2.4b). This other electron is excited within the conduction band to a higher-energy state and thermalises back to the band edge subsequently. Since both electrons need to be close to each other and to a hole Auger recombination is a three-particle process. For this reason, Auger recombination generally becomes important for relatively high charge carrier concentrations to enable high enough probabilities for all three charge carriers involved to encounter each other. This process is assumed to be less relevant in PSCs under normal operation compared to the other two recombination pathways.

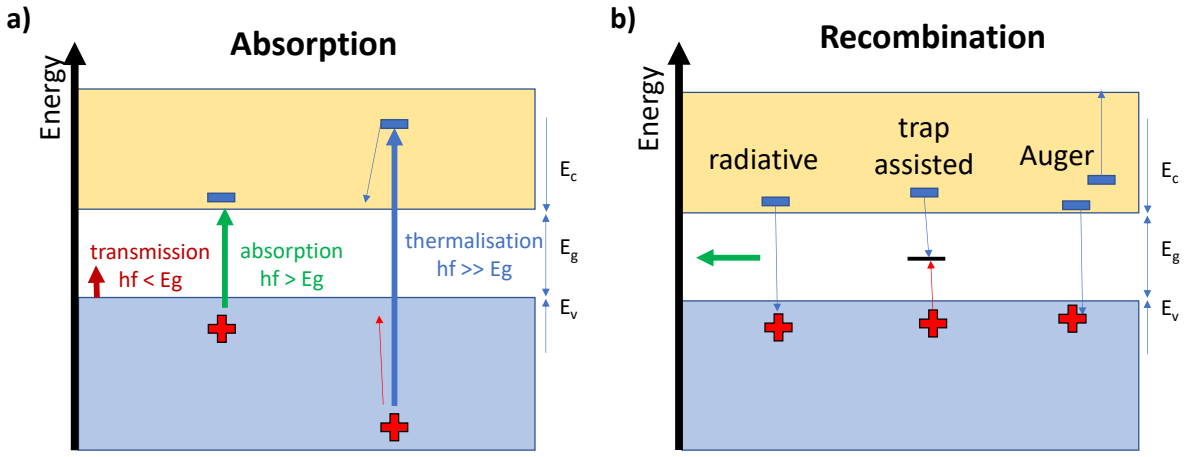



**Figure 2.4 Absorption and Recombination**

(a) Absorption and charge carrier behaviour dependent on the photon energy hf relative to the band gap Eg. If hf < Eg the photon passes through the material (red arrow). If hf ≥ Eg absorption takes place (green arrow). If the photon energy is larger than the band gap the energy difference will be thermalised with the charge carriers relaxing back to the band edges (blue arrow). (b) Different types of charge carrier recombination, including the respective energy dispersion processes.

## 2.2 Photovoltaic Effect

### 2.2.1 Light

Light in everyday language refers to electromagnetic radiation of wavelengths between ultraviolet (UV) light at around 400 nm to infrared (IR) radiation at around 1000 nm. The source of the incident daylight at the Earth's surface is radiation emitted by the sun. The spectrum of this light follows approximately the blackbody radiation of a body at the temperature of the sun. The deviation from this black body radiation is caused by absorption inside the sun's and the Earth's atmosphere. This absorption depends on the gas concentration and the path length of the light in the atmosphere. To enable comparison of PV devices measured in a laboratory environment, a standardised light spectrum was needed. For terrestrial applications, a spectrum calculated to the equivalence of passing through 1.5 times the thickness of the Earth's atmosphere has been used. This spectrum is called AM1.5g (air mass 1.5 globally). The power density of AM1.5g is 1000 W/m$^2$ and will also be referred to as one sun intensity.

For space applications, the AM0 spectrum is used, which is the spectrum at the top of the Earth's atmosphere without any Earth-atmosphere-related absorption.

### 2.2.2 Photo Absorption

The Lambert-Beer Law describes how light is absorbed in semiconductors. The intensity of light striking a semiconductor follows an exponential decay on its path inside the material:

$$I_{Ph}(hf, z) = I_{Ph}^{0}(\lambda) \cdot e^{-\alpha(hf)z} \qquad 2.11$$

Where $I_{\mathrm{Ph}}^{0}$ is the intensity of the light at the top surface of the semiconductor, z is the penetration depth, hf is the energy of the light, and α is the material and wavelength-dependent absorption coefficient. As mentioned in Indirect vs Direct Band Gap, α is larger, resulting in a stronger light absorption, in direct band gap semiconductors. Because of reflection the internal $I_{\mathrm{Ph}}^{0}$ is smaller than the external incoming $I_{\mathrm{Ph}}^{0}$.

Upon photon absorption within a semiconductor, an electron is excited from a lower to a higher-energy state similar to the thermal excitation mentioned (see Energy States and Bands). Whether this happens depends on the absorption probability of the material for a given light energy. Three cases can be distinguished in a simplified approach:

1. $hf < E_g$ → no absorption
2. $hf = E_g$ → absorption
3. $hf > E_g$ → absorption and thermalisation of energy difference $\Delta E = hf - E_g$

where hf is the energy of the incoming photon and $E_g$ is the absorber band gap (Figure 2.4a). In case 3. charge carriers are excited to a state away from the band edges. These charge carriers are called hot carriers. Hot carriers thermalise back to their lower-energy states on the band edges. The optical charge carrier generation $G_{\mathrm{opt}}(\lambda, z)$ inside the material follows:

$$G_{opt}(hf, z) = I_{Ph}^{0}(\lambda) \cdot \alpha \cdot e^{-\alpha(hf)z} = \frac{dI_{Ph}(hf,z)}{dz} \qquad 2.12$$

## 2.3 Solar Cell Working Principles

A solar cell is a device that converts incoming light into an electrical output. Multiple solar cells are usually connected in parallel and series in a single packaging, forming a solar module or solar panel. This work focuses on improving materials for a single solar cell. This can later contribute to improved

solar panels. However, integrating these materials and solar cells into modules was not part of my work, and is hence not discussed in this thesis.

### 2.3.1 Charge Separation

To generate electricity, a solar cell relies on charge carriers (electrons and holes) that are generated in the absorber layer when photons are absorbed (see Photo Absorption). If these photogenerated carriers are separated and transported to the respective electrodes, the charge imbalance leads to an external voltage in a solar cell device. When the external circuit is connected, this potential drives a current, enabling the conversion of absorbed light into usable electrical power. The internal electric field of the device, typically established by a built-in potential at a junction (see Contact Potential), drives this separation. Without extracting the charges, they recombine at the rate U equaling the generation rate G. For the charge carriers to conduct usable work, they must be extracted before recombining. The lifetime of charge carriers (the time they are present until they recombine) can be calculated through the lifetimes of each of the recombination processes:

$$\frac{1}{\tau_{total}} = \frac{1}{\tau_{rad}} + \frac{1}{\tau_{trap}} + \frac{1}{\tau_{Auger}}. \qquad 2.13$$

To achieve an efficient extraction, the devices need to employ a structure of having extraction layers, as described in Device Structures below close enough to the point of charge generation. The distance between the charge generation and extraction layer needs to be in the order of the diffusion length of the carriers inside the absorber layer. The cell can be kept at different voltages as described below in Current Density-Voltage Behaviour.

### 2.3.2 Device Structures

All solar cells are made up of multiple layers with different functions. The core is the light absorber in which holes and electrons (see 2.1.1 Energy States and Bands) are generated upon photon absorption (see 2.2 Photovoltaic Effect). This layer is usually used to classify solar cells into different technologies (see 1.2 Photovoltaics). In the work presented in this thesis, I use lead halide perovskite semiconducting material as the light absorber (see 2.4 Perovskite Solar Cells).

After the charge generation, the opposingly charged holes and electrons need to be spatially separated to generate a voltage. This can be achieved by creating a junction inside the light absorber (like the p-n homo junction in differently doped silicon or the CdS/CdTe heterojunction in CdTe). Another way is to sandwich the absorber layer between two charge transport layers, one of them selectively accepting electrons, called the electron transport layer (ETL), and the other one holes, called the hole transport layer (HTL). Under illumination, a voltage forms between the junctions at the charge transport layers interfacing with the light absorber.

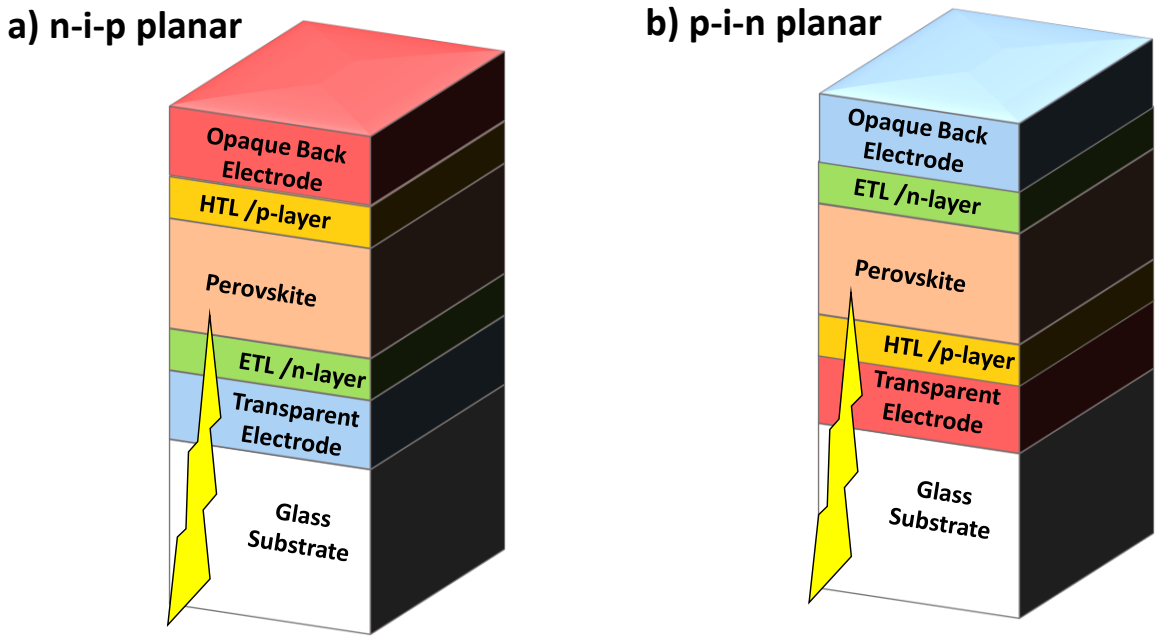



**Figure 2.5 The n-i-p and p-i-n Structures**

(a) The device structure of an n-i-p perovskite solar cell with light entering (from the bottom) through the electron transport layer (ETL) into the perovskite layer. (b) The inverted p-i-n structure with the hole transport layer (HTL) on the light-facing side of the perovskite solar cell device.

In PSC, charge transport layers are used around an intrinsic, undoped perovskite layer. The HTL is referred to as the positive (p) layer, the ETL as the negative (n) layer, and the perovskite as the i-layer. If the ETL is placed on the light-facing side, the architecture is called n-i-p (Figure 2.5a). If the HTL is used on the light-facing side, the architecture is called the p-i-n structure(Figure 2.5b). In this work, I use mainly the p-i-n structure. In this structure, a transparent HTL is needed. Compared to the n-i-p, where usually metal oxides are used as transparent ETL, the transparent HTL in p-i-n is, in most cases, an organic material.

An important parameter for the successful solution processing of nanometer-thick layers is the wettability. Wettability describes how well a liquid spreads on a surface. Poor wettability can lead to non-conformal and incomplete layer formation in a solution process. Standard methods to improve the wettability, like ultraviolet-ozone treatment, cannot be used on organic layers without destroying them. That makes the perovskite deposition on organic HTL more challenging compared to inorganic ETL, which tolerates such treatments. I insert a layer of alumina nanoparticles between my polymeric HTL polyTPD (Poly(N,N'-bis-4-butylphenyl-N,N'-bisphenyl)benzidine) and the perovskite layer to enhance the wettability.

After charge generation and separation, the charges need to be drawn from the device to provide power. The p- and n-layers need to be separately contacted by an electrode for this purpose. On the light-facing side, this electrode needs to be transparent to let the incoming light through to the absorber layer. While metal grids are commonly used in silicon solar cells, in thin film and perovskite devices, usually transparent conductive oxides (TCO) are used. The two most common TCOs are indium tin oxide (ITO) and fluorine-doped tin oxide (FTO). In Chapter 6 I show a direct comparison between these two materials and investigate their respective influences on the long-term stability of PSC. On the light-averse side, an opaque electrode material can be used. Commonly evaporated metal layers or printed carbon electrodes are used. Both were examined throughout this work.

Carbon electrodes form a special case as they can be used in the “hole-transport layer-free” architecture. In this architecture, an ETL/perovskite bilayer is followed directly by a carbon electrode. The carbon electrode then accepts holes directly from the perovskite layer. There have been discussions about the carbon behaving hole-selective. We investigate this hole selective behaviour and the ability of carbon electrodes to accept electrons instead of holes from a PSC. The results are presented in Chapter 4.

### 2.3.3 Current Density-Voltage Behaviour

An important part of the behaviour of a solar cell is its current-voltage output. To measure this behaviour the bias applied to the solar cells is swept through a defined voltage range and the corresponding current is measured. It is common to plot the applied voltage against a current density $J$ instead of absolute current values to be able to compare solar cells with different active areas. A

good solar cell shows a diode behaviour. Ideal diodes follow the ideal diode equation of current density out $J$ for an applied bias $V$:

$$J(V) = J_0 \cdot \left(e^{\frac{eV}{k_B T}} - 1\right) \qquad 2.14$$

In the dark, an ideal solar cell's behaviour would follow the ideal diode equation. Therefore, the plotted $JV$ scan should show a close-to-squared shape with a constant current for a voltage range from zero until close to the internal diode's turn-on voltage. Then, there should be a rapid decrease in the current. The more a real cell deviates from this shape, the more it shows non-ideal internal resistance behaviour (see Series and Shunt Resistance below). This could be caused by weak charge separation, low shunt resistance lowering the current density and/or bad charge extraction and high series resistance lowering the voltage.

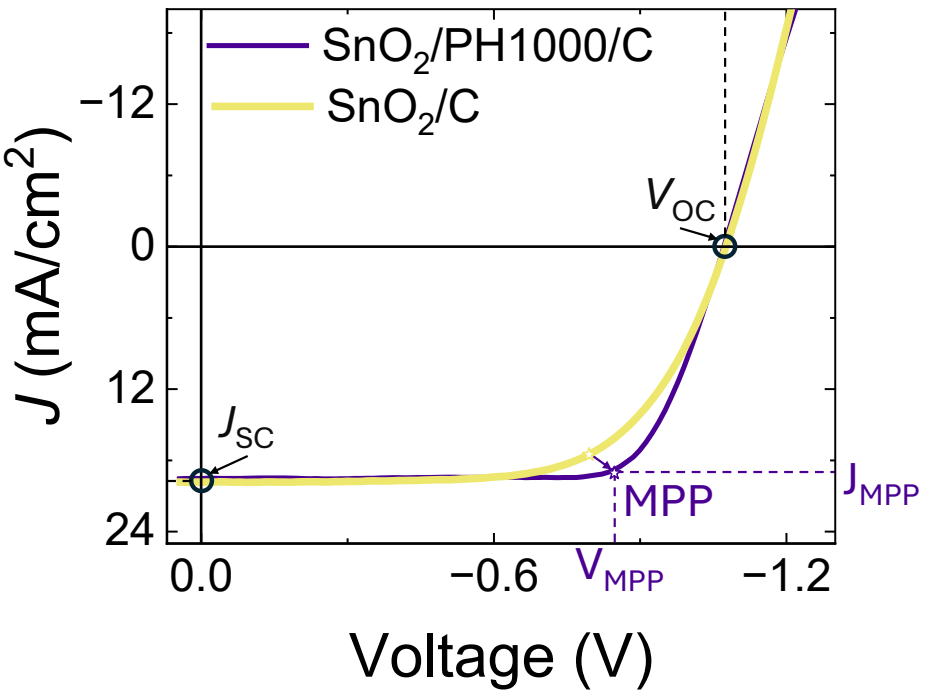



**Figure 2.6 Example of Current Density-Voltage Scans**

Current Density-Voltage (JV) forward scans for two different cell stacks. The short circuit current density ($J_{SC}$) and open circuit voltage ($V_{OC}$) are indicated by black circles. The two device stacks both start with FTO/polyTPD/perovskite/PCBM, and one is completed with $SnO_2$/carbon (yellow) and the other one with $SnO_2$/PH1000/carbon. While both devices have almost the same $V_{OC}$ and $J_{SC}$, the device with a PH1000 layer between the tin oxide ($SnO_2$) and carbon runs through a higher-power $JV$ area. It shows the more ideal and more square-shaped behaviour and has a higher fill factor (FF) than the one without. The maximum power point (MPP) - the highest J · V product - is indicated with a star in the same colour as the $JV$ curve it is part of. The $J$ and V values corresponding to the champion cell MPP ($J_{MPP}$ and $V_{MPP}$) are indicated on the axes.

The current density at zero voltage is called short circuit current density ($J_{SC}$) and the voltage at zero current is called open circuit voltage ($V_{OC}$). In the case of a non-ideal solar cell, all generated charges would be extracted and $J_{SC}$ would equal the amount of generated charge carriers per area. The *JV* behaviour of an ideal solar cell under illumination can be modelled by an equivalent circuit with a current source (representing the light-generated $I_{Ph}$) in parallel to the internal diode (Figure 2.7a). The external *JV* behaviour of such a device would hence follow:

$$J(V) = J_0 \cdot \left(e^{\frac{eV}{k_B T}} - 1\right) - J_{SC} \qquad 2.15$$

The product of voltage and current under illumination gives the cell's output power. The maximum possible product out of related current and voltage values along a *JV* scan is the maximum power point (Figure 2.6). The corresponding bias and current density are called $V_{mpp}$ and $J_{mpp,}$ respectively. For a perfectly squared *JV* scan, $V_{mpp}$ would take the same value as $V_{oc}$ and $J_{mpp}$ would equal $J_{sc}$. The ratio between the products of the two *JV* pairs provides, therefore, a measure of how close a *JV* curve is to an ideal square. This measure is called the fill factor, *FF*:

$$FF = \frac{V_{mpp} * J_{mpp}}{V_{oc} * J_{sc}} \qquad 2.16$$

The fill factor is the ratio of the area of the square spanned by $V_{OC}$ and $J_{SC}$ that is "filled" by the measure *JV* scan. The light influx of the simulated sun spectrum can be described as power input to the cell. By comparing this input power with the maximum output power from the JV scans, the power conversion efficiency (PCE) of the cell can be calculated:

$$PCE = \frac{P_{out}}{P_{in}} = \frac{V_{oc} * J_{sc} * FF}{P_{sun}} = \frac{J_{MPP*} V_{MPP}}{100\ {}^{mW}/_{cm^2}} \qquad 2.17$$

The simulated sunlight (as described in Light above) has a power of 100 mW/cm$^2$. Hence, the power density as a product of J · V in mW/cm$^2$ equals in value of the corresponding PCE in %.

### 2.3.4 Series and Shunt Resistance

An ideal solar cell can be represented by a diode with a current source in parallel (see Figure 2.7a) with the current source being the light-generated charge flow. In real solar cells, this ideal behaviour is never fully achieved. The deviation between the real and ideal case can be modelled by adding shunt (or parallel) resistance ($R_{SH}$) and series resistance ($R_S$) to the circuit (Figure 2.7b). At zero

current (V = $V_{OC}$), no current flows through $R_S$, so the voltage drop across $R_S$ and its influence on the $V_{OC}$ are zero. At V = 0 (close to) all current flows through the terminal and ~ 0 current through the $R_{SH}$, making the voltage drop and influence of $R_{SH}$ at zero volts zero as well. Out of the *JV* scan, it is possible to calculate an estimate for these resistors (Figure 2.7c). The estimate for $R_S$ is obtained from the slope of the *JV* curve at V = $V_{OC}$, and the estimate for $R_{SH}$ from the slope of the *JV* at V = 0 V.

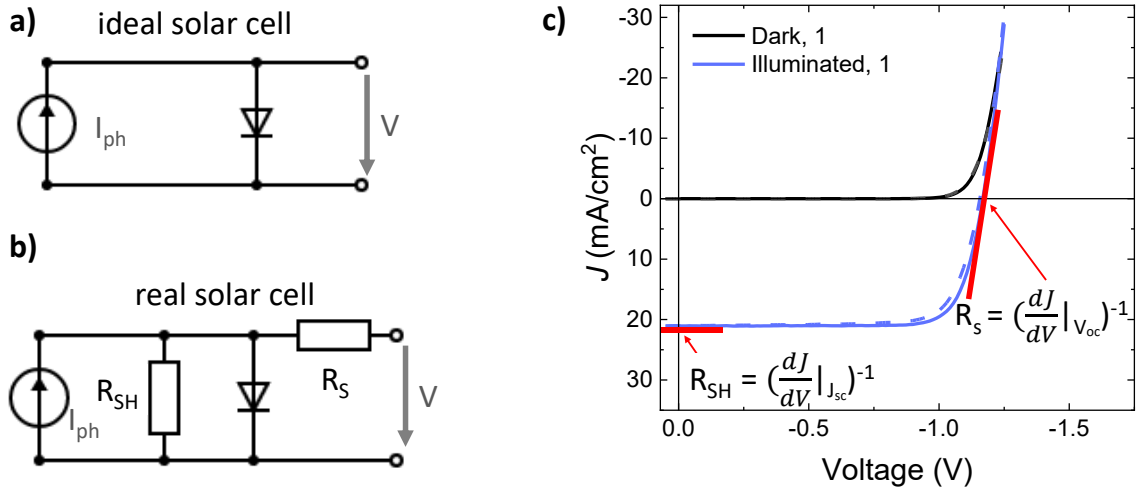



**Figure 2.7 Equivalent Circuit of a Solar Cell**

An ideal solar cell can be modelled with the circuit diagram in a). Real solar cells differ from this behaviour. The deviation can be modelled by introducing a shunt resistance $R_{SH}$ and a series resistance $R_S$ as displayed in b). The values for $R_{SH}$ and $R_S$ can be obtained from *JV* scan data as shown in c). The shunt resistance equals the inverse first derivative of the curve at $J_{SC}$. On the other hand, $R_s$ equals the inverse slope at $V_{OC}$. For a solar cell close to the ideal behaviour, $R_{SH}$ takes values close to infinity and $R_S$ approaches zero. Hence, the slope of the resulting *JV* curve should be close to zero at $J_{SC}$ and close to infinity at $V_{OC}$. This coincides with the ideal diode squarish *JV* behaviour with an FF of one mentioned in this chapter.

### 2.3.5 Hysteresis

Most PV technologies show the same *JV* behaviour, regardless of the parameter settings used to perform the *JV* scan. This has led to the rise of the *JV* scan as the easy and quick standard technique to assess PV behaviour. In PSC, however, the *JV* behaviour depends hugely on the scan conditions like scan speed, pre-biasing,[39] and most importantly, as shown by Snaith et al., the scan direction.[40] The scan from slide reverse bias condition through 0 V to higher forward bias conditions is called a forward scan. When scanning in the opposing direction (from forward bias conditions > $V_{OC}$ towards reverse bias conditions $\leq$ 0 V), the scan is called a reverse scan. In PSC, both under dark and illumination conditions, the two scan directions can sometimes show severely hysteretic behaviour.

Therefore, it is crucial to always present the results for both scan directions when showing *JV* results of PSC. I reveal an extreme case of hysteresis in transport layer-free PSC carbon devices in Chapter 4 (Figure 4.8). To generally avoid strong hysteresis in my standard devices I use in this work exclusively the p-i-n structure that is known to show less hysteresis.[41,42]

This hysteresis may be caused by ions moving in the crystal lattice during the IV scan.[39,43] The extent of hysteresis can be described by comparing the PCE of reverse and forward scans against each other. The fraction of reverse to forward scan is called the hysteresis index. I use that index to compare devices with Cr and without the Cr buffer layer in the Chapter 6 Sustainable Electrode Materials. Because of this hysteresis, the PCEs of neither of the scan directions reflect a realistic value for the efficiency of the cells. Other values need to be used in addition to providing a realistic picture of a steady-state condition.[40,43] For this reason, I present mostly stabilised values in this thesis. I will use the *JV* scans mostly for qualitative analysis of the device's behaviour. For quantitative analysis a stabilised maximum power point tracked efficiency ($\eta_{MPP}$ or MPPT efficiency) will be used as opposed to a $\eta_{PCE}$ derived from a *JV* scan. Same for open circuit voltage and short circuit current density, where I will denote the values obtained from a steady-state measurement by $_{SS}V_{OC}$ and $_{SS}J_{SC,}$ respectively, as opposed to $V_{OC}$ and $J_{SC}$ for values obtained from *JV* data. The measurement protocol for each of the measurements for these values is explained in more detail in the chapter Solar Simulator below. A steady-state fill factor $_{SS}FF$ will be calculated in the following way:

$$_{SS}FF = \eta_{MPP} / (_{SS}V_{OC} \cdot {}_{SS}J_{SC}) \qquad 2.18$$

While $_{SS}FF$ is not related to any measured *JV* curve, it does not describe an area of a *JV* graph being filled. It is nevertheless a useful indicator of a device's stabilised performance around the MPP in comparison to its output $_{SS}J_{SC}$ and $_{SS}V_{OC}$, and will be used throughout this work.

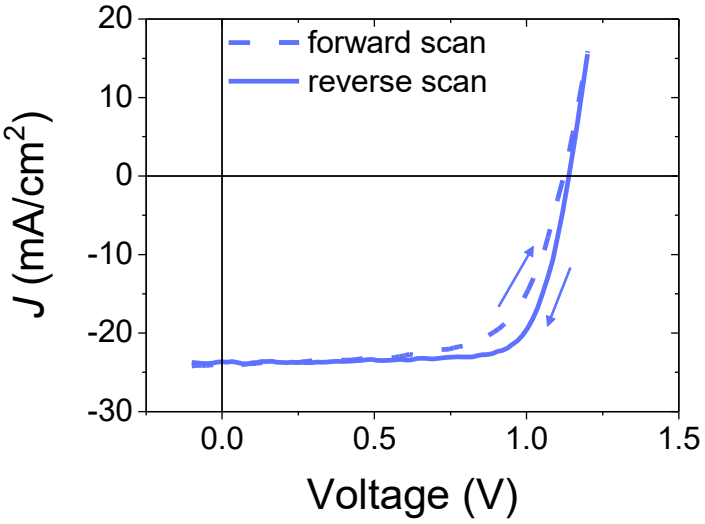



**Figure 2.8 Current Density-Voltage Scan Hysteresis**

Current Density-Voltage (JV) scans in the forward and reverse direction of a perovskite solar cell device. The *JV* behaviour shows a scan direction dependency, with the forward scan running at a lower power than the reverse scan.

## 2.4 Perovskite Solar Cells

As described above, perovskite semiconductors have emerged as a promising new material for photovoltaic applications. I use these materials for solar cells in this thesis because of their advantageous properties like solution processability, direct and tuneable band gap, high defect tolerance and absorption.[49-51] These properties allow for increased efficiencies beyond the limits of the current Silicon Photovoltaics technology and new fields of application like flexible, super lightweight, and (semi)transparent devices for building-integrated PV (Figure 2.9). The perovskite material and its properties will be explained in detail in this chapter.

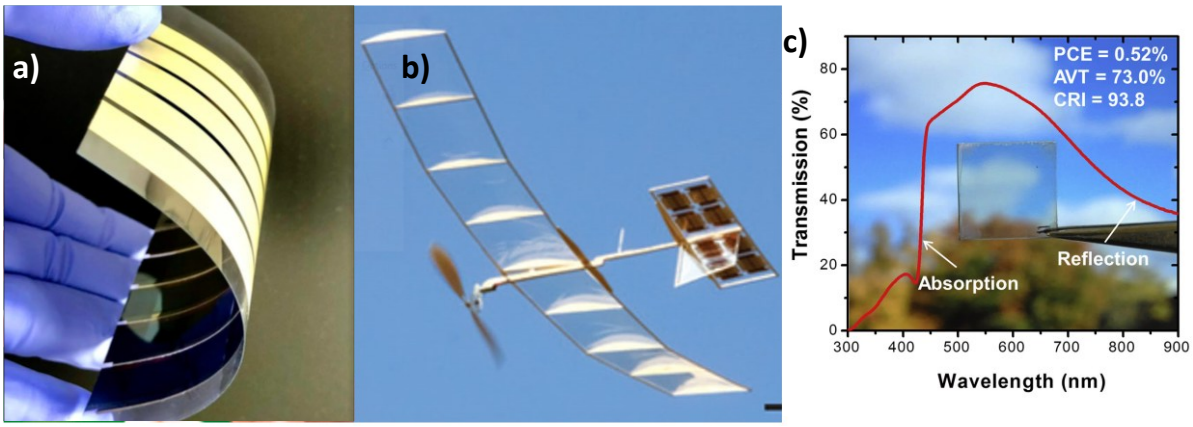



**Figure 2.9 Applications for Perovskite Solar Cells**

(a) A flexible perovskite module (photo by Hasitha Weerasinghe/CSIRO[47]). (b) Super lightweight power supplies for an unmanned aerial vehicle. Adapted with permission from Kaltenbrunner et al.[48] copyright 2015

Springer Nature. (c) A transparent perovskite solar cell for UV light harvesting. Adapted with permission from Liu et al.[49] copyright 2018 Elsevier.

### 2.4.1 Perovskite Crystal Structure

In the perovskite semiconductor used as an absorber layer in PSC, the ions are arranged in a cubic or tetragonal structure (Figure 2.10). Distortion to other crystal symmetries results usually in the loss of the desired optoelectronic properties. The lattice points in the crystal structure in a perovskite are occupied by two different cations "A" and "B" and three anions "X". The B cations are divalent and therefore much smaller ionic radius than the monovalent A cations (Figure 2.11). The crystal structure of the perovskite semiconductor derives its name from the perovskite mineral, where these ions are in a $CaTiO_3$ stoichiometry. Because of their stoichiometry and different radii, certain ion combinations crystallise in this $ABX_3$ structure (Figure 2.10). The shown structure is of an ideal cubic perovskite structure case, where the B cation is on the position (½ ½ ½) of the unit cell in an octahedron surrounded by six X anions on the face sites of the unit cell. The twelve-fold oriented A cations are at the corner positions - (0 0 0) position. The different relative sizes of the ions can - among other factors - result in a distortion away from the ideal cubic to the tetragonal case where the aforementioned octahedrons are tilted in opposing directions necessitating a unit cell expansion.[50,51]

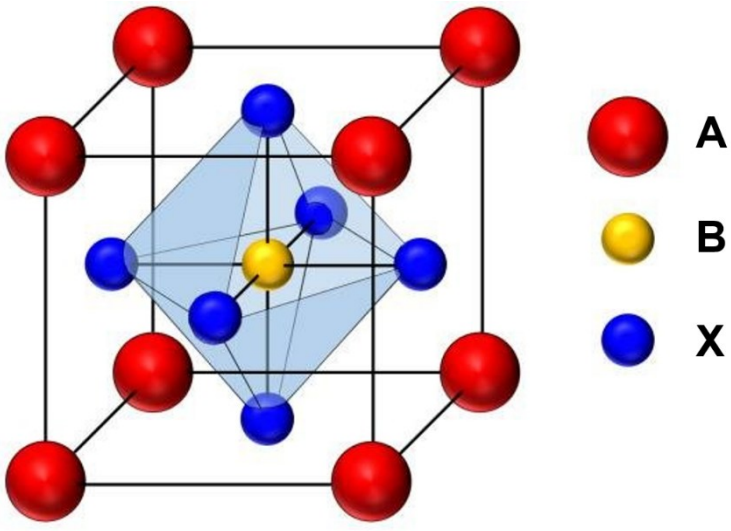



**Figure 2.10 Perovskite Crystal Structure**

Crystal structure of perovskite materials with the respective positions of the A, B and X ions in the lattice. The blue semi-transparent shape visualises the halide octahedron framing the centre metal ion. Adapted from Giovanni, 2017.[57]

A simplified way to determine whether a combination of ions with specific ionic radii $R_A$, $R_B$, and $R_X$ could crystallise in the perovskite structure, the Goldschmidt tolerance factor t can be used:

$$t = \frac{(R_A + R_X)}{\sqrt{2}(R_B + R_X)} \qquad 2.19$$

If the ionic radii combination leads to $0.8 < t < 1.0$ these ions can form a perovskite. The fulfilment of the Goldschmidt tolerance factor is a necessary but not a sufficient condition for a combination of ions to be able to crystallise in the perovskite structure. For example, the combination of formamidinium ($FA^+$), lead ($Pb^{2+}$), and iodide ($I^-$) into an $FAPbI_3$ perovskite which is widely used as an absorber layer in PSCs, leads to a tolerance factor of 0.99. This composition is, therefore, within the 0.8 - 1.0 range. However, $FAPbI_3$ crystallises at room temperature preferably in a hexagonal phase which does not show the desired photoactivity. It can be transferred from this phase into the perovskite phase by heating it to high temperatures.[53]

Besides $FA^+$, methylammonium ($MA^+$) or caesium ($Cs^+$) are commonly used as A-site cations. In most of the used absorber materials, the B-site is occupied by lead ($Pb^{2+}$) or tin ($Sn^{2+}$). The X-site is usually occupied by a halide like $Cl^-$, $Br^-$, or $I^-$ (Figure 2.11). This semiconducting ionic material is therefore often called organic-inorganic hybrid lead halide perovskite. In the first report about perovskites as light-absorbing material by Tsutomu Miyasaka's group in 2009 perovskite ($MAPbI_3$ and $MAPbBr_3$) was used as a sensitiser on $TiO_2$ in a solar cell.[54]

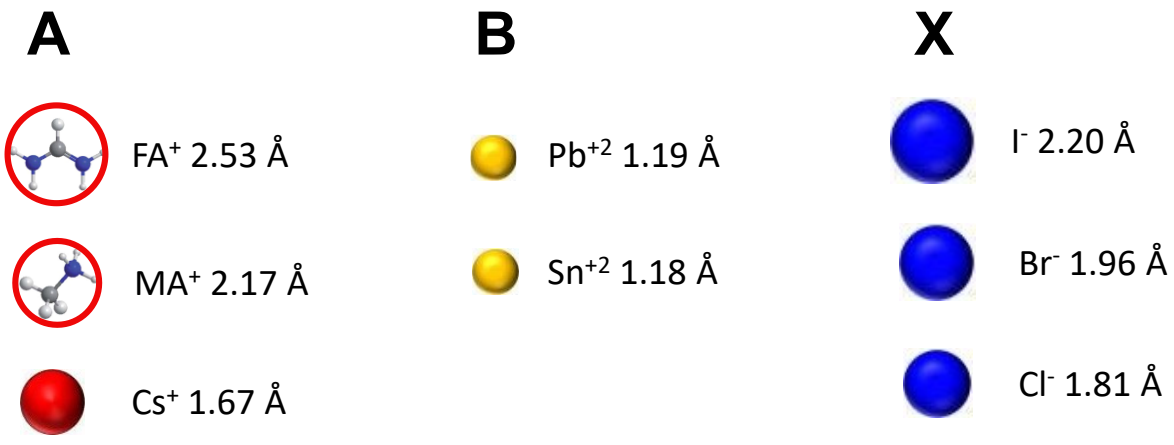



**Figure 2.11 Ionic Radii**

Relative sizes and ionic radii of commonly used ions for light absorber in perovskite solar cells. The monovalent A-site cations are much bigger compared to the divalent B-site cations. There is a notable difference in the size of the different A-site cations compared to each other. Ionic radii of inorganic ions are according to García et al.[55] FA and MA molecules from Tonui et al.[55,56] FA and MA molecules from Tonui et al.[56]

The Goldschmidt tolerance factor mentioned above was developed for oxide-based fully inorganic perovskites. Its application to hybrid organic-inorganic perovskites is complicated by the behaviour of the organic cations in the lattice. In contrast to inorganic ions, organic cations cannot be treated as hard spheres in this crystal lattice model. However, the Goldschmidt tolerance factor is based on the volume minimisation maximum packing density of hard spherical ions in a crystal lattice. To account for the deviation of organic ions from hard spheres Gholipour et al.[57] introduced globularity (shape factor) into these considerations. Through globularity, it is possible to explain why the use of certain organic cations results in the perovskite crystal structure, even though the ionic radii of the cations do not fulfil the Goldschmidt tolerance factor. An example shown by Gholipour et al. is the possible incorporation of significant amounts of ethyl ammonium (EA) into perovskites, although it is too large according to the tolerance factor (Figure 2.12a). The incorporation of imidazolium (IA), on the other hand, was impossible even though it has a fitting ionic radius similar to the one of FA which has been used successfully in PSCs (Figure 2.12a-b).

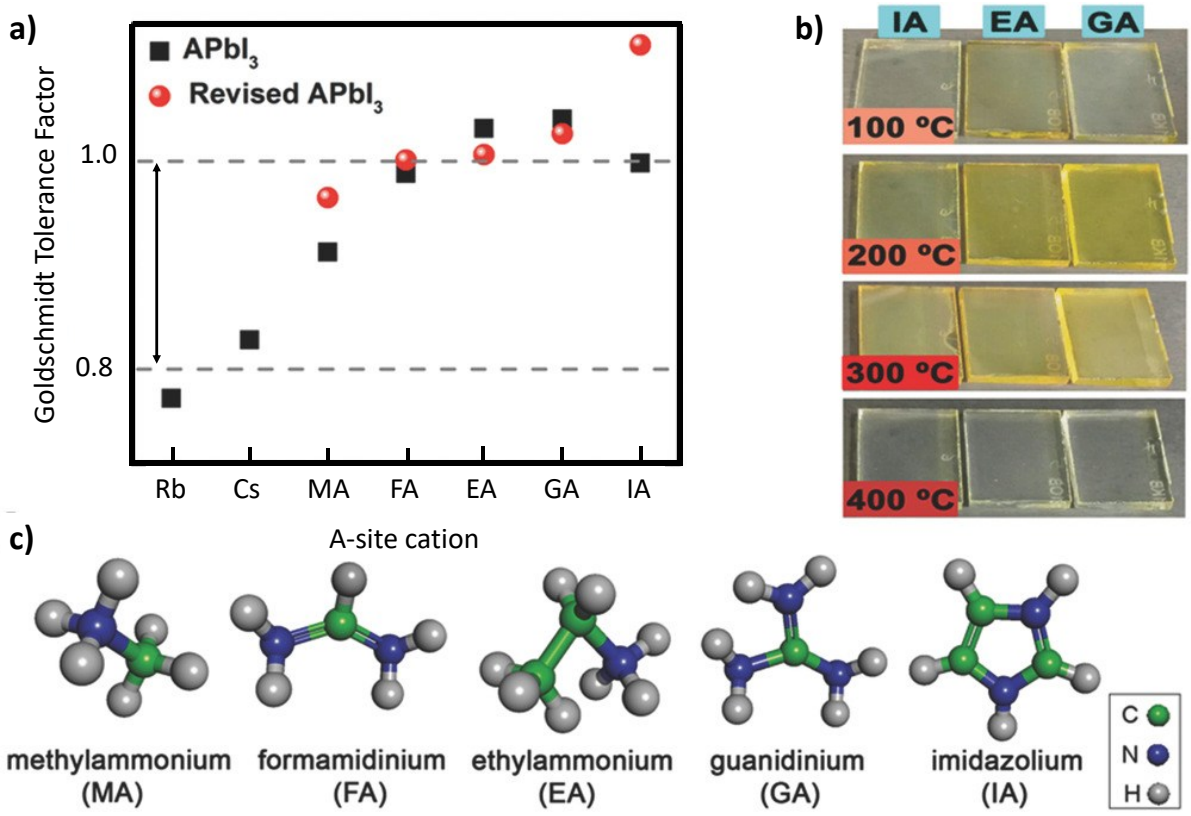



**Figure 2.12 Globularity Factor of Organic Cations in a Perovskite Lattice**

(a) The Goldschmidt Tolerance Factor was calculated with real ionic radius (black squares) of monovalent cations intended to be used in a lead halide perovskite. The resulting tolerance factor using revised ionic radii accounting for their globularity is shown in red circles. To form a perovskite crystal structure values between 0.8 and 1.0 are needed. (b) Films deposited on glass out of different A-site cations and $PbI_2$ annealed at different

temperatures. (c) Ball-and-stick molecular models of different organic cations. Figure adapted with permission from Gholipour et al.[57] copyright 2017 of John Wiley and Sons.[57] copyright 2017 of John Wiley and Sons.

### 2.4.2 Mixed Ion Perovskites

It is also possible to use multiple different ions on the sites of each of the $ABX_3$ ions. For example, Saliba et al.[58] showed improvements through using a mixture of caesium, formamidinium and methylammonium on the A-site in a triple cation CsMAFA perovskite and later with the addition of rubidium as a quadruple perovskite.[59] In such a mixed A-site cation perovskite the value of $R_A$ would be obtained by calculating the average according to the used ratio between the ions. It is possible to incorporate small amounts of other A-site cations having too small or too big, according to the Goldschmidt tolerance factor, as long as the weighted average $R_A$ fulfils the requirement.

The same is possible for mixtures on the other crystal sites. A prominent example of a mixed B-site is the so-called PbSn perovskites discovered by Eperon et al.[60] which are used to achieve low band gaps. Mixed halides (X-site) perovskites like double or triple halide perovskites are used to achieve high band gap perovskites.[61,62] This band-tuning ability is further explained in the section Tunable Band Gap below. For the vast majority of experiments in this thesis, I use the double cation and double halide lead perovskite $FA_{0.83}Cs_{0.17}Pb_{1.01}(I_{0.90}Br_{0.10})_3$. I found this perovskite to have a band gap of 1.61 eV, classified as an intermediate band gap. It can, therefore, be used as a top junction on a silicon bottom cell but also as an efficient single junction device. The band gap of this perovskite can relatively easily be widened by increasing the bromide ratio relative to the iodide as has been shown by McMeekin et al.[62] and Lin et al.[63]

### 2.4.3 Defect Tolerance

An important material property of perovskite semiconductors is that most defects forming in the crystal lattice only form shallow traps. Because the energy levels of the atomic orbitals of Pb and I are situated close to the band edges, iodine and lead interstitials and vacancies cause defect states close to the band edge as well (Figure 2.13). Perovskite is described, therefore as a defect-tolerant material.[64] This is an important contributor to the impressive rise in PCEs over the last decade. Newer research, however suggests that, while not impacting the device efficiency to a great extent, defects

might have implications on the perovskite stability.[70-72]

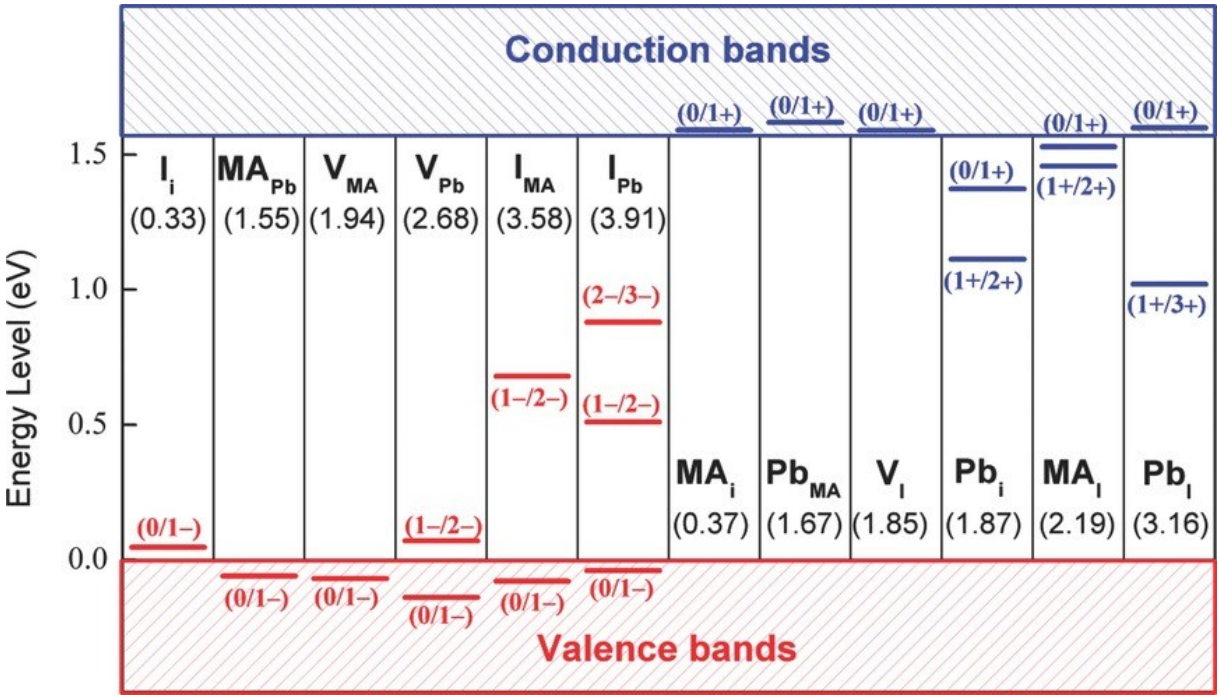



**Figure 2.13 Defect Level in Methylammonium Lead Halide Perovskites**

Calculated energy levels of different types of point defects in methylammonium lead halide perovskites. Methylammonium is denoted as MA, and Kröger-Vink notation is used to describe the type of defect with the ion occupying the point defect written in normal text, the occupied site in subscript, and the defect charge in superscript. For each defect, the formation energy for a neutral charge is shown in parentheses. Figure reproduced with permission from Yin et al.[64] copyright 2014 John Wiley and Sons.

### 2.4.4 Solvent Processing

One of the contributors to the rapid rise in efficiencies of PSC is the solution processability of perovskite semiconductors. Other materials used for PV applications, like Silicon and III-V semiconductors, need complex processes and ultra-high purity as described in Section 1.2. Perovskite, on the other hand, because of the defect tolerance described above, can be deposited with facile methods, including solution processing. For these methods, the ions desired to be incorporated into the perovskite crystal lattice are dissolved in a solvent in the right stoichiometry. This way, a precursor ink is produced. The ink is deposited as a wet film on a substrate. For the devices fabricated in this thesis, I deposited the precursor ink on TCO substrates with an HTL deposited before the perovskite. As a deposition technique, spin-coating was used. Spin-coating is an easy laboratory-

based technique to reliably produce thin films to accuracy in the nm range (see Spin-Coating in Methods).

While this method is not necessarily transferable to an industrial process, other methods like slot-die-coating are considered scalable and use similar precursor inks. Solution process methods only require simpler equipment possibly enabling very low capital expenditure (CapEx). Using solution processing for perovskite and transport layers aligns very well with capitalising on the advantage of carbon electrodes, being one of the electrode materials that can be deposited via a solution process as well (see chapter Carbon-Based Electrodes). Even if the solution process would not translate to commercial advantage, using these techniques at a laboratory level allows a much higher throughput with quicker and easier processing than vacuum-deposition-based techniques. For this reason, I mostly use solution processes for the perovskite and other layers in the device stacks in this work.

### 2.4.5 Tunable Band Gap

The mentioned solvent-based approach enables versatile, potentially cheaper production processes such as ink printing. Changing the ratio of ions in the final solid solution of perovskite makes it possible to adjust its band gap. The effect is most pronounced with the X-site ions. This way, PSC can be tuned to absorb only certain wavelengths, letting others pass through, as visualised in Figure 2.14. These advantages can allow for different ways PSC could penetrate a market dominated by crystalline silicon. They could function as a layer in multijunction PV, for example, together with crystalline silicon in tandem solar cells, replace silicon because of being potentially cheaper in production and installation, or enable new applications like flexibility, semi-transparent, and/or indoor PV (see examples in Figure 2.9).[44]

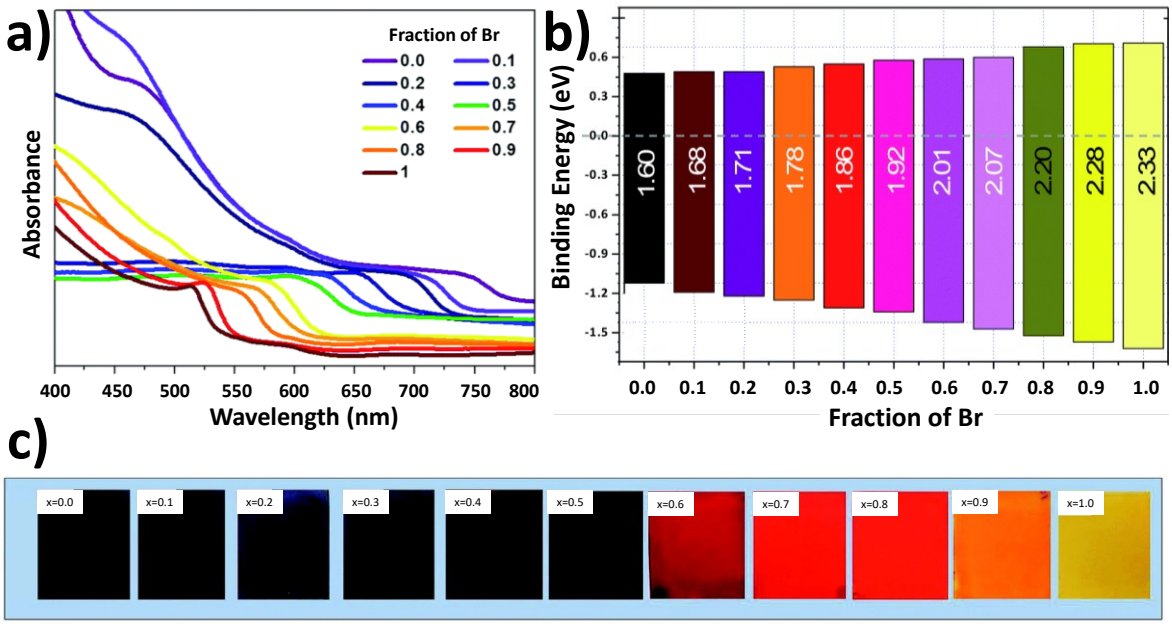



**Figure 2.14 Adjustable Band Gap of Perovskite Material by Ion Replacement**

(a) The absorption behaviour depends on the composition of perovskites based on varying the iodide-bromide ratio in $MAPb(I_{1-x}Br_x)_3$ (b) Corresponding band gaps of these ratios. (c) The visible effect on the film colour. Figure adapted from Park et al.[68]

## 2.5 Stability Challenges

In this thesis, I investigate electrode materials for stable PSC. This chapter addresses general laboratory PSC stability issues before converging on electrode-specific challenges. While PSCs offer major advantages, as described in the previous chapter, their most critical drawback, arguably, is the limited long-term stability of such devices. Unlike silicon solar cells, which last for decades, the longest reported PSC stability tests reach about 10,000 hours (~1 year).[69] This chapter explores the underlying issues causing this low stability. As detailed by Boyd et al.[70] stability challenges in PSCs arise from exposure to multiple environmental stressors, including light, heat, and oxygen. The stressors mostly act simultaneously under real-world operating conditions. I confirm in this work previous findings that the combined effects of these stressors are more detrimental than individual influences. The emphasis lies, hereby, on intrinsic stability challenges in perovskite, including light-, heat-, and redox-related degradation processes that packaging cannot solve. A detailed review of existing literature on electrode stability challenges follows the chapter on general stability problems of perovskite material.

### 2.5.1 Perovskite Instabilities

Perovskites are an ionic-bond-like, soft, and polycrystalline material. These properties make them prone to various degradation pathways like ion migration, redox reaction, and hydrate formation. Degradation from moisture and oxygen ingress can be mitigated but not fully prevented by suitable packaging.[70,71] However, degradation due to exposure to heat and light is inevitable for solar cell devices and cannot be solved to the same extent by encapsulation. To achieve light and heat stability, I build on previous results from our group by Lin et al.[63] The improved stability stems from the use of ionic additive passivating defects in the perovskite layer enhancing its resistance against decomposition. I will not further improve the intrinsic stability of the perovskite layer because, as shown in Chapter 6, the perovskite stability is not the bottleneck to the PSC device stability. Hence, I focus instead on improving the PSC devices by optimising the contact layers and electrode materials for extended stability.

Perovskite stability and electrode degradation are linked through the formation of reactive halide species, including radicals, upon perovskite degradation under operational stressors, which can accelerate electrode degradation. These reactive species can create conditions that enable or accelerate electrode degradation. This interconnectedness underscores the need for knowledge of the degradation of perovskite light absorbers to also understand electrode-related challenges. Although the perovskite material is not altered in this work, understanding its intrinsic stability remains crucial, and relevant factors are explained here. Because of the combined impact of the mentioned stressors, I primarily conduct stability tests in this work under a combined stressor environment of light, heat, and oxygen. The influences of light and heat will be treated here separately for simplicity but should be understood as intertwined and inseparable in driving degradation pathways.

#### 2.5.1.1 Heat Stability

PSCs experience significant heat load under operational conditions. As described in the section about Photo Absorption, hot charge carriers are generated upon absorption of photons with energy greater than the absorber band gap ($hf > E_g$). These carriers relax to the band edges, releasing energy as heat (Figure 2.4). This, combined with parasitic absorption in layers other than the absorber layer, contributes to the overall thermal load. Thermal load is intrinsic to all PV technologies. Solar cells

can encounter temperatures above 60°C and stress from hot-cold cycling due to day-night and weather changes.[70,71] Even though temperature control of solar cells is investigated (primarily to increase the efficiency of Si-PV), it is not in widespread use and may not be viable, particularly for small-scale applications like on private roofs.[72]

PSC devices' intrinsic stability to this unavoidable heat load must be high enough to enable long-term stability. A significant challenge to achieve this is the thermal degradation and decomposition of the organic cations in the PSC, such as MA and FA. These ions can thermally decompose into volatile organic species, a phenomenon particulary pronounced for MA. Several thin film studies show rapid thermal decomposition of MA-based perovskites.[79-81] This decomposition causes a material loss and fast degradation of the optoelectronic properties of $MAPbI_3$ perovskites exposed to heat. $MAPbBr_3$ perovskites are significantly more thermally stable.[74] However, their band gap of over 2 eV is too high for single-junction PV applications. To achieve higher thermal stability of perovskite and PSC devices, I do not use $MAPbI_3$ in this work.

To investigate the detailed thermal decomposition, Shi et al.[76] have performed gas chromatography on multiple different perovskite compositions and precursor powders during thermal annealing. They identified typical volatile degradation products for different perovskite compositions at different temperatures. Decomposition reactions can be derived from the degradation products. For being heated at 85 °C, which can be considered a realistic operating temperature of PV, they proposed the reactions below. With MA being $CH_3NH_3$, FA is $CH(NH_2)_2$, and halides like I and Br are represented by X:

$$CH_3NH_3X_{(s)} \rightarrow CH_3X_{(g)} + NH_{3\,(g)} \qquad 2.20$$

$$3CH(NH_2)_2X_{\,(s)} \rightarrow H_3C_3N_{3\,(g)} + 3NH_{3\,(g)} + 3HX_{\,(g)} \qquad 2.21$$

These reversible reactions become irreversible degradation when the gaseous degradation products become unavailable for the reverse reaction due to leaving the crystal. MA proves to be significantly less thermally stable. It starts to decay at moderate temperatures of around 70 °C and decomposes quickly at elevated temperatures of 140 °C. These temperatures can be reached during solar cell operation and encapsulation, respectively.

MA has also been shown to destabilise mixed cation perovskites (see 2.4.2 Mixed Ion Perovskites). This is explained by Shi et al.[76] via a reaction between MA and FA decomposition products. This reaction removes FA decomposition products, making them unavailable for the reverse reaction. This way MAFA mixture may result in significantly lower thermal stability, even though it stabilises the crystal against unwanted phase transitions.

Niu et al.[77] show that replacing a fraction of the A-site cations with Cs (see 2.4 Perovskite Solar Cells) lead to a strongly enhanced thermal stability (Figure 2.15).

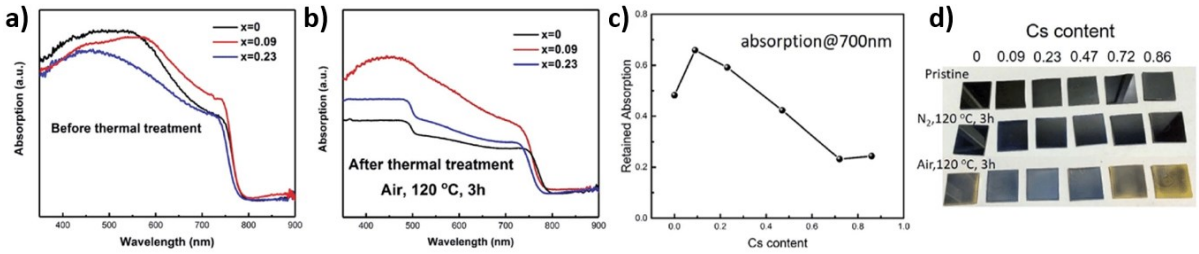



**Figure 2.15 Improved Thermal Stability by introducing Cs Cations**

(a) Perovskite films with different CsMA ratios of $Cs_xMA_{1-x}PbI_3$ before thermal treatment, with x representing the Cs content. (b) The same perovskite films after a thermal treatment at 120 °C for 3 hours in ambient air. (c) Retained absorption at 700 nm for perovskite films with Cs content from 0 to 0.86. (d) Photographs of perovskite films after exposure to different atmospheres and temperatures. Adapted from Niu et al.[77]

Further, Shi et al.[76] have shown that encapsulation of a PSC can significantly slow down the thermal decomposition. The thermal decomposition is, therefore, at least partly suppressed by trapping the decomposition products. This trapping causes a higher degradation product concentration inside the perovskite layer, shifting the equilibrium to the educt side, effectively stopping further degradation. Throughout this work, I employ different strategies to trap the decomposition products inside the perovskite layer to slow down degradation, including on-cell full-area encapsulation in the Chapter 6 and a graphene diffusion barrier in the Chapter 5.

Introducing small amounts of Cs as cations and Br as halides can improve thermal stability (see 2.4 Perovskite Solar Cells).[70,78] Niu et al.[77] show that replacing a fraction of the A-site cations with Cs leads to a strongly enhanced thermal stability (Figure 2.15). It was further shown by McMeekin et al.[62] that mixed A-site FACs perovskites without the thermally unstable MA show high thermal stability. This perovskite shows advantages in terms of possible band gaps that can be achieved and in terms of stability. A perovskite with pure FA and the A-site shows a phase instability transitioning

from a tetragonal perovskite crystal structure to an undesired hexagonal phase. Additionally, $FAPbI_xBr_{x-3}$ shows a miscibility gap with certain iodide-to-bromide ratios, and hence certain band gaps, being impossible to achieve. To achieve good thermal stability, and test our results on a versatile perovskite I used caesium and bromide-containing and MA-free perovskite with the composition $Cs_{0.17}FA_{0.83}Pb_{1.01}(I_{0.9}Br_{0.1})_3$ for most experiments.

Another issue with the thermal stability of PSC devices is caused by their layered architecture (see Device Structures) with multiple different layers often displaying different thermal expansion coefficients. For example, the thermal expansion of glass and most TCOs is significantly lower than that of most commonly used perovskite materials. Thermal cycling can cause delamination of the different layers, causing a loss of electrical connection and ultimately device failure.[79,80] Erdil et al.[81] show in p-i-n devices, similar to the ones used in this work, that the $C_{60}$ and $SnO_2$ layers are the mechanically weakest in the device stack in terms of their adhesion. Further, Erdil et al.[81] show that delamination in devices occurs at these interfaces, both in indoor and outdoor stability testing. A delamination at the ETL, either at the perovskite/PCBM or PCBM/$SnO_2$ interface, is also a contender for the instability I discovered in the devices shown in Chapter 4.

#### 2.5.1.2 Light Stability

Like heat, light is a stressor that PV devices must inevitably withstand to be operational. A challenge related to light-induced degradation is halide species forming upon light exposure. This process has frequently been proposed to be caused by the capture of light-generated holes $h^{\cdot}$ by a halide. In the following, the process is explained for iodine situated on defects like interstitials ($I_i^X$) or on regular lattice points ($I_I^X$). The $h^{\cdot}$ capture causes the generation of atomic ($I^{\cdot}$) radicals in the crystal. Radicals are highly reactive species that can cause further degradation when reacting within the cell. If two of these iodine atoms meet, they combine into a volatile $I_2$ molecule that can eventually leave the perovskite, leaving behind two iodine vacancies ($V_I^{\cdot}$):

$$I_I^X + h^{\cdot} \rightarrow I_I^{\cdot} \qquad 2.22$$

$$2I_I^{\cdot} \rightarrow 2V_I^{\cdot} + I_{2(g)} \qquad 2.23$$

Halides are very reactive and nucleophilic.[82,83] They can undergo redox reactions with metals (see below),[90-92] and deprotonate organic cations[85] and organic compounds in the transport layers forming

volatile hydrogen halides. Zhao et al.[86] found that halide redox reactions play a dominant role in PSC degradation even in MA-free perovskites. Halides leaving the absorber layer lead to irreversible damage through material loss. Because halides are a necessary part of the perovskite material reactions related to halides are difficult to avoid. As shown by Wang et al.[87] exposure to $I_2$ can accelerate the degradation of FACs perovskites severely. To reduce the formation of iodine and the degradation caused by it the $h^{\cdot}$ described above needs to be reduced. Since this $h^{\cdot}$ capture happens more on iodine defect sites a more defect-free perovskite becomes desirable. As described in the section about Defect Tolerance the presence of these defects does not affect the performance of PSC negatively in the same way defects affect other PV materials. They might have, however, a negative effect on the stability as described here.[88] A high crystallinity perovskite and passivated defects can help to suppress the iodine formation.[89] To fabricate such a perovskite I used an ionic additive, which has been proposed by Lin et al.[63]

Although $PbI_2$ is unintended in perovskite films, it is commonly present in most films due to varying stoichiometry resulting from simple processing methods. This minority phase of $PbI_2$ is particularly problematic for light stability. For the stable (FA,Cs)Pb(I, Br)$_3$ perovskite used in this work, it has been shown that unwanted $PbI_2$ patches in the film degrade faster upon light exposure than the perovskite itself (Figure 2.16a).[49,63] For this reason, the excess of lead iodide in the precursor powder was kept as small as possible (0-1%). A slight excess was used to prevent a very detrimental $PbI_2$ deficiency. While a 0-5% $PbI_2$ excess resulted in well-working devices even small deficiencies reduced the device performance and current density strongly (Figure 2.16b).

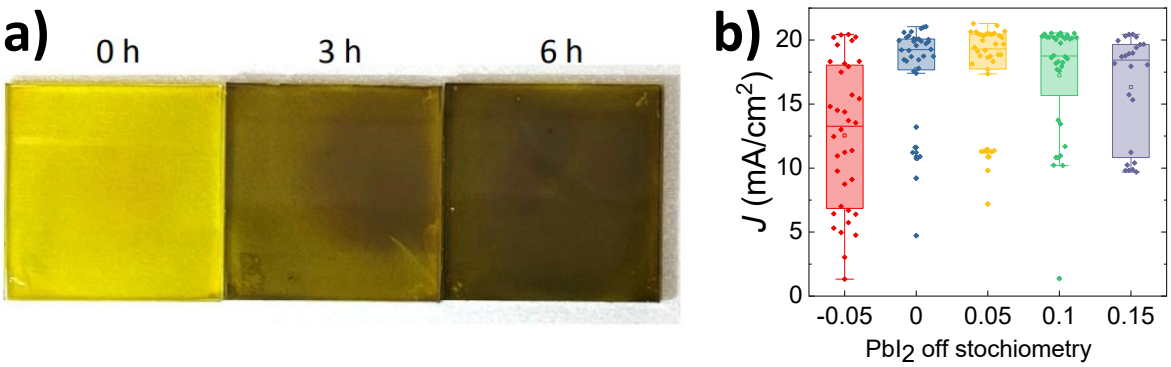



**Figure 2.16 Lead-Iodide Light Instability and Excess**

(a) Lead-Iodide ($PbI_2$) thin film behaviour when being aged in an $N_2$-filled glovebox under a white LED light at 85C. The film colour changes quickly from the characteristic yellow colour of $PbI_2$ to dark brownish. These

results highlight the instability of lead iodide itself towards light and heat exposure. Adapted from Lin et al.[63] (b) Current density (*J*) values for perovskite solar cells prepared with precursor solutions with different $PbI_2$ stoichiometries relative to the FACs A-site where -0.05 means a relative 5% deficit of $PbI_2$ ($FA_{0.83}Cs_{0.17}Pb_{0.95}$), 0 means a 1:1 ratio of Pb to (FACs) and so on.

### 2.5.2 Electrode Materials and Stability Issues

A major challenge to translating laboratory success into the industry is the stability and scalability of the perovskite technology. While much of the literature focuses on stabilising the perovskite light absorber, the stability impact of other materials in the device stack, including the electrodes, has received less attention. It has been shown that metal back electrode materials have a substantial detrimental influence on PSC operational stability.[71,84] In contrast to the impact of oxygen and moisture, degradations associated with the metal electrode cannot be solved by encapsulation, as the electrode is an intrinsic part of the device that cannot be locked out by packaging.

There are two major degradation processes involving the metal electrode. The first and more severe one is related to the formation of halide - particularly iodide - phases on the metal electrode surfaces. This process is pronounced for less noble metal electrodes like Ag and Al[71] and will be explained below. The second process is the diffusion of metal ions from the electrode into the rest of the device stack including the perovskite absorber. While this first process is to some extent limited to less noble metals, the second process has been reported to happen for almost all metals.[71,90,91] Instead of encapsulating the whole device a barrier between the metal and the rest of the device can be used. Another possible strategy to solve metal-induced instabilities is a total replacement of the metal with other electrode materials as explained below in 2.5.3 Carbon-Based Electrodes and 2.5.2.3 Metal Oxide Instabilities.

#### 2.5.2.1 Metal Halide Formation

The formation of metal halides is a metal electrode-related issue unique to PSC. Reactive halide species form in the perovskite layer upon light exposure as described in Perovskite Instabilities.[84] Other PV technologies do not contain such reactive species. This makes PSC unique in that cheap industrial metals cannot easily be used because of instability. It has been known from early on, that metals tend to interact with perovskite material and negatively influence the stability of PSC. Silver has been shown by Kato et al.[84] to react with halide species leaving the perovskite layer (see Figure

2.17a). This leads to the formation of silver iodide and accelerates perovskite degradation by providing a sink to leaving degradation products. The same has been shown for less noble metals like copper[91,92] and aluminium.[93] Xu et al.[94] show that halide redistribution through the $I_i^+/I_X^-$ redox shuttle causes halide segregation in PSC under different bias conditions. Depending on the electrodes used the process causes a different halide redistribution. If a silver electrode is present it functions as a sink for the $I_X^-$ species suppressing the redox shuttle process.

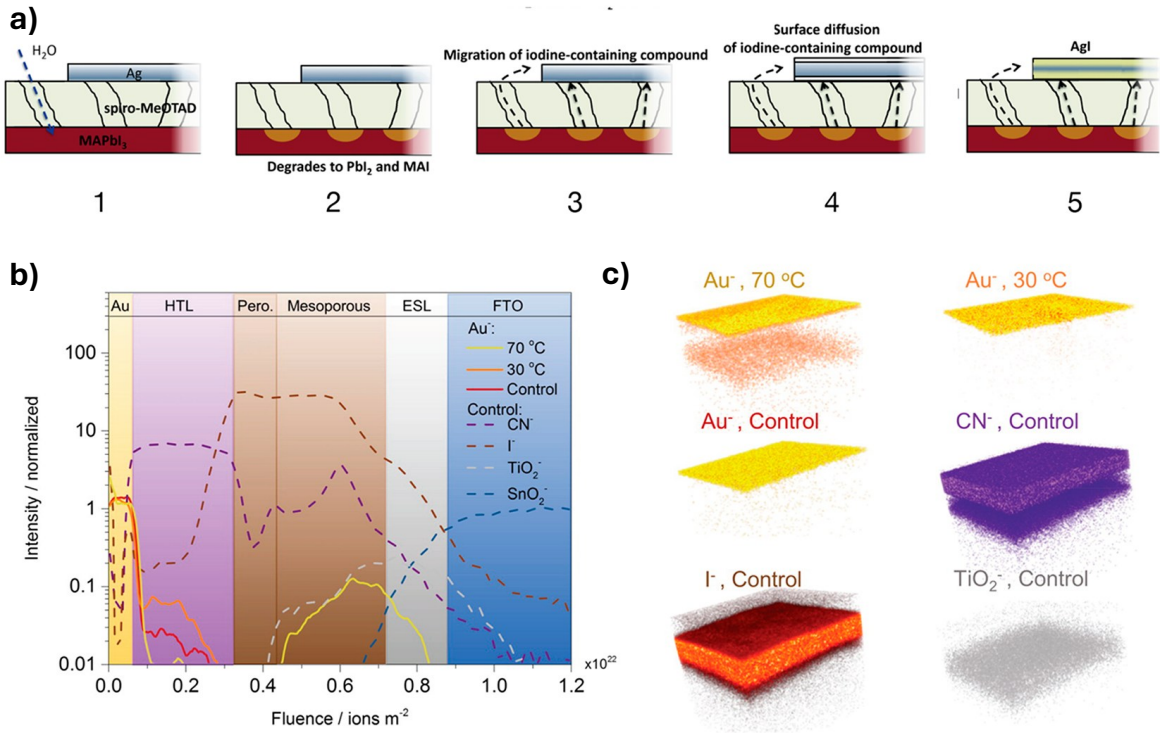



**Figure 2.17 Effects of Metal-Induced Perovskite Solar Cell Degradation**

(a) A suggested route for the formation of silver iodide. The perovskite degrades when exposed to the environment. Formed gaseous iodide-containing degradation products then reach the transport layer electrode interface as well as the top of the electrode. Subsequently, the metal degrades from the top and the bottom simultaneously. In (b) and (c), the diffusion of gold into the PSC is shown for different temperatures. (b) The TOF-SIMS depth profile of the control and two devices aged at 30°C and 70°C. (c) A 3D animation of how different species are distributed within the devices related to the TOF-SIMS data. At 70°C, the gold diffuses far into the device and accumulates at the perovskite ESL (ETL) interface. (a) Adapted with permission of Kato et al.[84] copyright John Wiley and Sons and (b) and (c) adapted with permission from Domanski et al.[71] Copyright 2016 American Chemical Society

Since most noble metals with better stability towards halides, like Au, are too expensive for industrial applications, it would be desirable to enable the use of less noble metals. Therefore, there have been efforts to prevent the reaction of Ag with the perovskite material. One strategy applied to achieve this is the use of an impermeable buffer between the two of them. Seo et al.[95] used aluminium zinc

oxide deposited via atomic layer deposition and Boyd et al.[96] a barrier design with ITO. Both processes lead to significantly improved stability. They involve, however, a separate deposition process, causing a larger expenditure of time and higher costs in device fabrication.

#### 2.5.2.2 Metal Ion Diffusion

The described problem of metal halide formation is a more severe problem with less noble metals. Noble metals like Au are more inert to halides. They are therefore frequently used in PSC research as a supposedly stable electrode material. However, the price of Au is several orders of magnitude higher than the one of Ag and other common metal electrode materials. This raises concerns about the suitability of Au for industrial large-area fabrication of PSC. Besides metal halide formation, there is another metal-related stability challenge: the diffusion of metal ions into the absorber layer. This is a well-known problem in silicon PV where metal ions diffusing into the silicon absorber cause deep trap states (see Trap Assisted Recombination Processes) drastically reducing the performance of the PV device.[97]

Domanski et al.[71] have reported that under heat-light conditions of one sun and >70 °C Au ions can also diffuse into the perovskite layer (Figure 2.17b and c). They showed with time-of-flight secondary ion mass spectrometry (TOF-SIMS) that at elevated temperatures of >70 °C, significant amounts of Au diffuse through the entire thickness of the perovskite layer, accumulating at the bottom ETL/perovskite interface. Multiple metal ions form deep trap states inside the perovskite, which are detrimental to the PSC device performance and stability. Ming et al.[90] calculated the energy levels of different metal impurities in $MAPbI_3$. They found that, for example, an $Au_{Pb}$ defect forms a state close to mid-band gap, potentially causing an efficient recombination centre, explaining the degradation observed by Domanski et al. According to Ming et al., multiple metals show different energy barriers to diffuse into a $MAPbI_3$ layer. They found that for example $Au_i^+$, $Cu_i^+$, $Ag_i^+$, and $Ni_i^+$ have relatively low diffusion barriers of <0.5 eV while $Cr_i^+$ shows a higher diffusion barrier of 0.83 eV. These calculative results are in line with findings that a thin Cr layer of a few nm below an Au electrode improves the stability of PSC devices by preventing the diffusion of $Au^+$ ions into the device. Such a Cr interlayer was proposed by Kaltenbrunner et al.[48] and was further analysed by Domanski et al.[71] In Chapter 6 of this work, I show results of using such a Cr interlayer with different metals than Au, investigating whether the Cr layer can be used to not only to address metal diffusion

but also metal halide formation. It has been proposed early on to use a thin layer of Cr below Au to stop atoms diffusion into the perovskite.[48,71]

#### 2.5.2.3 Metal Oxide Instabilities

This section addresses the stability challenges posed by using metal oxide materials in PSC device stacks. I will first introduce the stability issues with light-facing metal oxide transport layers and then transition to instabilities of transparent conductive oxides (TCO) namely indium tin oxide (ITO). As light-facing metal oxide transport layers NiO and $TiO_2$ are in frequent use (see above in 2.3.2 Device Structures). $TiO_2$ was the first ETL used for PSCs[54] and has maintained a dominant role as the most used ETL in n-i-p PSC for about a decade.[98,99] NiO, on the other hand, is the base of almost all inorganic HTL in p-i-n PSC.[126-128]

Both $TiO_2$[129-131] and NiO[106,107] are used as photocatalysts to decompose organic species. This casts arguable doubt on their use under illumination in contact with a material containing organic species like perovskite. Leijtens et al.[108] demonstrated early on that light-induced instability in $TiO_2$-sensitised cells arises from the desorption of oxygen from the $TiO_2$. Defects at the $TiO_2$/perovskite can significantly reduce device performance and accelerate this oxygen desorption process.[109] Wang et al.[110] demonstrated that the synergistic effect of iodine vacancies in perovskites and oxygen vacancies in $TiO_2$ leads to decreased stability, enhanced ion diffusion, and reduced charge lifetime. These defects create midgap trap states and accelerate charge recombination. There are ample efforts to stabilise the $TiO_2$/perovskite interface mainly through passivation of the interface defects.[111–113] Peng et al.[114] for example use ultrathin passivation layers using PMMA:PCBM mixtures to effectively suppress interfacial recombination at the perovskite/$TiO_2$ interface. Passivation of the $TiO_2$ perovskite interfaces also enabled one of the latest records in triple mesoporous carbon devices by Liu et al.[115] (see Chapter 2.5.3 below). Because of the instability of $TiO_2$ most of the perovskite n-i-p community has, however, moved to the more stable $SnO_2$.[116,117] Similar to $TiO_2$, NiO also has been shown to have high surface reactivity leading to degradation at the perovskite interface, affecting device stability.[111,118] Due to the stability challenges associated with these materials, we decided out of an abundance of care to exclude the use of light-facing metal oxide transport layers altogether in this work. Instead, a polymer-based HTL is used to ensure high stability.

Like $TiO_2$ and NiO, TCOs are also employed on the light-facing side. The vast majority of Thin Film Technologies and multijunction technologies use TCOs, with ITO being the most common, as the electrode material or as an interconnecting layer between junctions. Silicon Photovoltaics, on the other hand, use metal grids as transparent electrodes. As interest in thin films and multijunction devices grows, a thorough understanding of TCOs becomes increasingly important. While metals often cause instabilities in PSC (see Section 2.5.2 above), TCOs have been proposed as a more stable alternative to metal or as barrier layers between the metal and the rest of the device stack.[70,96] However, the stability influence of different TCO materials remains inadequately studied, particularly for PSC. The most widely used TCO in both perovskite and perovskite-silicon-tandem solar cells is indium tin oxide (ITO).[147-151] Even though ITO is known to have low chemical and thermal stability,[119,124,125] there is no comprehensive literature on if and how this material instability translates to reduced device stability of solar cells using ITO transparent electrodes. While it is mentioned in published research that the use of fluorine-doped tin oxide (FTO), instead of ITO, improves the operational stability of PSCs,[126] there is currently neither a thorough side-by-side study on full devices nor sufficient research on the underlying reason for this observed effect.

Kerner et al.[127] show that when ITO films are in direct contact with a methylammonium lead triiodide ($MAPbI_3$) or a formamidinium lead triiodide ($FAPbI_3$) perovskite layer, a solid-state reaction between the materials can be triggered upon exposure to temperatures of 85 °C or -0.8 V of applied bias. Zhou et al.[128] studied the effect of indium doping on methylammonium lead triiodide perovskites. They showed that replacing as much as 1% of the lead stoichiometry with indium could negatively influence the photoluminescence of the resulting perovskite films. Replacing 5% of the lead with indium results in a significant reduction of device performance from above 13.5 to 4.4%. Zhou et al.[128] further show via density-functional theory calculation that $In^{3+}$ doping into $MAPbI_3$ causes mid-band-gap states to form, which is consistent with reduced photoluminescence.

My work shows that these processes are relevant to the ageing behaviour of positive-intrinsic-negative (p-i-n) formamidinium caesium lead iodide bromide perovskite solar cells. In the first such direct comparison, I age otherwise identical devices made on ITO and FTO substrates at operational

conditions of 65 °C under one sun illumination for 800 h. Devices on ITO show a much quicker degradation compared to their FTO counterparts (see Chapter 6).

### 2.5.3 Carbon-Based Electrodes

Carbon-based electrodes have emerged as a promising alternative in PSC, offering a range of beneficial properties derived from different carbon allotropes. This section explores the role of various carbon materials in PSCs, highlighting their distinct characteristics and functionalities. First, the fundamental properties and applications of these allotropes will be discussed, followed by a section exploring the advantages they provide in device performance and stability. Finally, the implementation strategies for integrating these carbon-based materials into PSC architectures will be explained in detail.

#### 2.5.3.1 Carbon Allotropes and their Properties

The most common use for carbon-based materials in PSC is opaque back electrodes. These electrodes are mostly prepared out of carbon pastes. These carbon pastes - including the ones used in this work - usually consist of carbon black particles, graphite flakes, solvents, and possibly binder material. A cross-section of a full device comprising such a carbon electrode prepared by blade-coating and drying a paste on a PSC device stack is shown in the scanning electron microscopy (SEM) cross-section in Figure 2.18. All materials used in these pastes are inexpensive and available on the market on an industrial scale. The paste conductivity arises predominantly from the graphite flakes. These flakes are composed of multiple layers of carbon atoms arranged in interconnected hexagons also called a honeycomb structure. The orbitals of the individual carbon atoms in an undisturbed layer are in an $sp^2$ hybridisation and a non-hybridised p-orbital configuration. Every carbon atom is connected to three other atoms via σ bonds formed by the $sp^2$ orbitals. These bonds are responsible for the strong mechanical stability in-plane direction. The π electrons in the $2p_z$ orbitals are delocalised over the plane and are the reason for the exceptional high conductivity of graphite in-plane direction. A carbon layer in this configuration of a one-atom thickness is called graphene. Multiple graphene layers held together by van der Waals interactions between them form graphite used in the pastes.[129]

The other carbon allotrope added to most pastes is carbon black. It consists of paracrystalline nanoparticles produced by incomplete combustion of hydrocarbon materials. The carbon black improves the bonding between the graphite flakes. In Figure 2.18 they are visible as spherical aggregates filling the gaps between the much bigger platelet-like shaped graphite flakes. Carbon black is far less conductive than graphite because of the lower number of hybridised orbitals compared to covalent bonds and the lower crystallinity compared to graphite. However, adding carbon black to the paste, due to its bridge-building function, improves the conductivity of the resulting electrode. The ratio of these two components, as well as the graphite flake size, are crucial parameters. They can be used to tune the properties of the carbon electrode.[142] Bigger flakes increase the electrode's conductivity but decrease the number of connection points to the underlying layer. Therefore, an optimal graphite flake size must be achieved to maximise charge extraction while maintaining high conductivity through the carbon electrode.[131]

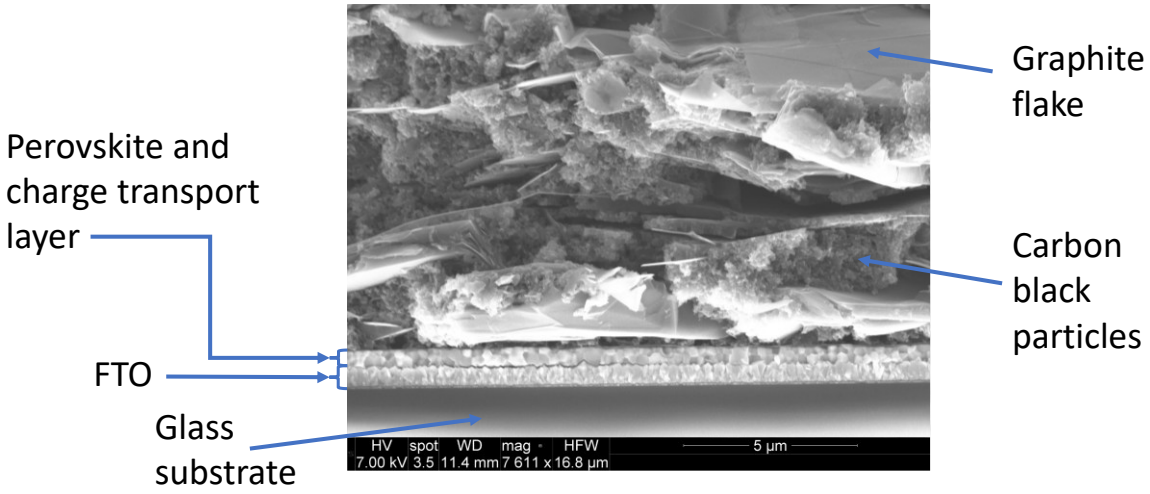



**Figure 2.18 Carbon Perovskite Solar Cell Scanning Electron Microscopy Cross-Section**

Cross-sectional scanning electron microscopy image of a complete perovskite solar cell with a blade-coated carbon electrode. The heterogeneous upper region is the carbon electrode, consisting of micrometre-sized platelet-shaped graphite flakes and intercalated nanometre-sized spherical carbon black particles. Below this, two distinct crystalline layers (~500 nm each) are the transparent conductive oxide and the perovskite absorber. The charge transport layers, each thinner than 30 nm, are not well resolved at the applied magnification (×7,611). The carbon electrode extends approximately 10 µm beyond the visible image section.

Besides using graphite as the main conductive material in carbon electrodes there is an interest in using other carbon allotropes like graphene and carbon nanotubes (CNTs) in PSC. Both allotropes show distinct material properties, including the previously mentioned strong in-plane electrical conductivity, along with remarkable mechanical and chemical stability relative to their size.

Graphene and CNT films can be prepared into transparent films that have been proposed as transparent electrodes for PSC. They show however lower electrical conductivity at the same optical transparencies compared to the state-of-the-art TCOs. Efforts to still use these materials include raising their conductivity for example by doping the graphene or CNT. Another promising material property is the chemical impermeability of graphene. In Chapter 5.1 I use this property to improve the stability of perovskite films and explore how to use it in PSC devices.

#### 2.5.3.2 Advantageous Properties of Carbon-Based Materials

The mentioned issue of redox reactions and interdiffusion between perovskite material and metal electrode materials does not apply to carbon-based electrode materials. Carbon allotropes do not show any tendencies to interact negatively with the perovskite due to the mentioned strong covalent bonds and their inert[132] and hydrophobic behaviour.[133,134] These material properties suggest that carbon electrodes might help to overcome the stability problems of metal electrodes mentioned in the previous chapter.

Besides these known advantages of carbon-based materials most stacks used to demonstrate device stability use an evaporated gold electrode. Chang et al.[135] have calculated the costs for a perovskite module in US$/m$^2$ if such a laboratory stability stack would be used in a large-scale module. Whilst these results have limited relevance for industrial applications, they highlight the major problem with the current approach to stability research for PSCs on a laboratory scale. Most of the stability research uses raw materials that are prohibitively expensive and unlikely to ever be used on a large industrial scale. If evaporated gold is used for a perovskite module, the material and processing of the gold electrode would be responsible for 74.7% of the total device cost (Figure 2.19). Other methods need to be used to show the stability of PSC at a laboratory scale applying inexpensive materials to enable the technology transfer from laboratory to industry.

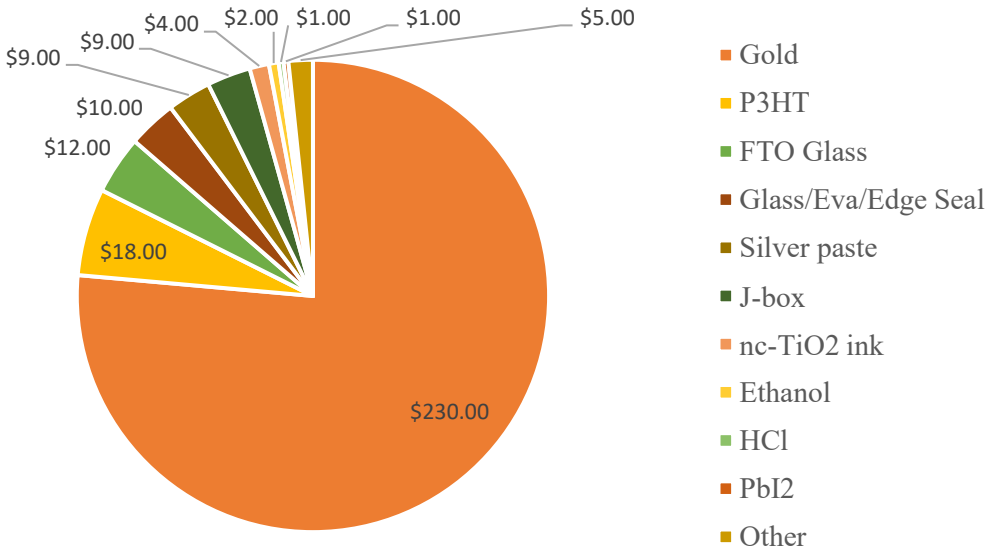



**Figure 2.19 Material Costs Common Laboratory Perovskite Solar Cell as Module**

Material costs for materials used in a laboratory PSC. The prices are in US dollars per $m^2$. Values taken from Chang et al.[135]

Carbon-based materials present a potential alternative opaque back electrode, addressing the cost limitations of gold and the stability challenges associated with other metals. They can be applied by facile processing techniques at atmospheric pressure (Figure 2.20a).[131,136] Carbon electrodes are widely used in numerous large-scale industrial applications like lithium-ion batteries. They show excellent electrical conductivity, chemical stability, and cost-effectiveness. Carbon is the most abundant element that is commonly used as electrode material. Graphite, the conductive carbon allotrope used in the electrodes, is orders of magnitude cheaper compared to raw materials used in both metals and TCOs (Figure 2.20b). The raw material cost per kilogram of graphite is more than 100 times below the price of Ag and more than 6,000 times lower than that of gold.

Finally, and probably most importantly, carbon-based materials are promising for their stability track record in PSC. One example showing this stability potential is the mentioned 10,000 h stable PSC with carbon electrodes by Grancini et al.[69] Carbon-based materials are inert at PSC operational conditions. I observe colour changes in silver electrodes upon heat and light exposure in ambient air, indicating the degradation and formation of silver halides (see 2.5.2.1 Metal Halide Formation). In carbon-based electrodes, on the other hand, there are no visible signs of degradation (Figure 2.20c). The absence of visible degradation in carbon electrodes is not surprising given the material properties of carbon.

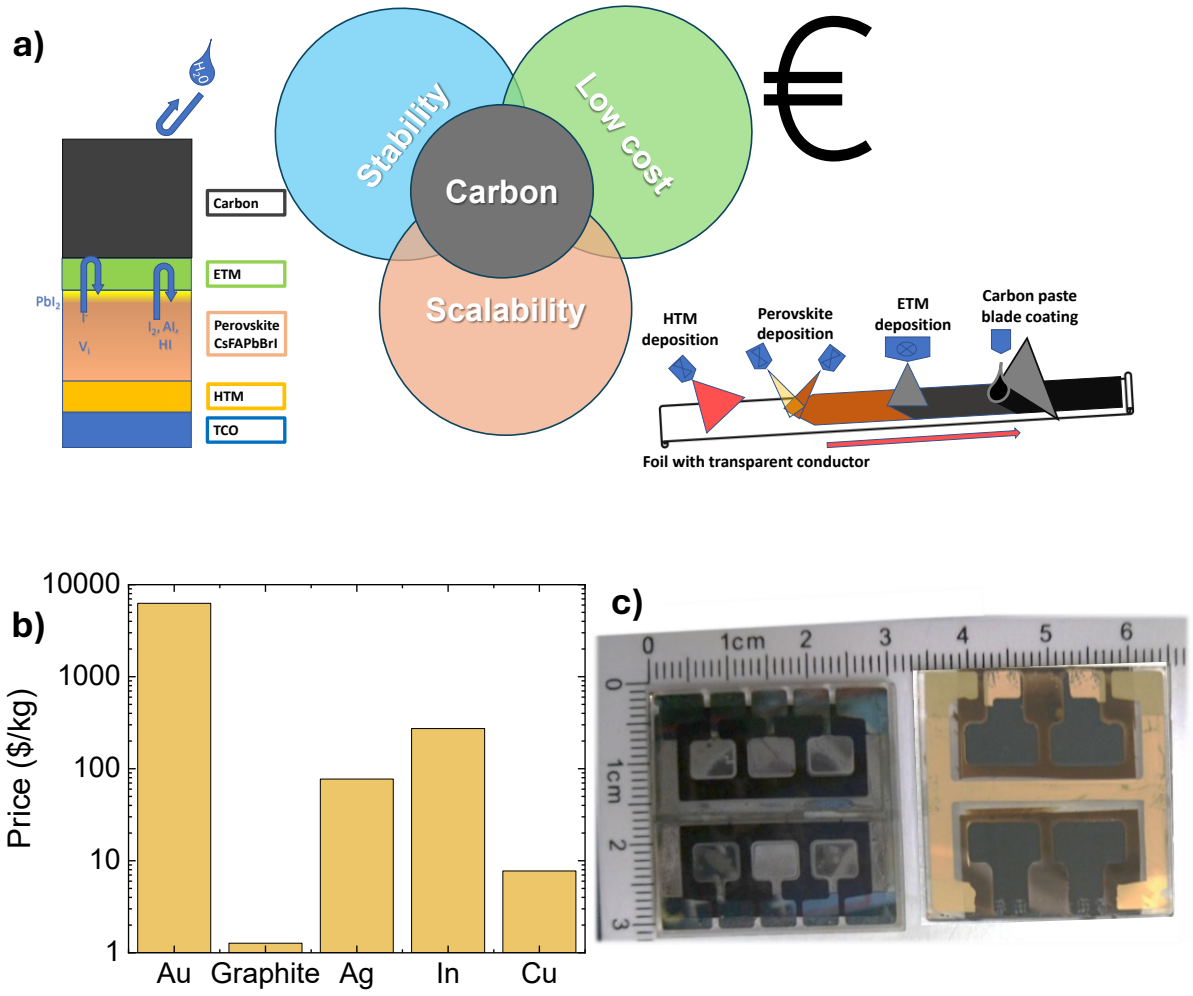



**Figure 2.20 Carbon Electrode Advantages**

(a) Suggested material advantages of carbon-based electrode materials for PSC. (b) Raw material prices in US$/kg for different materials commonly used for electrode preparation of PSC. Prices from the German Federal Institute for Geosciences and Natural Resources.[137] (c) A PSC with silver electrodes and one with carbon electrodes after one week of ageing at 65°C under 1 sun0.76 suns illumination and ambient atmosphere. The silver electrodes on the PSC to the left side show significant inhomogeneity and change in colour compared to pristine silver electrodes. The carbon electrodes on the right do not show any visible colour changes. Signs of degradation in the perovskite around the electrode are visible for both devices.

Because of the thickness in the order of tens of micrometres and the strength and flexibility of the carbon film it might even protect against mechanical damage to the device. This thickness also helps to achieve reasonable conductivities. Carbon electrodes show slightly higher sheet resistances of about 10 $\frac{\Omega}{\square}$ compared to about 1 $\frac{\Omega}{\square}$ of evaporated metal electrodes.[138] To achieve this a thickness of tens of micrometres is needed compared to only about 100nm100 nm thick metal electrodes. A strategy to improve the conductivity of carbon electrodes is doping. Similar to semiconductors (see Doping) impurities purposefully introduced into the carbon materials can increase the number of free charge carriers and change the energetic behaviour of the resulting electrode. The carbon work

function has been reported to be around -5.0 eV similar to the -5.1 eV one of gold commonly used to fabricate stable PSC.[136] This work function is suitable but slightly lower than the optimum for extraction out of ETL.[139]

Besides enhancing the conductivity doping can also be used to shift the work function of the carbon electrode material closer to the work function of the adjacent transport layer to improve the charge extraction (see Contact Potential). This doping can, for example, be achieved by tuning the carbon black oxygen content as Tian et al.[140] show or by doping boron into the graphite lattice making it more p-type as shown by Duan et al.[141] The perovskite field can built here on extensive knowledge by other fields using carbon electrodes for example biochemical sensors and electrochemistry. In this thesis, I present a detailed study of the energetic alignment of different ETLs with the carbon electrode in Chapter 4. Further, I hypothesised the mentioned oxygen doping of carbon electrodes as a potential degradation pathway of carbon electrodes. I later ruled this pathway out in Chapter 5.1 by showing similar ageing behaviour in devices aged in ambient air and $N_2$ environment.

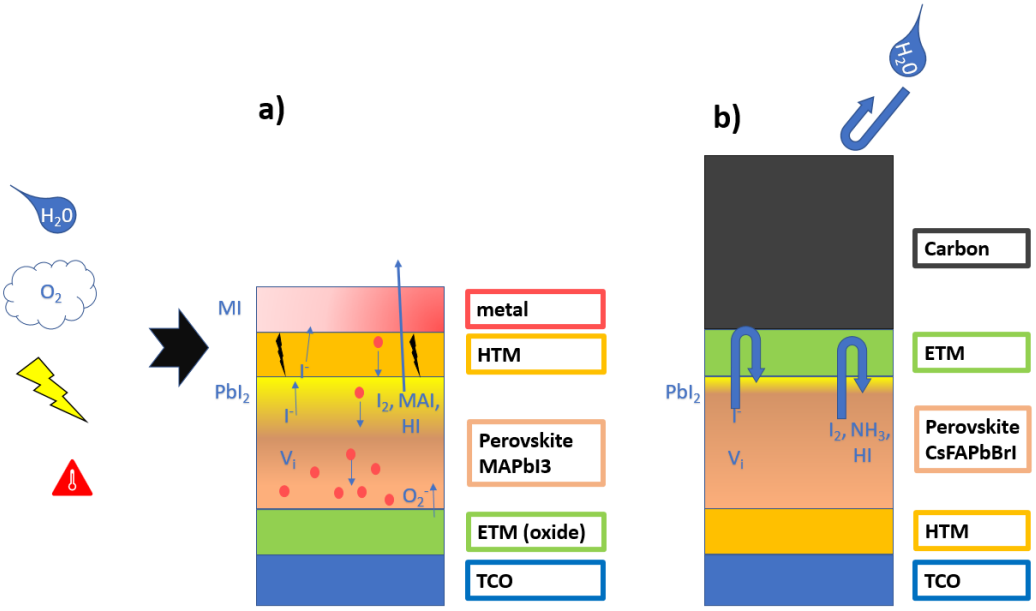



**Figure 2.21 Stability advantages of a Carbon PSC**

(a) Degradation pathways in an unstable perovskite solar cell stack without any material choices to mitigate stress-induced instabilities. A light-facing oxide-based transport layer on the bottom of the stack causes oxide species to react with the perovskite causing decomposition and trap state formation (see Metal Oxide Instabilities). An unstable perovskite (in this example $MAPbI_3$) decomposes easily upon exposure to environmental stressors. Volatile species can leave the layer. The metal electrode reacts with leaving halide species, accelerating the material loss. Additionally, metal species can diffuse into the perovskite layer causing trap states and degradation. (b) Influences of material choices on the stability of perovskite solar cells. Avoiding an unstable metal oxide and preventing direct perovskite metal oxide contact improves the stability of this

contact. An MA-free perovskite composition enhances the heat stability of the perovskite layer. A carbon electrode does not show the electrode-related stability issues that metal electrodes cause leading to potentially higher device stability.

While metals do react with halides that might leave the perovskite carbon-based materials do not.[132] Therefore, carbon electrodes do not accelerate the decomposition pathways of perovskite crystal degradation releasing halides.[70,96,131,142] Because of the mentioned hydrophobic behaviour of carbon-based materials, carbon electrodes can provide a barrier preventing moisture ingress to the perovskite. Using a carbon electrode on a PSC can this way inhibit moisture-induced degradation, lowering the susceptibility to moisture ingress into a device. More moisture-resistant devices can help reduce encapsulation requirements, thus cutting costs and facilitating production.[133,134]

Carbon electrodes are further thermally stable up to very high temperatures and show no tendencies to diffuse or release material into the subjacent layers.[175-177] In addition to the significant stability advantage, it has been reported that carbon-based materials are potentially easier to process compared to other electrode preparations.[136,146] Carbon electrodes can be processed at ambient conditions via scalable processes. The main reported carbon deposition techniques for opaque back electrodes are explained in the section following here.

#### 2.5.3.3 Carbon-Based Electrode Preparation Types

PSC with carbon back electrodes can be divided into three different technologies. One possible technique builds on high-temperature carbon treatment to form a porous carbon electrode on a porous insulating spacer material separating the carbon electrode from the ETL and the TCO contact preventing shunts (see Figure 2.22). In these devices, a dried and sintered stack of mesoporous ETL, such as $TiO_2$, mesoporous insulator, such as $ZrO_2$ or $Al_2O_3$, and mesoporous carbon is infiltrated with perovskite. Each of the three mesoporous layers is sintered at high temperatures (> 400 °C). Since the perovskite cannot sustain temperatures that high,[144,147] it needs to be introduced into the pore volume after the heat treatment.[131,136] Since not only the perovskite but also most of the used HTLs would not withstand a 400 °C sintering step, almost all of the high-temperature carbon devices are HTL-free.[131,136] This architecture was first developed by Kay et al.[148] in 1996 for dye-sensitised solar cells. It was first used in PSC by Ku et al.[149] in 2013. Last year (2024) Liu et al.[115] reported a PSC using this triple mesoporous HTL-free architecture with enhanced $TiO_2$ perovskite interface,

reaching a PCE of 22%. Because the triple mesoporous cells are so different in nature of production and charge carrier dynamics from other perovskite solar cells,[150,151] including those in this thesis, I will not discuss them further in more detail.

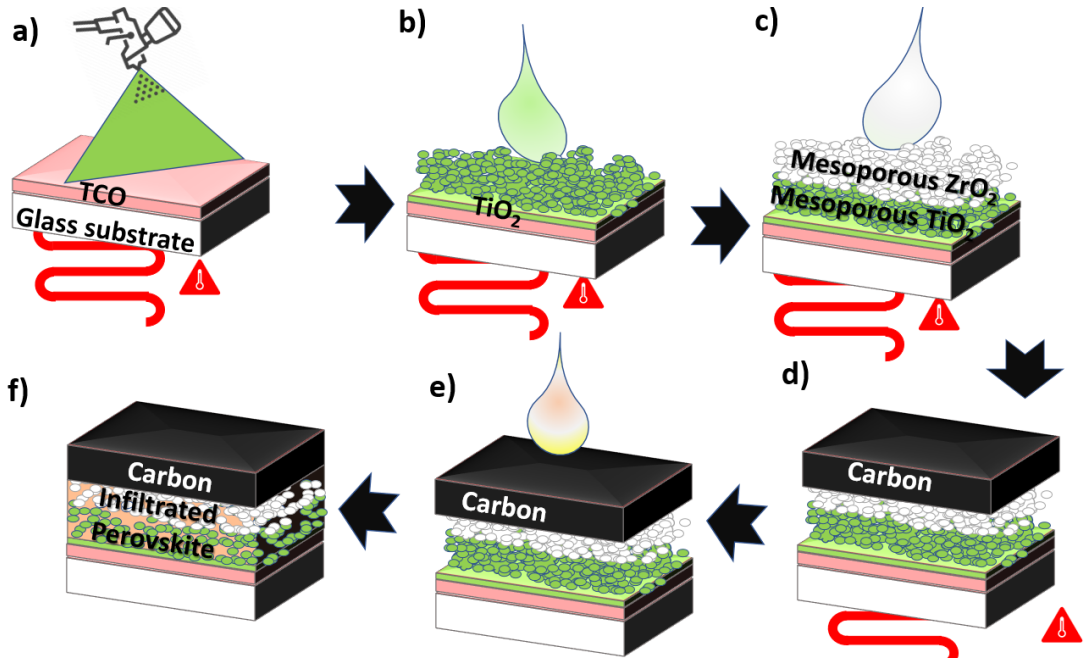



**Figure 2.22 High-temperature Carbon Treatment - Triple Mesoporous Structure**

(a) – (f) The fabrication steps for a perovskite solar cell of the triple mesoporous structure. (a) Deposition step of the hole-blocking layer $TiO_2$ (usually by spray pyrolysis) onto an FTO substrate. (b) The mesoporous $TiO_2$ layer is applied and sintered at high temperatures. (c) An insulating mesoporous $ZrO_2$ layer is applied and sintered at high temperatures. (d) A mesoporous carbon electrode is deposited on top and sintered at high temperatures. All the steps a) - d) involve temperatures from about 400 - 450°C. (e) The heat-sensitive perovskite is infiltrated in the triple mesoporous scaffold after the high-temperature steps. No hole transport layer is used in this architecture.

Triple mesoporous devices are also always perovskite single junctions. Including several different perovskite compositions in this infiltration process would be difficult. While this triple mesoporous route has led to impressive stability,[69] efficiency, and module records,[115,131,136] identifying a viable pathway for advancing this technology in multijunction PV remains challenging. The high temperature used in the process would also require a high energy expenditure in production and make using flexible substrates almost impossible. For this reason, I focus on carbon electrodes fabricated through low-temperature routes.

Besides the high-temperature mesoporous architecture, there are two different established methods to fabricate PSC with carbon back electrodes. For both, the carbon electrodes are applied on the back

of an already completed PSC stack. The processing temperatures of the carbon layer need, therefore, to stay below temperatures that damage the perovskite or other layers below the carbon while depositing the electrode. The fabrication of low-temperature-carbon (LTC) based PSC is very similar to traditional PSC. Therefore, this method can build upon several years of perovskite production experience. This is important for the perovskite layer itself since solvent engineering and fine-tuning of the deposition have led to big improvements in the crystallinity of this layer over the past decade. In high-temperature carbon cells, the perovskite must crystallise in the pore volume (Figure 2.22). This limits the pathways through which the solvents can evaporate. Additionally, it constrains the dimensions of the crystals. There is still less understanding of these directed forces acting on the crystallites and of the course of crystallisation in the carbon pore volume.[131]

One of the LTC methods uses a carbon paste deposited directly as a wet film onto the device stack via methods like blade-coating, screen printing, or slot-die-coating (Figure 2.23a).[131,136] With blade-coating of carbon electrodes PCEs of up to 21% have been demonstrated.[152,153] Subsequently, the film is dried driving out the solvents. This method is relatively facile in that it requires only one simple deposition step and has a similar process flow to the well-established metal electrode process in PSC. To avoid redissolving underlying layers solvent orthogonality is important to consider when processing one solution layer on top of another. This is especially important for carbon blade-coating because of the much larger thickness and volumes of solvents in this layer in comparison to the other layers in a PSC as visible in the SEM cross-section in Figure 2.23c. This is for example explained further in Beynon et al.[154]

Another strategy to avoid the carbon paste dissolving the top transport layer or perovskite can be the use of a buffer layer providing a solvent barrier between the carbon paste and the rest of the stack while processing. Zouhair et al.[155] used an about 90nm thick 2D perovskite layer as a buffer between their 3D perovskite and their carbon film. They achieved an impressive stabilised PCE of 17.8% without using any hole transport layer (HTL). However, their stack comprised $TiO_2$, which is linked to instability issues (see 2.5.2.3 Metal Oxide Instabilities).[103,108,156,157] One of the only few publications of carbon electrodes on p-i-n configuration by Babu et al.[158] also uses such a buffer layer. They evaporate a layer of 5 nm Cr to protect the stack from solvent damage. We used their research as our starting point and replicated their success with Cr/C electrodes, achieving efficiencies

of 17.7% MPPT, exceeding their efficiencies of 14.5%. However, an evaporated metal layer contradicts some of the advantages of using a solution-processed carbon electrode.

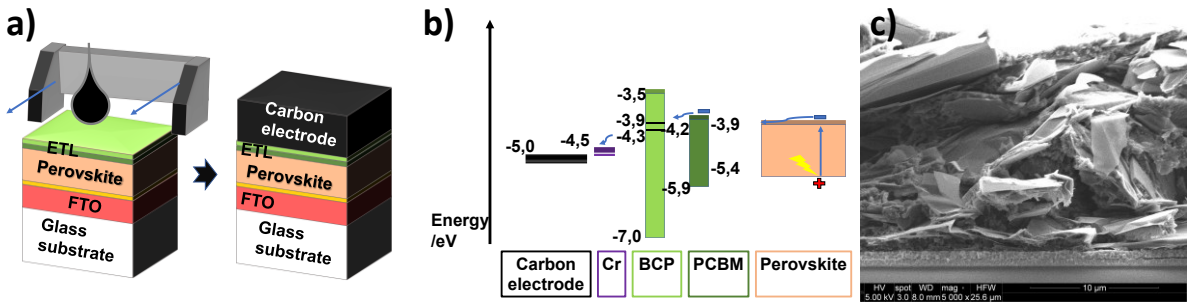



**Figure 2.23 Blade-Coating Process Schematics**

(a) Schematics illustrating a carbon electrode preparation using the blading-coating process. A thick carbon paste film is applied onto a beforehand prepared perovskite solar cell (PSC) stack. (b) The energy alignment of the layers used in the first successfully prepared carbon PSC stack in the p-i-n configuration. (c) An SEM cross-section of such a device.

During my master's thesis in the same research group, I designed an electrode layout and implemented a blade-coating process compatible with the laboratory and testing setups in the group. I was able to build on this success when starting the work for my PhD. A commercially available carbon paste by Dyenamo AB was used at the beginning of this work and I later transitioned to a paste provided by a collaborator. To ensure scalability, low material use and less hysteretic behaviour the carbon electrode was applied to PSCs I used the p-i-n structure (see 2.3.2 Device Structures). This structure is generally less reported, and especially underexplored in combination with carbon electrodes. The energy levels of the used materials are visualised in Figure 2.23b. The work function of carbon as described above is relatively low for electron extraction but has been used to extract holes in direct contact with the perovskite even without an HTL.[131,159,160] This complicated the use of the electrode in the p-i-n structure as explained in Chapter 4.

For the second LTC method, the carbon electrode is prepared by hot pressing. Before the press transfer onto the stack, the carbon electrode is prepared as a film on a host substrate and dried completely (Figure 2.24). This way solvent exposure to the stack is avoided. By optimising the thickness and flexibility of the carbon film, Zhang et al.[161] achieved an efficiency of 19.9% with a press transferred carbon electrode. Later Sutherland et al.[162] demonstrated a 20.3% efficient small scale device by optimising the lamination process. They used isostatic pressure to laminate the carbon

electrodes onto the device stack. However, the field was struggling to use the approach to produce electrodes with bigger active areas. Most of the successful press transfer carbon films were done on 0.1 $cm^2$ devices.[161,163] Su et al.[138] were able to solve this issue by using an aluminium foil as a host substrate that would remain an integral part of the electrode on the device. They, however, encounter issues of delamination of the Al foil from the carbon resulting in problems with achieving long-term stability of the C/Al electrodes. Sepalage et al.[164] tried to solve this issue by applying an evaporated Cu layer or a blade-coated silver layer to connect the carbon with the aluminium foil. However, the evaporated Cu layer contradicts the advantages of using carbon-based electrode materials. All press transfers described above have been exclusively performed on n-i-p devices. In this work, I implement the first press transfer on p-i-n devices in collaboration with Luke Sutherland from Commonwealth Scientific and Industrial Research Organisation (CSIRO), Clayton, Australia and Hadi Mohammadzadeh from Fraunhofer Institute of Solar Energy (ISE), Freiburg, Germany.

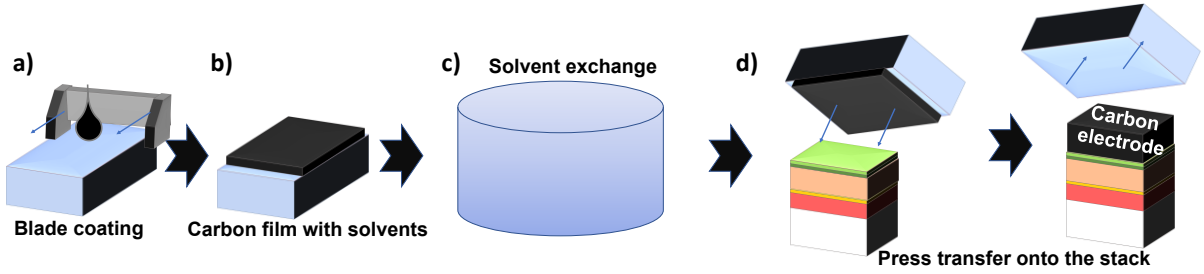



**Figure 2.24 Press transfer of a Carbon Electrode**

(a) A carbon paste with a high boiling point solvent is blade-coated onto a carrier material. (b) The resulting wet film on the carrier material is then immersed into a bath of low boiling point solvent like for example ethanol (c). This process removes the high boiling point solvents from the thick film through solvent exchange. The low boiling point solvents evaporate subsequently more easily either in a curing step or left for air drying. (d) The dried carbon film is then transferred via high-pressure press transfer. The substrate can either be removed as illustrated in d) or in the case of conductive substrates like metal foils, become part of the final electrode setup.

The low-temperature process reduces energy expenditure compared to high-temperature carbon and thermal metal evaporation. The low material and energy efficiency of evaporation and sputtering processes to achieve patterned metal electrodes might make this process less suitable for commercial PSC production. In contrast, carbon electrodes could be deposited at ambient pressure and moderate temperatures. Methods like the blade-coating used in this work are suitable for upscaling to high throughput industrial processes potentially allowing for super low CapEx fabrication of PSC. This

method allows for large and flexible substrates, a wider variety of transport layers, and the conduction of all available perovskite deposition processes.[131] Beynon et al.[154] show that carbon stencil printing of the carbon paste used in this work can be integrated into a roll-to-roll process that can be used for high-throughput production. Therefore, I explore both possible low-temperature carbon routes in this work.

In conclusion, carbon electrodes are suitable for PSC to suppress almost all major degradation pathways linked to electrode materials in PSC. They can be prepared in three ways including one high-temperature and two low-temperature fabrication techniques. The latter two promise excellent scalability for low CapEx fabrication of PSC and the first one has demonstrated over 10,000 h stable devices. As part of this work, I achieved the first reported device with p-i-n architecture without any thermally evaporated layers by using a low-temperature (80°C) blade-coated carbon electrode (see Chapter 4).

# 3 METHODS

## 3.1 Device Fabrication

Most devices were fabricated in the Clarendon Laboratory at the Department of Physics of the University of Oxford. Some layers were also deposited in other laboratories at the University of Oxford. All devices in the section General Stability of Cr Metal Bilayers and some devices in the section Adhesion of Laminated Carbon Films were manufactured at the Fraunhofer Institute for Solar Energy Systems ISE in Germany. Some layers, but not full devices, were produced by collaborators at different locations including the Technical University of Denmark in Denmark and the CSIRO in Australia.

### 3.1.1 Materials

Poly(4-butylphenyl-diphenyl-amine) (polyTPD) was purchased from 1-Material. 2,3,5,6-Tetrafluoro-7,7,8,8-tetracyanoquinodimethane (F4-TCNQ) was purchased from Lumtec. Lead iodide ($PbI_2$, 99.999%, metals basis), caesium iodide (CsI, 99.99%), and lead bromide ($PbBr_2$, ≥98%) were purchased from Alfa-Aesar, Thermo Fisher. Formamidinium iodide (FAI) and carbon paste (DN-CP01) were purchased from Dyenamo AB. 1-butyl-1-methylpiperidinium tetrafluoroborate ($[BMP]^+[BF_4]^-$, 99%) was purchased from Sigma-Aldrich. [6,6]-phenyl-C61-butyric acid methyl ester (PC61BM, >99.5%) was purchased from Solenne BV. Bathocuproine (BCP, 98%) was purchased from Xi'an Polymer Light Technology Corp. Aluminium zinc oxide (AZO) and $SnO_2$ nanoparticles were bought from Avantama AG. Tetrakis(dimethylamino)Tin (TDMASn) for ALD and AP-CVD precursor was bought from Pegasus Chemicals. Deionised water ALD was used as the oxidiser. PEDOT:PSS dispersion in $H_2O$ was purchased from Ossila. Unless stated otherwise, all other materials and solvents were purchased from Sigma-Aldrich. All materials were used as received without further treatment or purification.

### 3.1.2 Substrate Preparation

FTO substrates were used for all devices fabricated in Oxford. The substrates were either bought pre-patterned from Latech or unpatterned from Pilkington. Unpatterned substrates were chemically etched with Zn powder and 2 M HCl to fit the electrode pattern. During etching the active area was covered with a Kapton polyimide tape. Devices were then scrubbed with a toothbrush with DI water and Fairy washing up liquid, rinsed with deionised (DI) water, and sonicated for 15 min in each aqueous solution of 10 vol% Decon 90 cleaning liquid in DI water, DI water, Acetone, and isopropyl-2-alcohol (IPA). Subsequently, substrates were UV ozon-treated for 15 min.

### 3.1.3 Precursor Solution Preparation

All precursor solutions for Spin-Coating (see below) were prepared by weighing dry powder materials into a vial. Amber vials were used to prevent the photodegradation of materials. A high precision balance (Kern ABJ 80-4NM) was used to weigh the exact weight to an accuracy of 0.2 mg. The weighing was performed in an $N_2$-filled glovebox free of any solvent handling. Powder-filled vials were then vacuum sealed and transferred into a separate $N_2$-filled glovebox. A magnetic stirbar was added to the vials. Subsequently, the exact volume of solvents was pipetted into the vial to achieve the desired concentration of solution or dispersion. Unless mentioned otherwise, all precursor solutions were prepared fully in the $N_2$ environment, stirred overnight (~14 h), and filtered with a 22 µm PTFE filter.

### 3.1.4 Thin Film Deposition

As described in Device Structures, solar cells consist of multiple functional layers for light absorption and charge separation. In PSC these layers have thicknesses between one nanometre to one micrometre. A uniform layer thickness and good conformal coverage of the subsequent layer is needed. To achieve such layers different deposition techniques were used and are explained here.

#### 3.1.4.1 Spin-Coating

In spin coating, a thin layer is deposited out of a precursor solution containing the desired material to form the final layer dissolved in a solvent. During the process, a substrate is rotated at high

rotations per minute (rpm). The spin speed and the concentration were used to tailor the film thickness. A higher spin speed or a lower concentration can be used to deposit a thinner final film. I used spin speeds between 1,000 and 6,000 rpm and concentrations between 0.025 and 1,000 mg/ml for different processes.

The solution was dispensed onto the substrate at a specific volume out of a pipette. This can be done while the substrate is spinning ("dynamic spin-coating") or before the start of the spinning ("static spin-coating") as shown in Figure 3.1a - b. Due to the fast rotation, the solution spreads evenly onto the substrates forming a thin wet film. The solvents are removed through combinations of spinning, thermal drying on a hot plate, and in the case of the perovskite the introduction of an antisolvent (see Perovskite Layer and Figure 3.1c - d). The perovskite precursors salts in the wet film with solvents that dissolve these powders are exposed to a solvent in which the precursors have a low solubility. This makes them crystallise (partially) driving out the initial solvents. The antisolvent method strongly improves the crystallinity of the resulting thin film.[165,166]

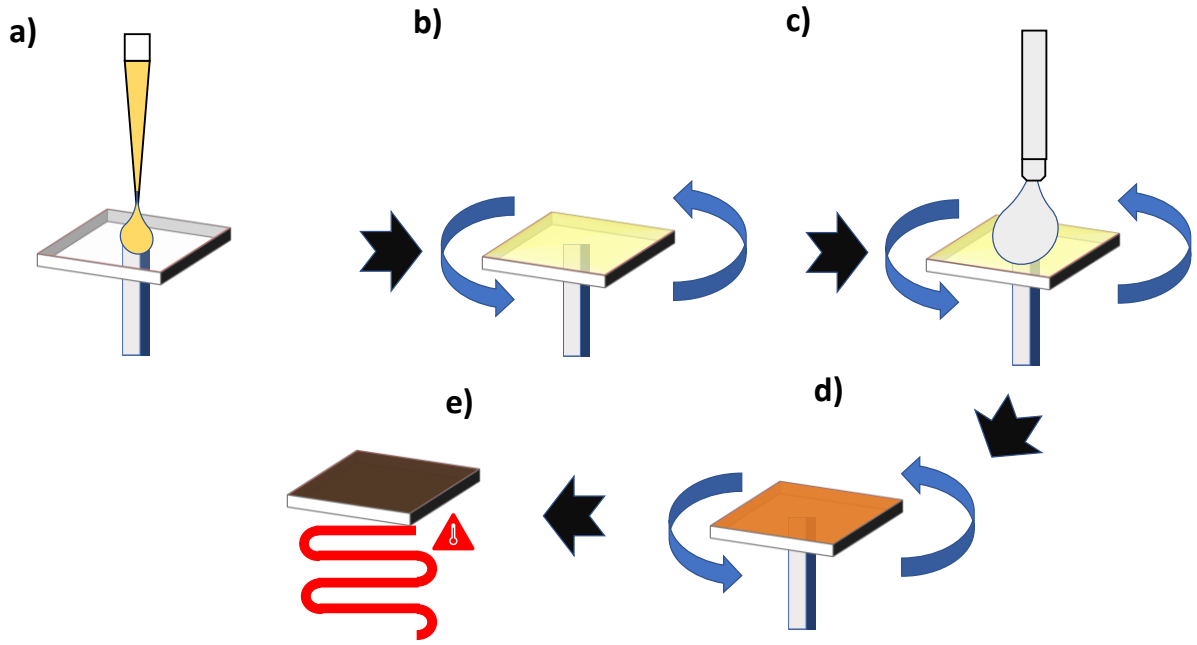



**Figure 3.1 Perovskite Spin-Coating with Antisolvent Quench**

(a) A perovskite precursor solution is dropped onto a substrate. (b) The substrate rotates at high rotations per minute (rpm). (c) An antisolvent is dropped onto the spinning substrate. (d) The perovskite crystallises in small domains. (e) Remanent solvents are removed and the crystallinity is improved in a hot plate annealing step after the spin-coating programme.

#### 3.1.4.2 Blade-Coating

For the blade-coating, a paste similar to the precursor solution in spin-coating but with higher viscosity was used. The paste is spread over the desired area by dragging a metal blade over the substrate. The thickness of the wet film is defined by the distance between the metal blade and the substrate. The film is then dried driving out the solvents. Different methods can be used for this drying process. In this work, I explored heating on a hot plate, hot gas flow over the substrates, and solvent exchange to remove the solvent. Blade coating was used for the deposition or preparation of carbon Electrode.

#### 3.1.4.3 Thermal Evaporation

Thermal evaporation was performed to deposit a solid-state material without any solvent or other intermediate precursor of the material. The evaporations were run in a chamber containing one or more material sources and a substrate holder. The chamber was pumped to a high vacuum to lower the evaporation temperature of the desired material. The material source was usually either a crucible, made of a heat-resistant ceramic and heated by a resistive heating coil wrapped around it, or a "boat" made of a heat-resistive metal. The Cr depositions forms an exemption (see 3.1.8.1 Cr Interlayer). The boat was hereby simultaneously the container for the material and the resistive heating element. The opening of the boat or crucible was pointed in the direction of the substrates. The material was placed in the form of a pellet or powder either into a crucible or onto a boat. The material was then heated up by resistive heating until it was released usually as material clusters into the chamber drifting towards the substrates where the material condensate forming a layer of the desired materials.

The rate of material deposition was monitored through a quartz crystal microbalance (QCM). The frequency at which the QCM vibrates changes with the weight of the material deposited on it. This change in frequency is linked to a specific change in layer thickness on the substrate via a tooling factor. The tooling factor depends on the geometry and was found for each material and chamber to be able to monitor the layer thickness of a specific evaporation. In this work thermal evaporation was used for the deposition of metallic electrodes, the ETL materials $C_{60}$ and BCP, and the encapsulation material $MoO_3$.

#### 3.1.4.4 Atomic Layer Deposition

A method to achieve very conformal layers of different atoms is atomic layer deposition (ALD). Atoms are deposited onto the substrate one atomic layer after another in cycles. The substrates are held in a reactor and are exposed at certain times to precursor gases. Each exposure is followed by a purge to remove the gas from the chamber before introducing the next precursor gas. The precursor gas consists of the atom that is desired to form the layer with some ligands attached to it. The atom with the ligands is brought into a gaseous state and introduced into the chamber.

In the chamber, it condensates onto the substrates and the ligands are removed from the atom in a thermally activated surface reaction on the substrate leaving behind ideally only the desired atom on it. Excess precursor gas and ligand decomposition products are removed by a purge before the next layer of a different atom type is introduced. This results in the deposition of a layered structure of alternating arrangement of two distinct types of atoms in a periodically repeating sequence. In real ALD systems, the complete removal of the ligands is challenging, leaving behind some quantity of ligands in the film. In this work, an ALD was used for the Tin Oxide. Hereby I encountered quality differences between the materials with different ALD systems in different laboratories (see Chapter 4).

### 3.1.5 Wetting Agent

As mentioned above (3.1.4.1), in solution processing, the material to be deposited is dissolved in a host solvent. For successful film formation, the solution must spread uniformly across the surface to ensure continuous and conformal coverage after solvent evaporation. When the host solvent exhibits poor wettability on that surface, a wetting agent is deposited beforehand to reduce the contact angle and promote uniform spreading of the solution.

Alumina nanoparticles ($Al_2O_3$ np) were used on a hydrophobic material (in this work, mostly the organic HTL polyTPD) to increase the surface roughness and provide some hydrophilic sites for the solution to spread over the substrate. Because the $Al_2O_3$ np is an insulating material, a non-continuous layer was deposited. All substrates were transferred back into an $N_2$-filled glovebox. An $Al_2O_3$ np dispersion was prepared by mixing a 20 wt% $Al_2O_3$ np dispersion in IPA (as bought CAS 1344-28-

1, nanoparticles, <50 nm particle size (DLS), Sigma Aldrich) with more IPA in a ratio of 1:125 further diluting it down. The wetting layer was spin-coated at 5000 rpm for 40 s.

### 3.1.6 Perovskite Layer

The perovskite precursor solution was prepared by stirring overnight 3.3 mg ($[BMP]^+$ $[BF_4]^-$), 256.2 mg CsI, 827.9 mg FAI, 2295.5 mg $PbI_2$, and 319.2 mg $PbBr_2$ in 3.2 ml DMF and 0.8 ml DMSO to obtain 4 ml of 1.45 M solution of $Cs_{0.17}FA_{0.83}Pb_{1.01}I_{2.73}Br_{0.27}$ in 4:1 DMF:DMSO. The perovskite layer was spin-coated with 250µL of precursor solution in a two-step programme at 1000 rpm for 5 s and 5000 rpm for 30 s. An antisolvent quench was performed by dropping 400 µL of Anisole antisolvent on the spinning substrate five seconds before the end of the programme (see Spin-Coating). Subsequently, the perovskite films were annealed for one hour at 100 °C.

### 3.1.7 Electron Transport Layer

#### 3.1.7.1 PCBM

I prepared a fresh PCBM solution at most every 6 weeks by dissolving 20 mg/ml in 3:1 di-chlorobenzene:chlorobenzene. After perovskite deposition, the substrates were left for a 10 min cooldown each on a cleanroom wipe before the PCBM deposition. I spin-coated the PCBM dynamically 50 µL of solution at 2000 rpm for 20 s and annealed for 5 min at 100 °C.

#### 3.1.7.2 C60

For the $C_{60}$ in Chapter 4 the perovskite films were transferred into a custom-built evaporation chamber. The $C_{60}$ layer was deposited under a high vacuum (~$10^{-7}$ mbar) at ~0.15 Å/s to achieve thicknesses of 20-70 nm. All other C60 layers used in this work were deposited in the National Thin Film Cluster Facility for Advanced Functional Materials (NTCF) by Dr Jin Yao with a thickness of 20 nm at high vacuum.

#### 3.1.7.3 BCP

BCP (0.5 mg $ml^{-1}$, Xi'an Polymer Light Technology Corp) was dissolved in IPA by stirring overnight at 70 °C and filtered with a 0.22 µm PTFE filter. The BCP solution (70 µl) was spin-coated dynamically on the PCBM layer at 5000 rpm for 30 s and subsequently dried at 100 °C for 1 minute.

#### 3.1.7.4 Tin Oxide Atomic Layer Deposition

ALD thin film of $SnO_2$ in Oxford was deposited in a Picosun ALD (R-200), which is part of the NTCF. The substrates were kept at 100 °C during the deposition. $N_2$ was used as a carrier and purging gas. The vessels for TDMASn and DI water were maintained at 70 and 20 °C, respectively. 20 nm thick $SnO_2$ films were achieved by depositing 140 cycles consisting of 1.6 s of TDMASn pulse/10 s purging/1 s of water pulse/10 s of purging for a single cycle.

The ALD in Freiburg was deposited in a glovebox-mounted GEMstart ALD system with a deposition substrate temperature of 80 °C, with TDMASn and DI water as precursors, and with 121 cycles to achieve a thickness of 20 nm.

#### 3.1.7.5 Interlayers

All interlayers were, if not stated otherwise, deposited onto the PCBM by a 70 µL dynamic spin-coating step, in an $N_2$-filled glovebox, at 5000 rpm for 30 s, and subsequently dried at 100 °C for 1 minute. Polyethylenimine Ethoxylated (PEIE) and Polyethylenimine (PEI) were prepared at concentrations of 0.05 and 0.025 wt% in IPA and deposited. Zirconium(IV) acetylacetonate (ZrAcac) was dissolved in IPA at a concentration of 1 mg/ml and deposited. AZO and $SnO_2$ nanoparticles were diluted in IPA in varying rations (1:0, 1:1, 1:2, 1:3, 1:5, and 1:10), sonicated and filtered, and deposited. PH1000 was deposited undiluted, or diluted in varying ratios in methanol or IPA at 4000 rpm for 40 s in ambient air followed by an anneal at 100 °C for 10 min. Deviating modes of preparation are described in detail in the results section.

#### 3.1.7.6 Graphene

The graphene films were purchased from 2D, a spin-off of the Technical University of Denmark (DTU). The graphene is secured on a PDMS (Polydimethylsiloxane) release layer and covered by a PVA (Polyvinyl Alcohol) for protection. The films were cut in the desired shape (covering the active area on the substrate) and then submerged in DI water overnight to remove the PVA protective layer. The PDMS/graphene was placed with the graphene facing down directly onto the perovskite layer. The graphene was transferred from the PDMS onto the perovskite by heat and pressure either by a hot lamination machine (DTU) or by rolling on with a glass vial followed by a hotplate anneal (at

the University of Oxford). Transfers at DTU were done in ambient conditions, where the films were exposed to roughly 1 hour of ambient during processing.

### 3.1.8 Electrode

Before the electrode deposition, substrate areas designated for the common counter electrode were prepared. The HTL, perovskite, and ETL were mechanically scraped off these areas, exposing the underlying TCO which is more resistant to the mechanical procedure. This ensured direct counter-electrode contact with the TCO (Figure 3.2). For devices intended for encapsulation additionally, all four edges were scraped off the HTL/perovskite/ETL stack to ensure direct contact between the later applied encapsulation and the glass substrate without a prone to degradation perovskite layer in between. All the different electrodes used in this work are explained in this section.

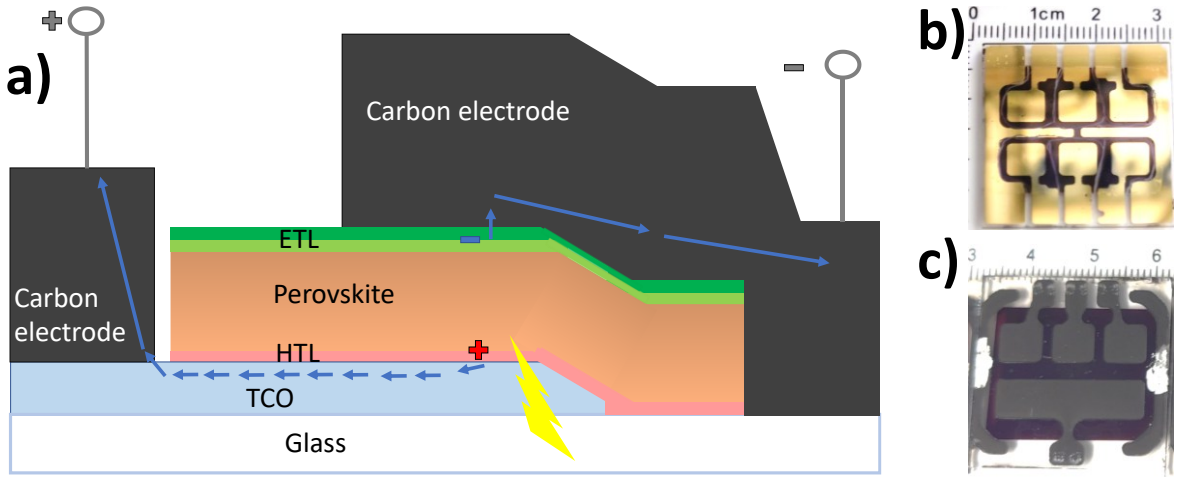



**Figure 3.2 Electrode Design**

(a) Schematics of the working principle of a single junction p-i-n perovskite solar cell with a carbon electrode. Light enters the cell from the bottom through the glass and the transparent conductive oxide (TCO). Positive charges are transported through the hole transport layer (HTL) and the TCO before being collected at the common carbon counter electrode to the left. Negative charges are collected through the back electrode of each of the devices to the top right. (b) A substrate with six devices with evaporated Au electrodes with an active area of 0.25 $cm^2$. (c) A substrate with four devices with blade-coated carbon electrodes with an active area of three times 0.25 $cm^2$ and one device with 1.00 $cm^2$.

#### 3.1.8.1 Cr Interlayer

For the $Cr/Cr_2O_3$ interlayer, 5 nm of material was evaporated from a Cr source. For devices fabricated in Oxford, a Cr-coated tungsten wire was used as the source (results shown in Chapters 66.3.1 and 66.3.4). Devices fabricated in Freiburg were prepared using a Cr electron beam source.

#### 3.1.8.2 Metals

All metal layers were thermally evaporated at pressures below $2.0 \cdot 10^{-6}$ torr. Metal pellets (Au, Ag, Cu, or Al) were loaded in a tungsten boat. The substrates were loaded face down into a substrate holder with shadow masks covering the areas of the substrate that are intended to be free of evaporated metal. This way, a pattern of metallisation is achieved, separating patches of metal into the electrodes of distinct devices and metal contacts of the counter electrode. The holder was kept rotating during the deposition. The first nanometre was evaporated at a lower rate of 0.1 Å/s to avoid damage to the underlying layer. The rate was then slowly increased to up to 1.0 Å/s. I performed the Cr, Au, and Ag depositions in Oxford on a Kurt J. Lesker Nano 36 evaporator and the Cr/Al depositions on a thermal Evaporator custom-built by Angstrom and part of NTCF.

#### 3.1.8.3 Carbon Blade-Coating

Two different pastes were used throughout this work. One was bought from Dyenamo AB, used as received and dried with a hot air gun at a distance of 17 cm for 5 min. The other was produced by combining 1-Butanol solvent and ethyl cellulose to form a 12.5% weight resin followed by mixing under high shear using a speed mixer to combine a 21.7% weight addition of Carbon made up of Graphite (Imerys Timrex) and Carbon Black (Imerys Ensaco 360G) in a 2.6:1 ratio and dried on a hotplate at 80 °C for 10 min.

Carbon electrodes were blade-coated using a micrometre adjustable blade (Figure 3.3). The electrode was patterned by masking areas on the substrate with a polyethene sticker while blade-coating. I designed the stickers with Computer-aided design software. The Green Tree Ltd dye cut the designed stickers. The substrates with the masking sticker and carbon paste wet film were dried together as described above. After the drying step, the sticker was removed leaving behind the desired electrode pattern (Figure 3.2c).

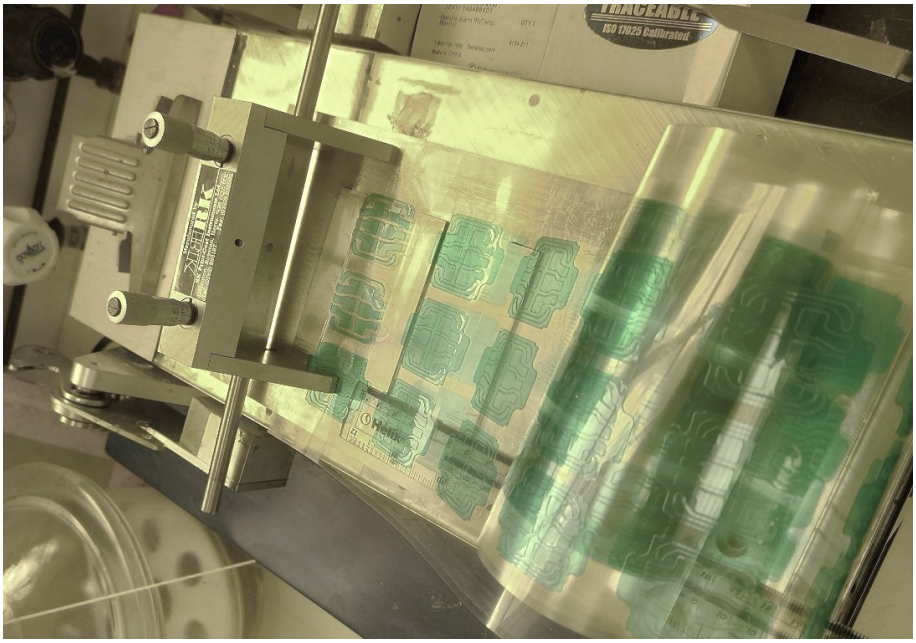



**Figure 3.3 Blade-Coating Setup**

The micrometre adjustable blade on the left side and the stickers used for carbon electrode patterning to the centre-right.

#### 3.1.8.4 Carbon Lamination

For the laminated carbon electrodes, a thick film of a carbon paste was blade-coated onto a glass substrate. A solvent exchange and drying were performed. Initially, electrodes were prepared by Dr Luke Sutherland at CSIRO, Clayton, Australia as detailed in Sutherland et al.[162] and later by Hadi Mohammadzadeh at Fraunhofer ISE, Freiburg, Germany as detailed in Mohammadzadeh et al.[167]

### 3.1.9 Hole Transport Layer

The hole transport layer solution was prepared by dissolving 1mg/ml polyTPD with 20 $_{wt}$% F4-TCNQ in toluene by stirring overnight at 70-80 °C in an $N_2$-filled glovebox. This stock solution was used for up to six weeks. Directly before spin-coating, the solution was filtered with a 22 µm PTFE filter and transferred out of the glovebox. PolyTPD was then spin-coated dynamically at 2000 rpm for 20 s and substrates were annealed at ambient air for 7 min at 130 °C.

## 3.2 Ageing

### 3.2.1 Encapsulation

Devices were encapsulated with a glass slide glued to the back side of the substrate over the active area with a UV-activated epoxy (Everlight Eversolar AB-341). The epoxy was applied to the glass slide before the substrate was placed in the correct position onto the epoxy glass slide followed by 3 minutes of UV-curing. For devices in the ITO versus FTO study (see Chapter 6 section ITO and FTO Transparent Electrodes), a recessed cavity glass with epoxy deposited only at the raised edge of the encapsulation glass was used. For all other studies, the glass slide was fully covered by the epoxy.

To ensure good glass-epoxy-substrate contact and avoid edge effects, perovskite material was removed from the substrate at the edge of the encapsulation area. For the outdoor ageing in Chapter 4, pre-existing devices were used so that the perovskite removal could not be done retrospectively to ensure a good encapsulation. For the second Cr-metal study in Chapter 6 Sustainable Electrode Materials, a 32 nm layer of $MoO_3$ was evaporated over the active area before the glass slides were glued on.

### 3.2.2 Outdoor Ageing

The outdoor ageing test was performed in Freiburg, Germany (48.010°N, 7.832°E, Köppen-Geiger climate zone Cfb). Devices were mounted to a fixed-plane measurement array with an inclination of 32° on a rooftop. The ageing started on 5th April 2023 and ran for 2500 h. During the outdoor ageing, periodic reverse scan current-voltage measurements were performed on all cells in intervals of 15 min. In between the measurements, cells were kept under open circuit conditions, short circuit conditions or under load, at their respective maximum power points as indicated in the results. We only used data from measurements performed at a global irradiance higher than 150 $W/m^2$ (0.15 suns) for performance analysis.

### 3.2.3 Accelerated Ageing

If not stated otherwise all ageing was performed in ambient air in an air-conditioned laboratory unencapsulated and under $V_{OC}$ bias conditions.

### 3.2.3.1 "Freiburg" box

Devices were put into 3D-printed black holder active side facing up into a home-built ageing box. The box was illuminated with a sulphur light. The temperature was controlled with varying fan speeds to keep the air temperature in the chamber at 40 °C. The temperature on the back side of the glass encapsulation was measured with a thermocouple Greisinger GTH 1170 Digital Quick Response Thermometer to be between 50 and 68 °C as shown in Figure 3.4. Due to the thermal conductivity of glass, there can be an expected temperature gradient through the encapsulation glass thickness. Hence, the perovskite active layer can be significantly higher than the 50 and 68 °C range.

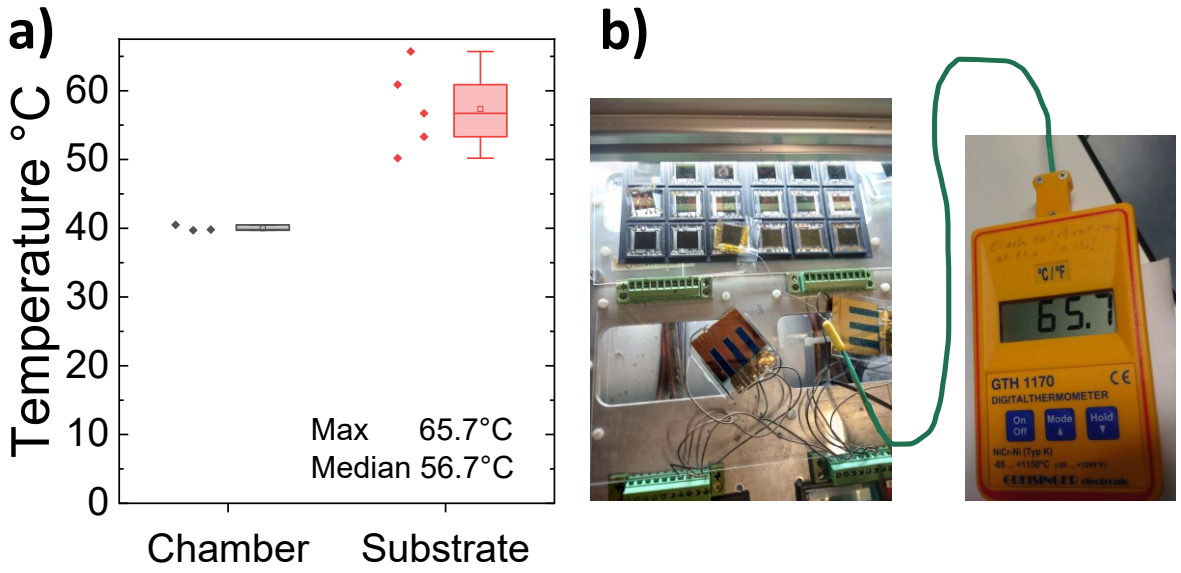



**Figure 3.4 Ageing chamber Cr/metal study**

Measured temperatures inside the ageing chamber are shown in (a). The "Chamber" values indicate the measured air temperature inside the ageing chamber and "Substrate" values are measured with a thermocouple taped in thermal paste onto the back encapsulation glass as displayed in (b). It can be assumed that the temperature of the backside of the encapsulated glass is not hotter than the temperature of the active layer inside the device encapsulation.

### 3.2.3.2 Atlas boxes (65 and 85 °C light ageing)

Devices were placed in a black (anodised) metal rack facing the glass side up in a closed Atlas box (Figure 3.5). Their active layer was kept at 65 °C or 85 °C (as measured and controlled with a black temperature standard). The ambient temperature in the chamber was around 35 °C. They were illuminated with a Xenon lamp SunTest CPS Plus simulated AM1.5 sunlight (760 W/m$^2$). The temperature was regulated by reducing the heat induced by the illumination with varying fan speeds.

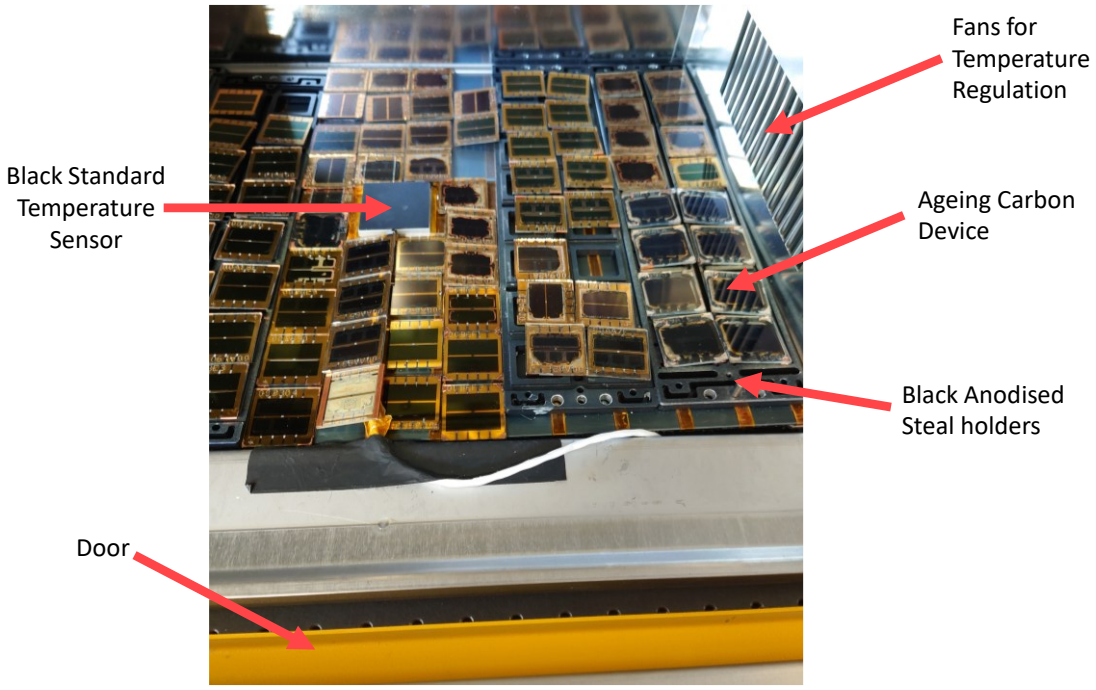



**Figure 3.5 Atlas Ageing Box**

Perovskite solar cell devices inside an ambient air Atlas heat and light ageing setup. The black temperature standard and anodised metal rack are visible. The photo was taken with an opened door while the box was turned off for unloading samples.

#### 3.2.3.3 Nitrogen heat-light ageing

Perovskite films were placed standing upright in an infrared oven. The substrates were held by an aluminium plate facing the glass door of the oven. A three-colour plant growing lamp was placed to illuminate the substrates through the oven door. The oven was controlled to be at 65 °C for the first 300 h and then to 85 °C from 300 to 3750 h. The oven, however, could only reach up to 70 °C when set to 85 °C. The whole setup was based inside a $N_2$-filled glovebox. For the Cr/Ag vs Ag $N_2$ study the same oven was operated without the LED light and with an aluminium cover to keep devices completely in the dark. The dark experiment was run for 20,000 h.

#### 3.2.3.4 Light ambient ageing

Devices were placed glass side up onto a Peltier cooler below a three-colour plant growing lamp (Figure 3.6). The devices were kept at 25 °C. The setup was in ambient air in an air-conditioned laboratory.

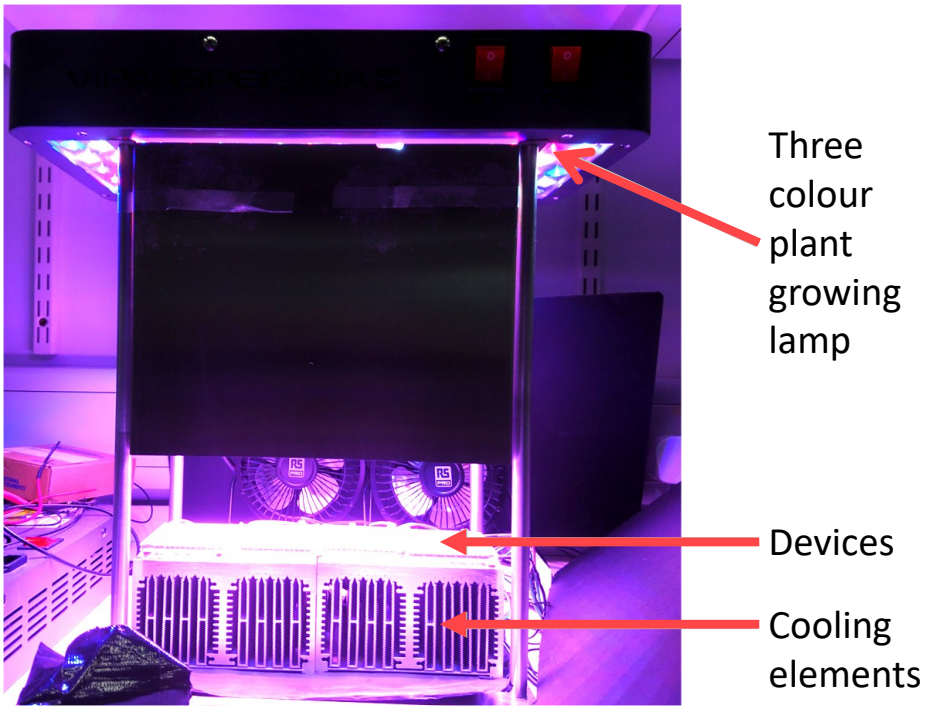



**Figure 3.6 Ambient 25 °C ageing setup**

The ambient room temperature light ageing set under operation. A three colour light emitting diode array (plant growing lamp) illuminates perovskite solar cell devices placed onto a cooling element keeping the device at 25 °C.

#### 3.2.3.5 Nitrogen heat ageing

Devices were placed in a rack covered with a metal tray inside an infrared oven kept at 85 °C inside an $N_2$-filled glove box.

## 3.3 Characterisation

### 3.3.1 Solar Simulator

A solar simulator was used to determine the *JV* characteristics and stabilised power (MPPT), voltage ($_{SS}V_{OC}$), and current ($_{SS}J_{SC}$) output of devices. The result of an MPP tracking is shown in Figure 3.7a. All light measurements were performed under AM1.5G illumination (WaveLabs Sinus-220 solar simulator) with 100 mW $cm^{-2}$ equivalent irradiance (certified by KG3-filtered Si reference photodiode). The used spectrum of the light source is shown in Figure 3.7b. Voltage was swept from 1.4 V to − 0.05 V and back at a rate of 0.3 V $s^{-1}$ with a maximum current cut off at 50 mA/$cm^2$. The device's active areas were defined by black anodised metal shadow masks. Note that the axes are inverted (Figure 2.6). The data was plotted in this way to align with the established convention in solar research, where the *JV* curve is plotted in the fourth quadrant, recognised as the power-

generating quadrant. The voltage and current signs are reversed due to the measurement setup. Because of how devices are contacted during the measurement, p-i-n and n-i-p devices have inherent polarity differences. As a result of the measurement protocol, p-i-n and n-i-p devices exhibit opposite signs for voltage and current, necessitating different power quadrants when plotted directly. To maintain consistency with convention and enhance comparability, all devices are represented within the fourth quadrant, irrespective of the voltage and current polarity assigned by the measurement software.

For stabilised $_{SS}V_{OC}$ and $_{SS}J_{SC}$ measurements, devices were held at 0 V or $_{SS}V_{OC}$ for 10 s. For stabilised power measurements, an MPP tracker based on a gradient descent algorithm was employed to measure the maximum power for 30 s. A quasi-steady-state FF was calculated by dividing the product of V and $J$ at the max power measured by the steady-state PCE measurement by the product of steady-state $_{SS}V_{OC}$ and $_{SS}J_{SC}$ as described in Current Density-Voltage Behaviour. In a small number of older studies, a Stabilised Power Output (SPO) efficiency was used instead of the MPPT efficiency. The SPO was obtained by keeping the device for 15 s at a fixed $V_{MPP}$ bias obtained from the $JV$ scans.

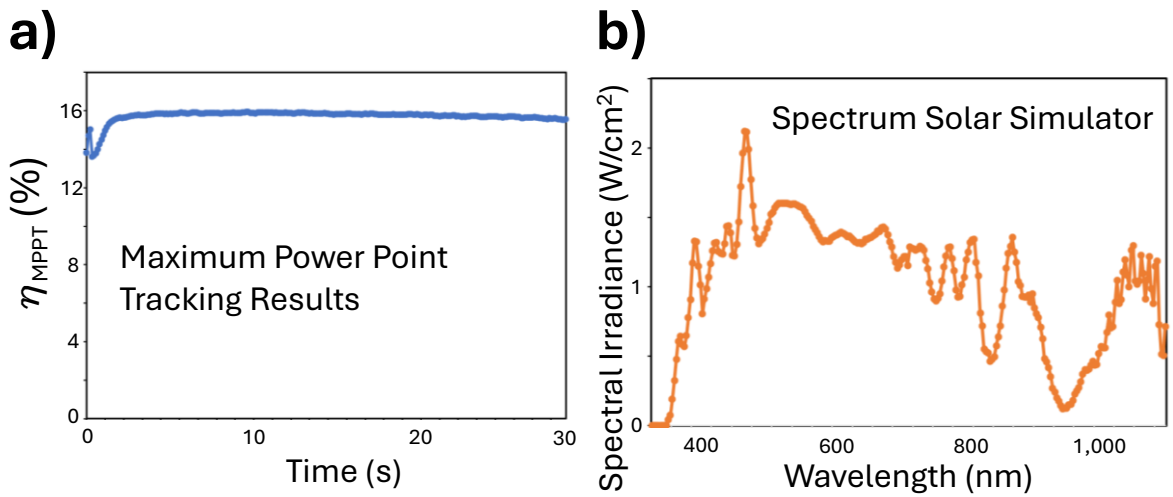



**Figure 3.7 Solar Simulator Operation**

(a) An example of an MPP tracking of a PSC. (b) The calibrated spectrum at the beginning of the solar simulator measurement.

### 3.3.2 Scanning Electron Microscopy

Samples for top view were prepared by depositing the perovskite layer as described above on a TCO substrate. The film was mechanically removed with a razor blade on the edges and a cross in the middle of the substrate. Conductive tape was applied over the area with exposed TCO. For cross-sections, we prepared samples by diamond scribing the edges and cleaving the substrates mechanically. The breaking point was set to lie the active area of devices. All samples were grounded to the sample holder with conductive tape. A Hitachi S-4300 scanning electron microscope was used for imaging. A working distance of 8 - 10 mm, a spot size of 3.0, and an acceleration voltage of 5 kV were used.

### 3.3.3 Four Point Probe Measurements

Four probe measurements were used to obtain the sheet resistivity of materials. The setup and the sample preparation are visualised in Figure 3.8. A film of the material of interest was deposited on clean, 1.5x1.5cm glass substrates. A well-defined gold electrode structure was evaporated on top of the material. In the channel between the gold electrodes, a current was forced through the materials layer. In the middle third of the channel, the voltage drop was measured. Out of the known current and the measured voltage the sheet resistance was calculated with the equation below. With the known thickness of the deposited layer, it is also possible to calculate the resistivity of the layer. The sheet resistivity is independent of the layer dimensions and given in $\frac{\Omega}{\square}$ (Ohm Square). In contrast, the resistivity is given in Ωm and depends hence on the dimensions of the layer.

$$\rho_{\square}\left(\frac{\Omega}{\square}\right) = \frac{\pi}{ln\,(2)}\,\frac{V}{I} \qquad 3.1$$

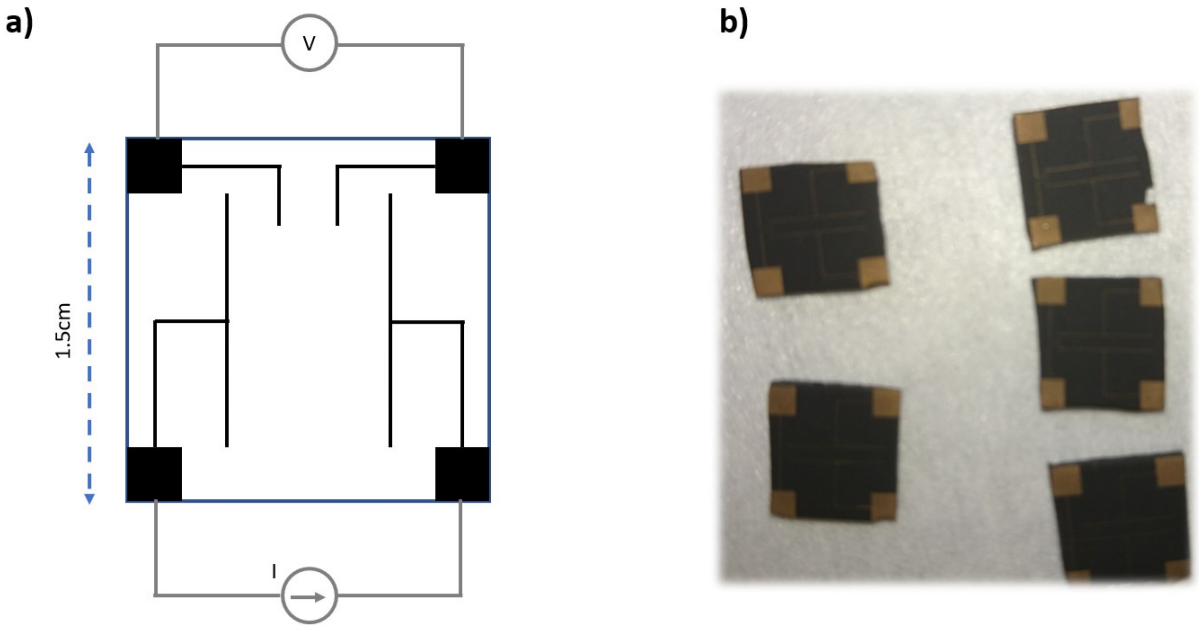



**Figure 3.8 Four Probe Measurement**

a) The schematics of the 4-probe measurement setup used for this work. The blue square is the glass substrate with the layer of interest on it. The black structures are 75 nm thick gold electrodes evaporated on top of the material. The squares in the corners are the places where the probes are lowered to connect the measurement setup to the sample. (b) Substrates prepared in the described way.

### 3.3.4 Photoluminescence Quantum Yield

For photoluminescence, quantum efficiency films were excited by a 405 nm laser (Roithner laser MLL-III-405-200 mW) and a 532 nm laser (Roithner laser RTLMLL-532-1.5-3W). A large spot size of 0.15 $cm^2$ was used. Laser intensities were adjusted to be equivalent to one sun for the given band gap of 1.61 eV. Measurements were carried out in an integrating sphere, and a calibrated grating spectrometer (QEPro, OceanInsight), using previously established protocols. Photoluminescence Quantum Yield of samples was determined according to the method of de Mello et al.[168] The resulting PL signal was collected via a fibre bundle (Ocean Optics QR600 7 SR125BX) coupled with a spectrometer (QE Pro, Ocean Optics). An empty measurement was taken with each sample to determine the background and stray contribution.

### 3.3.5 Time-Resolved Photoluminescence

The photoluminescence decay curves were collected on a FluoTime 300 (PicoQuant GmbH) using a TimeHarp 260 as a time-correlated single photon counting setup (TCSPC) and a pulsed laser diode

with an excitation wavelength of 405 nm (LHD-P-C-405, PicoQuant GmbH). The repetition rate of the diode was 0.5 MHz. Charge carrier lifetimes for each perovskite sample were calculated out of the photoluminescence decay signal by Dr Manuel Kober-Czerny as the time where the signal has decayed to 1/e of the initial signal.

### 3.3.6 X-Ray Diffraction

Full device stacks on TCO substrates were prepared as samples for X-ray diffraction (XRD). Diffraction patterns were obtained by using a Cu Kα X-ray source (λ=1.5406 Å) and a Panalytical X'PERT Pro X-ray diffractometer. Scans were conducted for two hours per sample in ambient air and an automatic sample changer was used.

### 3.3.7 Kelvin Probe

Measurements were carried out using a KP Technology APS04 integrated Kelvin probe system using a gold-plated tip (ϕ: 2 mm). Samples were left to equilibrate in the dark under measurement, with the work function reported being the stabilised value. Work function values were obtained in measurements in air and in an $N_2$ environment, to check for potential degradation during long measurements in air.

### 3.3.8 Ambient-pressure Photoemission Spectroscopy

Measurements were carried out in the same setup described above (KP Technology APS04 integrated Kelvin probe system). Samples were illuminated by a UV lamp with a fitted monochromator, scanning from low to high energy whilst the gold-plated tip was biased at +10 V and held at a position close (~ 1 mm) to the sample. The generated photocurrent ($I_{ph}$) was recorded for each incident photon energy and was plotted as either $\sqrt[2]{I_{ph}}$ for metallic surfaces or $\sqrt[3]{I_{ph}}$ for semiconducting surfaces. HOMO/VBM levels were found by the intersection of the linear region of the square/cube-root photocurrent response and the baseline.

### 3.3.9 External Quantum Efficiency

The external quantum efficiency of devices was determined using Fourier transform photocurrent spectroscopy. We used a custom-built set-up based on a Bruker Vertex 80 v Fourier transform interferometer. The PSC devices were masked with a metal aperture such that the whole active area was illuminated (same procedure as for the Solar Simulator). To determine the EQE, the photocurrent spectrum of the tested device was divided by the spectrum of a calibrated Si reference cell (Newport) of a known EQE. The reference cell was measured at the beginning of each set of measurements.

The equivalent short circuit current density under 1 sun irradiance from the EQE measurements, was calculated through the overlap integral of the AM1.5 photon flux (φAM1.5) spectrum with the EQE:

$$J_{SC} = q \int_0^{\infty} EQE(\lambda)\phi_{AM1.5}(\lambda)\, d\lambda \qquad 3.2$$

where q is the elementary charge ($1.602176634\times10^{-19}$ C) and λ is the wavelength of the probing light.

Band gaps were determined from EQE by plotting $(E \cdot EQE)^2$ against E. The intersection of a linear fit to the EQE onset to 0 was used as the EQE band gap, as described by Carron et al.[169]

### 3.3.10 Time of Flight Secondary Ion Mass spectrometry

The time-of-flight secondary ion mass spectrometry (TOF-SIMS) analyses were carried out by ION-TOF GmbH in Münster, Germany on a TOF.SIMS 5 system. The instrument is equipped with a reflectron-type analyser and a microchannel plate detector. A Bismuth liquid metal ion source (LMIS) was employed for mass data acquisition. Mass data was acquired using the $Bi^{3+}$ cluster ion. Mass data acquisition was performed by raster scanning over a 100 × 100 $\mu m^2$ area. A 25 keV $Bi^{3+}$ primary ion beam with a 0.18 pA current was used. A cycle time of 100 μs was employed for mass data acquisition (with masses ranging from 1 to 830 u). A Cs ion source was employed as the sputter/etch tool. The area analysed by the LMIS was at the centre of the sputter/etch crater formed using a scanning Cs+ beam. A 3 kV Cs+ primary ion beam was employed. The Cs+ sputter/etch area was 400 × 400 $\mu m^2$. The depth profiling analyses were performed in the 'interlaced' mode, where the sources can operate simultaneously and continuously.

### 3.3.11 Atomic Force Microscopy

For AFM measurements a Park NX10 AFM system with NCM-NHCR tip and Park SmartScan software was used in non-contact mode. On each sample, 5 μm scan areas were measured across the substrate and compared to a larger scan to confirm a proper representation of the topography. AFM Z height images were processed and analysed with Gwyddion software.

# 4 INTERFACIAL LAYERS FOR P-I-N PEROVSKITE SOLAR CELLS WITH CARBON ELECTRODES

## 4.1 Motivation

Perovskite solar cells have achieved high power conversion efficiencies. However, they usually rely on metals and vacuum deposition, necessitating more complex and expensive deposition equipment as well as causing stability issues (see 2.5 Stability Challenges). Carbon-based materials offer a cost-effective and potentially more stable alternative (see 2.5.3 Carbon-Based Electrodes). The vast majority of carbon-electrode PSCs use the negative-intrinsic-positive (n-i-p) or "hole-transport layer-free" architectures. Here, we present a systematic study to assess the compatibility of “inverted”, p-i-n configuration PSC contact layers with carbon rear electrodes. I identify incompatibilities between common electron transport layers and carbon electrode deposition process and a previously unobserved semiconducting behaviour in carbon electrodes with distinctive implications for charge extraction and electronic behaviour. To overcome the issues caused by this behaviour, I introduce a double-layer atomic layer deposited tin oxide ($SnO_2$) and Poly(2,3-dihydrothieno-1,4-dioxin)-poly(styrene sulfonate) (PEDOT:PSS), yielding 16.6% PCE and a retained 94% performance after 500 hours of outdoor ageing. This study is a crucial step forward for printable, metal electrode- and evaporation-free solar technologies.

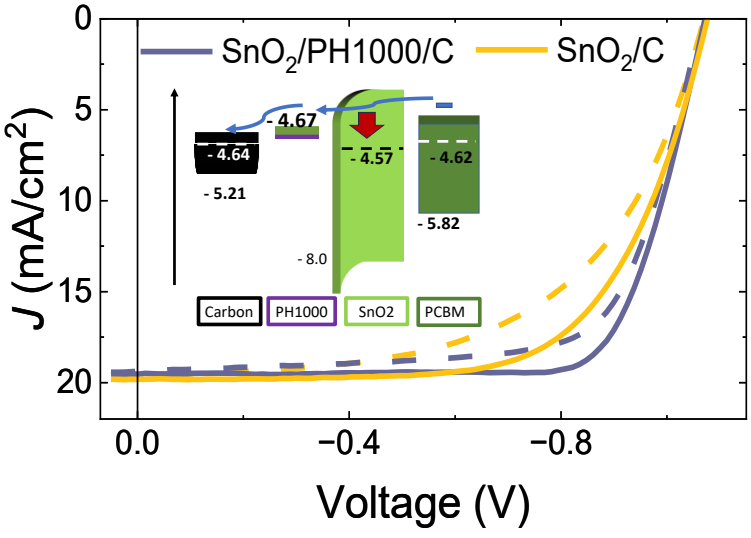



**Figure 4.1 Advantages of a PH1000 Layer at the Carbon $SnO_2$ Interface**

Current density-voltage (JV) curves of the best devices with and without a PH1000 layer between the carbon electrode and the atomic layer deposited $SnO_2$ electron transport layer. The dashed and solid lines represent

the forward and reverse scans of a single device, respectively. The device with a PH1000 layer shows in both scan directions a higher fill factor and higher performance than the one without. The inset shows a proposed energetic behaviour of the electron transport and electrode materials inside the device with a PH1000 layer. The energetic values for each material were obtained by Katherine Stewart and Charlie Henderson with Ambient-pressure Photoemission Spectroscopy for the valence band maximum and with Kelvin Probe for the work functions.

## 4.2 Introduction

Electrodes collecting charges are essential for both the performance and stability of Perovskite solar cells (see chapters Device Structures and Electrode Materials and Stability Issues). Unlike the bottom electrodes, which are usually commercial Transparent conducting oxides (TCOs) such as ITO and FTO, the terminal counter electrode is fabricated in various materials and processes and significantly influences device operation.[71,84,96,170] However, in state-of-the-art perovskite solar cells (PSCs), noble metals are predominantly used as counter electrodes. These metals have been linked to long-term stability issues as heat and light drive halide and metal interdiffusion, creating unwanted interfaces or charge recombination sites.[71,84,86,171] Incorporating a buffer layer (for example Cr) has been reported to prevent this diffusion by promoting Cr/Au alloy and effectively immobilising Au.[48,71] Indium-based TCOs have also been successfully employed as counter electrodes and are considered more inert than noble metals under device operational conditions. These two strategies will be investigated in a wider exploration in Chapter 6 Sustainable Electrode Materials. When TCOs are used, additional metals such as silver are often integrated as grids or fingers to boost charge transport and minimise series resistance.[96] Despite these approaches to improve stability, the scarcity of these materials remains a challenge for TW-scale production of solar cells.[172] This leads researchers to explore sustainable alternatives like the carbon electrodes used in this chapter.[131,136]

Carbon-based electrodes are an attractive alternative as they are based on a highly abundant element.[172] These electrodes can be produced via simple wet coating processes like slot-die, blade-coating or screen-printing, which might bring lower material and energy use compared with thermal evaporation or sputter coating (Figure 2.20a and Figure 2.23a).[211-213] Graphite-based carbon electrodes show good electrical conductivity, chemical stability, and cost-effectiveness (Figure 2.20b). Due to graphite displaying covalent bonds as opposed to metallic bonds, interdiffusion of the

carbon electrode with the perovskite is impossible and reactions with halides are far less likely compared to metallic electrodes. Being able to produce PV modules via these methods, having very high throughput, in atmospheric pressure and low temperatures remains attractive for low CapEx factories.[176]

Most PSCs with carbon-based electrodes (C-PSCs) use the n-i-p structure or the hole-transport layer (HTL)-free architecture.[131] However, the transport layers used in n-i-p devices, such as $TiO_2$ and Spiro-OMeTAD, are frequently linked to instabilities. Within the field of PSC, the p-i-n structure has been known to be more stable and has recently surpassed n-i-p devices in terms of absolute record efficiency of 26.2%.[215-217] Despite the stability and now efficiency advantage of p-i-n cells, there is limited literature on how to effectively use carbon electrodes with them. The transport layers in p-i-n devices are significantly thinner than in their n-i-p counterparts. This creates challenges for the mechanical and solvent stability of these thin layers when depositing carbon films on top. These challenges may explain the relatively low number of reports on C-PSCs with p-i-n structures compared to HTL-free and n-i-p C-PSCs.

One known issue of compatibility of carbon pastes and ETLs is that the solvents in the paste can dissolve the relatively thin ETL. I confirm the difficulties of solvent compatibility in this chapter. This can be prevented by introducing a buffer layer to act as a solvent barrier. Babu et al. 2020 [158] use a 5 nm thick layer of evaporated Cr as a buffer layer in p-i-n carbon devices, reaching steady-state efficiencies of up to 14.5%. I confirm this strategy in this thesis, breaking the efficiency record of Babu et al, achieving up to 17.7% with a PCBM/BPC/Cr/C ETL-electrode combination. However, an evaporated metal layer contradicts some of the perceived advantages of using a solution-processed carbon electrode.

As an alternative to the Cr/C electrode, I show efficient and stable p-i-n C-PSCs by ensuring carbon electrode process compatibility with an atomic layer deposition (ALD) $SnO_2$ buffer layer. The ALD layer prevented solvent damage by the carbon paste to the organic electron transport layers (ETL). This way, we achieved open circuit voltages ($V_{OC}$) comparable to metal electrode devices. We reveal that the carbon electrode top surface does not behave metallically but is semiconducting in nature. This behaviour is well suited for hole contact to the valance band or highest occupied molecular

orbital (HOMO) of a hole transport layer (HTL), but poorly matched to contact with the conduction band or lowest unoccupied molecular orbital (LUMO) or an ETL. To improve the electrical contact between the $SnO_2$ and the carbon electrode, we used a semi-metallic PEDOT:PSS (PH1000) as an interface layer, preventing the formation of a Schottky Barrier (see 2.1.6 Contact Potential). This approach yielded higher initial performance up to 16.6% compared to 13.7% without treatment (Figure 4.13) and slower degradation of the C-PSCs when aged under 85 °C and 0.76 suns and outdoor conditions (Figure 5.1). This contributes to the wider perovskite fields as a stepping stone, enabling carbon electrodes on p-i-n devices without any thermal evaporation step.

## 4.3 Results

Because of the outlined advantages of combining the p-i-n structure with carbon electrodes, this chapter describes some of the challenges in achieving this combination. These challenges include processing issues such as solvent damage to ETLs due to the carbon paste and energetic alignment issues between the carbon electrode and the commonly used ETLs. I also present a solution to overcome these challenges and discuss some fundamental problems using this solution as an example.

### 4.3.1 Solvent Damage-Related Issues of Carbon Electrodes

To investigate the nature of the carbon/ETL interface, we chose the simple device stack of FTO/polyTPD/perovskite/PCBM/Carbon. Devices with this architecture and carbon electrodes showed hysteretic JV behaviour and low voltage as displayed in Figure 4.2a. The resulting low maximum power point tracked efficiencies for these devices are displayed in Figure 4.2b.

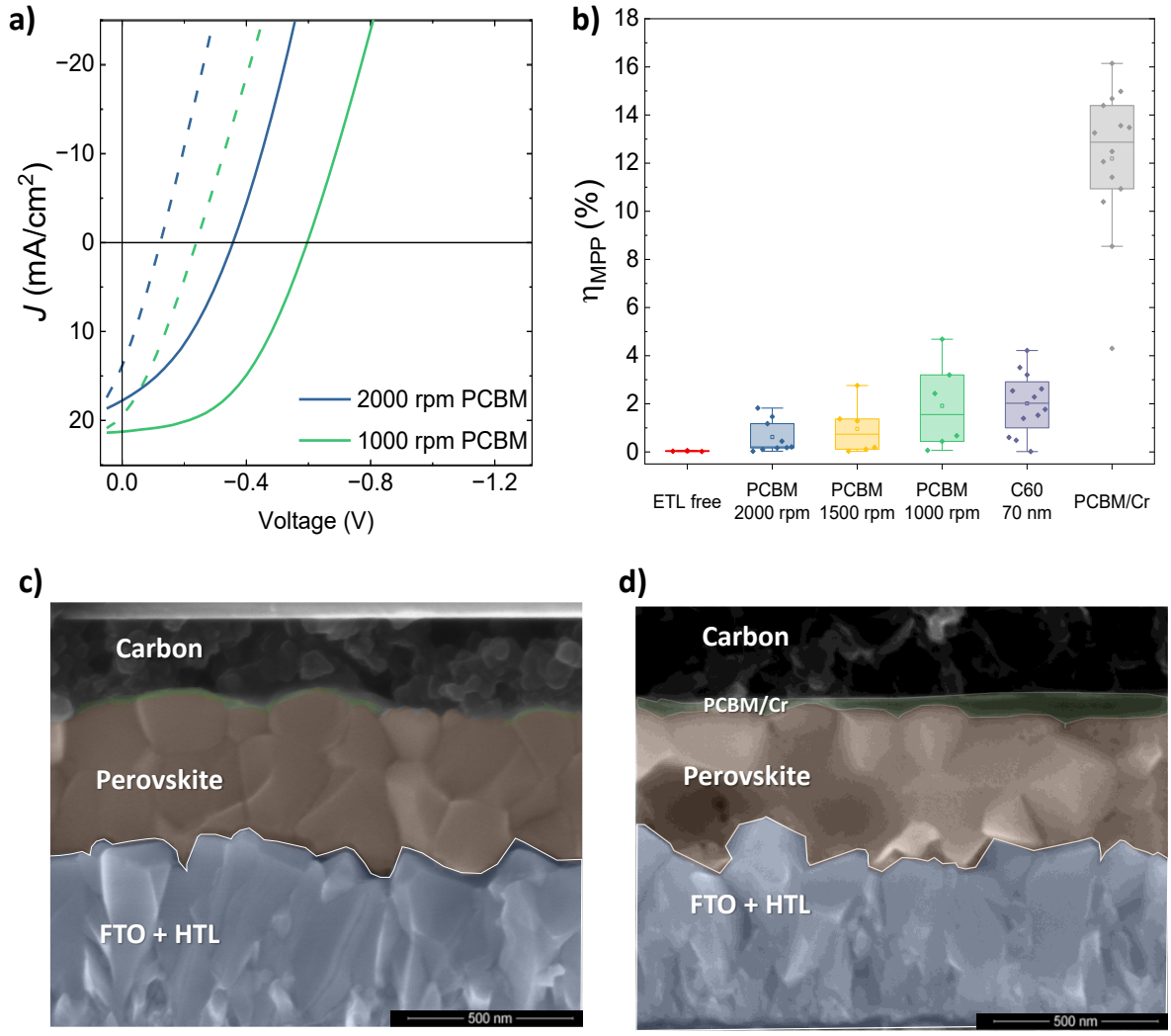



**Figure 4.2 Carbon Paste Dissolving Fullerene-Based Layers**

(a) The *JV* characteristics of devices with PCBM layers deposited with different spin speeds between the perovskite absorber layer and the carbon electrode. The dashed and solid lines represent the forward and reverse scans of a single device, respectively. MPP tracking efficiencies of different device types are shown in (b). (c) And (d) the SEM cross-sections of a device with PCBM deposited before Carbon without (c) and with (d) a 5 nm Cr buffer layer in between. The extent of FTO, perovskite, and PCBM layer (if visible) is indicated by an artificial transparent blue, brown, and green colour scheme.

To examine potential damage to the ETL, we increased the PCBM thickness from zero- no ETL deposited - to 30 nm (standard thickness) and then to an increased thickness of approximately 70 nm by reducing the deposition spin speed from 2000 to 1000 rpm. Increasing the thickness results in enhanced maximum power point tracked efficiency from 0% for no ETL, to less than 2% for 2000 rpm (30 nm), and up to over 4% for 1000 rpm (70 nm). The current-voltage behaviour of each thickness is shown in Figure 4.3.

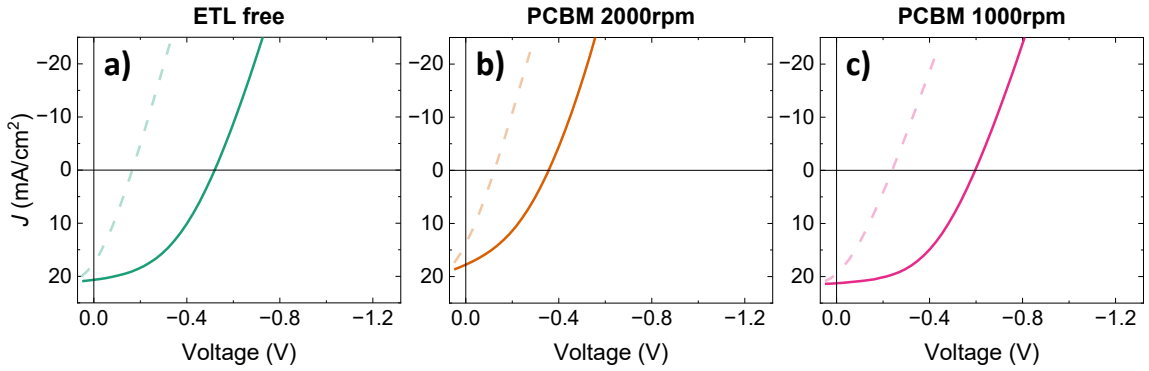



**Figure 4.3 *JV* of Devices with Different Electron Transport Layer Thicknesses**

(a) - (c) The *JV* scans of the champion devices without an ETL, PCBM deposited with a spin speed of 2000 rpm, and PCBM deposited with a spin speed of 1000 rpm, respectively. In each of (a) - (c) the dashed and solid lines represent the forward and reverse scans of a single device, respectively.

While it is difficult to give an exact layer thickness for such a thin layer when spincoating, thermal evaporation should give more precise control. I tested, therefore, the behaviour of devices with a 70 nm layer of evaporated $C_{60}$, followed by carbon paste deposition, also due to the expected higher resistance of this layer to solvents. These devices lead to similar behaviour and performance to 1000 rpm PCBM deposition. A continuous fullerene layer of that thickness should cause a considerable series resistance in a device. However, none of the *JV* scans, as shown in Figure 4.2a and Figure 4.3, show resistive behaviour of the expected magnitude. On the other hand, when using a 70 nm $C_{60}$ layer with a gold electrode, the devices show a big series resistance and zero efficiencies (Figure 4.4).

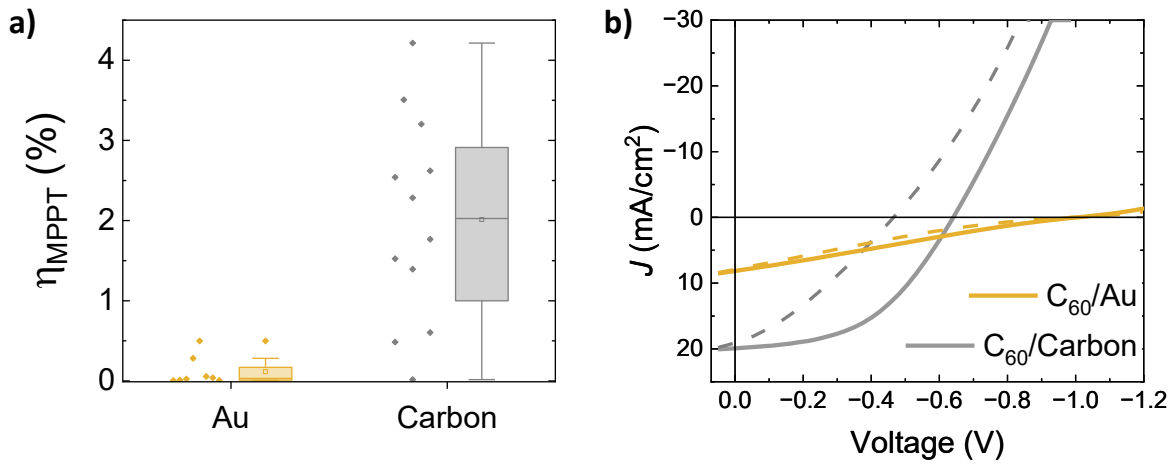



**Figure 4.4 Gold and Carbon Devices with 70 nm Evaporated $C_{60}$**

(a) The statistical distribution of performance via a 30s MPPT of gold and carbon devices with a 70 nm thick evaporated $C_{60}$ layer. (b) Characteristic *JV* scans of such devices. The dashed and solid lines represent the forward and reverse scans of a single device, respectively.

Devices with the thick $C_{60}$ layer and gold electrodes showed very high series resistance, resulting in a low current density and a fill factor of about 0.25. Devices with carbon electrodes reached maximum power point tracked performances of up to 4.2%. The *JV* scans showed high hysteresis and low $V_{OC}$.

To explore why our p-i-n carbon cells work so poorly, we imaged and scrutinised cross-sections of the devices via scanning electron microscopy (SEM). In the cross-section shown in Figure 4.2c, we cannot discern the ETL layer between the carbon and the perovskite layers. The absence of the ETL is not punctual but widespread throughout the device (Figure 4.5b). Likely, the carbon paste has completely dissolved the deposited fullerene layer.

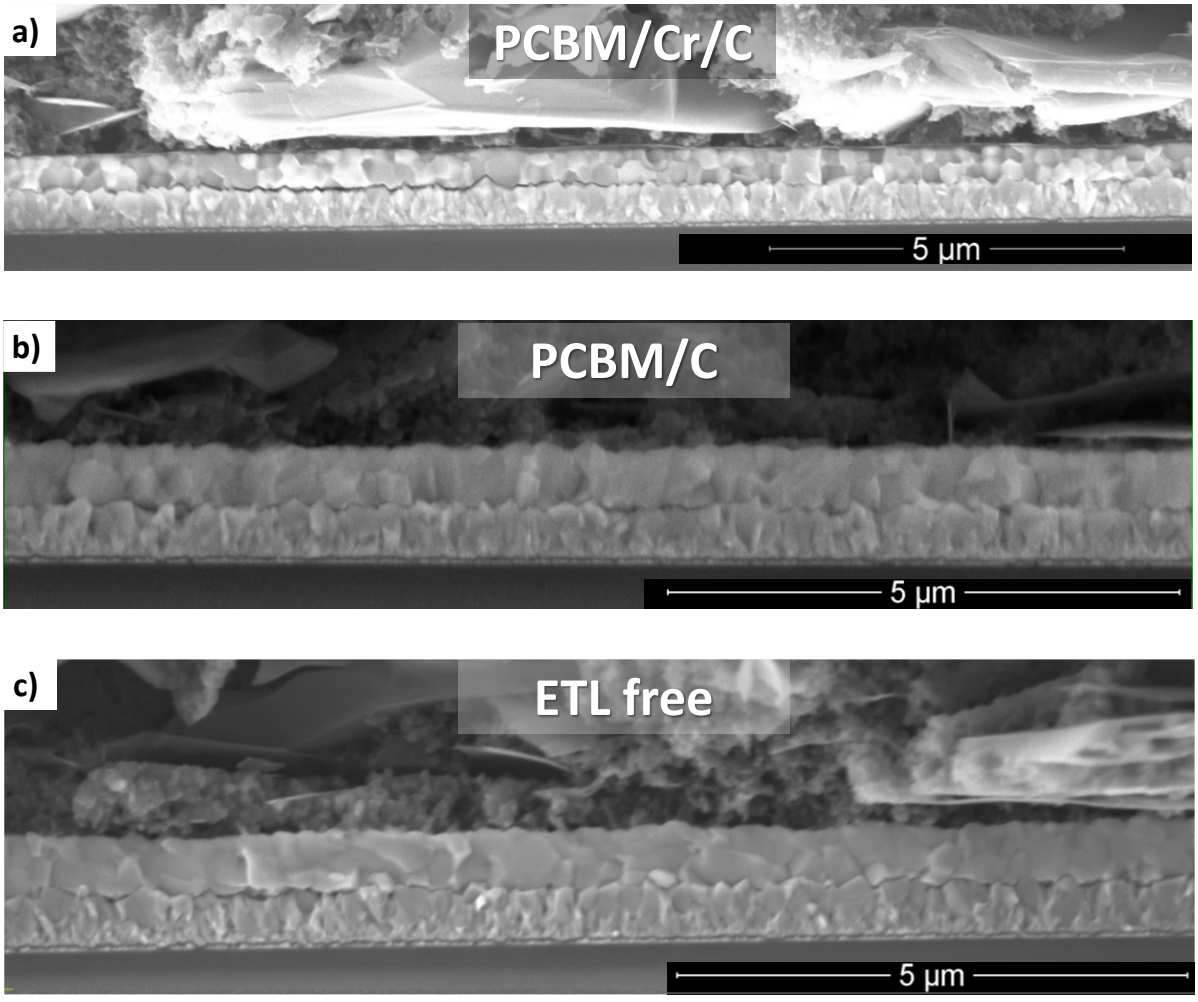



**Figure 4.5 PCBM Carbon Device Cross-Sections**

The SEM cross-sections (a) - (c) show devices with PCBM and 5 nm Cr, only PCBM, and no ETL in the stack between perovskite and the blade-coated carbon electrode.

Babu et al.[158] addressed the challenge of solvent damage by using a thermally evaporated chrome layer between a PCBM layer and the carbon electrode similar to the one used in Chapter 6. This way

they achieve a device with a stabilised performance of 14.5%. I implemented this method during my master's thesis and adapted it to my stack during my PhD.

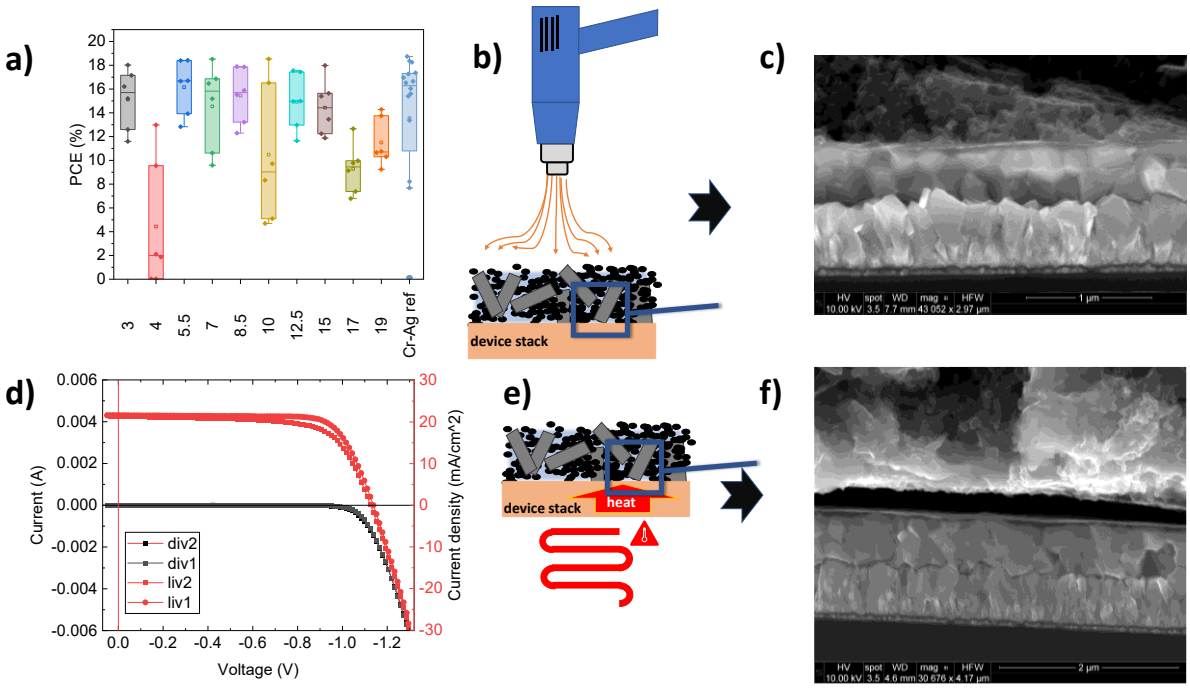



**Figure 4.6 Carbon Paste Curing Methods**

(a) The performance of devices with an evaporated chromium layer underneath the carbon electrode when cured for different times in minutes mentioned on the x-axis, under a heat gun and aged for 16 h in a 65 °C light ageing box. Plotted to the very right is the performance of metal electrode references, labelled Cr-Ag reference. (b) Schematics of the heat gun curing. (c) and scanning electron microscopy cross-section of a device cured with the heat gun. (d) The *JV* parameter of the best carbon device with reverse scan PCE of 18.5% and a stabilised efficiency of 17.7%. The two red curves and the two black curves are the forward and reverse scans of a single device under AM1.5g illumination and dark conditions, respectively. (e) Schematics of the hot plate curing and the scanning electron microscopy cross-section of a device resulting from such a curing with a large void about 300 nm high and 5,000 nm wide between the carbon and the rest of the device.

Further, I implemented their heat gun curing process as displayed in Figure 4.6b in our lab. I completed optimising this process on my devices regarding performance and stability at the beginning of my PhD. With the setup I used, I needed much milder curing compared to the one used by Babu et al.[158] including a more than four times bigger distance of 22 cm, instead of 5 cm, between the heat gun and the substrate. The heat gun curing resulted in better-performing devices and a better-attached carbon electrode. This was evident in a better mechanical adhesion observed while preparing devices and in the absence of microcavities in devices prepared by heat gun curing (see Figure 4.6c versus f). Besides the distance, the curing time and temperature were important for device stability and performance. The results of one measurement of one of the curing time optimisation

experiments are shown in Figure 4.6a. This optimisation resulted in devices with stabilised efficiencies of up to 17.7%. The long-term stability of these devices was, however, lower than the stability of my devices with a metal electrode (Figure 4.7).

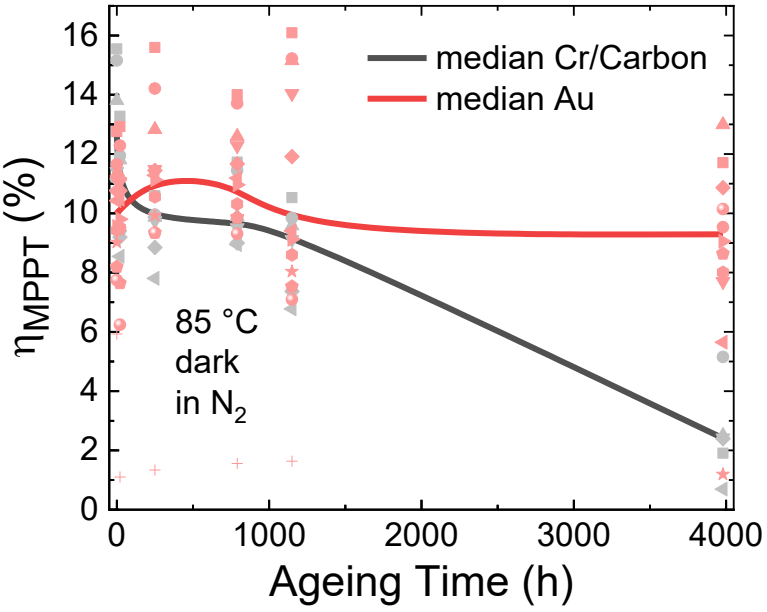



**Figure 4.7 Buffer Layers for Carbon Perovskite Solar Cells**

Stability comparison between Cr/Carbon and metal electrodes. Devices with the two electrode materials were aged in an $N_2$ environment and at 85°C.

Building on results reported by Babu et al.[158] we used a 5 nm layer of evaporated Cr between the PCBM and the carbon electrode. As shown in Figure 4.2b, devices with such a Cr buffer layer showed high steady-state efficiencies of up to 16.2%. Once again, inspecting cross-sectional SEM images for the devices with the Cr buffer layer shows a visible ETL layer running between the perovskite and the Cr/Carbon layers (Figure 4.2d and Figure 4.5a).

To further investigate the charge selectivity of the perovskite/PCBM/carbon layers, I produced transport layer-free stacks on ITO substrates. ITO/perovskite/Carbon stacks without any transport layer showed identical *JV* behaviour to ITO/perovskite/PCBM/Carbon stacks (Figure 4.8a). The reverse scan runs through the second quadrant indicating a hole instead of electron selectivity. For devices with a Cr interlayer between the PCBM and carbon, the scans run through the fourth quadrant showing the intended electron selectivity of the contact. The sign change in steady-state $V_{OC}$ measurements in Figure 4.8b confirms that trend with ITO/perovskite/Carbon stacks generating n-i-p steady-state open circuit voltages of >0.5 V under illumination and ITO/perovskite/PCBM/Cr/Carbon of around -0.25 V (Figure 4.8b).

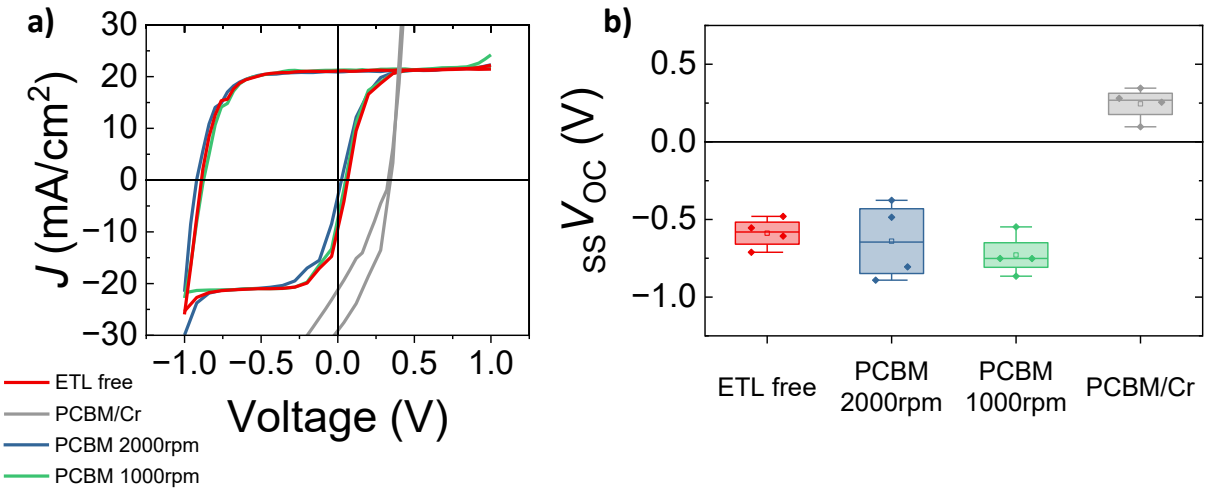



**Figure 4.8 Half-Stack polarity of PCBM/Carbon Devices**

JV characteristics in (a) and steady-state open circuit voltage reached after 60 s ($_{SS}V_{OC}$) in (b) of i-n half-stacks. The two curves of the same colour in (a) represent the forward and reverse scans of a sample. All half-stacks were fabricated with perovskite on ITO, then either directly followed by carbon depicted in red and called ETL-free, ITO/perovskite/PCBM with two different spin speeds followed by carbon shown in blue and green and ITO/perovskite/Cr/Carbon displayed in grey. The ITO/perovskite/Carbon stack without any transport layer behaved very similarly in *JV* and $_{SS}V_{OC}$ to the half-stacks where PCBM was deposited between perovskite and carbon. The *JV* curves in reverse scans run through the second quadrant, showing n-i-p device behaviour with over 12% PCE. The forward scan runs close to the origin showing minimal p-i-n behaviour. Both scans of the devices with evaporated Cr between PCBM and carbon go through the fourth quadrant, showing far less hysteresis and p-i-n-like behaviour. The steady-state open circuit voltage of ETL-free and PCBM without Cr devices has a negative sign indicating n-i-p device behaviour whereas the ones with Cr buffer have a positive sign showing p-i-n-like behaviour.

### 4.3.2 Solution-Processed Buffer Layers

Since the chromium buffer layer is processed via thermal evaporation at a high vacuum ($< 3.0 \cdot 10^{-6}$ torr) it gives away the advantage of the carbon electrode being processed at ambient conditions. I was, therefore, striving to substitute the chromium nano-layer with a layer processed at ambient pressure ideally via a simple solution process.

To achieve a working buffer layer, I tried materials with the following properties:

1. Good charge selectivity and extraction properties of electrons in PSC
2. Suitable energy level to be combined with carbon and PCBM
3. Processable out of alcohols (orthogonal solvent system to carbon paste and PCBM)
4. High conductivity
5. High heat and mechanical stability

To obtain a full solution-processed PSC, we investigated a selection of solution-processed layers that are typically used in p-i-n devices, to see if any of them can be a substitute for evaporated Cr. Based on the existing literature we explored materials that have been shown to work well in stable inverted solar cells between a fullerene-based layer and a metal electrode. First, the metal oxide nanoparticles, tin oxide[220-224] and aluminium zinc oxide (AZO),[95,184] secondly the polymer polyethylenimine (PEI),[185,186] and last the large molecules zirconium acetylacetonate (ZrAcac),[187,188] and Bathocuproine (BCP),[189] and a cross-linkable fullerene derivative[190,191] called PCBCB provided by a collaborator. The layers were prepared as stated in Methods Interlayers.

None of these materials led to working devices in combination with a blade-coated carbon electrode. The results of the former three are visible in Figure 4.9. The contact between carbon and Bathocuproine (BCP) showed highly resistive and ohmic behaviour. It did not result in any rectification but in straight *JV* lines under light and dark with geometric fill factors of ~0.25 (Figure 4.9c). The used tin oxide was prepared with $SnO_2$ nanoparticles as in Lemercier et al.[183] This resulted in devices with very low current and performance, as displayed in Figure 4.9. Several thickness optimisation experiments were run on the material, all with similar results. PEI behaved similarly to the $SnO_2$ nanoparticles with very low current densities and performance. Inspection with top-light optical microscopy confirmed that both layers were still present on the device stack after the carbon paste was applied. A continuity of layers of $SnO_2$ nanoparticles has been confirmed in SEM cross-sections like the one in Figure 4.10. This, and the *JV* behaviour, present a different outcome from the case of carbon blade-coating directly onto the PCBM in the section above.

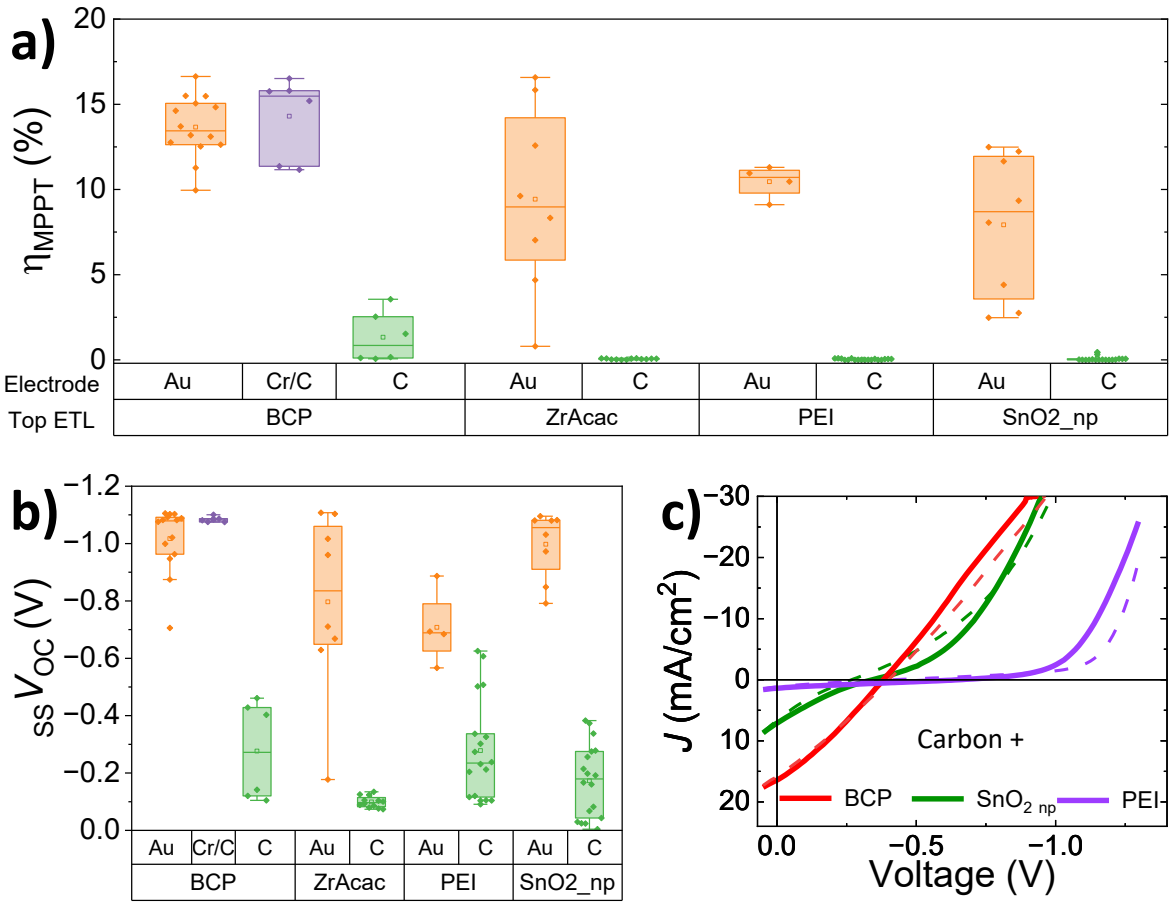



**Figure 4.9 Alternative Solution-Processed Buffer Layers**

(a) and (b) show the MPPT performance and open circuit voltage of devices containing different layers between the PCBM ETL and the gold or carbon electrode. Gold device data is plotted in orange and carbon device data in green. For BCP there are also devices with 5 nm evaporated Cr under the carbon electrode. (c) The current density-voltage (JV) behaviour of the best device of each transport layer class with carbon electrode. The dashed and solid lines represent the forward and reverse scans of a single device, respectively.

The measured work function of carbon (Figure 4.13) electrodes used are close to the reported work functions of metal electrodes. Since metal electrodes work well with the same materials I expected these commonly used layers to work with the carbon electrode as well. However, replacing the evaporated Cr layers with these standard solution-processed ETLs does not result in the desired contact with the carbon electrode. Directly replacing metal electrodes with blade-coated carbon does not yield high-performing devices for any of the mentioned solution-processed layers. Although all these materials form good contact with metal (Figure 4.9), none demonstrate effective contact formation with the carbon electrodes.

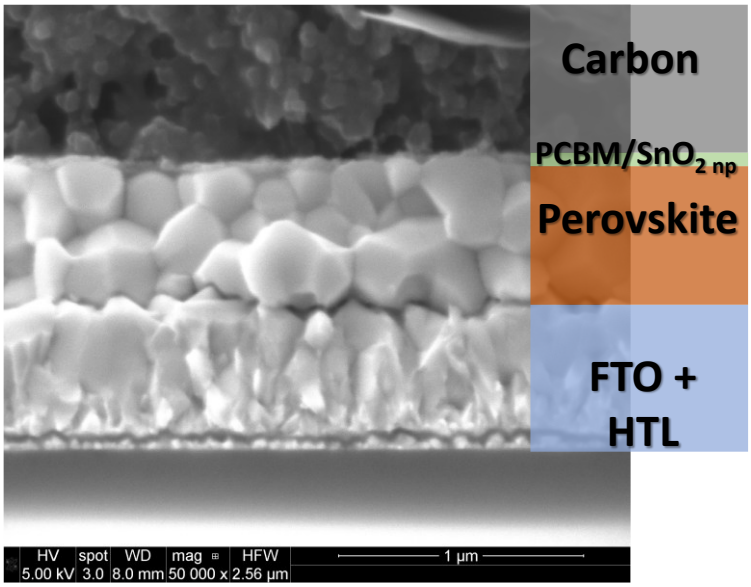



**Figure 4.10 $SnO_2$ Nanoparticle Carbon Device Scanning Electron Microscope Cross-Section**

A scanning electron microscope cross-section of a device with an electron transport layer (ETL) compromising spin-coated layers of PCBM and tin oxide nano particles ($SnO_2$ np). The location of this ETL within the device stack is indicated by a green bar.

While buffer layers lead to high maximum power point tracked performance when used with metal electrodes they cause poor rectification in the dark and poor MPPT performance in devices with carbon electrodes (Figure 4.9a and b). *JV* curves for carbon devices with some of the materials are shown in Figure 4.9c. The *JV* characteristics with carbon devices show high series resistance and interface contact issues for all the materials. A 5 nm thick layer of evaporated Cr alleviates these contact issues completely for BCP (Figure 4.9a and b). Devices with the Cr nano-layer under a bulk carbon electrode performed similarly to gold devices. SEM cross-sections of devices with a layer of $SnO_2$ nanoparticle between the PCBM and blade-coated carbon showed a continuous ETL without signs of solvent damage (Figure 4.10).

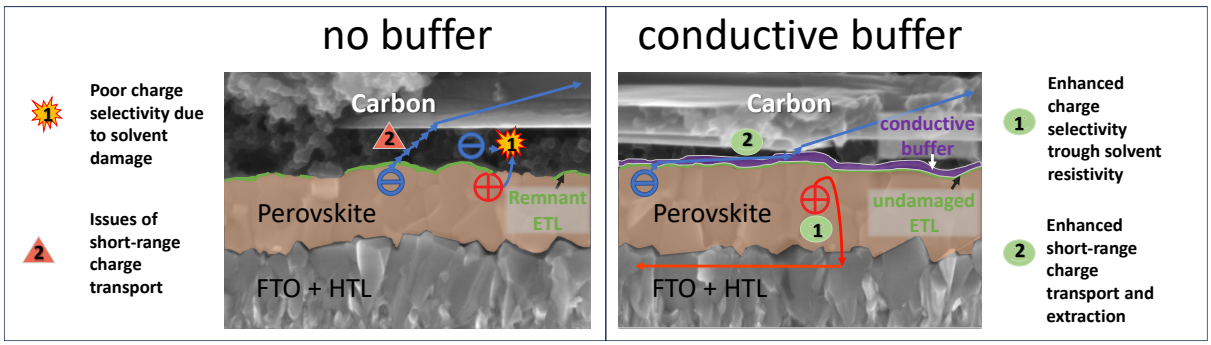



**Figure 4.11 Carbon Devices with and without a Buffer Layer**

The coloured SEM cross-sections above show on the left-hand side how a device without a buffer layer loses performance due to solvent damage to the ETL and hindered charge transfer to graphite flakes. The right-hand

side exemplifies how a device with a buffer layer can perform due to good charge selectivity and extraction.

### 4.3.3 Atomic Layer Deposited Tin Oxide ($SnO_2$) as a Buffer Layer

Because these solution-processed materials appear to be unsuitable to be used with carbon pastes, we present an alternative using a layer of $SnO_2$ grown by atomic layer deposition (ALD). While not a solution process, ALD is a promising high throughput deposition technique of aluminium oxide, for example in silicon solar technology,[192] and can be adapted to ambient pressure[193] and roll-to-roll processes. Atmospheric pressure ALD and pulsed chemical vapour deposition (CVD) have been used successfully in perovskite solar cells.[194,195] Blade-coated carbon electrodes are scalable and roll-to-roll compatible as shown by Beynon et al.[154] Our resulting devices, which employ an ALD deposited $SnO_2$ interlayer between the PCBM and the carbon paste, are to the best of our knowledge, the first p-i-n perovskite solar cells without any layer deposited in an evaporation process. The $SnO_2$/C devices were more stable than Cr/C devices when aged under 0.76 sun illumination at 65 °C (Figure 4.12). The higher retained MPPT efficiencies for $SnO_2$/C devices were mainly due to a higher retention of $V_{OC}$. However, our devices exhibit a relatively low fill factor and deliver efficiencies of around 12% (Figure 4.13a).

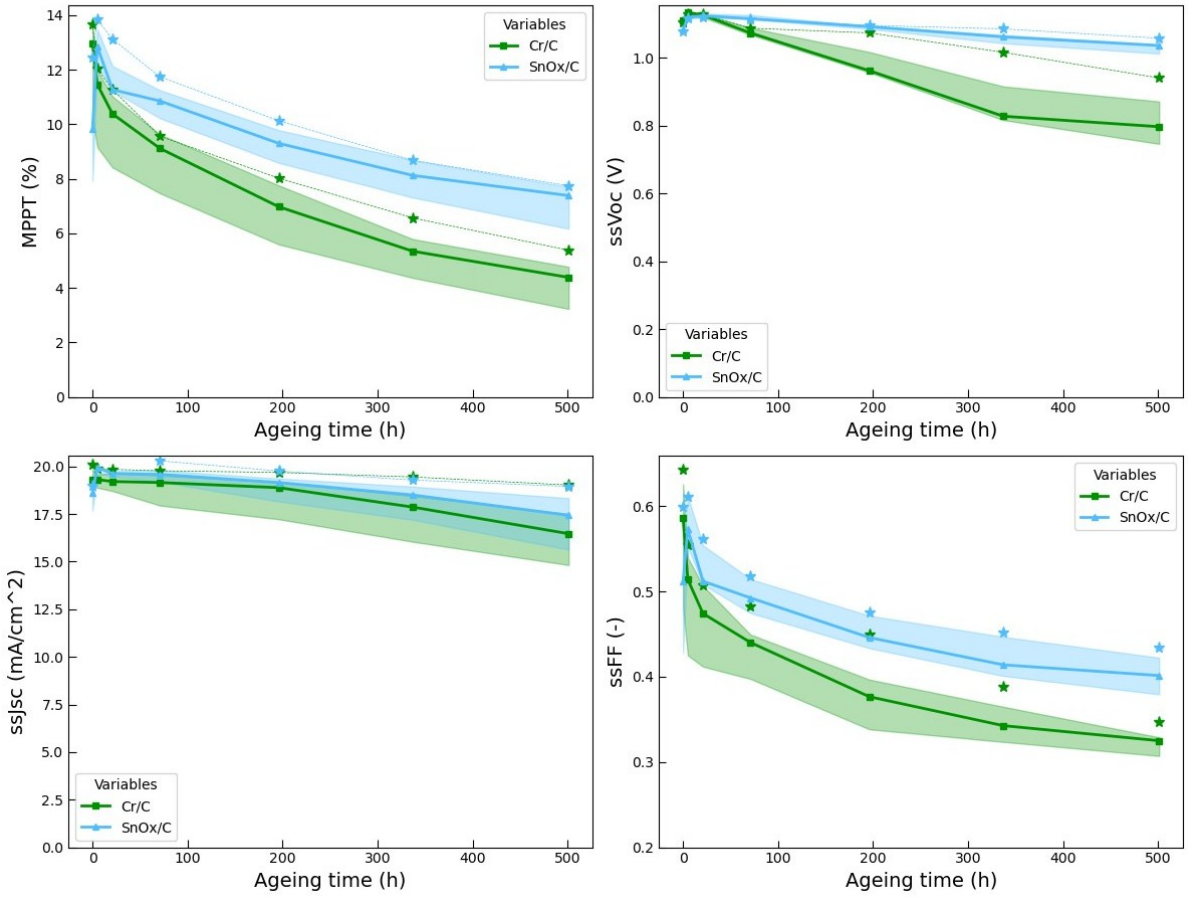



**Figure 4.12 Stability of $SnO_2$ Buffer Compared with Cr**

The graph displays the ageing behaviour of PSC using two different electrode configurations, Cr/Carbon and $SnO_2$/C. Maximum power tracking (MPPT) was utilised to obtain the performance values. The median performance of six 0.25 $cm^2$ and two 1.00 $cm^2$ Cr/Carbon devices is depicted by green squares, and a solid green line is used to represent the median values. Similarly, the median performance of nine 0.25 $cm^2$ and one 1.00 $cm^2$ $SnO_2$/Carbon devices of the same active area is represented by blue triangles, with a solid blue line fitted to these values. Four $SnO_2$/Carbon devices were excluded from the statistic because of the performance below 5% before starting or ageing. Shaded areas of the same colours are plotted above and around the solid median lines, representing the extent of the first and third quartiles, respectively. Notably, the Cr/Carbon devices exhibit significant initial degradation due to loss of fill factor and development of s-kinks. The $SnO_2$/Carbon cells demonstrate an improvement during the first five hours of ageing due to improved fill factor and current density. Over the course of 500 h, the Cr/Carbon showed faster degradation compared to the $SnO_2$/Carbon devices mainly due to a strong loss in open circuit voltage. All devices were glass-glass encapsulated with UV-cured glue. Ageing was performed under 0.76 sun equivalent illumination by a pulsed halogen light bulb at 65 °C in ambient air.

### 4.3.4 A PH1000 Interface Layer

Since $SnO_2$ is frequently and successfully used in contact with fullerene ETLs, we assume that the electrically deficient interface is the $SnO_2$/Carbon interface. To further improve the electric contact

between the $SnO_2$ and the carbon, we assessed different conductive materials as thin interlayers, including evaporated silver and chromium and solution-processed PEDOT:PSS type PH1000, and show the resulting device efficiencies in Figure 4.13b. The metals were evaporated with 3 nm thickness and PEDOT:PSS was spin-coated with a 1:10 dilution in methanol at high spin speeds to achieve a few nanometre thick layer. Devices with the PH1000 as an interface modifier showed the highest performance and best reproducibility (Figure 4.13b) and the highest fill factor (Figure 4.13a).

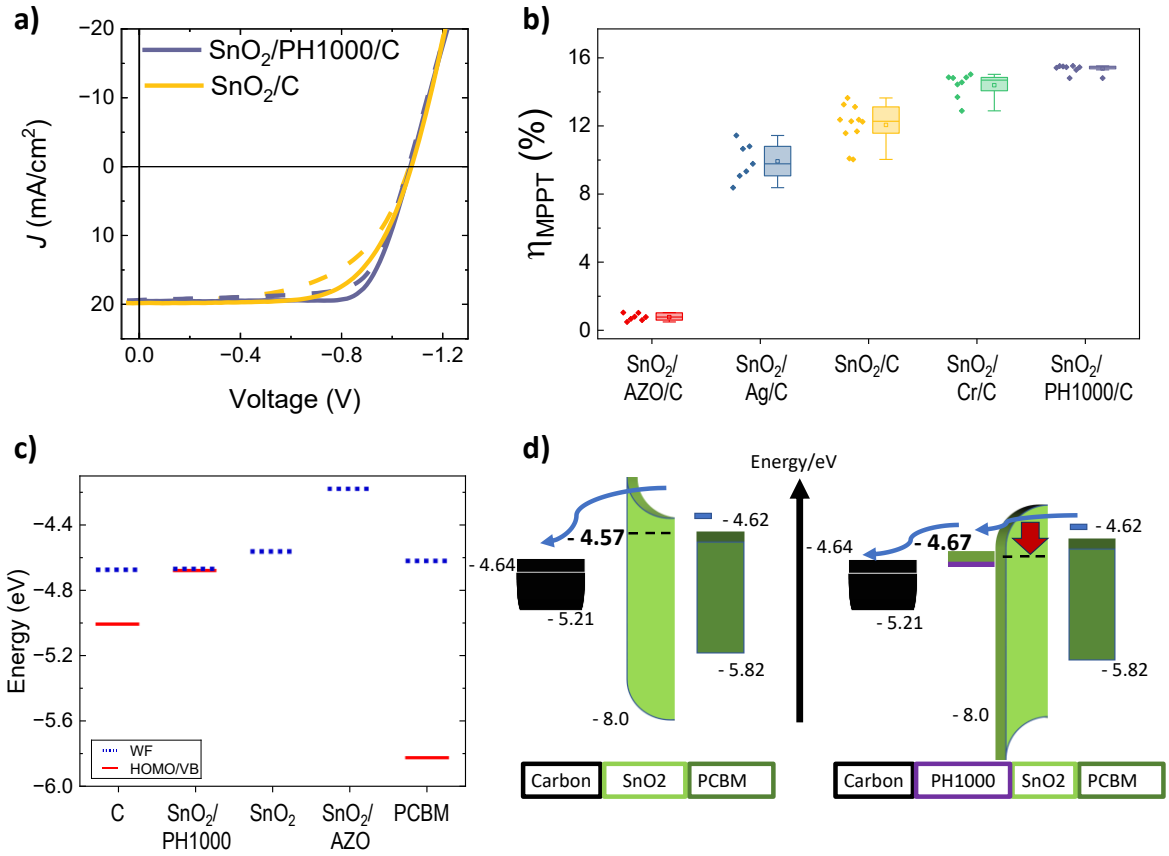



**Figure 4.13 ALD $SnO_2$/Carbon**

(a) th JV scans of champion p-i-n carbon devices with and without PH1000 between the $SnO_2$ layer and the carbon. The dashed and solid lines represent the forward and reverse scans of a single device, respectively. (b) The maximum power point tracked performances of devices with different surface modifiers between $SnO_2$ and carbon are. (c) The position of the work function (WF, blue dotted line) and the valence band maximum or highest occupied molecular orbital (VBM or HOMO, red solid line) are compared for different materials in the electron collection layer stack. Each symbol represents a set of Kelvin Probe and Ambient-pressure Photoelectron Spectroscopy measurements on the given material by Dr Katherine Stewart and Charlie Henderson. For multiple measurements, the average values were taken. The sketch in (d) shows the expected effect of the PH1000 modification in charge extraction and band alignment. All values in the sketch are from our measurement results shown in (c).

Because PEDOT:PSS layers are known to be conformal and dense[196] we investigated the possible closure of pinholes in the $SnO_2$ layer with atomic force microscopy (AFM) measurements, Figure 4.14. Dr Katherine Stewart and Charlie Henderson performed all AFM measurements. A negligible reduction in the surface roughness from 5.8 to 5.5 nm of the $SnO_2$ on perovskite was observed following the application of the PH1000. However, there were no major differences in the surface morphology of device stacks with and without PH1000 on top of the $SnO_2$ ETL and no pinholes were found in the $SnO_2$ without the PH1000, suggesting interface morphology is not the main mechanism of the PH1000 device performance enhancement. (Figure 4.14).

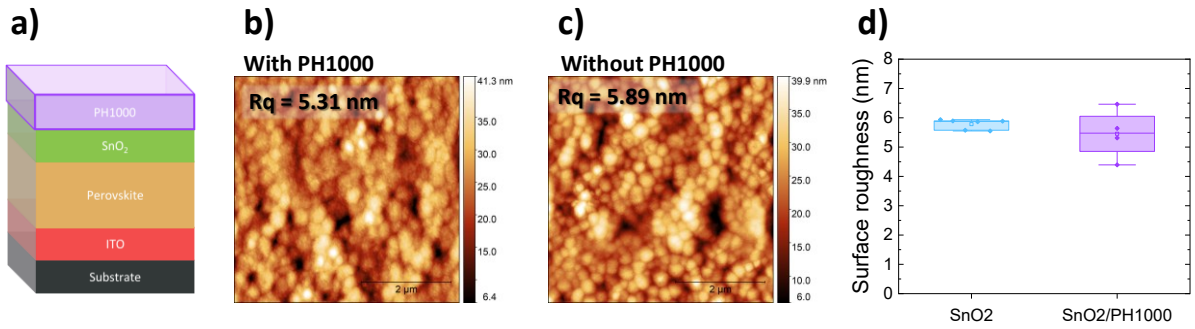



**Figure 4.14 Atomic Force Microscopy Results**

(a) The schematic of prepared samples with PH1000 on top of ITO/perovskite/$SnO_2$ samples. (b) A representative Atomic Force Microscopy (AFM) scan for such a sample. (c) A sample of the same kind of sample without the PH1000. (c) A comparison of surface roughness values for both examples is shown in (d). All AFM measurements were conducted by Dr Katherine Stewart and Charlie Henderson.

Since PH1000 is known to be conductive and its work function is similar to that of graphite,[197] we tested whether the few nanometre thick spin-coated layer can significantly alter the surface work function (WF) and electric behaviour compared to untreated $SnO_2$. With Kelvin Probe (KP) measurements, we were able to detect a slight change in WF of the $SnO_2$ top surface from approximately -4.57 down to -4.67 eV for $SnO_2$/PH1000 as shown in Figure 4.13c and sketched in Figure 4.13d. This way the WF of the ETL at the top surface is at a very similar energy level as at the average measured work function of the carbon electrode (4.67 and 4.64 eV respectively), indicating perfect energy alignment between the two layers.

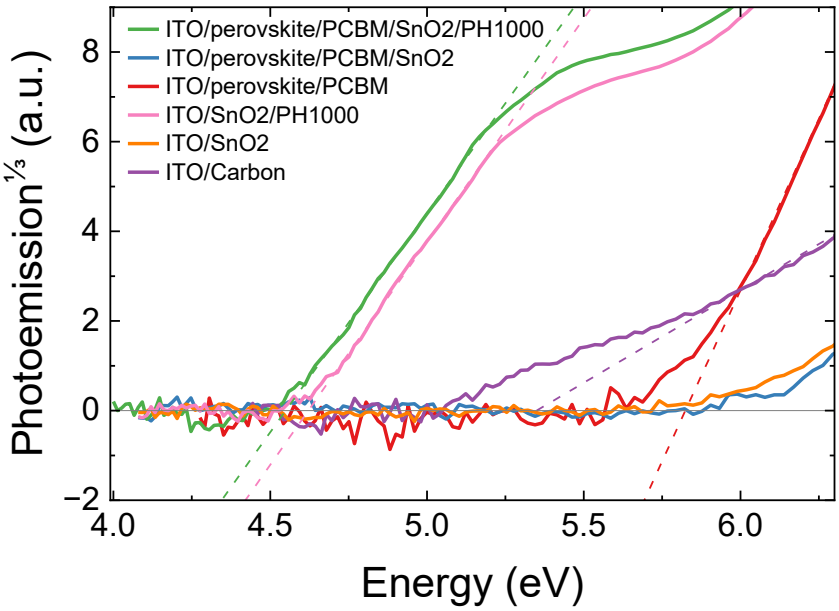



**Figure 4.15 Ambient-Pressure Photoemission Spectroscopy Results**

The Ambient-Pressure Photoemission Spectroscopy measurements for the results in Figure 4.13. Solid lines represented the measured photoemission and dashed lines the fit to the data. The measurements were performed by Dr Katherine Stewart and Charlie Henderson.

To investigate the interface energetics, I prepared samples of all the different layers involved in the electron extraction in all tested device configurations. Samples were prepared in the form of half-stacks (unfinished devices up until the layer of interest), with some additionally prepared directly on ITO substrates. All samples were then examined by Dr Katherine Stewart and Charlie Henderson at Imperial College London. Ambient-pressure Photoemission Spectroscopy (APS) measurements showed a valence band maximum (VBM) shift from below the detection limit for pristine $SnO_2$ up to 4.68 eV when the PH1000 treatment was used (Figure 4.13c and d). The VBM of the modified ETL is therefore at the same level as its WF, indicating a metallic-like behaviour of this interface. Between the carbon work function and its APS-measured HOMO on the other hand, there is a surprising difference of about 0.3 eV indicating a semiconducting behaviour of this surface. All measurement data leading to the data plotted in Figure 4.13c are shown in Figure 4.15. Our measurements show that the PH1000-treated $SnO_2$ achieves energy alignment with the carbon electrode at the interface, with both layers displaying work functions of around -4.7 eV. However, the metallic behaviour of the $SnO_2$/PH1000 layer and the semiconducting nature of the carbon surface point to an intricate interaction, which we will discuss later on.

To test the general validity of the findings, I tested the procedure in different labs, with another carbon paste, and different perovskites. I found that treating the $SnO_2$/Carbon interface with PH1000 worked even better when used in a different lab, with a different ALD system, on a CsMAFA triple cation perovskite and with a different carbon paste. As shown in Figure 4.16, the difference between treated and untreated $SnO_2$ was even larger compared to the previously presented results, when a GEMStar ALD system and slightly lower process temperatures (80 instead of 100 °C) were used. Untreated devices reached a maximum PCE of 3.3%, and devices with the PH1000 interlayer reached up to 15.2%. This finding is a possible explanation for previous reports of a bad interface between ALD $SnO_2$ and carbon by Babu et al.[158]

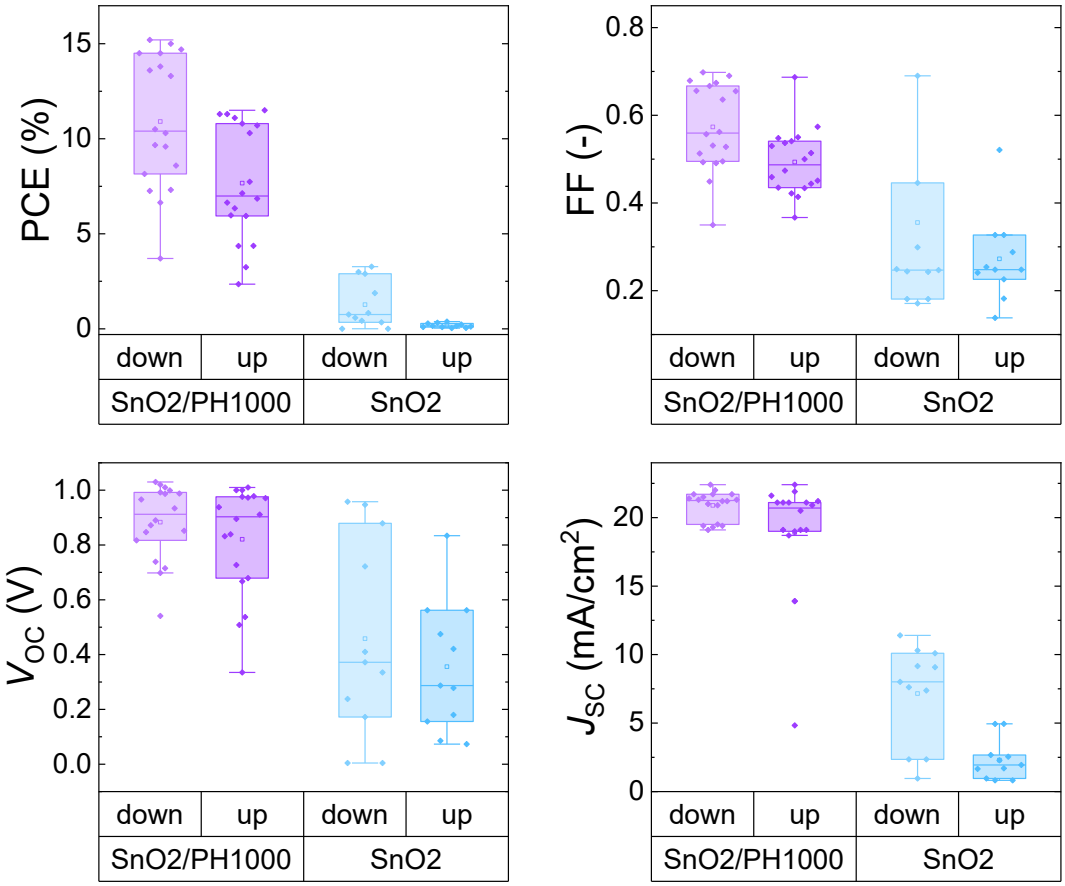



**Figure 4.16 Transferability of PH1000 Treatment of $SnO_2$**

Device parameters for blade-printed carbon devices with an $SnO_2$ ALD layer with and without PH1000 are shown. The shown parameters are retrieved from current voltage scans, devices have an active area of 0.0676 cm$^2$, and the used perovskite is a triple cation double halide. A GEMStar ALD system was used for the $SnO_2$ layer.

I found that the performance of devices with $SnO_2$/Carbon depends strongly on the ALD setup and parameters used. This could also explain why Babu et al.[158] report this material combination not to work. The use of the PH1000 layer increases the batch-to-batch as well as the lab-to-lab reproducibility. Note the larger number of devices without PH1000 performing between 0 and 2% as shown in Figure 4.17. None of the devices not containing the PH1000 performed between 16 and 18%.

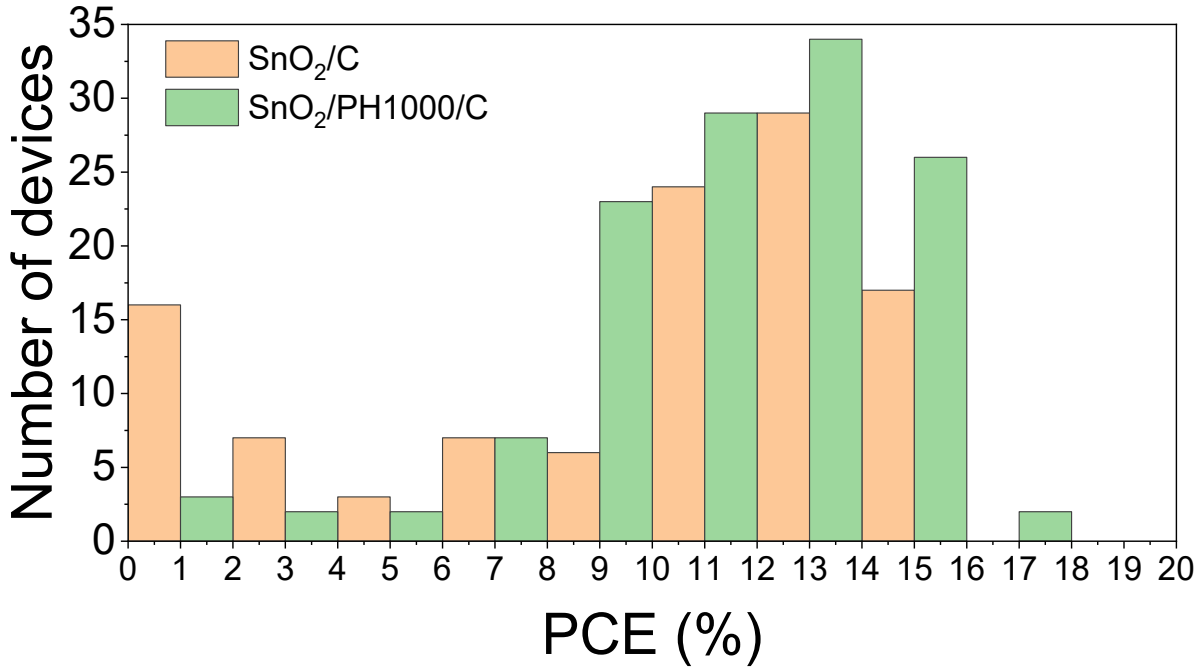



**Figure 4.17 Multiple Batch Statistics of $SnO_2$/Carbon with and without PH1000**

The number of p-i-n devices finished with $SnO_2$/Carbon and $SnO_2$/PH1000/Carbon performing in 2% performance pockets is shown. The devices were fabricated over one and a half years in two different laboratories.

## 4.4 Discussion

Carbon is more commonly employed as a hole-collection contact in perovskite solar cells and has been reported to exhibit hole selectivity when directly contacting the perovskite. [149,131,136,115] Despite this charge-selectivity being important for device performance, it has not been thoroughly investigated. We found that the surface of the processed carbon films may be semiconducting, rather than conducting,, as previously assumed. Our KP and APS measurements show that the surface of carbon electrodes had an energy difference between its WF and the HOMO onset of about 0.3 eV indicating that it is not behaving purely as a metallic material (Figure 4.13c). This might block

electrons from reaching the metallic bulk of the carbon electrode while facilitating the extraction of holes. The absence of voltage in MPPT efficiency for ETL-free devices suggests that pure carbon electrodes in direct contact with perovskite are selective to holes but do not facilitate electron extraction in planar HTL/perovskite/carbon stacks. This is consistent with the findings presented in Figure 4.8 showing that an ITO/perovskite/Carbon device displays n-i-p-like behaviour.

Our studies provide strong evidence that fullerene-based electron transport layers are partially removed when carbon paste is blade-coated on top. Similar current-voltage characteristics were observed in devices without an ETL and those with just a fullerene layer as ETL below the blade-coated carbon electrode (Figure 4.2 and Figure 4.8) suggesting low-charge carrier selectivity into the carbon electrode. This is further supported by the severe series resistance losses observed in gold-electrode samples with a thick C60 layer, while no such losses occurred in carbon-electrode samples. This indicates that the $C_{60}$ was at least partially removed (Figure 4.4). Besides these indirect electrical measurements, cross-sectional SEM images of devices with fullerene layers followed directly by blade-coated carbon in Figure 4.2d, indicate that the fullerene layer is removed during the blade-coating process. A solvent-resistant and highly conductive interlayer is needed between ETL and carbon electrodes to enable p-i-n devices to work with this electrode.

The fact that carbon pastes can damage charge selective layers has already been reported for hole transport layers in n-i-p devices.[131,198,199] Here, we present comprehensive evidence that this may be even more detrimental in p-i-n devices, which incorporate comparatively thin ETL in the range of 30 nm. We suggest that the damage may be caused by solvents in the carbon paste dissolving the fullerene layer.

The n-type interfacial layer BCP shows the desired energetic behaviour only when used in contact with metals.[200] With carbon electrodes, BCP and other similar layers produce poor contact and high electrical resistance (Figure 4.9). Layers of these materials, like the $SnO_2$ nanoparticles, are shown in the SEM cross-section in Figure 4.10, after blade-coating the carbon electrodes on top of them, suggesting that these materials remain intact after coating with carbon, but introduce severe resistive barriers.

Based on our experimental data, we propose that in devices with metal electrodes, it might be easier for charges to tunnel through the thin insulating interfacial material (like BCP) into the metal. In contact with carbon, electrons would need to tunnel through both the interfacial layer and the semiconducting top layer of the carbon-based material. This is consistent with previous reports suggesting that inter-band-gap states form in contact between metal and interfacial layers allowing the charge transfer[189,201] into metals but not carbon. It is important to note that, in contrast to evaporated metal electrodes, carbon electrodes display a much more heterogeneous interface, both in terms of morphology since they are made from particles ranging between tens of nm and tens of μm, as well as for composition, with carbon electrodes consisting of mixtures of carbon black, graphite particles and further additives (cf. SEM cross-sections in Figure 4.10 and Figure 4.5). If graphite flakes are not close enough to the electron transport layer, tunnelling from the ETL into the graphite might not be possible as sketched in Figure 4.11.

On the other hand, we found that materials that are highly conductive and less n-type such as chromium, silver, and the PH1000-coated $SnO_2$, form good electrical contact with graphite-based electrodes. $SnO_2$ provides only the solvent resistivity but not an optimal connection to the carbon electrode. Treating it with conductive PEDOT:PSS, PH1000, enhances the connection enabling electron injection from the ETL into the carbon. The two materials, $SnO_2$ and PEDOT:PSS in combination can substitute the chromium layer. The closer the work function of the conductive interlayer is to that of carbon, the better the fill factor and performance of the resulting devices. This trend places PH1000 above Cr, which we illustrate in Figure 4.13c.

## 4.5 Conclusion

In conclusion, the difference in the electronic contact behaviour of carbon and metal electrodes in p-i-n devices has long been overlooked and possibly impeded the field's progress in the direction of p-i-n devices with graphite-based electrode materials. Most common electron transport layers in p-i-n devices are either incompatible or severely damaged by the carbon blade-coating process. A dense $SnO_2$ layer in combination with a highly conductive interlayer enables an ohmic contact with a carbon electrode on a p-i-n stack. The $SnO_2$ layer prevents the removal of the underlying PCBM layer, whilst the conductive interlayer inhibits the formation of an energetic barrier and enables

improved charge extraction. Achieving this can pave the way to high-performing, low-cost, and high-throughput photovoltaics. It may also enable the use of carbon electrodes on all-perovskite tandem devices which are mostly realised in p-i-n architecture.

# 5 STABILITY ENHANCEMENTS THROUGH THE USE OF CARBON-BASED MATERIALS

This chapter explores the effect of different ways of laminating carbon-based materials with pressure (and heat) onto thin films and ways to exploit these techniques in PSC. Firstly, I examine the difference between laminating a dried carbon film as an electrode onto p-i-n devices compared to blade-coating a wet film and drying it on the device. Secondly, I investigate the use of continuous graphene mono-layers as diffusion barriers and inside-device encapsulation.

## 5.1 Carbon Film Lamination for Inverted Perovskite Solar Cells

In this chapter, I explore stability challenges with the p-i-n device architecture developed in Chapter 4. A significant motivation for investigating carbon electrodes in perovskite solar cells was the hypothesis that they can enable higher operational stability than cells using metallic electrodes that are not gold, which is prohibitively expensive and unsuitable for TW-scale PV deployment.[172] A trade-off between the curing of the carbon paste wet film and damaging the device stack and achieving a completely dried film is presented as the probable underlying issue. To address this stability challenge, an alternative carbon deposition technique is explored. Building on the results, I aimed to develop a p-i-n C-PSC with a laminated (hot-pressed) carbon electrode (see 2.5.3 Carbon-Based Electrodes). A key motivation here is to improve the stability through the use of laminated carbon instead of a blade-coated carbon preparation. This hypothesis is based on a possible better solvent extraction. This method has not been reported for p-i-n cells so far. After presenting the stability issues, this chapter explores the feasibility of laminated carbon electrodes for p-i-n perovskite solar cells, focusing on adhesion properties, interfacial charge extraction, and device performance. By systematically investigating different ETL modifications and processing parameters, I aim to identify key factors influencing adhesion and charge extraction for laminated carbon. I show an improved adhesion can be achieved through modifications of the laminated carbon and by using the interfacial layers explored in Chapter 4. These insights contribute to the ongoing development of printable and scalable perovskite solar cells.

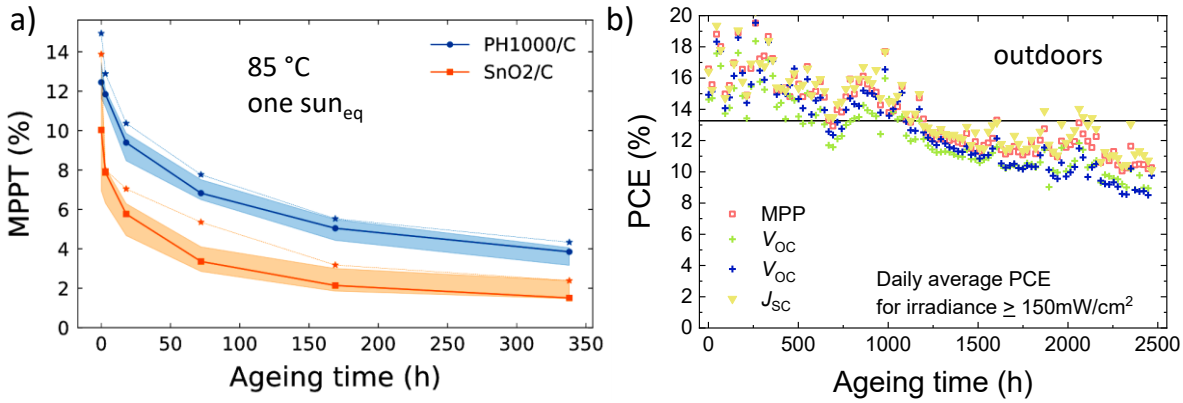



**Figure 5.1 $SnO_2$/PH1000/Carbon Stability**

(a) The statistical development of maximum power point tracked performance upon ageing under 0.76 sun equivalent illumination at 85 °C in ambient air is shown for $SnO_2$/PH1000/Carbon and $SnO_2$/Carbon. The continuous dark blue line with circles and the light orange line with squares show the median values for $SnO_2$/PH1000/Carbon and $SnO_2$/Carbon, respectively. The shaded area around this line indicates the spread from the first to the third quartile. The stars above each of the shaded areas represent the respective champion values. Details of the statistics are mentioned in Figure 5.7. Daily average PCE values for devices aged in an outdoor setup are visible in (b). Four $SnO_2$/PH1000/Carbon devices were kept at different bias conditions and periodically tested.

## 5.1.1 Results

### 5.1.1.1 Stability Challenges

I first investigated the stability of blade-coated devices with the architecture developed in Chapter 4. To investigate this hypothesis on our p-i-n carbon devices, we aged sealed cells under simulated sunlight at 85 °C and outdoors under real-world illumination. For the sealing, we employ a glass coverslip glued with a UV-curable epoxy resin. No edge sealant encapsulation nor desiccant was used. A photograph of the substrate as mounted on a roof is displayed in Figure 5.7b and further encapsulated devices are shown in Figure 5.2a. We note that this is not standard packaging for PV cells and modules for outdoor use, so our expectation was not to have extremely stable devices.

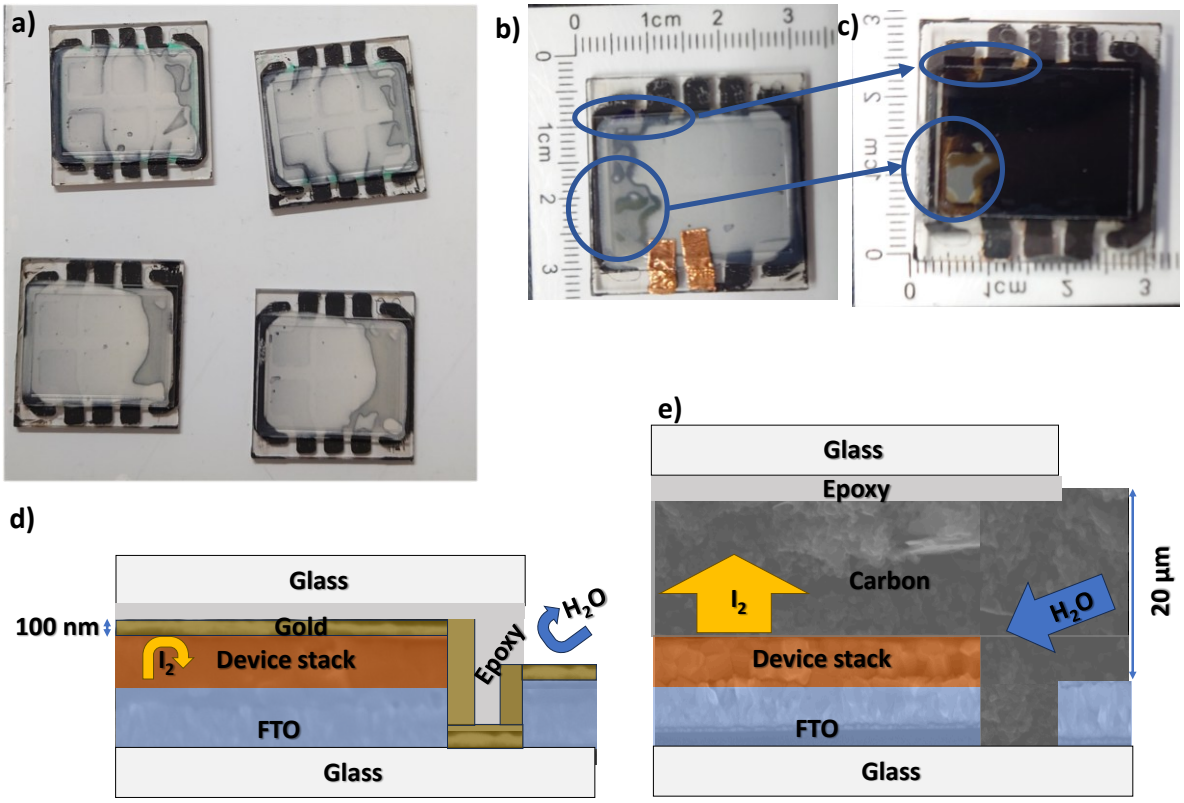



**Figure 5.2 Carbon Encapsulation**

Problems with encapsulating devices with a carbon back electrode are shown. Devices with epoxy on the back side are shown in (a). A close-up is displayed in (b). In (c), the same devices as in (b) have on the front side visible signs of degradation in the same areas where there is decorated epoxy on the backside. The anticipated schematics (not to scale) of an encapsulated device with a gold electrode are visible in (d). Problems with porous carbon electrodes when the same encapsulation is used are shown in (e).

Firstly, we show a comparison between the $SnO_2$/PH1000/Carbon architecture devices and $SnO_2$/Carbon cells without the PH1000 modification, aged at 85°C (Figure 5.1a and Figure 5.3). A considerable stability advantage was detected when the $SnO_2$ was treated with PH1000. Under this accelerated ageing condition, the $SnO_2$/Carbon champion device power conversion efficiency (PCE) fell rapidly in performance from 13.9% measured under continuous maximum power point tracking (MPPT) to 8.0% in only three hours of ageing. The degradation was mainly due to a rapid reduction in current density and fill factor (Figure 5.1a and Figure 5.3). The champion device with PH1000 reduced only from 14.9% to 12.9% MPPT at the same time. The $SnO_2$/PH1000/Carbon cells showed, after an initial burn-in, higher performance than the untreated counterpart. There was, however, also a reduction in fill factor for the PH1000-modified devices (Figure 5.7a and Figure 5.3).

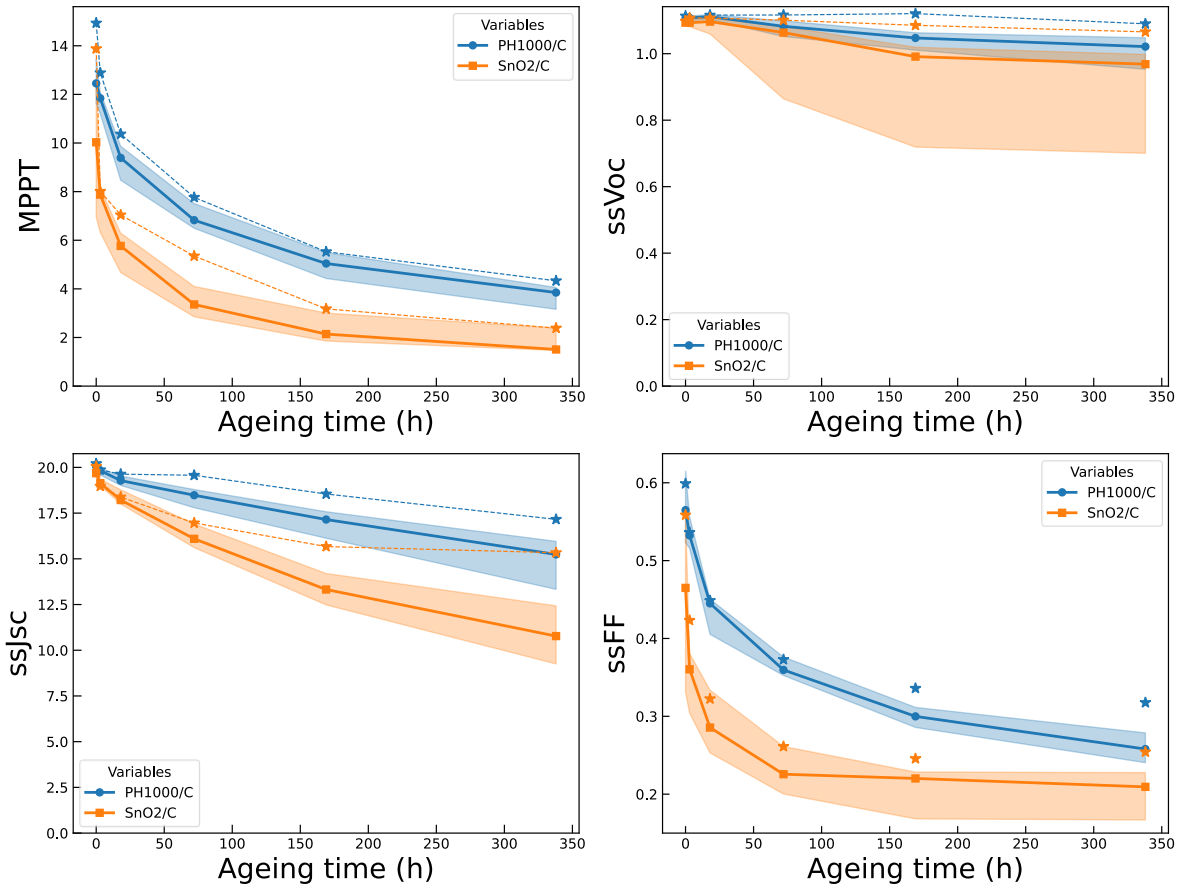



**Figure 5.3 Stability of $SnO_2$ compared with $SnO_2$/PH1000 Buffer**

The statistical development of maximum power point tracked performance parameters upon ageing under 0.76 sun equivalent illumination at 85 °C in ambient air is shown. The continuous blue line with circles and the orange line with squares show the median values for $SnO_2$/PH1000/Carbon and $SnO_2$/Carbon respectively. The shaded area around this line indicates the spread from the first to the third quartile. The stars above each of the shaded areas represent the respective champion values. For the $SnO_2$/Carbon 24 devices finished with these two layers were aged encapsulated. 11 devices of this category were excluded because of their initial performance before ageing being too low (< 5% MPPT). For the $SnO_2$/PH1000/Carbon 20 devices finished with these two layers were aged encapsulated. Four devices of this category were excluded because of their initial performance being too low (< 5% MPPT). All aged devices' active area is 0.25 $cm^2$.

This was due to the development of “s-kinks” in the current-voltage characteristics, as visible in Figure 5.7b and Figure 5.4c-e, indicating the emergence of an energetically unfavourable contact at least at one of the internal interfaces in the device. Carbon electrode devices with $SnO_2$ aged slower than metal-containing electrode configurations like Cr/Carbon and silver (see Figure 5.5 and Figure 4.12). Under 85 °C unencapsulated conditions, $SnO_2$/PH1000/Carbon was even more stable than gold electrodes (Figure 5.4). However, under 65 °C unencapsulated and 85 °C encapsulated gold electrodes were more stable than our carbon electrode as visible in Figure 5.4a and b.

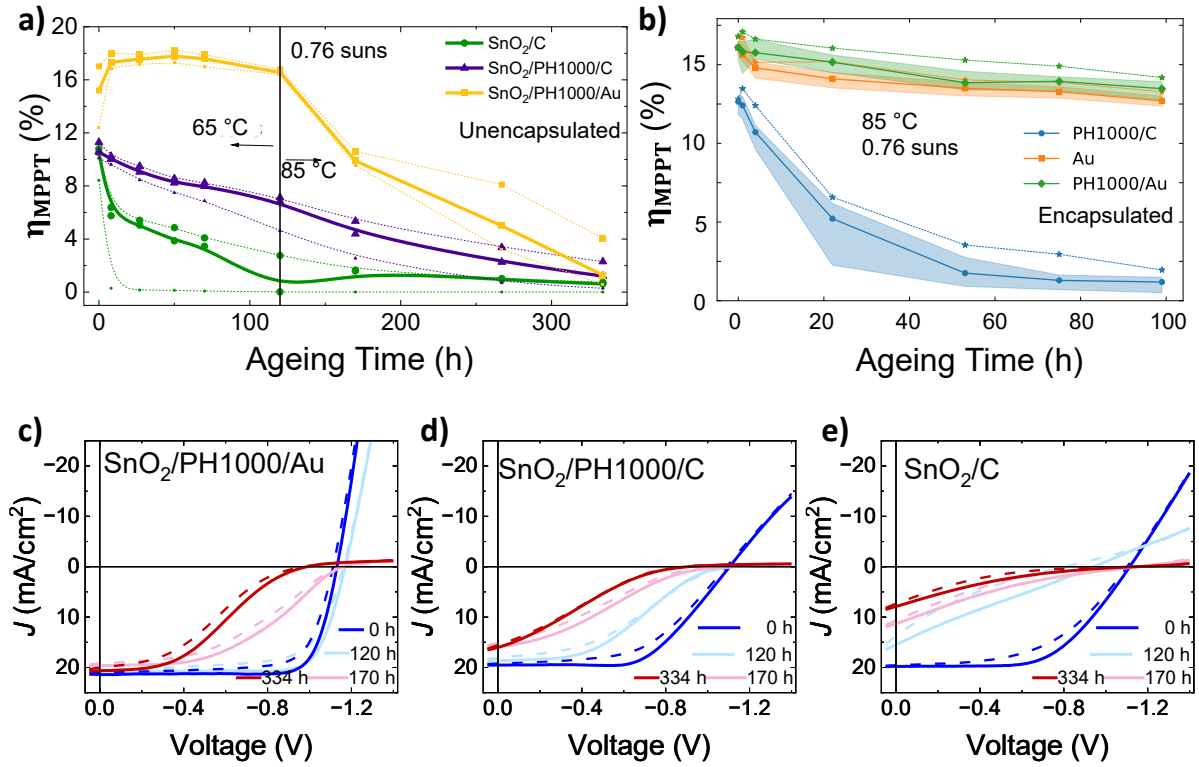



**Figure 5.4 Gold Carbon Ageing Comparison**

In (a), a comparison of the ageing behaviour of p-i-n perovskite solar cell devices finished with $SnO_2$/C, $SnO_2$/PH1000/C, and $SnO_2$/PH1000/Au is shown. They are represented by green circles, purple triangles, and yellow squares, respectively. The middle symbols connected by a solid line represent the median and the symbols above and below connected by dashed lines mark the first and third quartiles. Devices were aged unencapsulated in ambient air under 1 sun illumination. The temperature was kept for 120 h and 65 °C and then increased to 85 °C. The ageing behaviour of devices completed with $SnO_2$/Au, $SnO_2$/PH1000/Au, and $SnO_2$/PH1000/Carbon is displayed in (b). The medians for each parameter are shown in orange squares, green rhomboids, and blue circles, respectively. The shaded areas in the same colour around the median line show the extent from the first to the third quartile, and the star symbols above those shaded areas are the champion device performance. Current-voltage (JV) characteristics of the champion devices of the ageing study in (a) are shown in (c) - (e). Scans for the ageing times of 0 h, 120 h, 170 h, and 334 h are displayed from dark blue to dark red. The solid and dashed lines of the same colour represent forward and reverse scan of the respective devices.

Given the material properties of carbon, we would expect slower ageing compared to Au electrodes, as it has also been widely reported.[131,136,163] Surprisingly, at 65 °C, one sun, in ambient air, and unencapsulated we observe the opposite (Figure 5.4a). Gold is, however, too expensive for industrial applications and carbon electrodes still offer a stability advantage over other affordable electrode materials like silver (Figure 5.5). Further, with increasing the temperature from 65 °C to 85 °C under the same light ambient air ageing conditions, the gold electrodes pick up in ageing speed and show a similar but even quicker ageing path compared to carbon electrodes (Figure 5.4a, c-e). This stresses

the need to age at higher temperatures because of characteristic ageing behaviours of gold being reported to only show above 70 °C.[71]

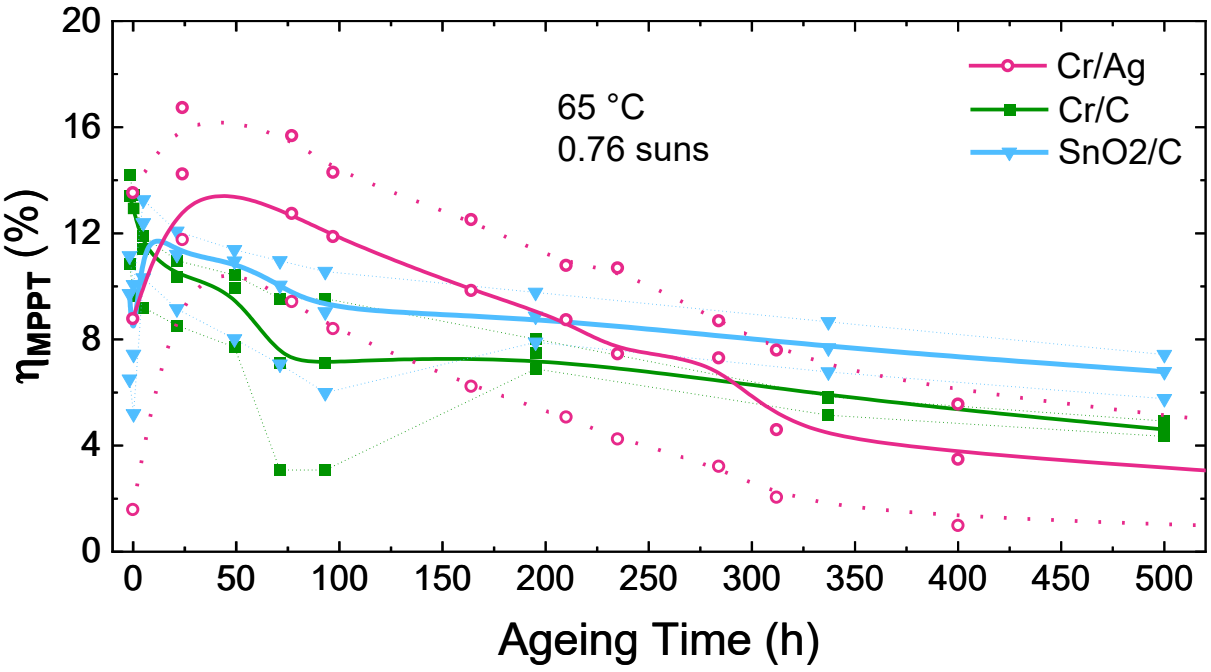



**Figure 5.5 Carbon versus Metal Stability**

The graph displays the ageing behaviour of PSC out of two ageing studies comparing three different electrode configurations, Cr/Ag, Cr/Carbon and $SnO_2$/C. Maximum power tracking (MPPT) was utilised to obtain the performance values. Green squares depict the median performance of six 0.25 $cm^2$ Cr/Carbon devices, and a solid green line represents a b-spline fitted to the median values. Similarly, the median performance of 12 $SnO_2$/Carbon devices of the same active area is represented by blue triangles, with a solid blue line fitted to these values. Pink circles represent the performance of 16 Cr/Ag devices. Dotted lines of the same colours and symbols are plotted above and below the solid lines, representing the first and third quartiles, respectively. Notably, the Cr/Carbon devices exhibit significant initial degradation, while the Cr/Ag and $SnO_2$/Carbon cells demonstrate an improvement during the first hours of ageing. The Cr/Ag devices show, after their initial increase, a quicker degradation than the carbon counterparts. All devices were aged under one sun equivalent illumination by a pulsed halogen light bulb at 65°C in ambient air.

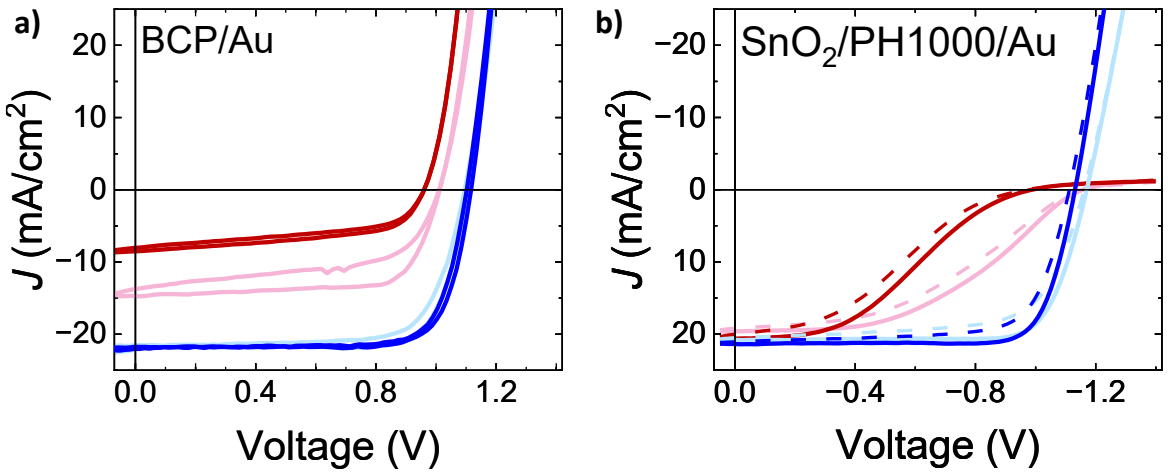



**Figure 5.6 BCP versus $SnO_2$/Au Ageing Behaviour**

The qualitative differences between *JV* curve development upon ageing are shown for polyTPD/$FA_{0.83}Cs_{0.17}PbI_{2.7}Br_{0.3}$/PCBM devices finished with BCP/Au in (a) and finished with $SnO_2$/PH1000/Au in (b). Devices were aged for different times under different but comparable conditions of one sun illumination in ambient air at elevated temperatures above 50 °C. BCP/Au devices age usually through a loss in current density while $SnO_2$ devices lose fill factor because of the development of "s-kinks". This generally holds for a wide range of light-temperature ageing conditions. The solid and dashed lines in (a) and (b) represent forward and reverse scan of the respective devices.

#### 5.1.1.1.1 Outdoor Stability

To investigate the ageing behaviour of carbon cells under real-world outdoor conditions, we mounted four solar cells with $SnO_2$/PH1000/Carbon electrodes in an MPPT system on a rooftop in Freiburg, Germany (longitude 48°). In Figure 5.1b we show the evolution of the daily average efficiencies of devices with this architecture kept at different bias conditions including short circuit, maximum power point and open circuit. All 4 devices tested were fabricated on the same glass substrate. The measured devices showed an initial PCE of between 14.6% and 16.6% at 931 W/m$^2$, which is well in line with its last measured performance under simulated sunlight. Surprisingly, the cells degraded at a similar rate, regardless of the electrical biasing conditions they were held at. The encapsulated devices maintained ~94% of their initial performance for about 500 h and 80% for about ~1200 h under real operation conditions (Figure 5.1b). Note that the device was exposed to ambient temperature cycles between -1 °C and 36 °C, with direct precipitation of up to 21 mm, as well as relative humidity between 40 and 80%. The irradiances reached values of up to over 1300 W/m$^2$ (Figure 5.7d).

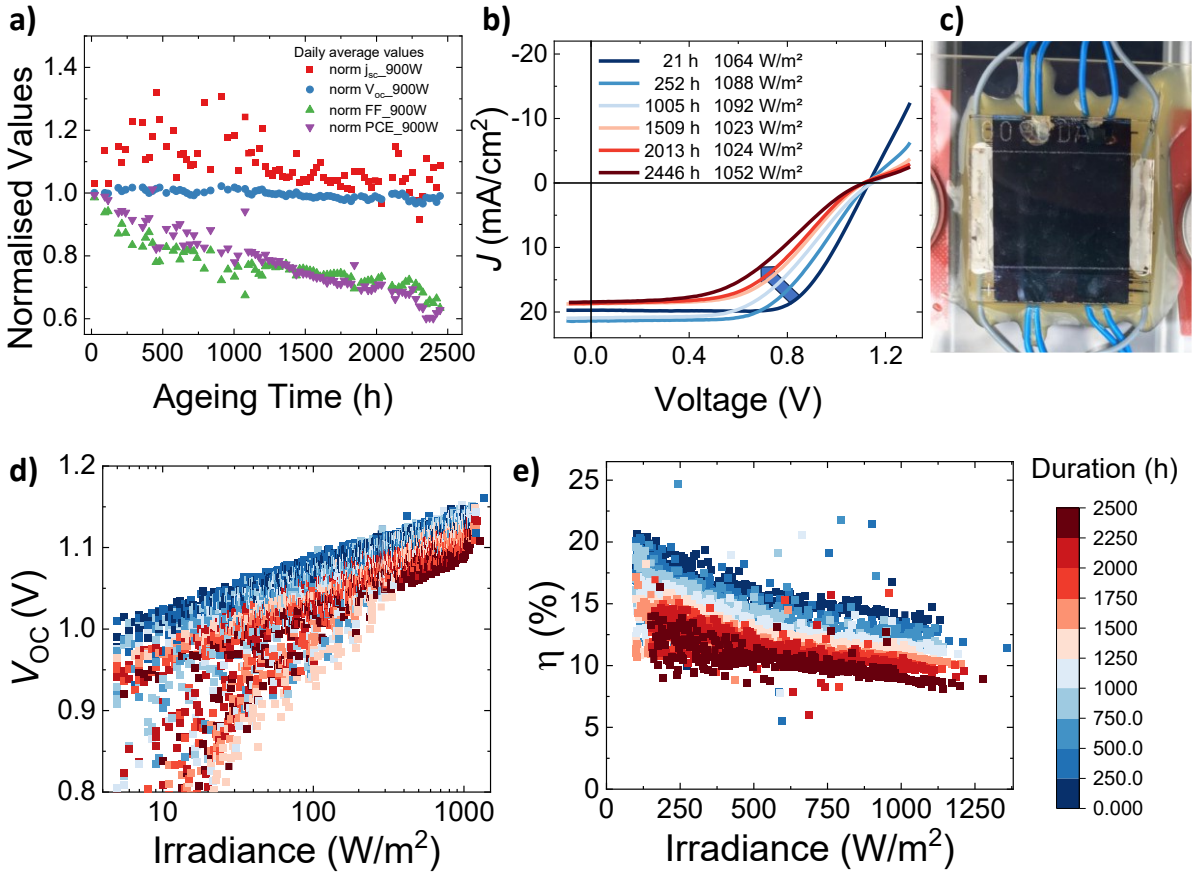



**Figure 5.7 $SnO_2$/Carbon Outdoor Stability**

(a) The relative development of performance parameters for devices aged outdoors. (b) The corresponding *JV* scans for different times of ageing. (c) A photo of the ageing device on the setup. The open circuit voltage values and efficiencies for different irradiance values and their change over ageing time are plotted in (d) and (e), respectively.

In Figure 5.7a the development of different performance parameters for a $SnO_2$/PH1000/Carbon device aged in an outdoor setup is shown. The $J_{SC}$ values in red fluctuated throughout the measurement considerably due to different irradiances between the days but did not degrade significantly over time. The $V_{OC}$ stayed stable in this ageing study while the FF decreased rapidly, causing the overall performance to drop. A photo of the device on and measurement rack after 500 h of ageing is displayed in (b). The legend of the colourmap of (c) and (d) goes from dark blue for pristine devices to dark red for devices aged 2500 h. As visible in (c) there is a large spread in $V_{OC}$ for the low irradiance for aged devices. Performance measurements below 150 W/m$^2$ were judged as unreliable and were not included in the efficiency statistics. Note the small decrease in $V_{OC}$ over the ageing time of only about 50mV at higher irradiances. Graph (d) shows that the efficiency of the devices is on average higher at lower irradiances.

5.1.1.1.2 Trapped Solvents

The higher stability of the stack with Au electrodes (Figure 5.4) shows that at least some device instability is directly or indirectly caused by the carbon electrode. I investigated solvents trapped in the carbon electrode as a possible reason for the instability of my C-PSC. For a preliminary screening on the influence of the carbon curing time, devices produced with the carbon paste bought from Dyenamo SA (see Carbon Blade-Coating). Devices were cured with a heat gun as shown in Figure 4.6b. The heat gun curing was performed for different lengths between 3 and 19 minutes. The performance of devices with these different curing times right after fabrication is shown with blue rhomboids in Figure 5.8. There was no observable trend in MPPT performance between devices produced with different curing times. Besides one device with four min curing time, all devices performed similarly. The best devices for all of the curing times performed around 16% MPPT efficiency.

To investigate the influence of this annealing procedure on the device stability all devices were aged unencapsulated under 0.76 suns, at 65 °C, and in ambient air for 190 h. The MPPT efficiencies of the same devices after the ageing procedure are shown with red circles in Figure 5.8. All three devices with four minutes showed zero performance after the ageing. One of the three devices, however, performed already at 0% before the ageing. Besides the four minute devices, all devices with annealing times between 3 and 8.5 minutes showed MPPT efficiencies between 5.2 and 14.8% after ageing. Devices with between 10 and 15 minutes of annealing performed between 1.9 and 12.8%. The devices with the longest annealing times of 17 and 19 minutes all performed around 1% MPPT after the 190 h ageing.

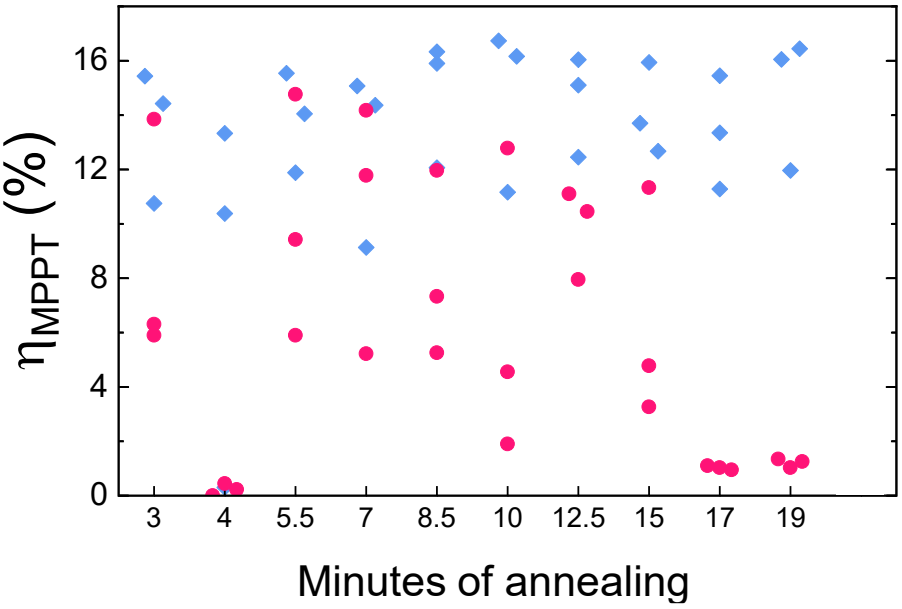



**Figure 5.8 Influence of Heat Gun Annealing Times on Stability**

Carbon perovskite solar cells were fabricated with different heat gun annealing times. Three devices per annealing time were manufactured. The Maximum Power Point Tracked (MPPT) efficiencies of those devices right after production are shown in blue rhomboids. All devices were then aged for 190 h unencapsulated under 0.76 suns, at 65 °C, and in ambient air. The MPPT efficiencies after this ageing step are shown with red circles.

Because of the unsatisfying stability of the heat gun-cured devices presented above, I investigated the stability of devices fabricated with a low-temperature curing paste provided by David Beynon from SPECIFIC, College of Engineering, Swansea University, Skewen, UK. Two pastes, “ink A” and “ink B” were tested. This paste can be cured at low temperatures of 80 °C for 5 min on a hot plate. Devices with this paste were tested in direct comparison to the heat gun-cured commercial paste by Dyenamo. The MPPT efficiencies of all produced devices (22 ink B, 30 ink A, and 28 “Dyenamo” devices) are shown in Figure 5.9. Using ink B did not lead to working devices in this stack. The best-performing device with 16.6% was fabricated using the “Dyenamo” paste. The median performance was, however, higher with the “ink A” devices which showed 13.3% median MPPT efficiency compared to 9.6% for the “Dyenamo” devices group. I proceeded with ink A prepared as described in 3.1.8.3 Methods - Carbon Blade-Coating. Because of the higher shown stability of $SnO_2$/PH1000/C compared to BCP/Cr/C I tested the following stability of the former one (Figure 4.12).

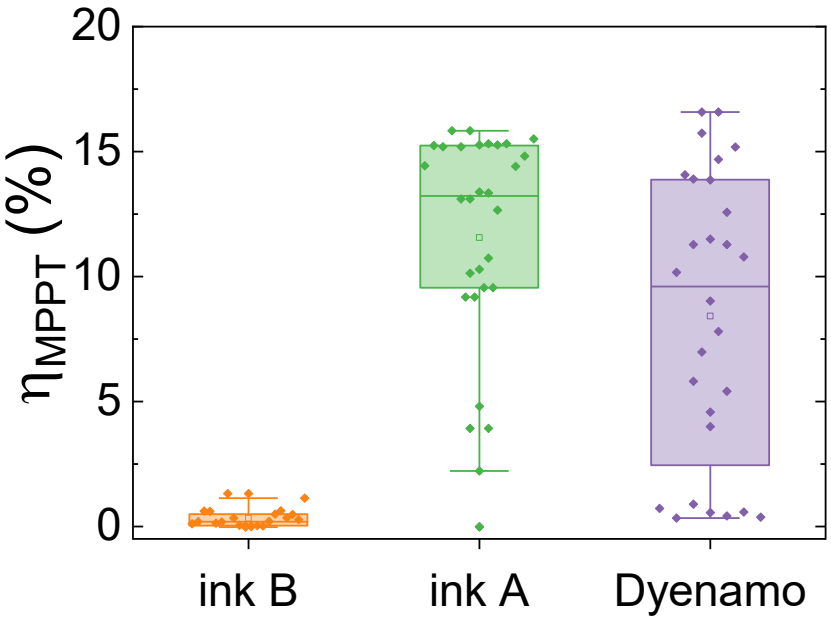



**Figure 5.9 Device Performance with Different Carbon Pastes**

Maximum Power Point Tracked (MPPT) efficiencies of devices with the stack FTO/polyTPD/$FA_{0.83}Cs_{0.17}Pb_{1.0}(I_{0.9}Br_{0.1})_3$/PCBM/BCP/Cr/C with different carbon pastes used for the fabrication of the Carbon top electrode. "Ink A" and "Ink B" were provided by David Beynon, University of Swansea and the "Dyenamo" paste a commercial paste bought from Dyenamo AB.

To optimise the carbon electrode curing conditions outside the complex device setting, I tested the sheet resistance $R_{\square}$ of carbon films on glass before using the conditions on C-PSC. I vary the curing time for "Ink A" between 5 and 30 min and the temperature is between 80 and 110 °C on a hotplate. The temperature and time range are chosen based on the stability of the rest of the PSC stack and the solvents used in the carbon paste. The materials and layers used in the PSC stack cannot easily withstand temperatures above 110 °C in air without initial degradation. The solvents in the carbon paste (see Carbon Blade-Coating) need at least 80 °C to ensure a good extraction. 50 and 100 µm are explored as the distances between the substrate and blade used for wet film coating. Four geometrical corrected resistance measurements are performed on different points of a 30×30 mm glass substrate with the carbon paste deposited on it. A minimum of two substrates were fabricated per condition.

An increase in the annealing time from five to 10 min resulted in a slight decrease in the median sheet resistance from 10.3 to 8.3 Ω/□ (see Table 1 and Figure 5.10a). However, a further increase to 20 min annealing at the same temperature resulted again in an increase of the median sheet resistance to 11.0 Ω/□. Further, I tested an increase of the annealing from 80 to 110 °C in steps of 10 °C while keeping the annealing time at 10 min. Raising the temperature resulted in a higher sheet resistance

(see Table 1 and Figure 5.10b). A 10 min anneal at 80 °C leads to the lowest resistance values for a 50 µm wet film.

**Table 1 Median Sheet Resistance of Carbon Electrodes Depending on Curing Conditions**

Median sheet resistance values of carbon thick films on glass substrate for different curing temperatures, times, wet film coating thicknesses, and numbers of coating.

| Temp | Time | Thickness | Coatings | Median R□ |
|---|---|---|---|---|
| °C | min | µm | - | Ω/□ |
| **80** | **5** | **50** | **1** | **10.3** |
| **80** | **10** | **50** | **1** | **8.3** |
| **80** | **20** | **50** | **1** | **11.0** |
| **90** | **10** | **50** | **1** | **10.2** |
| **100** | **10** | **50** | **1** | **15** |
| **110** | **10** | **50** | **1** | **11.9** |
| **110** | **30** | **50** | **1** | **12.9** |
| **80** | **10** | **100** | **1** | **10.4** |
| **110** | **10** | **100** | **1** | **9.1** |
| **80** | **10** | **50** | **3** | **4.5** |
| **80** | **10** | **50** | **2** | **6.7** |

The influence of an increase in the wet film coating thickness was investigated through a larger distance between the substrate and the blade. This would result in a larger thickness t of the final electrode. At the same material properties, most importantly, the same resistivity ρ, this would result in a lower $R\square$ because of the relationship:

$$R\square = \frac{\rho}{t} \qquad 5.1$$

Contrary to this, films with a larger coating thickness of 100 µm showed a higher median $R\square$ of 10.4 compared to 8.3 Ω/□ when annealed for 10 min at 80 °C (see Table 1 and Figure 5.10c). Increasing

the annealing temperature to 110 °C to ensure good solvent extraction of the thicker film resulted in a lower median $R\square$ than for a 50 µm film under the same annealing conditions (9.1 compared to 11.9 Ω/□). This is, however, larger than for samples with a 50 µm thickness dried at 80 °C.

To increase the final electrode thickness without needing a larger wet film thickness during the drying step, I investigated the effect of multiple consecutive thinner coatings. This way, solvents are first extracted from a thinner wet film before further increasing the thickness with additional coating steps. Increasing the number of coatings resulted in a large reduction in the $R\square$ of the final carbon film. The median values for one, two, and three coatings are 8.3, 6.7, and 4.5 Ω/□ respectively (see Table 1 and Figure 5.10c).

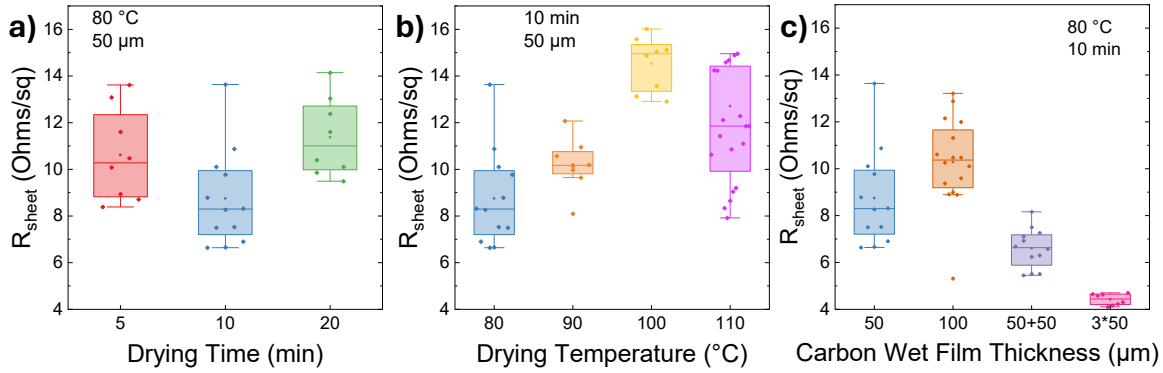



**Figure 5.10 Conductivity for Number of Carbon Coatings**

(a) Sheet resistance of carbon films on glass cured for different times at 80 °C on a hot plate. (b) Sheet resistance of carbon films on glass cured for 10 min at different set temperatures of the hot plate. (c) Sheet resistance of carbon films on glass for different wet film coating thicknesses in µm, all annealed at 80 °C for 10 min. The films labelled 3×50 and 50 + 50 are three and two consecutive coatings of 50 µm thickness with curing steps at the given temperatures in between and after each of the coating steps.

I investigated the effect of multiple carbon coatings on the device's performance by fabricating devices with the stack FTO/polyTPD/$FA_{0.83}Cs_{0.17}Pb_{1.0}(I_{0.9}Br_{0.1})_3$/PCBM/$SnO_2$/PH1000/C. I fabricated the carbon electrode of the devices by applying one, two, three, or four coatings, each by increasing the blade height over the substrates by 50 µm per coating, and each step was dried at 80 °C for 10 min (including in between the coating steps). Adding a second coating raises the MPPT efficiency from a median of 8.8% for one to 10.5% for two coatings (Figure 5.11a). However, applying three and four coatings did not enhance the device efficiency much further, causing only changes within the margin of error. While applying multiple coatings had only small effects on the

$V_{OC}$ and $J_{SC}$ of the devices, having more than one coating improved the $_{SS}FF$ from around 0.45 for one coating to around 0.55 for multiple coatings (Figure 5.11b).

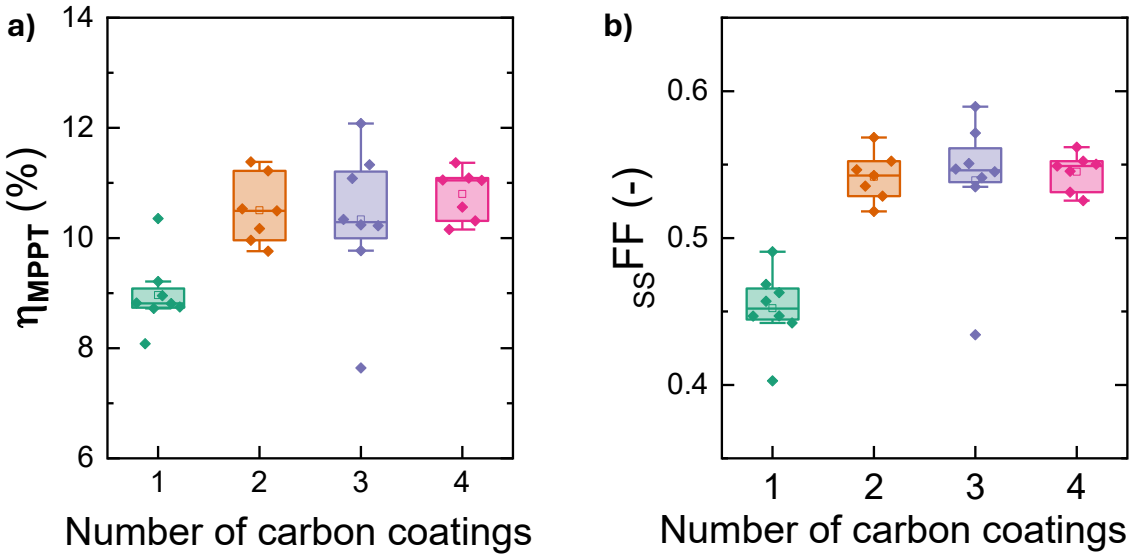



**Figure 5.11 Device Performance for Number of Carbon Coatings**

(a) The Maximum Power Point Tracked (MPPT) efficiencies of devices with one, two, three, or four consecutive coatings of a 50 µm thick carbon paste wet film, each followed by a 10 min annealing step at 80 °C. (b) The stabilised fill factor ($_{SS}FF$) of the same devices as in (a).

To further explore whether potential retained solvents play a role in the quicker degradation of p-i-n C-PSC compared to Au-based devices, David Beynon performed a Thermogravimetric Analysis (TGA) of the used ink A. A carbon paste sample was heated to the curing temperature of 80 °C while the absolute weight of the samples was measured. The temperature stage was set to 30 °C for one minute followed by a 2.5 min ramp up to 80 °C where the temperature was kept stable. While exposed to this temperature environment the weight of the carbon paste sample dropped from an initial 23.0 mg to 7.4 mg after 28 min of the programme (Figure 5.12). After 10 min at 80 °C (13.5 min of programme), the sample still weighs 13.8 mg.

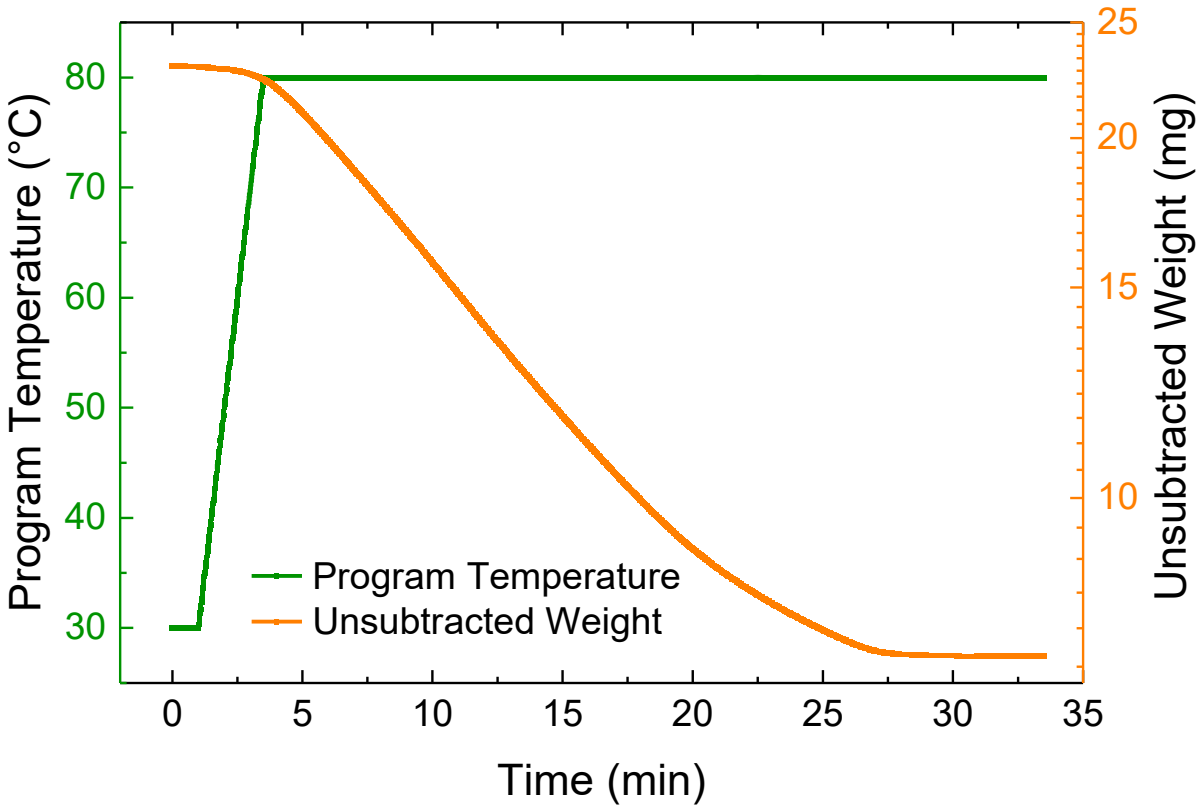



**Figure 5.12 Thermogravimetric Analysis of Carbon Paste**

The development of the weight of a sample of carbon paste used for electrode blade-coating upon heat treatment at the curing temperature of the blade-coated electrodes. The carbon paste specimen loses weight when heated for about 27 minutes. The analysis was performed by Dr David Beynon.

Based on the TGA and multiple coating results, 12 devices with a 10 min annealed carbon electrode and 12 with a 30 min annealed carbon electrode were prepared to investigate the influence of the longer anneal on performance and stability. All devices were annealed at 80 °C, double coated, and had the stack of FTO/polyTPD/$FA_{0.83}Cs_{0.17}Pb_{1.0}(I_{0.9}Br_{0.1})_3$/PCBM/$SnO_2$/PH1000/C. There was a negligible difference in median MPPT efficiencies between the two annealing conditions (12.7% for 10 min and 12.5% for 30 min). The champion devices for 10 min anneal showed 14.2% and the 30 min anneal champion 13.6% MPPT efficiency. All performance parameters showed only differences within the margin of error between the two annealing conditions.

Upon ageing encapsulated, in ambient air, under 0.76 suns, and at 85 °C, there are however, different behaviours between the two groups of devices (Figure 5.13). The 10 min annealed devices showed a quicker decay in ${}_{SS}V_{OC}$ than the 30 min annealed devices. After 500 h of ageing the 30 min devices still produced ${}_{SS}V_{OC}$ around 1.0 V while the median for the 10 min annealed group had dropped to a median of below 0.8 V. This higher retained ${}_{SS}V_{OC}$ is, however, more than offset by the larger initial

loss in $_{SS}J_{SC}$ and $_{SS}FF$ in devices with a 30 min annealing. After just 50 h of ageing, the $_{SS}FF$ of both groups had dropped significantly, with the 30 min annealed group showing an even stronger decrease from 0.55 at the start of ageing to 0.37, compared to 0.44 (from an initial 0.56) for the 10 min annealed devices (Figure 5.13). After 118 h of ageing, the 10 min annealed devices still had a median $_{SS}J_{SC}$ of 16.1 mA/cm$^2$ while the 30 min group had on median of 13.8 mA/cm$^2$.

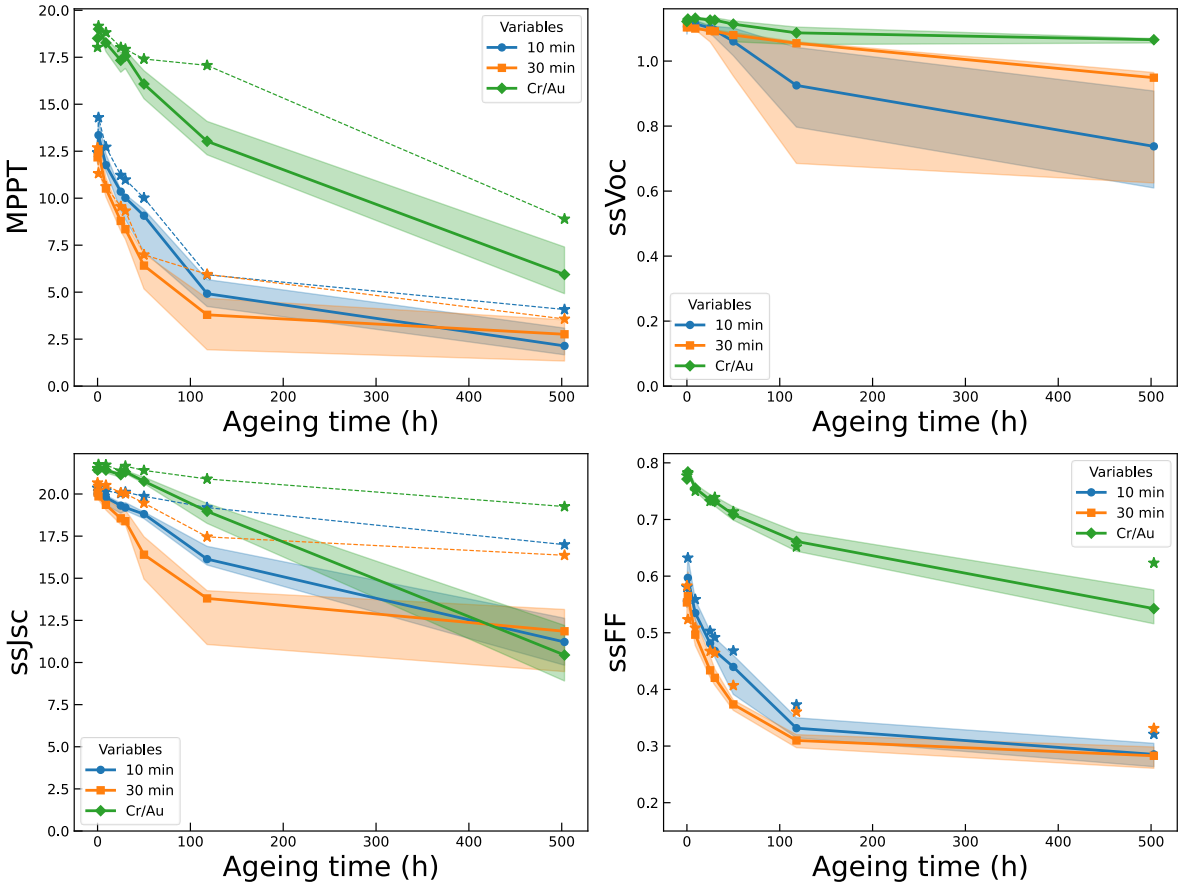



**Figure 5.13 Influence of 30 Minutes Anneal on Carbon Device Performance and Stability**

The statistical development of stabilised performance parameters upon ageing under 0.76 sun equivalent illumination at 85 °C in ambient air, including Maximum Power Point Tracked (MPPT) efficiencies, stabilised short circuit current density ($_{SS}J_{SC}$), open circuit voltage ($_{SS}V_{OC}$), and fill factor ($_{SS}FF$) are shown. The continuous blue line with circles, the orange line with squares, and the green line with rhomboids show the median values for $SnO_2$/PH1000/Carbon devices with a 10 min carbon curing, $SnO_2$/PH1000/Carbon devices with a 30 min carbon curing, and Cr/Au devices, respectively. The shaded area around this line indicates the spread from the first to the third quartile. The stars above each of the shaded areas represent the respective champion values. For each category, 24 encapsulated devices with an active area of 0.25 cm$^2$ were aged.

### 5.1.1.2 Adhesion of Laminated Carbon Films

Due to stability issues in blade-coated carbon devices described above, laminated carbon was explored as a potential solution (see Carbon-Based Electrodes). I investigate this alternative

deposition technique to explore a positive influence on the stability of C-PSC. As mentioned, the material properties of graphite itself should result in higher chemical and thermal stability of PSC under operation compared to metal electrodes. Because I did not observe this benefit in devices with blade-coated carbon electrodes, I hypothesise a problem with the processing of the carbon material into an electrode. The combination of heat and solvent exposure and the large pore volumes in carbon electrodes produced via the blade-coating technique could result in stability issues downstream.

Through the applied pressure during lamination, a reduced pore volume and potentially better adhesion at the $SnO_2$/C interface could help overcome the degradation at this interface. The mentioned adhesion of a laminated carbon electrode to the device stack is the most important processing consideration for this type of PSC device. There is ample literature on how to laminate on HTLs or directly onto perovskite layers, but no publication on how to achieve the same on ETLs. Mirroring the study presented in Chapter 4, the adhesion of laminated carbon electrodes to PCBM-based ETLs was systematically investigated. All explored ETL, pressure, and electrode combinations and the resulting adhesion and PCEs are listed in Table 2.

I fabricated the device stack up to the carbon lamination step, which Dr Luke Sutherland then carried out, as detailed in Sutherland et al.[162] Initial experiments using a carbon/silver bilayer electrode and a printed silver-alone electrode on PCBM show that neither adhered well under compression, even at the maximum available pressure of 360 MPa (Table 5 and Figure 5.14b). The electrodes detached completely after the lamination process. A dummy test using a spin-coated Spiro-O-MeTAD layer on top of PCBM demonstrates improved adhesion. This confirms the quality of the lamination process and previous literature showing a facile adhesion of laminated carbon electrodes ($C_{laminated}$) on Spiro-O-MeTAD, suggesting a weak mechanical contact specific to the PCBM/C interface rather than an inherent limitation to the lamination process.

To improve adhesion, an additional adhesive layer of PH1000 was introduced between the PCBM and the carbon electrode. This approach enhanced contact during lamination, confirming the improved adhesion of $C_{laminated}$ to PH1000. Because of the unfavourable energy alignment between PCBM and PH1000, the resulting PSC displayed low efficiency with a maximum power conversion efficiency (PCE) of only 1% (Table 2). The thicker PH1000 adhesive layer leads to excessive

resistance, limiting charge extraction and severe performance losses (Figure 5.14). An alternative approach investigated by Dr Luke Sutherland on the p-i-n stacks is to modify the carbon electrode prior to lamination by increasing surface roughness. This adjustment significantly improved adhesion without requiring an additional adhesive layer, leading to devices achieving a PCE of 3.14% with a PCBM/$C_{laminated}$ architecture.

To further improve both adhesion and charge extraction, we trial carbon lamination on the stack presented in Chapter 4. The carbon electrodes were laminated on the PCBM/$SnO_2$/PH1000 architecture. An $SnO_2$ ETL exhibits a preferential hole-extraction behaviour. The $SnO_2$ between PCBM and PH1000 ensures good energy alignment, charge extraction, and low recombination. The PH1000 enabled good adhesion. We test a PCBM/$SnO_2$/PH1000/$C_{laminated}$ stack, achieving an improved adhesion and a higher PCE of 5.67%. The still relatively low performance was due to an "s-kink" in the pristine devices. We attribute that behaviour to a degradation of the device stack between fabrication in Oxford, UK while being sent to Clayton, Australia for lamination.

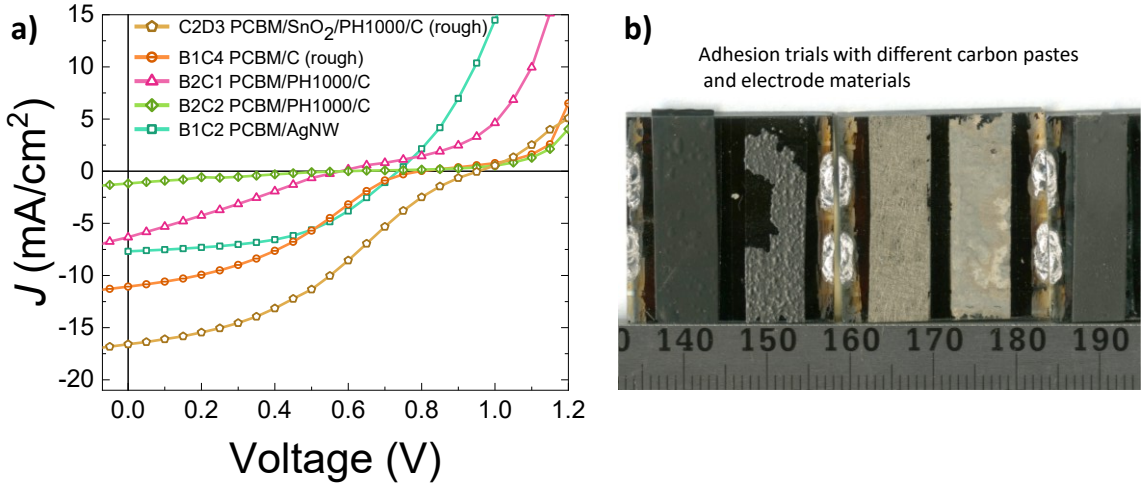



**Figure 5.14 Data First Lamination Experiments**

(a) Current density (*J*) voltage scans of p-i-n devices with different top electron transport layers and carbon electrodes. Laminations and measurements were performed by Dr Luke Sutherland. (b) Photo of laminated electrodes on p-i-n devices. The electrodes show signs of bubble formation and delamination. Photos by Dr Luke Sutherland.

**Table 2 Parameters First Carbon Lamination Experiments**

The parameters for the first three carbon electrode lamination experiments performed by Dr Sutherland on my samples. The carbon lamination was performed on different electron transport layers on p-i-n perovskite solar cells. Different pressure settings and carbon electrodes are used. The resulting adhesion and Power Conversion Efficiencies (PCE) are listed.

| Device# | Top layer | Carbon | Pressure (MPa) | Adhesion | PCE |
|---|---|---|---|---|---|
| B1C1 | PCBM | 4701s | 240 | Poor | N/A |
| B1C2 | PCBM | AgNW trial | 360 | Average | 2.82% |
| B1C3 | PCBM | 4701s | 360 | Poor | 0.04% |
| B1C4 | PCBM | 4701s rough | 360 | Good | 3.05% |
| B1C7 | PCBM | 4701s rough | 360 | Good | 3.14% |
| B1C8 | PCBM | Dyenamo rough | 360 | Poor | N/A |
| Dummy | PCBM/Spiro (by Dr Sutherland) | 4701s | 240 | Good | 1.17% |
| B2C1 | PCBM/PH1000 | 4701s | 360 | Average | 0.94% |
| B2C2 | PCBM/PH1000 | 4701s | 360 | Average | 0.16% |
| B2C3 | PCBM/PH1000 (thick - undiluted) | 4701s | 360 | Average | 0.04% |
| B2C4 | PCBM/PH1000 (thick - undiluted) | - | - | - | - |
| C2D3 (1) | PCBM/$SnO_2$/PH1000 | 4701s | 360 | Poor | N/A |
| C2D3(2) | PCBM/$SnO_2$/PH1000 | 4701s rough | 360 | Average | 5.67% |

Because of the unsatisfying performance of devices and the possible degradation while sending the unfinished devices between Australia and the UK, I transitioned to using another established carbon lamination process by Mohammadzadeh et al.[167] performed at Fraunhofer ISE, Freiburg, Germany. Hadi Mohammadzadeh performed the carbon lamination on the device stack locally. Because of the different lamination processes, I decided to screen again different ETL layers. I worked up the p-i-n PSC stack at Fraunhofer ISE to avoid the transport of unfinished PSC but achieve an immediate lamination after the PH1000 deposition. This included establishing the ALD $SnO_2$ and spin-coated PH1000 bilayer. Based on the results presented in Chapter 4 we tested different configurations between FTO/polyTPD/$FA_{0.83}Cs_{0.17}Pb_{1.0}(I_{0.9}Br_{0.1})_3$/PCBM and the carbon including BCP, BCP/Cr, $SnO_2$, and $SnO_2$/PH1000. We also tested treating the carbon electrode during the solvent exchange with PH1000 before laminating it onto BCP.

Surprisingly, the BCP/Cr layer, which resulted in my highest efficiencies with blade-coated carbon electrodes, did show low PCEs with the $C_{laminated}$ (Figure 5.15). The highest PCEs of PCBM/BCP/Cr/$C_{laminated}$ were around 7% compared to 17 - 18% for blade-coated devices (see Figure 4.6). The PCBM/$SnO_2$/PH1000/$C_{laminated}$ showed a very narrow distribution of PCEs, small hysteresis between up and down sweep, and high overall PCEs, with the champion device performing at 18.6% (Figure 5.15). Without the PH1000 in a PCBM/$SnO_2$/$C_{laminated}$ architecture, the PCEs were much lower and there was a large spread, with several devices showing close to 0% PCE. The median PCE of the group with $SnO_2$ without PH1000 was around 8% compared to ~ 17% when PH1000 was used. This is an even starker difference than the one observed for blade-coated devices in Chapter 4.

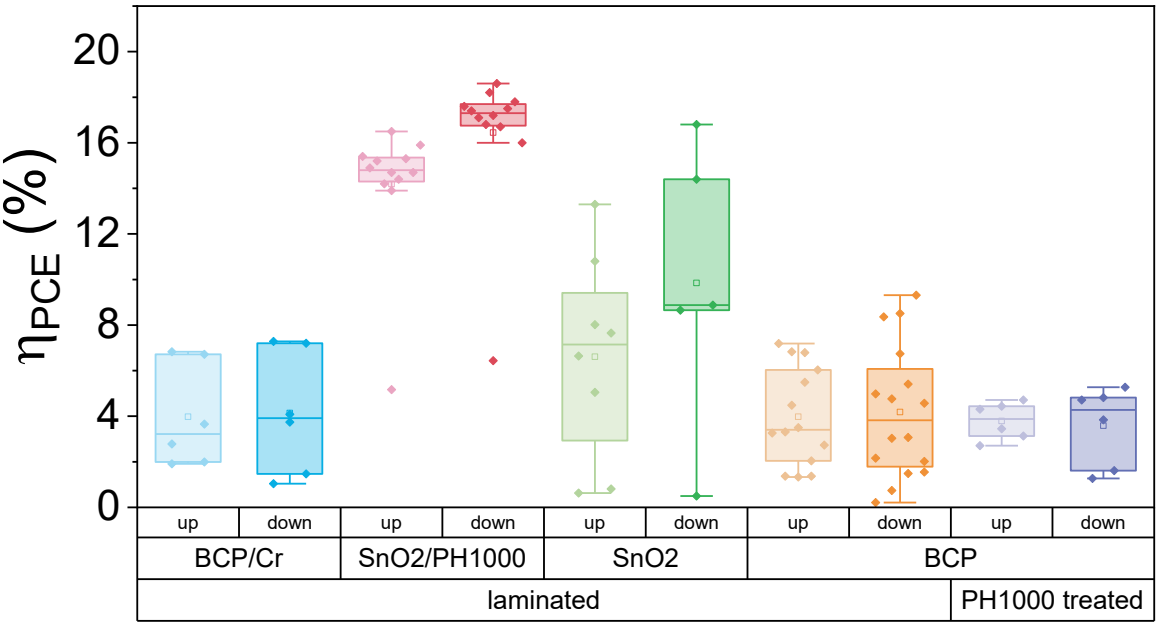



**Figure 5.15 First p-i-n Carbon Lamination**

Up and down sweep power conversion efficiencies (PCE) of devices with laminated carbon electrodes. All devices had the structure FTO/polyTPD/$FA_{0.83}Cs_{0.17}Pb_{1.0}(I_{0.9}Br_{0.1})_3$/PCBM, different materials as second electron transport layers including BCP/Cr, $SnO_2$/PH1000, $SnO_2$, and BCP. Some of the carbon electrodes were prior lamination, during the solvent exchange process, treated with PH1000. All laminations were done by Hadi Mohammadzadeh.

Laminating directly onto BCP led to PCEs of up to 9.3% (Figure 5.15). This is significantly higher than the achieved PCEs for blade-coating onto BCP of max 5% (Figure 4.9). Treating the carbon during the solvent exchange before the lamination with PH1000 did not lead to observable changes in behaviour (Figure 5.15).

To obtain a direct comparison between blade-coated and laminated carbon electrodes, I fabricate p-i-n stacks on two different kinds of substrates (ten 30×30 mm "Oxford" and five of type "C" 25×25 mm with the pattern of the group at Fraunhofer ISE). I blade-coated carbon electrodes on two of the Oxford-type substrates, fabricating 12 blade-coated (BC) devices. Hadi Mohammadzadeh laminated carbon electrodes on the other substrates. To confirm the efficiency values between different laboratories and obtain MPPT efficiencies, the devices on Oxford substrates were measured both in Oxford and Freiburg. The C substrates can, due to equipment limitations, only be measured in Freiburg.

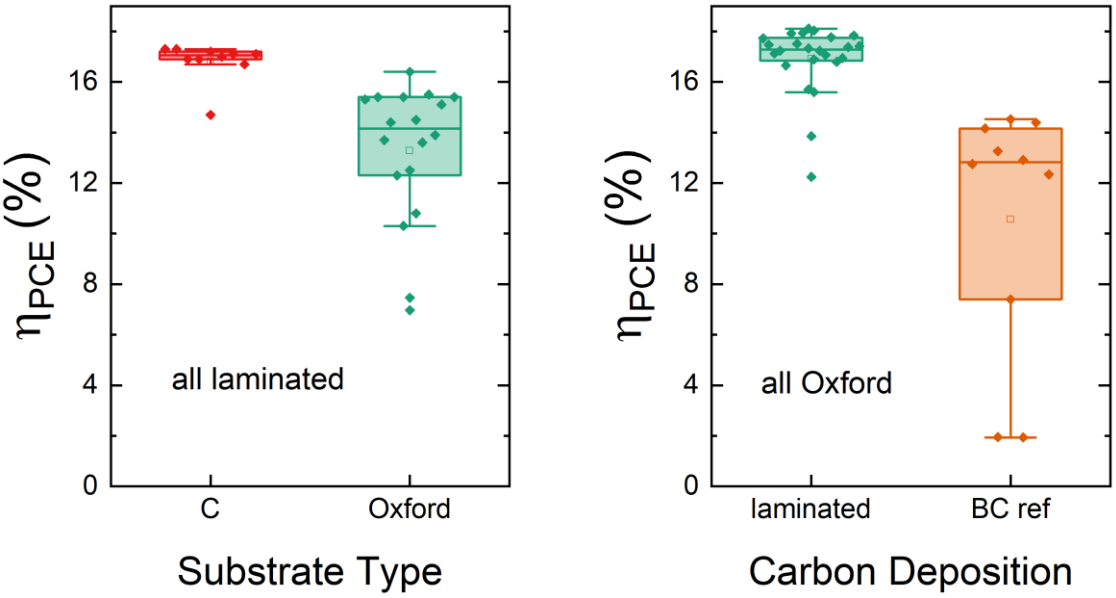



**Figure 5.16 Substrates and Laboratory Comparison of Carbon Electrodes**

(a) Power Conversion Efficiency (PCEs) of p-i-n devices on 25×25 mm ITO substrates (type "C") and 30×30 mm TEC15 FTO substrates (type "Oxford"). All devices were measured in Freiburg, Germany, and have the device stack polyTPD/$FA_{0.83}Cs_{0.17}Pb_{1.0}(I_{0.9}Br_{0.1})_3$/PCBM/$SnO_2$/PH1000/$C_{laminated}$. (b) PCEs of p-i-n devices of the same structure but with laminated and blade-coated (BC ref) carbon electrodes. All devices are measured in Oxford, UK and on TEC15 FTO substrates (type "Oxford"). The laminated devices in (b) are the same as the Oxford devices in (a).

The best reverse scan PCEs measured in Freiburg on C-substrates were 17.3% and on Oxford substrates 16.4% (Figure 5.16a). When measuring the same Oxford-substrate devices in Oxford, they showed a smaller spread in PCEs and a higher record PCE of 18.1% (Figure 5.16b). The PCEs of these laminated devices also showed a lower spread and higher values compared to blade-coated devices of the same architecture on the same substrates. The record PCE of blade-boated devices is considerably lower at just 14.5%. For the measurement in Freiburg, all devices were masked with a 0.09 $cm^2$ mask. In Oxford, the blade-coated devices were masked with a square 0.25 $cm^2$ mask. Due to the different electrode geometry, the same mask could not be used on the laminated devices. A rectangular 0.15 $cm^2$ was prepared for the laminated devices. The dimensions are chosen to have a similar dark-to-active area ratio for both types of masks to ensure a fair comparison between them.

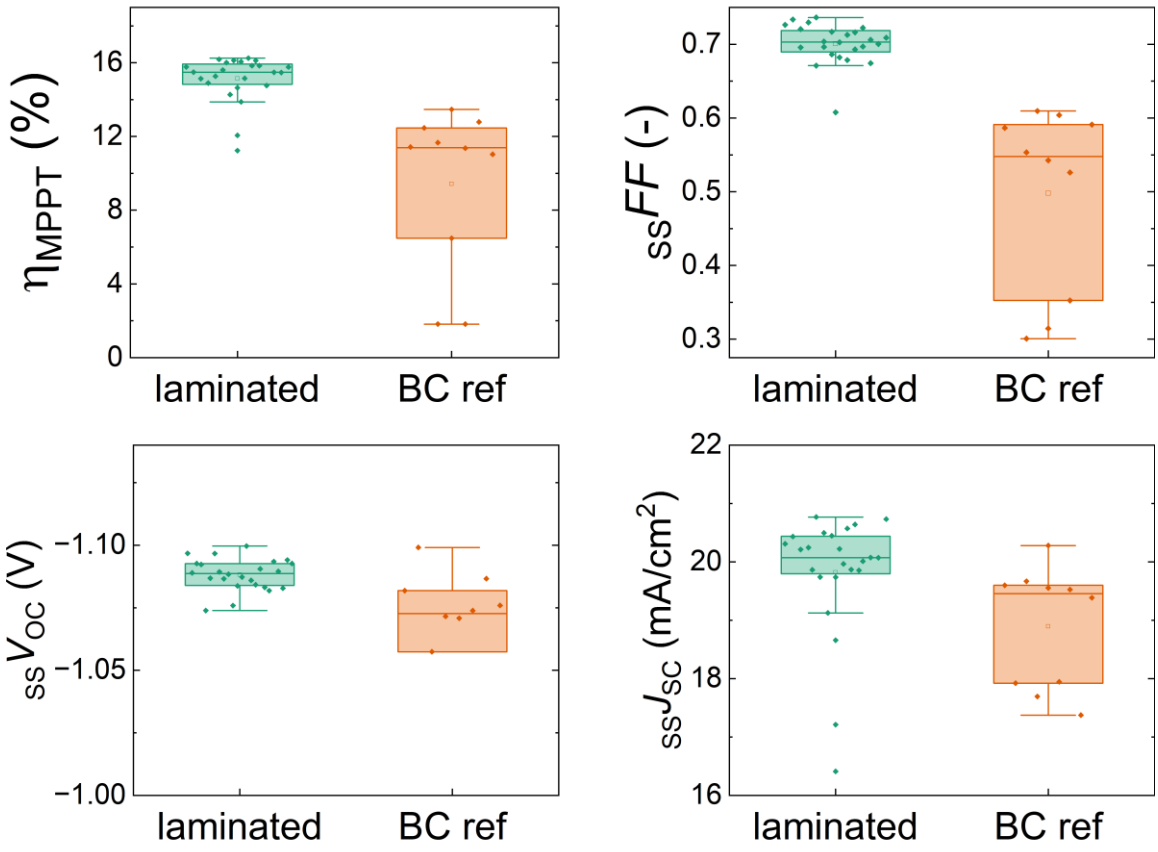



**Figure 5.17 Comparison of Blade-Coated and Laminated Carbon Electrodes**

(a) The maximum power point tracked (MPPT) efficiency of devices with the structure FTO/polyTPD/$FA_{0.83}Cs_{0.17}Pb_{1.0}(I_{0.9}Br_{0.1})_3$/PCBM/$SnO_2$/PH1000/C with laminated and blade-coated (BC ref) carbon electrodes. (b) The stabilised fill factor ($_{ss}$FF) of the same devices. (c) The stabilised open circuit voltage ($_{ss}V_{OC}$) of the same devices. (d) The stabilised short circuit current density ($_{ss}J_{SC}$) of the devices.

Stabilised measurements for MPPT efficiency, $_{ss}J_{SC}$, $_{ss}V_{OC}$, and $_{ss}FF$ were performed in addition to *JV* scans in Oxford. The laminated devices that reached PCEs of 18.1% (Figure 5.16b) reached in the same measurement run MPPT efficiencies of up to 16.3% while blade-coated devices achieved a maximum of 14.5% (Figure 5.17a). The median MPPT efficiency of laminated devices is 15.5% compared to 11.4% for blade-coated devices. The main reason for the higher efficiencies of the laminated devices is the higher $_{ss}FF$ of around 0.70 for laminated and 0.55 for blade-coated devices (Figure 5.17b). The values for $_{ss}J_{SC}$ and $_{ss}V_{OC}$, on the other hand, do not differ that much between the groups, showing only marginal differences (Figure 5.17c and d). The small boost in $_{ss}J_{SC}$ is consistent with previous findings by Mohammadzadeh et al.[167]

To examine the possible stability improvement of preparing the carbon electrode with the lamination process, I fabricate blade-coated full p-i-n devices and p-i-n stacks up to the ETL. Hadi

Mohammadzadeh then laminated carbon electrodes onto that stack. Based on my results of double blade-coated carbon electrodes (Figure 5.11), I also prepared devices that were then double-laminated by Hadi Mohammadzadeh with a second carbon electrode stripe laminated on top of the first one. The champion device with an MPPT efficiency of 19.3% is one with a single carbon lamination (Figure 5.18). The spread within the group of double-laminated devices was much narrower, with fewer outliers. The median MPPT efficiency of double-laminated devices is at 16.3%, 3.5 absolute per cent higher than the median MPPT efficiency of devices with a single lamination at 13.8%.

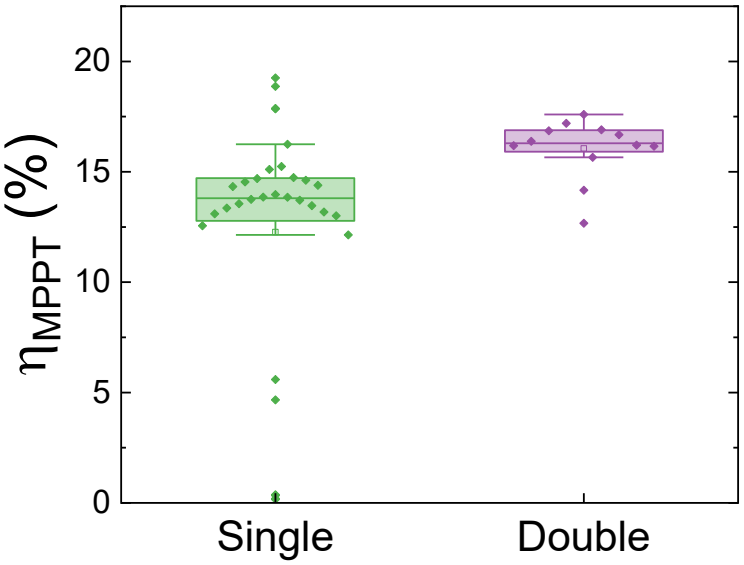



**Figure 5.18 Efficiency of Single and Double-Laminated**

The maximum power point tracking (MPPT) efficiencies of devices with the stack FTO/polyTPD/$FA_{0.83}Cs_{0.17}Pb_{1.0}(I_{0.9}Br_{0.1})_3$/PCBM/$SnO_2$/PH1000/C with a single and a double carbon lamination. An MPPT of 30 s is performed on each device. The carbon lamination was performed by Hadi Mohammadzadeh. Clemens Baretzky measured the MPPT efficiencies.

To exclude the influence of oxygen and moisture, especially to the hygroscopic PH1000 layer we decided to perform an in situ ageing experiment with an MPP tracking in an $N_2$ environment under one sun illumination. The experiment was performed at the University of Marburg by Lukas Wagner, Lea Obermüller, and Ali Reza Nazari Pour. Devices were aged unencapsulated and unmasked. To control the temperature, the devices were placed inside the $N_2$ ageing chamber onto an aluminium block with temperature control. Devices were separately connected and MPP tracked during the ageing period for 310 h. All devices showed a strong light-soaking effect, with performances increasing several absolute per cent upon the first two to twelve minutes of light exposure. The

laminated devices show a longer soaking effect, with the double-laminated device increasing from 12.5 to 15.6 mW/cm$^2$ after just over eleven minutes and the single-laminated device from 10.9 to 13.7 mW/cm$^2$ at the same time (Figure 5.19a). The light soaking took only about one minute for the two blade-coated devices, which increased from 11.0 and 12.0 mW/cm$^2$ to 12.7 and 13.6 mW/cm$^2$.

Both blade-coated devices showed a rapid exponential decay in power density. Within 17 min, the higher performing device fell from 13.6 to 12.7 mW/cm$^2$ before stabilising to a more linear decay. The second blade-coated device fell from 12.0 to 11.5 mW/cm$^2$ in an exponential decay lasting less than half an hour. Both laminated devices behave more stably after their respective light-soaks, showing minimal changes with a smaller linear decay within the first hour. Following the initial "burn-in", the blade-coated devices show a stronger linear decay than laminated devices. After 310 h of ageing, the two laminated devices perform at power densities of 9.6 for single and 9.3 mW/cm$^2$ for double-laminated devices. After the same time, the two blade-coated devices performed with 3.2 and 3.7 mW/cm$^2$.

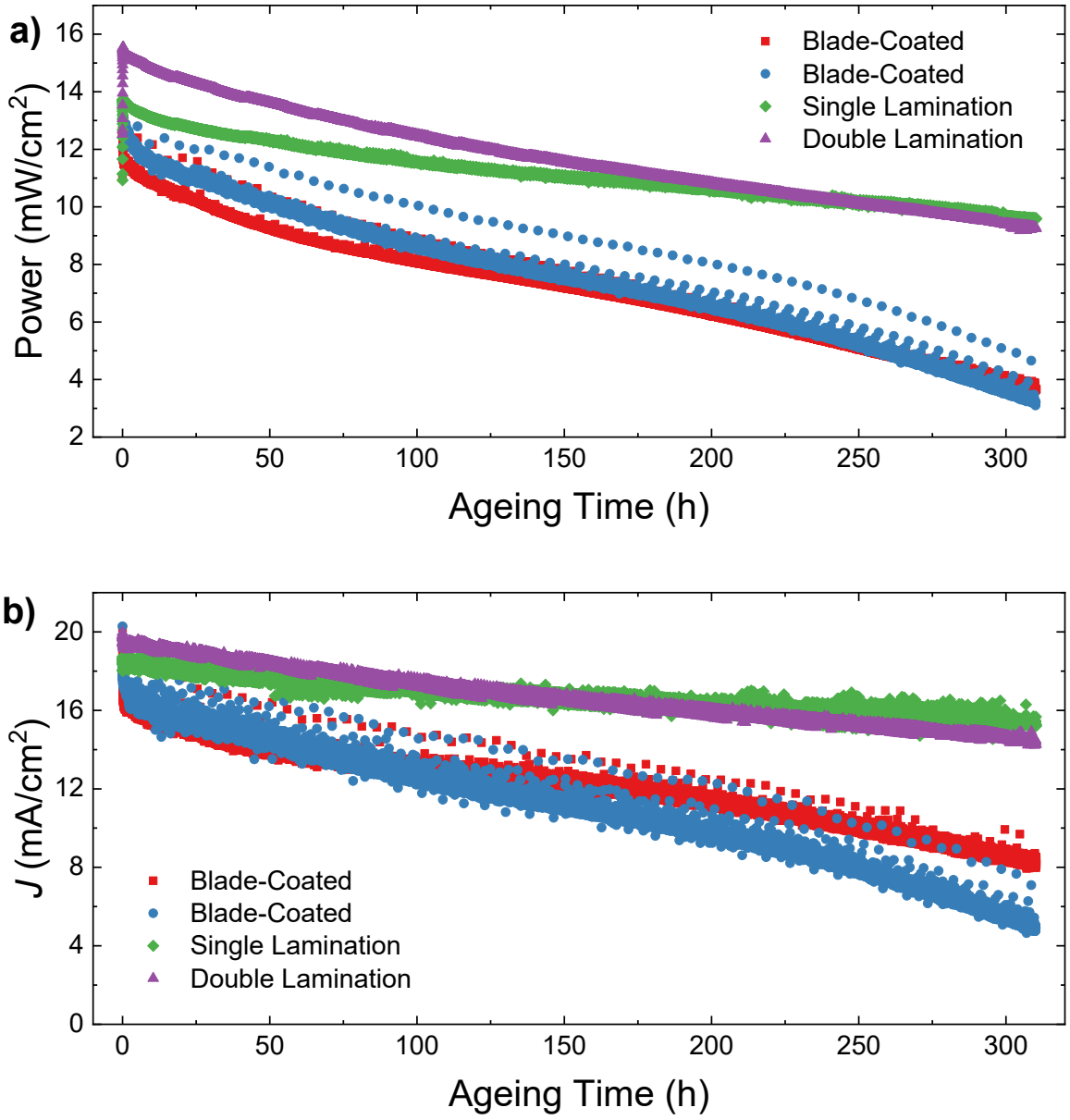



**Figure 5.19 Stability Comparison: Blade-Coated and Laminated**

(a) The power density of two blade-coated, one single-laminated carbon electrode, and one device with a double-laminated carbon electrode. The used architecture for all four devices was FTO/polyTPD/$FA_{0.83}Cs_{0.17}Pb_{1.0}(I_{0.9}Br_{0.1})_3$/PCBM/$SnO_2$/PH1000/C. All devices were MPP tracked while kept in a nitrogen environment under one sun on an aluminium block kept at 65 °C. No masking is applied and active areas are calculated out of the overlap of the carbon back electrode with the FTO. (b) The development of the current density (*J*) of the same four devices was tracked over time. Hadi Mohammadzadeh performed the lamination. Lukas Wagner, Lea Obermüller, and Ali Reza Nazari Pour conducted the ageing measurements.

While all devices showed a similar decline in FF, the difference in degradation speed in the power density was mostly due to different strong decay in current densities (Figure 5.19b). Because of the wide variation between the *J* values in the first measurement points, I take the average of the first 10 measured points as a better starting value and do the same for the last few points. The results are presented in Table 3 below. The current densities were initially 20.2 mA/cm$^2$ and 20.3 mA/cm$^2$ for

the two blade-coated devices and 18.6 mA/cm$^2$ for single and 20.0 mA/cm$^2$ for double-laminated.

**Table 3 Ageing Results Laminated and Blade-Coated Carbon Electrodes**

The average of the first 10 current densities ($J_{start}$) and the last 10 current densities ($J_{end}$), as well as the starting power density $P_{start}$ and the power density after 310 h of $N_2$-light-heat ageing $P_{end}$ for devices with different carbon electrode configurations.

| **Carbon** | ***J*** start (mA/cm$^2$) | ***J*** end (mA/cm$^2$) | **Power** start (mA/cm$^2$) | **Power** end (mA/cm$^2$) |
|---|---|---|---|---|
| single lamination | 18.4 | 15.4 | 10.9 | 9.6 |
| double lamination | 19.7 | 14.4 | 12.5 | 9.3 |
| blade-coated | 18.3 | 8.2 | 11 | 3.7 |
| blade-coated | 18.4 | 4.9 | 12.7 | 3.2 |

### 5.1.2 Discussion

Treating the $SnO_2$ top interface with PH1000 slows down the evolution of "s-kinks" in the current-voltage curves and inferred resistive behaviour under light and heat stress (Figure 5.4d, e). Devices with a $SnO_2$/PH1000/Carbon stack age more slowly than devices with BCP/Cr/Carbon or BCP/Cr/Ag (Figure 5.5). The treatment results in a slower drop in fill factor and higher retained power output upon ageing, as shown in Figure 5.1, Figure 5.3, and Figure 5.4.

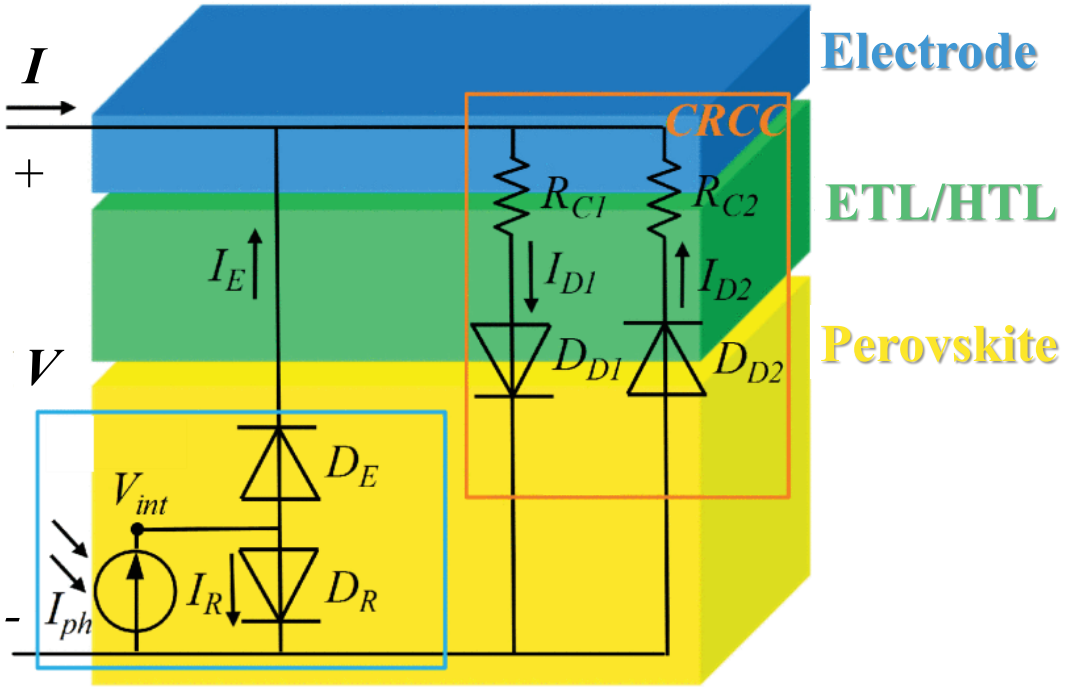



**Figure 5.20 Proposed Equivalent Circuit**

Equivalent circuit model for a perovskite solar cell contact displaying "s-kink" behaviour, as proposed by Chen

et al. The circuit combines two sub-circuits: the photo-generated current circuit (PGCC) and the carrier recombination current circuit (CRCC). The PGCC includes a current source representing the photocurrent and two diodes: a recombination diode ($D_R$) carrying the recombination current ($I_R$), and an extraction diode ($D_E$) carrying the extraction current ($I_E$). In CRCC, two diodes ($D_{D1}$ and $D_{D2}$) are used to model trap states capturing carriers under forward and reverse voltages, respectively. Two resistors ($R_{C1}$ and $R_{C2}$) are introduced to account for the ohmic contribution of the contacts. Figure adapted from Chen et al. © 2021 IEEE.[202]

An "s-kink" describes a deviation from ideal diode behaviour in the JV curve, where the current density drops at suboptimal voltages and then plateaus at this reduced level, often persisting up to voltages near $V_{OC}$. This behaviour has been frequently observed in non-optimised solar cell devices, including organic,[203–205] CdTe,[206] and perovskite solar cells.[202,207] Multiple different explanations have been reported. Tress et al., for example, reported that a severe imbalance in hole and electron transport properties can cause an organic solar cell device to display "s-kinks".[203] The most common explanation across different photovoltaic technologies, however, that a too large energy offset between two layers in the device, causes charge accumulation and recombination at the interface in question.[205–207] Both Jacobs et al.[208] and Prabu et al.[207] were able to model the "s-kink" behaviour of a device correctly using a large energy offset at the perovskite transport layer interface. While Prabu et al. model the current loss through recombination inside the bulk perovskite layer, Jacobs et al. use interface recombination. Prabu et al. and Chen et al. develop an equivalent circuit correctly representing the "s-kink" behaviour using a diode with opposite blocking direction to the internal diode in the ideal solar cell model (compare Figure 5.20 and Figure 2.7).[202] The absence of "s-kinks" in aged devices with BCP/Au instead of $SnO_2$/Au (see Figure 5.6), suggests that an energetic barrier forms at the $SnO_2$/electrode interface during combined light and heat stress. The PH1000 treatment only decelerates this degradation but does not fully prevent it. Future work on this interface is necessary to achieve the desired long-term stability.

The formation of an extraction barrier due to ageing can amplify pre-existing, otherwise minor, recombination processes. This alone can explain the appearance of moderate "s-kinks" in aged devices. If the extraction barrier forms alongside an increase in trap density, this combined effect accounts for the severe "s-kinks" observed in aged devices with $SnO_2$/carbon interfaces. A potential reason for the increased trap density is the formation of additional defects, such as halide vacancies, in the perovskite upon degradation.[209,210] The $SnO_2$ electron transport layer can further contribute to

this behaviour. The number of oxygen vacancies in $SnO_2$ is known to be crucial for both the efficiency and stability of the device. A high density of oxygen vacancies increases the conductivity of $SnO_2$ and enhances electron extraction. I therefore employed a $SnO_2$ layer rich in oxygen vacancies in the presented work to improve the device efficiency. However, Zhao et al. have reported recently that a high concentration of oxygen vacancies can lead to halide absorption by $SnO_2$ and increase its chemical interaction with FAI, accelerating perovskite degradation.[211] Our oxygen-vacancy-rich $SnO_2$ can thus provide pathways for halides to escape and it facilitates halide migration or loss. Additionally, its increased reactivity can contribute to the degradation of organic species such as PH1000 and/or the carbon electrode at the interface.

The still quicker-than-expected ageing of encapsulated carbon devices might be explained by our encapsulation method not being compatible with our carbon electrode. The carbon electrodes are fabricated with paste and in ambient air. Solvents, moisture, and or oxygen can adsorb to the large pore volume of the carbon electrode visible in SEM cross-sections in Figure 4.5 and Figure 4.2. They might be trapped inside the encapsulation if the viscous epoxy fails to infiltrate (as sketched in Figure 5.2e). The epoxy might also damage the carbon electrodes upon ageing, as visible in Figure 5.2a.

The pore volume may also provide an easier path for degradation products to leave the perovskite. This could also explain the quicker degradation of unencapsulated carbon electrodes compared to their gold counterparts at 65 °C under light (Figure 5.4a). It would also be in line with the reported high stabilities of so-called triple mesoporous carbon-electrode devices, where three mesoporous layers, including the pore volume of carbon, are infiltrated with perovskite.[69,136] If a proper encapsulation can be found for our carbon electrodes and if the interface with $SnO_2$ can be further optimised, we expect the carbon electrodes to be more stable than gold electrodes, fully showing their potential due to favourable material properties like inertness to halides.

I found a strong correlation between annealing time and device stability. A longer heat gun annealing of the carbon, while not resulting in any large difference in initial device performance, results in reduced device stability to light-heat ageing (Figure 5.8). The low stability of the 4-minute annealed devices is likely to be an outlier due to a faulty substrate or processing error. This might be because of heat damage to the device that does not influence the initial performance but acts as a starting

point for degradation. When curing the carbon paste on top of a device stack, there is an unavoidable trade-off between solvent extraction of the µm-thick paste and heat damage to the device.

Ink A displays a lower viscosity than the Dyenamo paste, leading to improved application and distribution on the substrate. This resulted in better reproducibility and a smaller spread in MPPT efficiencies (Figure 5.9). However, SEM cross-sections show no visible morphological differences between the carbon electrodes deposited from the two pastes. Ink A was more difficult to handle, which could present challenges for upscaling the process. However, these concerns can be allayed by the fact that Beynon et al.[154] successfully used the same paste for a role-to-role process.

One potential issue with carbon pastes is the presence of trapped solvents, which may reduce the conductivity of the carbon films.[212] Complete solvent extraction should, in principle, enhance conductivity by preventing insulating residues from remaining in the electrode. However, the observed increase in resistance for longer annealing times and higher annealing temperatures suggests that additional factors besides residual solvents influence overall conductivity. I found that rapid solvent removal can compromise the mechanical integrity of the electrode, leading to cracking and delamination. SEM cross-sections of hot plate-annealed devices showed delamination, likely due to bottom-up heating that drives solvent removal first from the bottom interface (Figure 4.6f). A schematic representation of this effect illustrates how directional heating influences the solvent extraction process and the resulting film integrity (Figure 4.6e). Further, I observed cracks in films exposed to too-fast drying procedures. This is expected to lead to reduced lateral conductivity. These defects are likely caused by rapid solvent evaporation, leading to an abrupt volume contraction, preventing the wet film from properly settling.

Multiple blade-coated carbon layers improve device performance compared to a single coating (Figure 5.11b). Devices with more than one coating show higher $_{SS}FF$ and reduced series resistance (Figure 5.11c). Increasing the film thickness with multiple coatings compared to only one thicker coating prevents the trapping of solvents due to intermediate solvent removal steps between the layers. Additionally, defects or cracks in the first carbon film may have been filled by subsequent coatings, improving film uniformity and electrical contact. However, I found no significant improvement in MPPT efficiency when increasing from two to three or four coatings, suggesting a

saturation effect. This is in contrast with carbon films on glass, where $R\square$ continued to decrease from two to three coatings significantly (Figure 5.11a). A possible explanation is that longer heat exposure in ambient air required for additional coatings introduces degradation effects to the rest of the PSC stack. These degradation effects can counteract the expected conductivity gains in the carbon electrode due to multiple coatings.

The TGA results in Figure 5.12 show that substantial amounts of solvents are removed until 28 minutes into the programme. At that time, the carbon paste sample is exposed to over 25 minutes of heating at the annealing temperature of 80 °C. This further shows that at the normal annealing conditions of 10 min, which were the optimal conditions for high-performing devices, there is a large weight of solvents remaining inside the electrode. After 10 min, the sample loses over 46% of its weight, indicating that almost half of the sample weight after the standard annealing period is made up of volatile components at 80 °C.

The sample in the TGA experiment shows a different geometry from a blade-coated carbon electrode and might show different behaviour regarding solvent extraction. We assume, however, that the sample's behaviour is, even though prepared differently, similar enough to the behaviour of the drying carbon electrodes because of comparable volume and the same material being used for the preparation. This way the results have severe implications for device stability. Since solar cells in real-world conditions can easily encounter temperatures higher than 80 °C, we age them at 85 °C. In a device prepared with a 10 min anneal there would be large weights of material volatilised in the electrode causing changes to the electrode. Further, as shown in Chapter 4, the solvents in the carbon paste can damage the fullerene layer leading to possible degradation at the perovskite/ETL and or ETL/electrode interfaces.

A 30 min anneal instead of a 10 min anneal did not solve the stability problems. The better retention of $V_{OC}$ is well in line with the hypothesis that the full removal of solvents from the paste prevents damage to the ETL and the degradation of this layer. The quicker decay in $J_{SC}$ indicates damage to the perovskite layer, possibly due to the excessive heat exposure of the device stack in air during the two 30-minute annealing steps. Most importantly, I observed a rapid decay in $_{SS}FF$ for both 10- and 30 min annealed devices. This indicates that the longer annealing does not solve the main degradation

pathway, which is the development of "s-kinks" due to the formation of an energetic barrier likely at the $SnO_2$/C interface. These results indicate that this phenomenon is caused by other issues, but not residual solvents.

While there were no problems for solvent extraction when laminated carbon electrodes were used, this process faced other challenges, including delamination issues. The poor adhesion of laminated carbon electrodes to PCBM can be due to several factors. PCBM forms a relatively smooth and chemically inert surface, limiting the available mechanical interlocking sites for the carbon electrode. The absence of solvents during the lamination process prevents partial dissolution or chemical bonding at the interface, which could otherwise aid adhesion. The successful adhesion observed on Spiro-OMeTAD suggests that surface roughness and chemical compatibility play crucial roles in forming a stable interface.

The improved performance observed with the PCBM/$SnO_2$/PH1000/$C_{laminated}$ architecture highlights the importance of interfacial engineering. The inclusion of $SnO_2$ as an additional ETL likely modified the electronic properties of the interface, reducing charge accumulation and the s-shaped *JV* characteristics. The improved adhesion in this structure can be attributed to the increased roughness of the modified carbon film, which provided a more mechanically interlocked interface while maintaining reasonable charge extraction.

Despite these advances, the maximum achieved PCE remains lower than expected for optimised p-i-n perovskite solar cells. This can possibly be improved by optimising the carbon processing. The lamination and the long transport of the samples from the UK to Australia might have caused interfacial degradation, limiting the efficiency of the resulting device.

The surprisingly low performance of the PCBM/BCP/Cr together with $C_{laminated}$ could be because of the low thickness of the Cr layer of just 5 nm (Figure 5.15). Such an evaporated nano Cr layer works well to prevent solvent damage and to ensure a good electrical connection between the ETL and the carbon electrode. However, for lamination, a thicker soft layer is needed to achieve good adhesion during the lamination process. The co-polymeric layer of PH1000 can fulfil this requirement, ensuring good adhesion, as mentioned above for the PCBM/PH1000 case. That is one of the probable reasons for the superior efficiencies of devices based on the PCBM/$SnO_2$/PH1000/$C_{laminated}$

architecture over devices with just $SnO_2$ without the PH1000 treatment (Figure 5.15). A further reason is likely the stoichiometry of the ALD $SnO_2$ in Freiburg, which we show in Chapter 4 to make a worse contact with the blade-coated carbon (Figure 4.16).

Notably, the MPPT efficiency of PCBM/BCP/$C_{laminated}$ was much higher than that of blade-coated devices using the same architecture. They still show a high series resistance in line with the missing charge transfer states in BCP without any direct contact with a metal layer (see Chapter 4 and Figure 4.9). However, the higher performance of laminated devices indicates that this was not the only problem encountered in the blade-coated devices before. The absence of changes when the laminated electrode was pre-treated with PH1000 before lamination, rather than applying the layer to the device stack, suggests that PH1000 is essential for protecting the underlying ETL and ensuring good adhesion, not just for facilitating charge transfer and transport.

The increased performance of p-i-n PSCs with laminated carbon electrodes, compared to blade-coated references (Figure 5.16 and Figure 5.17), is likely due to improved electrode morphology and interface quality. Mohammadzadeh et al.[167] showed that for the same pressing process when used on n-i-p PSC that the hot pressing reduces void formation within the bulk carbon electrode, enhancing its overall conductivity. Further and more importantly, it minimised micro-voids at the HTL/carbon interface, lowering contact resistance between the two layers. I also observed in SEM cross-sections of p-i-n PSC differences in the extent of micro-void formation depending on the carbon electrode curing process (Figure 4.6). This way, our findings on p-i-n with $C_{laminated}$ align with the previous reports on n-i-p devices, suggesting that the $SnO_2$/PH1000/$C_{laminated}$ architecture benefits from similar improvements.

Another possible contributor to the higher performance is the complete removal of solvents from the carbon electrode through solvent exchange and without excessive heating of the device stack. The heat pressing of the electrode is significantly shorter than the drying of the carbon electrode, reducing the heat exposure. The pressure during heating might also help prevent volatile species from leaving since increased pressure shifts the equilibrium more to the reactant side, away from the formation of gaseous products. This could further limit the thermal degradation during the short hot pressing compared to the thermal curing of the device on a hot plate at ambient pressure. A further reason for

the slightly higher $_{SS}J_{SC}$ in laminated devices has been described by Mohammadzadeh et al.[167] as more horizontal alignment of graphite flakes might improve the otherwise relatively poor back reflection of light by the carbon electrodes compared to metal electrodes.

The higher stability, especially regarding the better retention of *J* (Figure 5.19b) could be because of less thermal stressing of the perovskite layer in ambient air during the device fabrication. While the thermal stress during device fabrication is not higher than the stress during ageing, the stress can be more detrimental to an unfinished device stack and with oxidising species present than to a finished device stack in an inert atmosphere like $N_2$ or encapsulated environments. The slightly lower heat-light stability of the double-laminated devices might be because of the extra interface between the two carbon layers being another weak spot for degradation. The difference between single and double-laminated devices seems, however, to be within the margin of device-to-device fluctuation. The difference between the two identical blade-coated devices is similar, if not bigger than the difference between the two laminated devices.

### 5.1.3 Conclusion

In conclusion, the $SnO_2$/electrode interface is a weak point for device degradation. Applying a PH1000 layer improves the stability of this interface. Blade-coated carbon electrodes generally exhibit poor stability within the $SnO_2$/PH1000/C architecture but are more stable than $SnO_2$/C and silver devices. The method of carbon electrode preparation considerably affects device performance and stability. Multiple thinner layers in blade-coating provide an efficiency advantage over a single thin or thick layer. We observed a similar effect for multiple laminated carbon layers. The findings presented in this chapter also demonstrate the feasibility of laminated carbon electrodes for p-i-n perovskite solar cells, with adhesion challenges largely overcome through adjusted processing of the carbon electrode. Laminated carbon layers offer improved stability over blade-coated electrodes during heat-light ageing. These findings highlight the importance of stabilising interfaces and considering electrode preparation methods for the overall stability of PSCs. Even methods with no significant difference in initial device performance can lead to large differences in long-term stability. These effects are overlooked if the electrode is treated as a generic component of a PSC or if the stability is only tested on the highest-efficiency architecture.

## 5.2 Graphene Diffusion Barriers

As described in the chapter Perovskite Instabilities, a major factor in instability in perovskite semiconductors is the loss of volatile species, such as halide, methylammonium, or formamidinium-based compounds, from the perovskite absorber layer. These species form as a product of perovskite decomposition reactions that degrade the absorber layer under thermal stress and light exposure. Because the products are mobile inside the perovskite layer and relatively volatile, they can leave the layer. When leaving the perovskite layer, they might degrade the adjacent layers by doping them, shifting to unfavourable energy alignments, and this way hindering charge extraction.[213] Additionally, by leaving the perovskite, they shift the equilibrium towards the degradation reaction by removing the products and increasing the relative concentration of the educts. Another known problem with perovskite stability, as described in Electrode Materials and Stability Issues, is the diffusion of metal ions from the electrode into the perovskite layer forming recombination centres and degrading this way the optoelectronic properties of the perovskite.

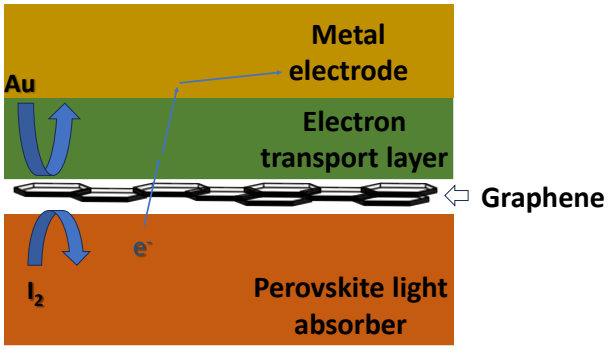



**Figure 5.21 Proposed Working Principle of a Graphene Diffusion Barrier in a p-i-n Device**

An impermeable graphene layer could prevent outgassing of volatile products of light-heat induced perovskite degradation, like the above-mentioned $I_2$. Such a layer could also inhibit the diffusion of metal ions, like $Au^+$, from a metal electrode into the perovskite layer. Because of the low thickness, charges should be able to tunnel through such a layer, presenting only minor changes to the local energetics.

In this chapter, I aim to address this challenge to perovskite stability by using a graphene layer on top of the perovskite layer. Graphene is a two-dimensional material consisting of a one-atom-thick layer of carbon atoms in a honeycomb structure, with each carbon atom in covalent bonds to three neighbouring atoms. A promising material property of graphene is its impermeability to any chemical species but hydrogen.[214] Employing a graphene layer on top of the perovskite layer might prevent volatile decomposition products from leaving (Figure 5.21). This shifts the chemical equilibrium of

the thermal- and light-composition reactions, slowing or stopping these difficult-to-avoid reactions inside the PSC device. The graphene can thus also prevent metal ions from diffusing into the perovskite and halides from reaching the back electrode, extending the stability of both the perovskite layer and the whole device by blocking multiple degradation pathways from taking place. Furthermore, the mechanical strength and flexibility of graphene ensure a seamless integration into PSC architectures, with minimal disruption to the device's optoelectronic properties.

The following chapter explores the potential of graphene-based barriers for enhancing perovskite stability. By creating a protective graphene layer that minimises the escape of volatile components, this work seeks to increase the operational lifetime of PSC. Additionally, the incorporation of graphene as a barrier material could prevent the interdiffusion of ions in multijunction perovskite tandems with different ion ratios in each junction. The project was done in close collaboration with Dr Abhay Shivayogimath at the Technical University of Denmark, who originally suggested the idea of using graphene as atomically thin barrier interlayers.

### 5.2.1 Increased Film Stability

To first test the hypothesis of increased stability of perovskite layers due to a protective layer of graphene, I fabricated thin films of perovskite on ITO substrates and perovskite/PCBM bilayers on ITO. The graphene films were produced and laminated onto some of the samples by Dr Abhay Shivayogimath. To exclude edge effects (of species diffusing around the graphene at the edges of the substrate), Dr Abhay Shivayogimath applied a Kapton$^{TM}$ polyimide film around the edges (Figure 5.22a).

The films were aged under 0.76 suns illumination, in ambient air, and at 85 °C. This is, as described, close to the maximum real-world conditions a solar cell encounters on a roof. The film quality was assessed in terms of optical appearance via photographs and optical microscope images. To further determine the quality of the perovskite film during the ageing x-ray diffraction (XRD) measurements were performed before ageing, after 40 h, and after 180 h of ageing.

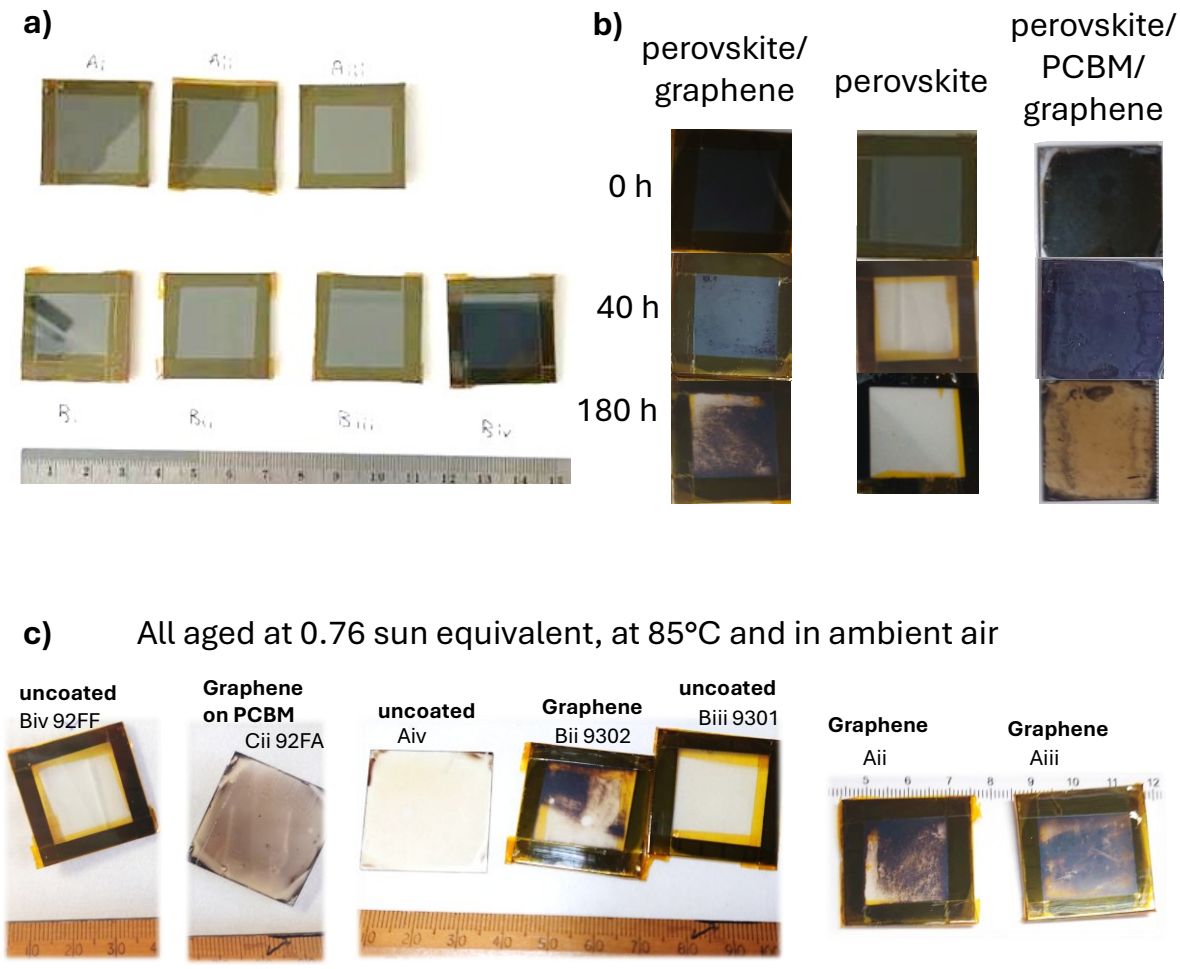



**Figure 5.22 Graphene-Encapsulated Films Ageing**

(a) Perovskite films with and without graphene lamination before ageing. Photos taken by Dr Abhay Shivayogimath. (b) Films at the beginning of the ageing trial, after 40 h, and after 180 h of ageing in ambient air under 0.76 suns at 85 °C. From left to right one graphene-encapsulated perovskite, one unencapsulated perovskite film, and one perovskite/PCBM/graphene sample. (c) Seven aged samples after 180 h of ageing in ambient air under 0.76 suns at 85 °C, including three encapsulated perovskite and three unencapsulated (uncoated) films. All graphene films were produced and deposited by Dr Abhay Shivayogimath.

Perovskite films without graphene discolour completely and become transparent after only 40 hours of ageing (Figure 5.22b). Only the areas under the polyimide tape maintained the perovskite material. On the other hand, perovskite films with a graphene film laminated on top of them stayed completely black for the first 40 h of ageing. Even after 180 h, there was still perovskite material left on graphene laminated samples (Figure 5.22b-c). Notably, the perovskite material loss was selectively in areas where there was visible damage to the graphene layer before the start of the ageing (Figure 5.23 and Figure 5.22b-c). While not observable in photographs, there was a colour difference between the perovskite in areas under intact graphene and under holes inside the graphene in optical microscope images. The areas under the damaged graphene areas appeared more yellow, showing an ongoing

degradation after 40 h. The areas under the graphene showed no colour change under the optical microscope after 40 h, but showed widespread formation of pin holes.

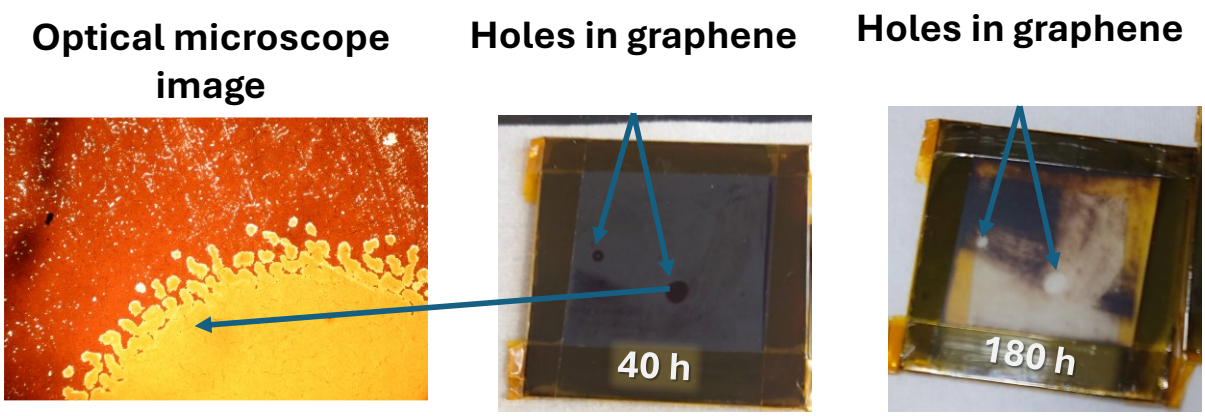



**Figure 5.23 Influence of Holes in Graphene on Film Ageing**

An optical microscope image (left) of the perovskite layer after 40 h of ageing was taken at the edge of a hole in graphene. The area covered by graphene shows a distinct brown perovskite colour while the area under the hole shows a yellow colour. In the photograph of the substrate after 40 h (middle) the same perovskite film still appears uniformly black - the usual colour of the used perovskite. The holes in the graphene are, however, clearly visible. After 180 h of ageing (right), the perovskite shows a clear loss of material and decolouration. The areas below the holes appear most transparent. All graphene films were produced and deposited by Dr Abhay Shivayogimath.

With XRD, I probed the crystallinity of the perovskite layer during ageing. The scans were performed as described in Methods X-Ray Diffraction. Eight samples were tested (three unencapsulated perovskites, three graphene-encapsulated perovskites, and two encapsulated perovskite/PCBM samples). The scans were performed before ageing (0 h), after 40 h, and after 180 h of ageing at 85 °C, under 0.76 suns in ambient air. The full spectra of the three coated and three uncoated perovskite films on ITO are shown in Figure 5.24. Samples are placed by hand into the XRD sample holders (as described in Methods X-Ray Diffraction).

The coated and uncoated samples show similar perovskite peak positions and intensity at 0 h before ageing (Figure 5.24a). This confirms the comparability of the films for the ageing experiment. After 40 h of ageing in uncoated samples, there was a considerable decrease in perovskite and $PbI_2$ peaks while ITO peaks remained unchanged (Figure 5.24b). After 180 h, there is no perovskite peak left in uncoated samples while the graphene-coated samples still show strong perovskite peaks (Figure 5.24c). To simplify and quantify the decrease in crystallinity, I chose the maximum counts at the peak at around 14.1 ° corresponding to the 1 0 0 perovskite peak as a figure of merit. All films but

one graphene-coated sample showed a good signal between 2,339 and 3,958 counts (Figure 5.25a). One of the graphene-coated samples showed an unusually low count of 1,633. This last sample might have degraded slightly during the transport and/or the graphene deposition. The peak for the other two graphene-coated samples shows at a by around 0.1° slightly lower 2 θ angles.

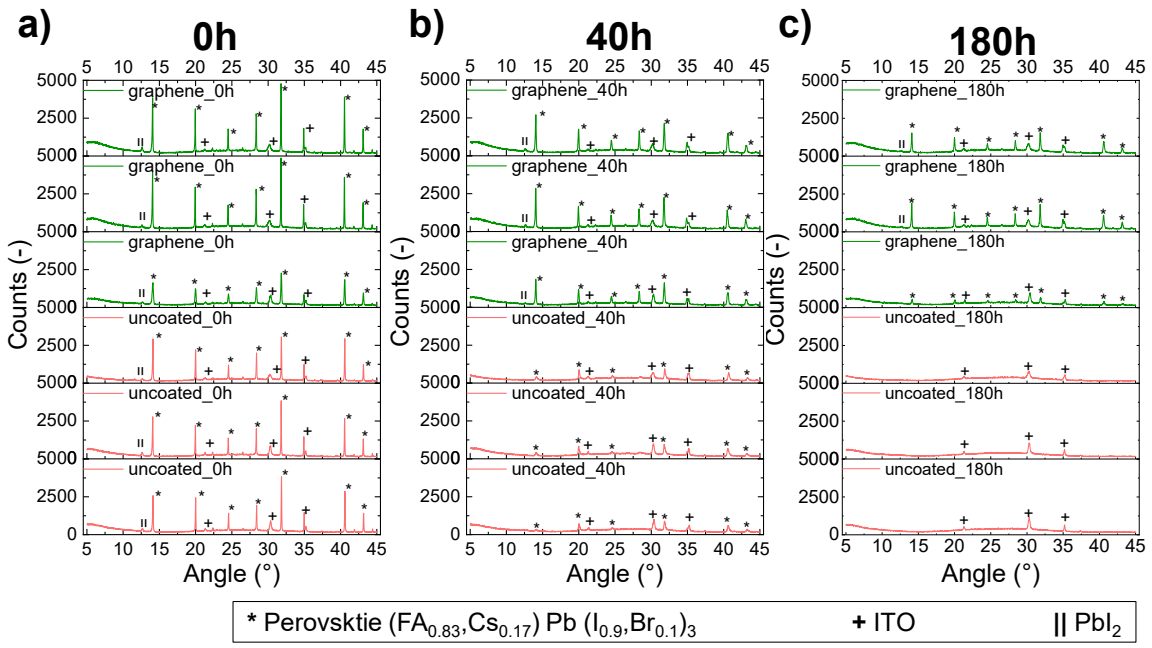



**Figure 5.24 Full-spectrum X-ray Diffraction of Aged Graphene Samples**

The X-ray Diffraction counts against 2 $\theta$ angle from 5 to 45° for three different graphene-coated and three uncoated perovskite films on ITO before ageing (a), after 40 h (b), and 180 h (c) of ageing at 85 °C, under 0.76 suns in ambient air. The peaks attributed to the $FA_{0.83}Cs_{0.17}Pb(I_{0.9},Br_{0.1})_3$ perovskite are indicated with a *, ITO-related peaks with +, and of $PbI_2$ by ||. All graphene films were produced and deposited by Dr Abhay Shivayogimath.

After 40 h of ageing the signal of all three uncoated samples approaches the noise floor (Figure 5.25b). The (1 0 0) peak in these samples was at only 357 to 438 counts compared to an average background signal of 210 counts. All coated samples, however, showed still clearly distinguishable peaks. The perovskite peaks in the samples with PCBM were lower than those without PCBM, with approximately 1,193 to 1,379 counts. The graphene-coated samples that showed signs of degradation before the start of ageing showed an increased 1 0 0 peak signal of 1,853 up from 1,633 before ageing. The other two graphene-coated samples again displayed very similar diffraction peaks with 2,707 and 2,855 counts. After 180 h of ageing the XRD signal of all uncoated samples and all samples with PCBM was at the noise floor showing no remaining perovskite peak (Figure 5.25c). The coated samples on the other hand showed 565 counts for the initially degraded sample and 1,539 and 1,886

counts for the other two. This is a remarkable ~48% of the signal in the pristine samples remaining after 180 h of 85 °C light ageing (Figure 5.25d).

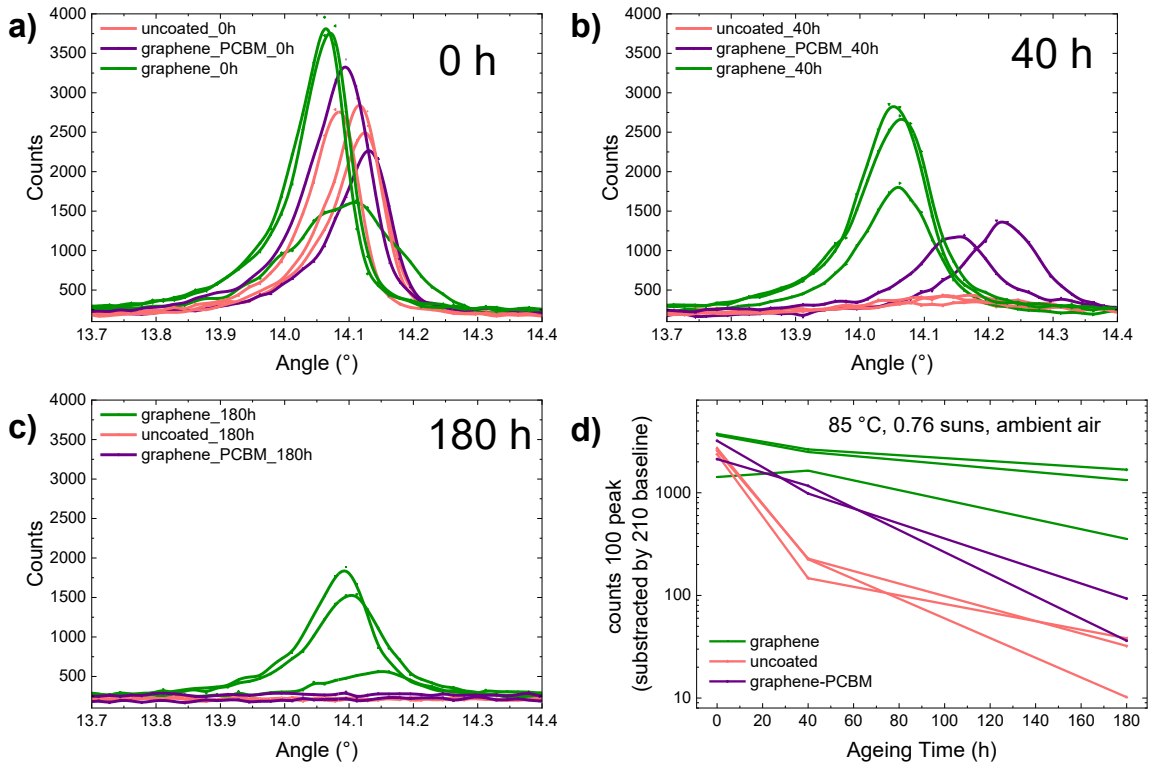



**Figure 5.25 X-ray Diffraction Graphene Ageing**

Counts around the (1 0 0) perovskite peak of samples with graphene encapsulation (green), perovskite/PCBM samples with graphene (purple), and unencapsulated samples (pink). The measurements were done before ageing (a), after 40 h (b), and 180 h (c) of ageing at 85 °C, under 0.76 suns in ambient air. (d) The maximum counts of peaks around 14.1° subtracted by 210 counts baseline against the ageing time on a logarithmic plot. All graphene films were produced and deposited by Dr Abhay Shivayogimath.

To display the change over the ageing period, the counts for each sample are plotted against the ageing time (Figure 5.25d). The counts were subtracted by the average baseline around the peak (208.9 counts) to show a peak approaching 0 above the noise floor in the graph. The graphene-coated samples without PCBM showed a much lower rate of degradation than all other samples. For both graphene-coated samples that showed normal behaviour at the start of the experiment, the counts were around 1,500, whereas the uncoated sample had less than 40 counts showing about three orders of magnitude higher retained perovskite signal.

The perovskite used was proposed and fitted by them to an orthorhombic (Pnma) crystal structure by Lin et al.[63] Consistent with Lin et al., I observe peak broadening accompanying the reduction in overall peak intensity. This observed broadening of the perovskite peaks can be explained by

increasing orthorhombic strain upon ageing.[63] The relative shift in observed peak positions can be caused by sample alignment errors when thin-film samples are not mounted perfectly flat. On substrates with crystallites in preferred crystallographic orientation, such misalignments can introduce apparent peak shifts on the order of the misalignment. This necessitates careful differentiation between intrinsic structural changes and artefacts induced by the experimental setup. I use the ITO substrate as an internal reference to assess a potential misalignment effect because it is fabricated to industrial standards and exhibits stable crystallographic peaks. I chose the (222) reflection of ITO, typically located at 30.34°,[215] as a marker because of its peak height and the absence of an overlap with perovskite peaks. However, the utility of this reference is limited by the relatively weak ITO signal, which is significantly reduced by the 500 nm-thick perovskite on top of it. As a result, the (222) ITO peak shows peak broadening and reduction of the signal close to the noise floor, complicating accurate peak position determination. I found positional deviations between –0.17° and +0.10° from the 30.34° angle, with an estimated uncertainty of ±0.3°. This is comparable in magnitude to the observed shift in the perovskite (100) peak, which varied by up to 0.17° within a single measurement series. However, correction of individual perovskite peak positions using the measured ITO deviations did not yield consistent alignment across the measurement series.

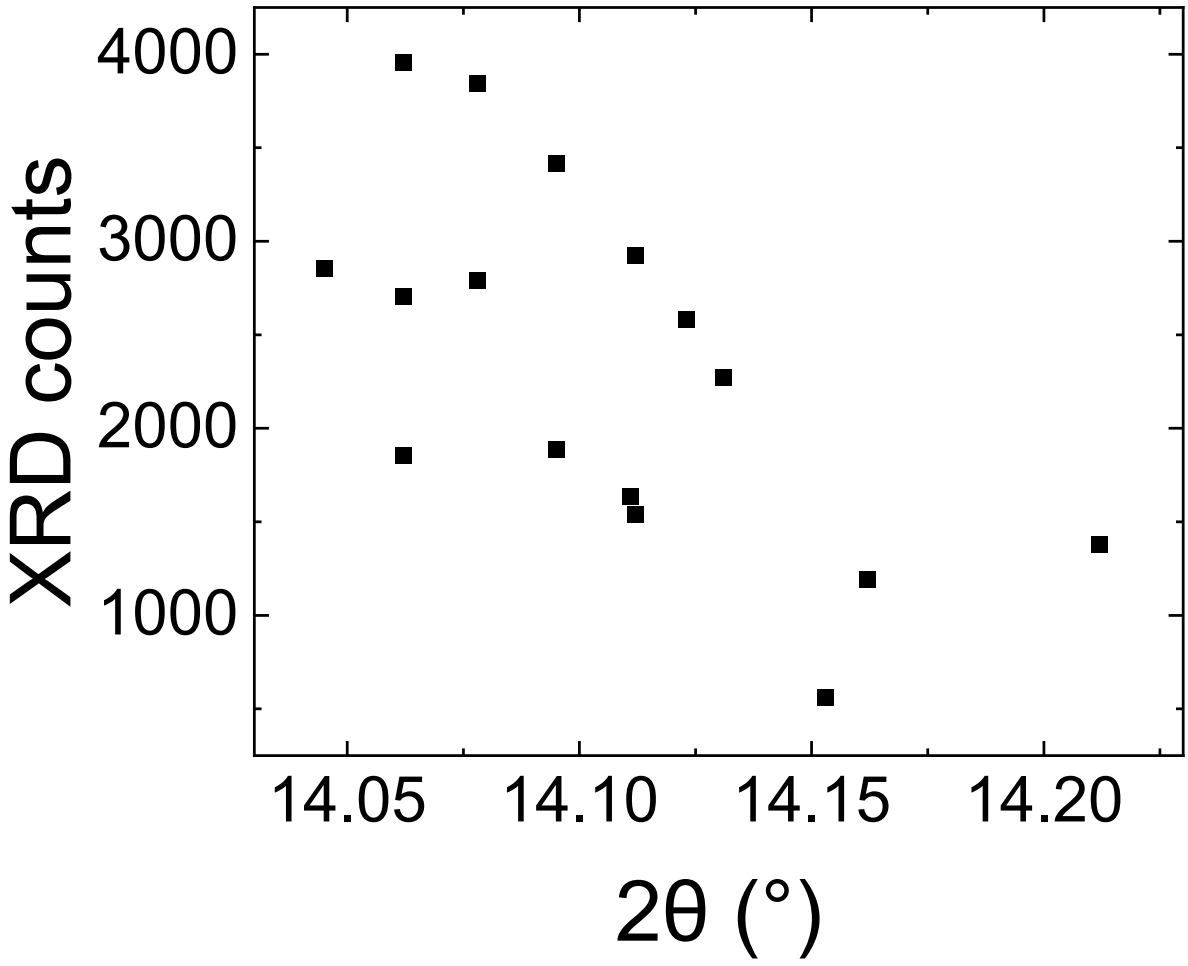



**Figure 5.26 Relation between Diffraction Signal and Peak Position**
The maximum counts and the peak position across all different samples and ageing times.

A reduction in the intensity of the 100 perovskite peak was correlated with a peak shift to higher 2θ angles for all samples (Figure 5.26). This consistent correlation suggests that the diffraction angle change is intrinsic rather than artefactual. The perovskite was deposited out of a precursor solution with 10% $Br^-$ and 90% $I^-$ relative to 101% $Pb^{2+}$. As mentioned, the total composition was $FA_{0.83}Cs_{0.17}Pb_{1.01}(I_{0.9}Br_{0.1})_3$. McMeeking et al. have reported for such a mixed $FA_{0.83}Cs_{0.17}$ perovskite a 100 of about 2θ ≈ 14.1° for bromide percentages of 0 – 10%.[62] For an increased bromide fraction, the peak shifts to up to 2θ ≈ 14.9° for 100% bromide. This trend reflects a reduction in the average unit cell size with increasing $Br^-$ content, consistent with the smaller ionic radius of $Br^-$ (1.96 Å) compared to $I^-$ (2.20 Å). This diffraction angle change indicates a decrease in the d spacing and has been fitted to a reduced cubic unit cell from a = 6.306 to a = 5.955 Å.[62,216] This behaviour follows Vegard's law, which states that the lattice constant varies linearly with the compositional ratio between the two components of the material.[217] The same kind of peak-shifting behaviour correlating to higher bromide and lower iodide content was also observed for other perovskites.[218] The peak shift

observed in conjunction with decreased signal intensity likely indicates a selective loss of iodide during ageing, effectively increasing the bromide content and leading to a contracted average lattice parameter in the remaining crystalline material.

Because of the much higher crystallinity maintained by graphene-coated samples and the correlation of better optical quality of the perovskite film in areas with intact graphene film, we conclude that there is a strongly improved perovskite stability due to the graphene lamination. This is likely due to both, retained volatile species in the perovskite film and the exclusion of oxygen and moisture from the films slowing down the degradation process. The lower stability of the coated samples containing a layer of PCBM is surprising. It has been reported that a PCBM coating improves the stability of the perovskite.[269-271] We conclude that the stability improvement of a well-laminated graphene layer hugely outweighs the advantage of the PCBM layer. Further, the graphene seems to better adhere to the perovskite than to the PCBM. This was also observed by Abhay Shivayogimath during the graphene lamination.

### 5.2.2 Implementation of Devices

The motivation for the graphene layer is to improve the stability of PSC. Because of the initial results on film stability in the previous chapter, a device integration of the graphene layer seemed more promising directly on top of the perovskite layer (Figure 5.21). Initially, the lamination process only allowed for substrate thicknesses of around one millimetre. Since our FTO substrates are much thicker than that (1.6 - 2.2 mm) and because of the initial success with films on ITO we did the first round of preliminary device integration of the graphene on ITO substrates. I coated polyTPD and perovskite as described in the Methods section. Subsequently, I sent the samples to Abhay Shivayogimath who laminated the graphene and sent them back to me. As references, three of the substrates were exposed to the graphene lamination environment (see comments in Table 4). These samples underwent the lamination process of heat press of the release layer foil of the graphene without graphene being loaded on the foil (see Graphene in Methods section). One further substrate was kept as a reference without being exposed to the lamination environment. Graphene was laminated on the remaining 11 substrates. Upon arrival in Oxford, the cells were completed with an ETL and gold electrodes.

Graphene coverage including all the wrinkles is crucial for good device performance because direct contact between gold and graphene would lead to internal shunting and increased recombination. Two different ETLs in direct contact were tested:

1. PCBM/BCP solution-processed via spin-coating
2. $C_{60}$/BCP via thermal evaporation

The second option was tested because the thermal evaporation process is known to lead to good conformal coverage on different surfaces. During the spin-coating for option one, I observed wetting issues of the graphene solution on the graphene leading to visible low uniformity of the PCBM on the graphene.

**Table 4 Samples First Graphene Batch**

| Sample ID | Type | Transferred | Comments | ETL | Median Efficiency |
|---|---|---|---|---|---|
| E1BD | control | none | control sample, no transfer, exposed to ambient transfers (~50 mins, humidity 50%, temp 22 °C) | PCBM | 17.8% |
| E1C2 | ref | reference | no graphene (effect of polymer/transfer process/ambient exposure) | C60 | 0.1% |
| ~~E1CE~~ | ~~ref~~ | ~~reference~~ | ~~batch 2, no graphene (effect of polymer/transfer process/ambient exposure)~~ | ~~PCBM~~ | ~~lost~~ |
| E1BB | ref | reference | batch 2, no graphene (effect of polymer/transfer process/ambient exposure) | PCBM | 16.7% |
| E1C1 | sample | graphene | batch 1, GR ID - QCF2B3BOT. | C60 | 0.1% |
| E1C0 | sample | graphene | batch 1, GR ID - QCF2B2BOT | C60 | 0.0% |
| E1BF | sample | graphene | batch 1, GR ID - QCF2B2BOT | C60 | 0.0% |
| E1BE | sample | graphene | batch 1, GR ID - QCFB | PCBM | 10.7% |
| E1BC | sample | graphene | batch 1, GR ID - QCFB | PCBM | 10.7% |

| | | | | | |
|---|---|---|---|---|---|
| E1B9 | sample | graphene | batch 1, GR ID - QCFB | PCBM | 13.4% |
| E1BA | sample | graphene | batch 1, GR ID - QCF2F | PCBM | 3.9% |
| E1B8 | sample | graphene | batch 1, GR ID - QCF2F | PCBM | 3.7% |
| E1CC | sample | graphene | batch 2, GR ID - QCF3B | PCBM | 1.2% |
| E1CB | sample | graphene | batch 2, GR ID - GG1003L | PCBM | 2.0% |
| E1CD | sample | graphene | batch 2, GR ID - GG1003L | PCBM | 1.0% |

Completed pristine devices showed a low shunt and series resistance in both light and dark *JV* curves (red curves in Figure 5.27d). The *JV* curve in the dark showed a strong deviation from the horizontal $J_0$. The $J_{SC}$ of a lot of the PCBM-based devices was unusually high for the perovskite absorber used. Because graphene is relatively conductive, I anticipated a lateral shunting between different devices and between the anode and cathode on the substrate (Figure 5.27c). This was confirmed by scratching around each of the six devices on the substrate isolating their respective back electrodes from each other and the common ground (Figure 5.27). This scratching procedure resolved the low shunt and series resistance leading to a more ideal *JV* behaviour (blue curves in Figure 5.27d). This was also visible in the MPPT performance of PCBM-based graphene devices more than doubling from a median of 3.9% to 9.5% and the champion device improving from 12.7% to 16.6% (Figure 5.27e).

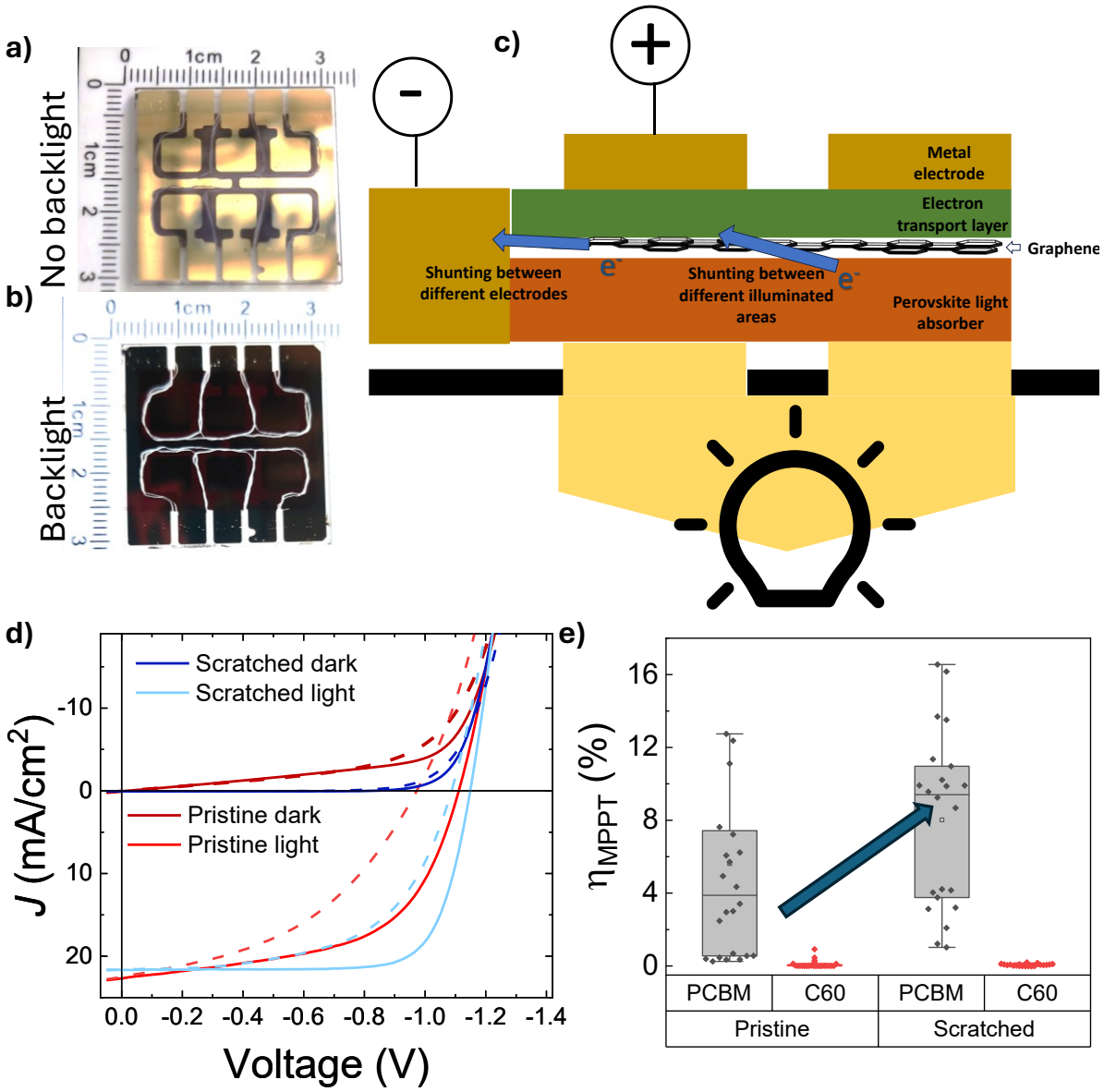



**Figure 5.27 Lateral Shunting Issues in Graphene Devices**

Substrates with scratch lines without a backlight (a) and with a backlight (b). (c) The fabricated device's structure under illumination indicating the presumed reason for the *JV* behaviour of pristine devices. (d) *JV* results of the first devices with integrated graphene layer between perovskite and PCBM. Pristine devices (red line) showed low shunt and series resistance and unusually high $J_{SC}$. The same device showed a much-improved *JV* behaviour when the different devices on the substrate were isolated by removing material between them by mechanical scratching (blue curves). (e) MPPT performance of pristine and scratched devices with a PCBM solution process-based ETL and a C60 thermal evaporation-based ETL. All graphene films were produced and deposited by Dr Abhay Shivayogimath.

Notably, while some PCBM devices performed well after the scratching, $C_{60}$ devices showed 0% MPPT performance. The performance was equally low for devices with and without graphene (Figure 5.28a). All $C_{60}$-based references and graphene devices showed zero $J_{SC}$ and an FF of around 0.25. The $C_{60}$ references, however, were able to output voltages of around 1.0 V and showed little hysteresis while the $C_{60}$ graphene devices showed severe hysteresis and a median $V_{OC}$ of 0.4 V

(Figure 5.28). The PCBM reference without graphene (Pref) showed a normal MPPT of up to 18.2% as expected for this stack. The reference devices with $C_{60}$ are all substrate E1C2 exposed to the lamination environment (see comments in Table 4). For the Pref, one device was exposed to the lamination environment (E1BB) while the other one was not (E1BD). The one without exposure performed slightly better and showed less spread in MPPT performance (Figure 5.29). The PCBM-graphene devices (Pgra) showed a much wider spread of MPPT performance with some of the substrates showing for all six devices on them only < 4%.

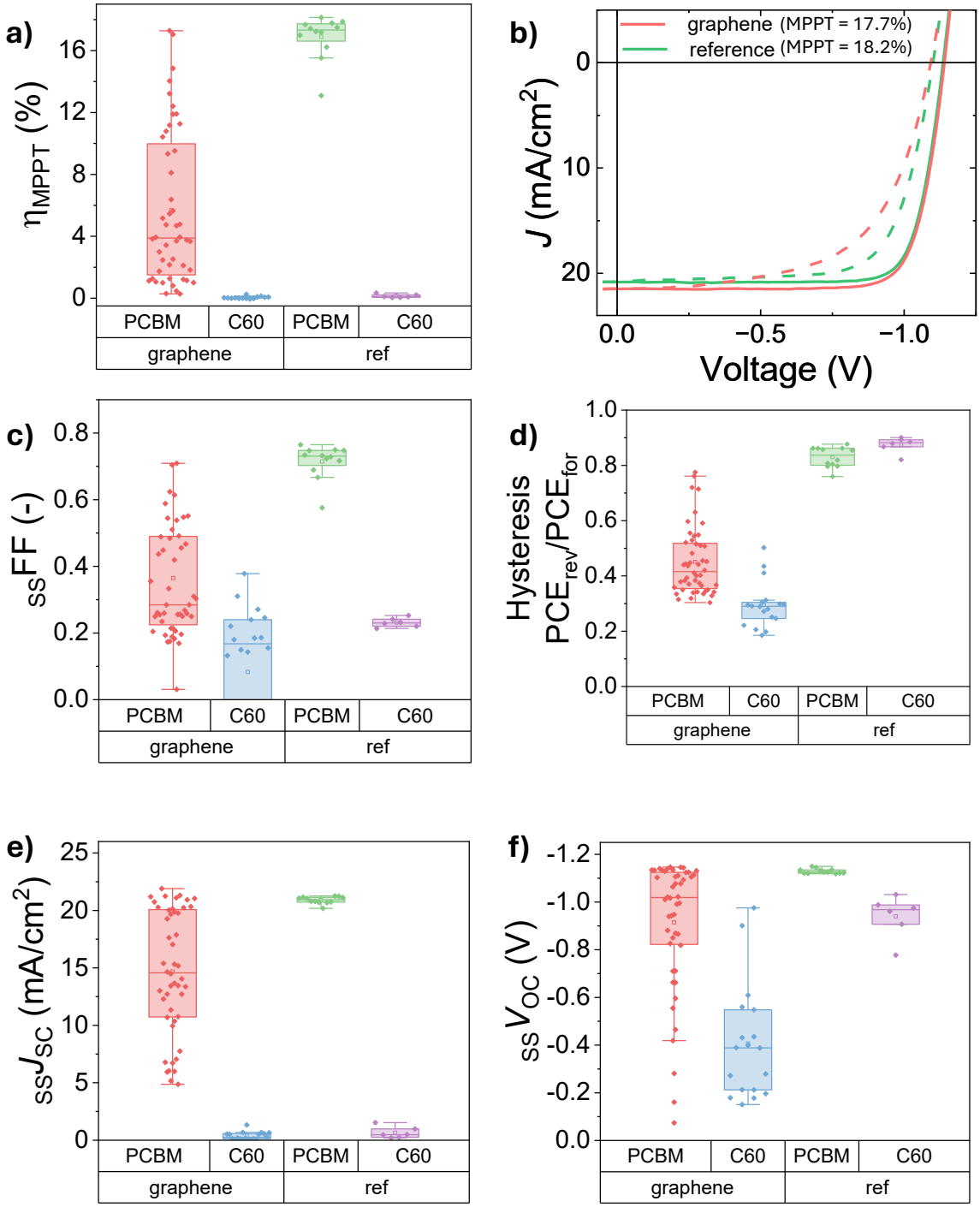



**Figure 5.28 Device Parameters First Batch Graphene**

(a) Maximum Power Point Tracked (MPPT) efficiencies of devices with graphene and without (ref) with solution-processed PCBM or thermally evaporated $C_{60}$ as ETL. (b) The Current Density-Voltage curves of the champion PCBM devices with and without graphene. The solid and dashed lines represent forward and reverse scan of a device. Device parameters of the same devices as in (a) with the stabilised Fill Factor (c), Hysteresis (d), stabilised $J_{SC}$ (e), and stabilised $V_{OC}$ (f). All graphene films were produced and deposited by Dr Abhay Shivayogimath.

Pgra champion displays, besides larger hysteresis, a similar *JV* behaviour to the Pref champion (Figure 5.28b). Statistically, Pgra shows a lower $_{SS}FF$ with a larger spread (Figure 5.28c). This is

consistent with the larger hysteresis in these devices leading to a median hysteresis factor of about 0.42 for Pgra and 0.84 for Pref, with 1.0 being an ideal, hysteresis-free device. Pgra also showed a larger spread in $_{ss}J_{SC}$ and $_{ss}V_{OC}$ than Pref. While the median $_{ss}V_{OC}$ was similar with 1.02 V for Pgra and 1.13 V for Pref, the median $_{ss}J_{SC}$ was with 14.6 mA/cm$^2$ considerably lower in Pgra than in Pref, which showed 21.1 mA/cm$^2$. However, the Pgraph champion devices showed higher $_{ss}J_{SC}$ values of up to 29.1 mA/cm$^2$ than Pref at 21.3 mA/cm$^2$ (Figure 5.28b and e).

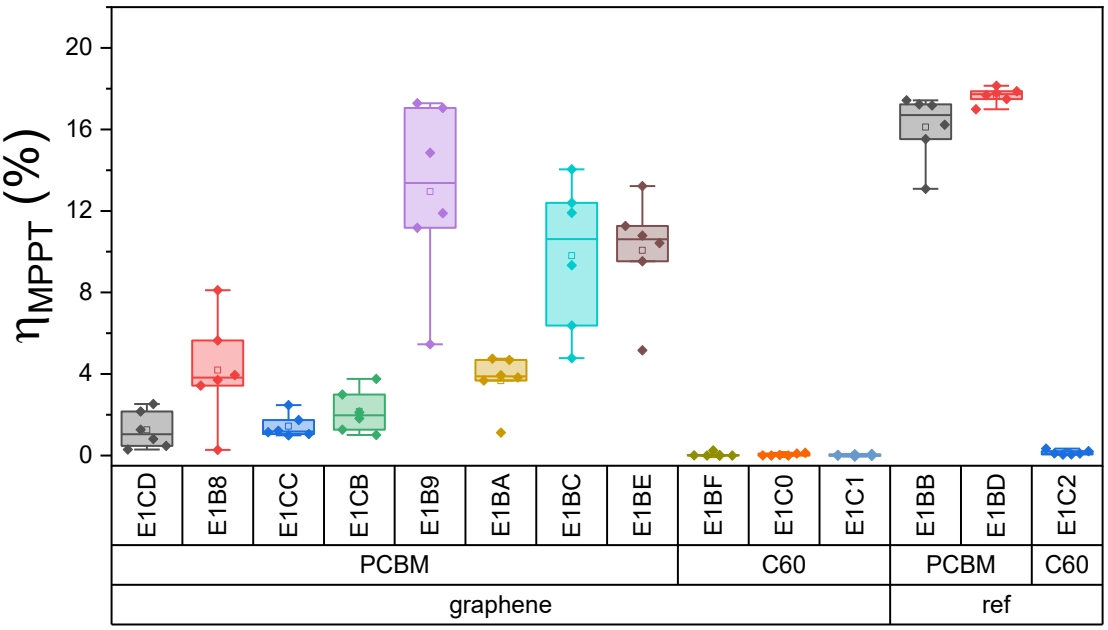



**Figure 5.29 Performance of Devices on each Substrate - First Batch Graphene**

The best Pgra performed similarly to the best Pref with the champion reaching 17.7% and 18.2% MPPT. All graphene films were produced and deposited by Dr Abhay Shivayogimath.

Because both graphene and reference devices with $C_{60}$ showed very poor performance we can rule out graphene to be the only problem in these devices. It is a known problem that when graphene is transferred off a release layer, there might be residuals of the polymers used around the graphene.[221,222] The resulting upper part of a PSC if residuals would remain on the graphene is shown in (Figure 5.30a). We assume the problem in $C_{60}$ devices to be with incompatibility of the evaporated $C_{60}$ with the remnants of the PDMS release layer used to deposit the graphene (see Graphene in Methods section). Since the Pref device that was exposed to the blank lamination process did show only a slightly reduced performance compared to the one that was not, we conclude that the PDMS does not pose a problem when PCBM is solution-processed on top. The problem might not occur to a catastrophic extent in PCBM devices because of the annealed annealing step of 5 min at 100 °C involved in the spin-coating procedure (see PCBM in Methods section). It has been shown, that

annealing can partially remove polymers from graphene layers increasing the conductivity. However, because of chemisorption residues of the polymer tend to remain on the graphene.[222] Annealing can further smooth the surface of the graphene.[223]

To investigate the possible problem of wrinkles, Dr Abhay Shivayogimath provided previous AFM measurements of transferred graphene films on silicon substrates. The AFM measurement shows wrinkles of up to 6 nm. Because of the thickness of the PCBM and $C_{60}$ of around 20 nm, we do not assume wrinkles of this height to cause severe problems to the device (Figure 5.30b). To explore the observed wetting issues of PCBM on graphene, Dr Abhay Shivayogimath performed contact angle measurements of water and diiodide-methane on top of PCBM and graphene (Figure 5.30c). Based on the very similar wetting angles we conclude that the coverage of PCBM is less likely to be the biggest underlying problem. Instead of wrinkles on top of the graphene or wetting issues on it, we hypothesise that voids between perovskite and graphene lead to a reduced contact area between the two of them. This would be consistent with the reduced FF being the biggest contributor to spread and performance loss in Pgra devices.

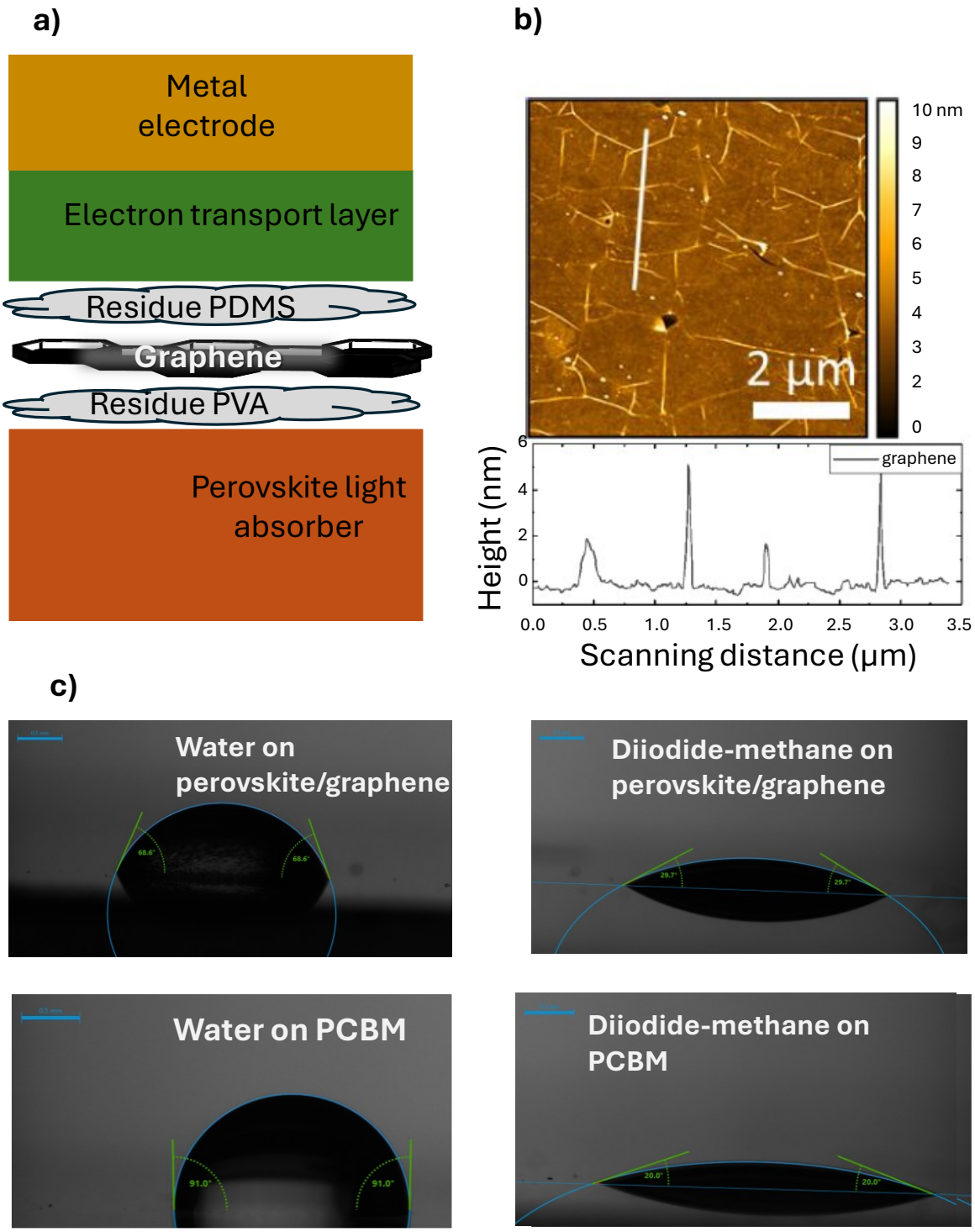



**Figure 5.30 Polymer Residues and Atomic Force Microscopy**

(a) The upper part of a device stack of a perovskite solar cell with the position of the graphene layer and the position of possible residues from the Polyvinyl Alcohol (PVA) protective and Polydimethylsiloxane (PDMS) release layer. (b) Atomic Force Microscopy (AFM) measurements on a graphene sheet show the height of the wrinkles of the as-deposited film. (c) Wetting angles of water and diiodide-methane on the graphene layer of an ITO/perovskite/graphene stack and on PCBM. All graphene deposition and measurements displayed here were performed by Dr Abhay Shivayogimath.

# 6 SUSTAINABLE ELECTRODE MATERIALS

In this chapter, I present results on how to universally stabilise PSC using non-noble metals as a back electrode by inserting a 5 nm thick evaporated Cr layer below. Further, I show the first side-by-side stability comparison of PSC with the two most common transparent electrode materials FTO and ITO. The details for all ageing studies in this chapter are listed in Table 5.

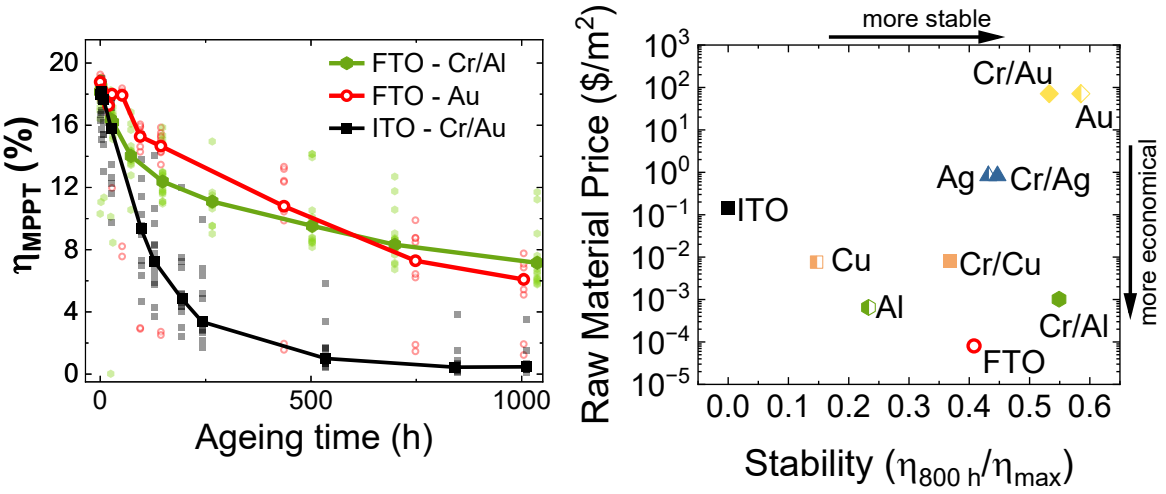



**Figure 6.1 Overview Sustainable Electrodes**

(a) The ageing behaviour of 24 devices with Cr/Al electrodes on FTO substrates was compared to 12 devices with Au electrodes on FTO and 12 Cr/Au on ITO substrates. The efficiencies were obtained via maximum power point tracking and devices were aged under 0.76 sun equivalent illumination at 85 °C. The three categories were aged in the same ageing box in overlapping intervals. The bold continuous lines and large symbols indicate the median of efficiencies. Smaller semi-transparent symbols show the performance of all devices of each category. Red circles represent the device data of FTO-based devices with Au electrodes, green octagons of FTO devices with Cr/Al and black squares represent the data of ITO-based Cr/Au devices. (b) Different opaque and transparent electrode materials are plotted according to the price of the metal raw materials contained in 1 $m^2$ of the electrodes prepared against the ratio of the maximum median efficiencies against the median efficiency after 800 h of heat-light ageing of PSC with these electrodes. The transparent electrodes ITO and FTO were aged with Cr/Au back electrodes in a separate study from the different metal electrodes which were all aged with ITO transparent electrodes. I calculated the metal raw material prices based on market prices and the volume bound in 1 $m^2$ of an electrode as used in a laboratory scale device. For ITO and FTO I only considered the prices of the Sn and In bound in the film as calculated by Wagner et al.[172] Preparation costs were not included.

## 6.1 Motivation

While perovskite solar cells (PSC) have shown a strong increase in efficiencies in the past decade, it is important to ensure devices maintain high efficiencies throughout suitable lifetimes. In this

chapter, I show how to prolong the lifetime of PSC by choosing materials for both the opaque back and transparent front electrodes.

As opaque back electrodes, evaporated Au electrodes are commonly used as a stable solution. Au is, however, unsuitable for industrial applications because of its high cost. Meanwhile, devices with cheaper, less noble metals have been considered too unstable (see Electrode Materials and Stability Issues). I introduce a 5 nm Cr interlayer beneath Cu, Ag, or Al electrodes to overcome this issue. The Cr interlayer provides a scalable solution addressing the instability of low-cost metals in PSCs, addressing a long-standing concern about commercialisation. It enables the use of these base metals as electrodes by strongly enhancing their stability in devices making them a viable alternative to Au. Devices with Cr/Al electrodes showed comparable stability to those with Au while being five orders of magnitude more cost-effective.

Further, I reveal a large difference in stability between transparent electrodes made of the most commonly used transparent conductive oxide, indium tin oxide (ITO), and fluorine-doped tin oxide (FTO) electrodes. While ITO-based devices degrade quickly within hours, FTO-based PSCs were significantly more stable, maintaining higher performance across ageing conditions at 25, 65, and 85 °C under continuous full-spectrum illumination. Our results showed a stronger relative decrease in photoluminescence quantum yield and charge carrier lifetimes of perovskite films and half-stacks aged on ITO compared to those aged on FTO substrates. Time-of-flight secondary ion mass spectrometry (TOF-SIMS) further shows the presence of significant amounts of $In^{3+}$ ions throughout the perovskite layers in aged and fresh ITO-based devices. Deliberately adding $In^{3+}$ to perovskite layers in FTO-based devices replicates the degradation behaviour observed in ITO-based devices.

To unify the results, I tested devices with Cr/Al bilayers on FTO substrates. These devices demonstrated exceptional stability across different laboratories. Champion devices retained over 66% of their initial efficiency after 1037 hours of ageing at 85 °C under full-spectrum illumination. These findings highlight the critical role of substrate and electrode material choice in the development of durable and scalable PSCs. These findings have more general implications for stable and cost-effective transparent and opaque electrode materials suitable for high-temperature halogenating environments.

## 6.2 Introduction

As discussed in the Chapter 22.5 on Stability Challenges, addressing instabilities in PSCs is important to ensuring long-term operational reliability and sustained emission-free electricity generation. While carbon electrodes, as discussed in Chapter 4, offer a stable back-contact solution for n-i-p devices, most PSCs rely on metal electrodes. However, comparative stability studies of different metal electrodes under realistic operating conditions remain limited. Most stability proofs on a laboratory scale still use Au electrodes. These electrodes can damage the perovskite as described in detail in Metal Ion Diffusion above. Kaltenbrunner et al.[48] used a thin layer of $Cr/Cr_2O_3$ under Au electrodes to improve the stability and performance of flexible PSC containing a gold back electrode. Domanski et al. show that such a $Cr/Cr_2O_3$ layer prevents gold migration and improves stability.[71] Yet, Au remains too expensive for industrial applications. Cu, Ag, and Al are low-cost alternatives to Au but suffer from rapid degradation due to metal halide reactions (see chapter 2.5.2.1 Metal Halide Formation). In this chapter, I explore three questions:

1. "How do PSCs with different industrial metal electrodes degrade under realistic operational conditions?"
2. "Can a $Cr/Cr_2O_3$ interlayer improve metal electrode stability across different metals?"
3. "How does the choice of transparent electrode affect PSC stability?"

The $Cr/Cr_2O_3$ is assessed due to its exceptional chemical and thermal stability, which enables its use as a protective layer in stainless steel applications.[224] A further advantage of this layer is that it can be processed in the same evaporator in one process step with the rest of the metal electrode. No extra vacuum deposition step is needed as opposed to, for example sputtered ITO as a buffer layer. This can save time and machinery for industrial production of PSC.

There are several studies on the chemical and thermal instability of ITO,[125,127] as described in detail in the chapter 2.5.2.3 Metal Oxide Instabilities. However, similar to metal electrodes there is a lack of comparative studies between different transparent electrodes. To investigate the questions above I present a comprehensive stability study using positive-intrinsic-negative (p-i-n) architecture comparing otherwise identical device stacks with different opaque back- and transparent front electrodes. All devices were aged at elevated substrate temperatures between 50 °C and 85 °C, 0.76

- 1.0 sun, full spectrum, and in ambient air. The 50-85°C range was chosen based on real-world conditions, where solar panels can reach these temperatures under direct sunlight. As a bias condition, I applied $V_{OC}$ based on industry standards. This ensures a realistic assessment of thermal stability while accelerating degradation for practical testing timescales (as described in Chapter 2 Background). The chosen range allows direct comparison with existing PV technologies and reflects expected operational stress.

I show that the cheaper industrial metals Cu and Al cause even more and quicker degradation than Ag. Further, I find that a nano-layer of Cr as proposed by Kaltenbrunner et al.[48] and Domanski et al.[71] can be used universally beneath other electrodes than Au including the less noble metals like Ag, Cu, and Al. The Cr layer improves the stability of all three less noble metals majorly with Cr/Al even exceeding the stability of Au electrodes. However, I did not observe the previously reported stability improvement of Cr/Au over Au.

Finally, I show that devices with an FTO instead of an ITO transparent electrode show a considerably lower degradation speed. These findings provide pathways toward improving the stability of cost-effective electrode materials for PSCs and other optoelectronic devices. My findings address key challenges in PSCs and have broader implications for electrode stability under light and heat exposure and in halogen-rich environments. These insights can help to improve the longevity and cost-effectiveness of transparent and opaque electrode materials, such as ITO and Al, widely used in devices beyond solar cells.

## 6.3 Results

### 6.3.1 Stability of Cr/Ag Electrodes

To investigate the effect of different opaque electrode materials, I fabricated identical p-i-n devices of a layer stack of FTO/polyTPD/$FA_{0.83}Cs_{0.17}Pb_{1.00}I_{2.7}Br_{0.3}$/PCBM/BCP (see Figure 6.2a and Device Fabrication for details). I use this layer stack because of its known long-term stability as reported by Lin et al.[63] and because I can achieve good reproducibility, using this stack on different substrates and with different back electrode materials.

I investigate the stability of these devices with a Cr/Ag or a Cr/Au bilayer with thicknesses of 5 and 100 nm respectively or devices with just 100 nm Ag electrodes in a mild thermal ageing test at 85 °C without light exposure in an $N_2$ atmosphere (unencapsulated). After 20,000 h of thermal ageing Cr/Ag devices performed significantly higher than Ag devices (Figure 6.2b). Further, in Cr/Ag devices the electrodes looked less degraded (more silver reflective) on the top and the perovskite layer also looked darker. By contrast in Ag devices both the electrode and the perovskite layer showed strong visible signs of degradation (Figure 6.3).

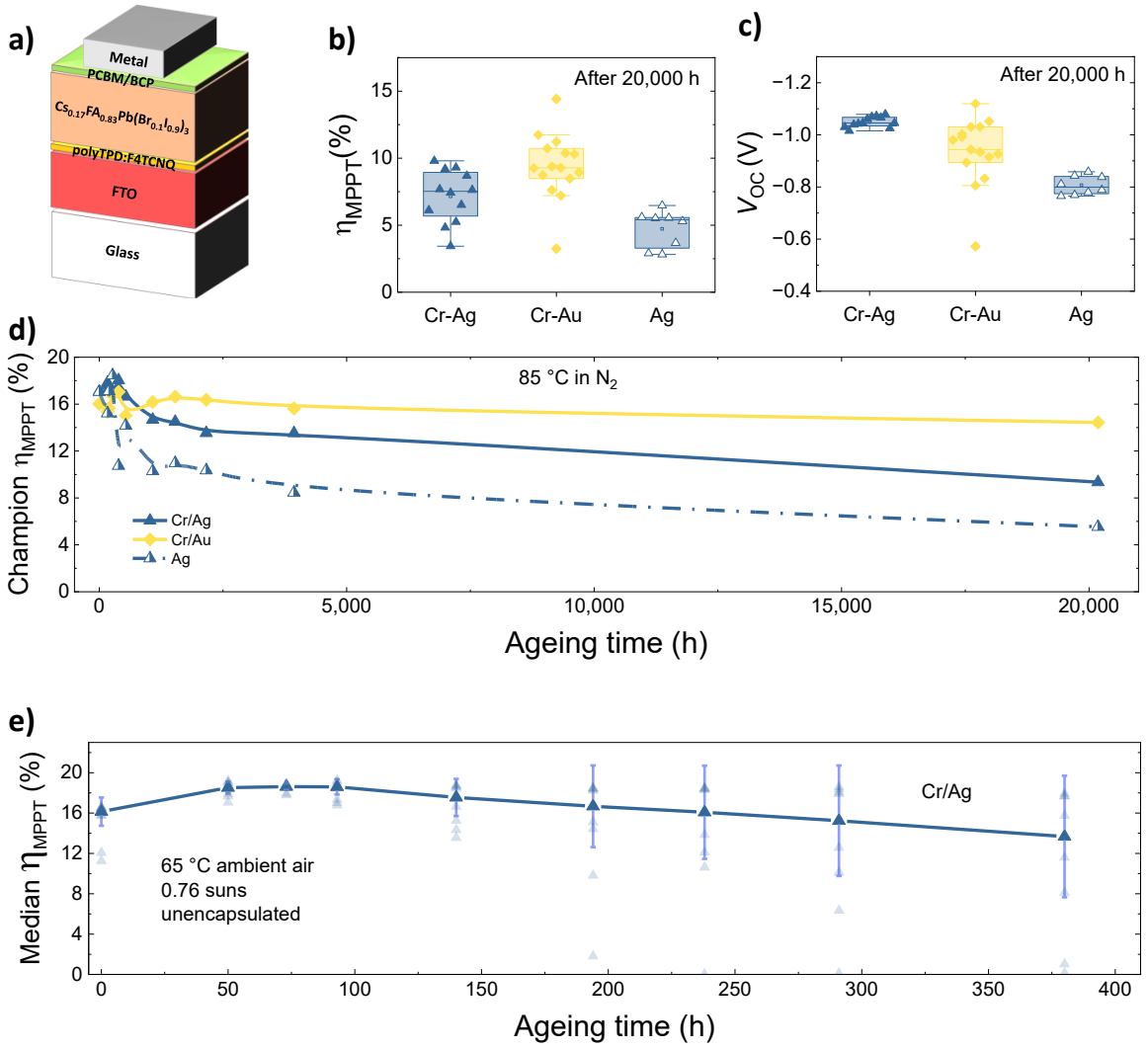



**Figure 6.2 Initial Cr/Ag stability results**

(a) The used device stack in the experiments. (b) and (c) show the statistics of MPPT efficiency and stabilised $V_{OC}$ respectively of all devices of each group with Cr/Ag, Cr/Au, and Ag electrodes after being aged at 85 °C in a dark $N_2$ environment for 20,000 h. (d) MPPT efficiency performance of the device performing best after 20,000 h out of the three categories during the 20,000 h of ageing. (e) Maximum power point tracked (MPPT efficiency) performance of devices with a Cr/Ag electrode over time when aged unencapsulated at 65 °C under 0.76 suns in ambient air. The error bars indicate the standard deviation, the solid line the median MPPT efficiency and the blue transparent triangles the MPPT efficiency of each individual device.

A major reason for the higher stability of Cr/Ag devices was the retention of open circuit voltage (Figure 6.2c) with all devices of this category still outputting over 1 V after 20,000 h while all Ag electrode devices had a $V_{OC}$ of ~0.8 V (Figure 6.2c). As shown in Figure 6.2d, the champion Cr/Ag device still performed with 9.4% MPPT efficiency (more than 50% of its maximum performance) while the champion Ag device had dropped to 5.5% (30% of its maximum performance). Both electrode configurations were however less stable than the champion Cr/Au electrode which maintained 85% of its maximum performance for 20,000 h.

Notable high stability was also found when ageing Cr/Ag devices unencapsulated at 65 °C under 0.76 suns in ambient air (Figure 6.2e). The best Cr/Ag device performed at 18.0% (97% of its maximum performance) after 380 h under heat-light ageing. Since Ag devices without the Cr layer are too unstable under this heat-light ageing condition in ambient air, I could not compare the stability of devices with Cr/Ag and Ag electrodes unencapsulated.

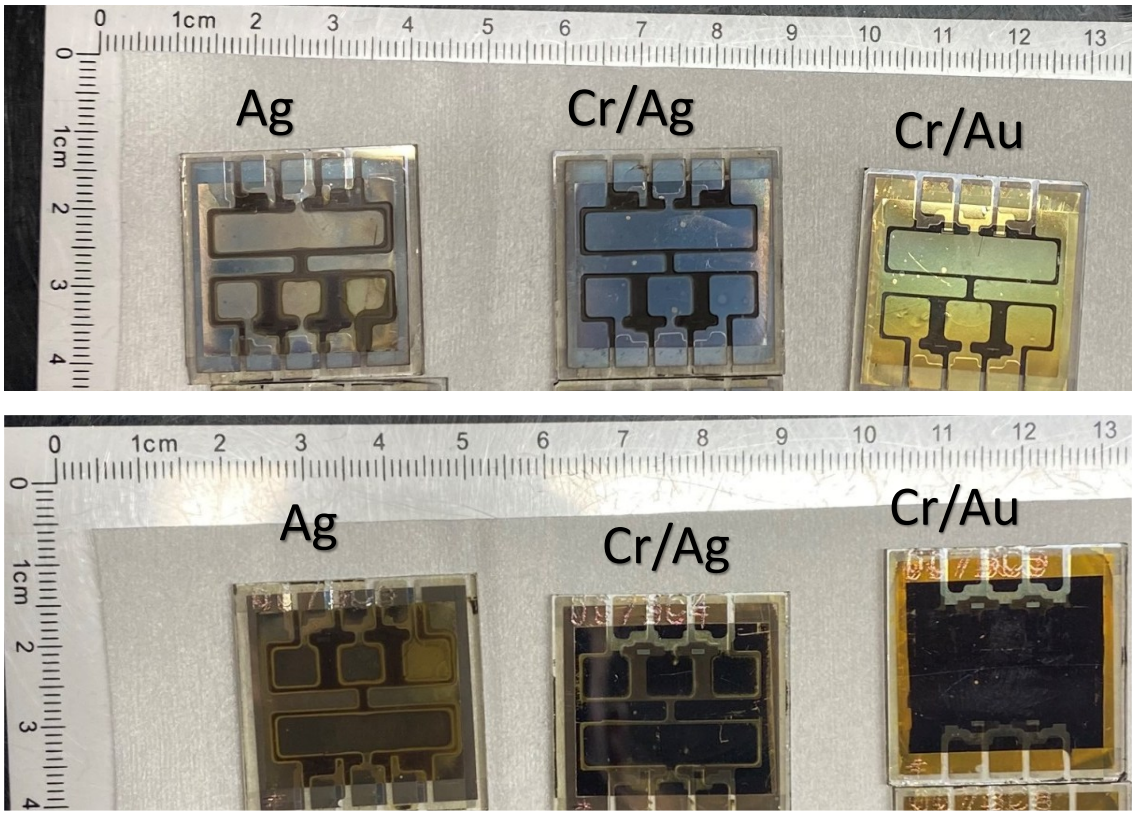



**Figure 6.3 Cr Metal Devices aged in Nitrogen**

Photos of the front and back of representative devices with an Ag, Cr/Ag, and Cr/Au electrode are shown after 20,000 h of ageing at 85 °C unencapsulated in a dark $N_2$ atmosphere. Cr devices had 5 nm of Cr evaporated before the Ag or Au was evaporated.

**Table 5 Overview ageing studies**

| Parameter | Light Source | Target Temp. | Temperature Control | Atmo-sphere | Encapsulation | Devices per parameter | Figures |
|---|---|---|---|---|---|---|---|
| Cr vs none<br>Au, Ag, Al, Cu | Sulphur lamp | 50 - 65 °C<br>(on substrate backside) | Fans (and ambient thermometer) | Ambient Air | $MoO_3$ and Glass coverslip with epoxy | 12 - 18 | Figure 6.9 |
| FTO vs ITO | Xenon lamp | 65 °C (black standard temperature) | Fans | Ambient Air | Glass coverslip with edge epoxy | 14 ITO, 16 FTO | Figure 6.19a |
| FTO vs ITO | LED three-colour growing lamp | 60 - 70 °C | Infrared oven with a metal plate | $N_2$ | PMMA | 1 substrate | Figure 6.19b-c,<br>Figure 6.20<br>Figure 6.21 |
| FTO vs ITO | LED three-colour growing lamp | 25 °C | Peltier cooler and fans | Ambient Air | Glass coverslip with edge epoxy | 15 ITO, 14 FTO | Figure 6.16 |
| Indium Iodide added | Xenon lamp | 85 °C (black standard temperature) | Fans | Ambient Air | Glass coverslip with full-area epoxy | 12 - 18 | Figure 6.22e |
| Cr/Al vs Au<br>ITO vs FTO<br>Cr thickness | Xenon lamp | 85 °C (black standard temperature) | Fans | Ambient Air | Glass coverslip with full-area epoxy | 12 - 24 | Figure 6.24 and<br>Figure 6.23 |
| Cr/Ag vs Cr/Au vs Ag | None | 85 °C | Infrared oven with a metal plate | $N_2$ | None | 8 - 16 | Figure 6.3 and<br>Figure 6.2 |

### 6.3.2 General Stability of Cr Metal Bilayers

To explore if the Cr nano-layer works with other less-noble metals I extended the investigation from Ag to also include Cu and Al electrodes. These two industrial base metals are chosen due to their cost-effectiveness, abundance, excellent conductivity, lighter weight, and recyclability. I fabricated devices identical in all aspects except their back electrodes using Au, Ag, Al, and Cu, with and without a Cr layer. Dr Markus Kohlstädt provided help with the deposition of the different metals and performed the encapsulation of the devices. The same device structure as for the Cr/Ag devices above was used, with the only difference being a change from FTO to ITO to obtain slightly higher performance because of the higher transparency of the latter (Figure 6.9a). All the devices were manufactured in laboratories at the Fraunhofer ISE in Freiburg, Germany. In pristine devices, there was no major difference in device performance for either of the different metal electrodes all performing with PCEs of up to 20% (Figure 6.4a). Current-voltage scans of the champion devices with various electrodes showed little difference (Figure 6.4b).

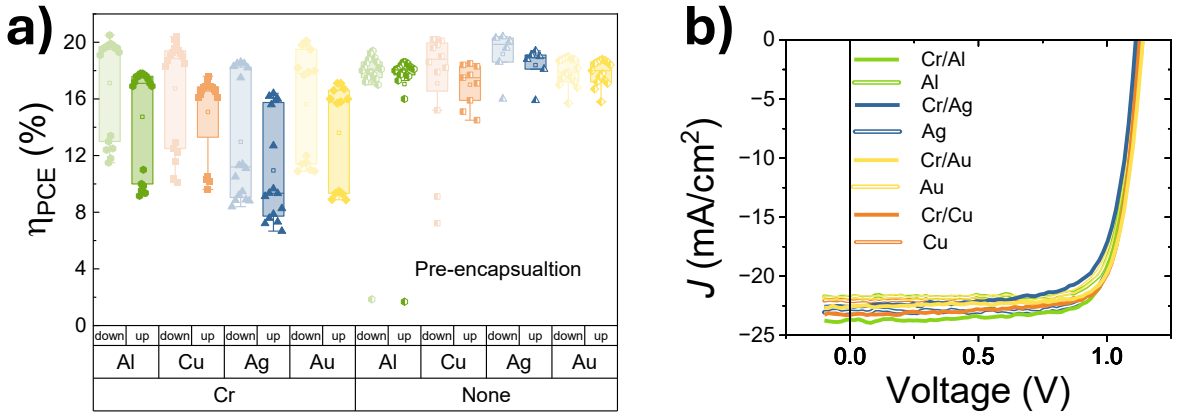



**Figure 6.4 Pre-Ageing Behaviour of Different Metal Electrodes**

(a) *JV* scan derived PCE values for both scan directions for different metal electrodes with and without the Cr layer before encapsulation and ageing. (b) *JV* down sweeps for the champion device of each category. The metal electrode deposition for the devices was performed with the help of Dr Markus Kohlstädt.

Devices with a chrome buffer layer, however, showed a wider spread of performance and a slightly increased hysteresis compared to non-Cr counterparts (Figure 6.4a and Figure 6.5). The spread of Cr-containing devices was in the form of a bimodal distribution with two clusters of devices in terms of their performance. The lower performing cluster of devices performing around 8 – 13% and the higher performing cluster contained devices with PCES between 16 and 21% for both scans. More

than half of Cr/Ag devices fell into the lower-performing-cluster. Therefore the median PCE Cr/Ag fell within the cluster of low-performing devices at ~10% (Figure 6.4a and Table 6).

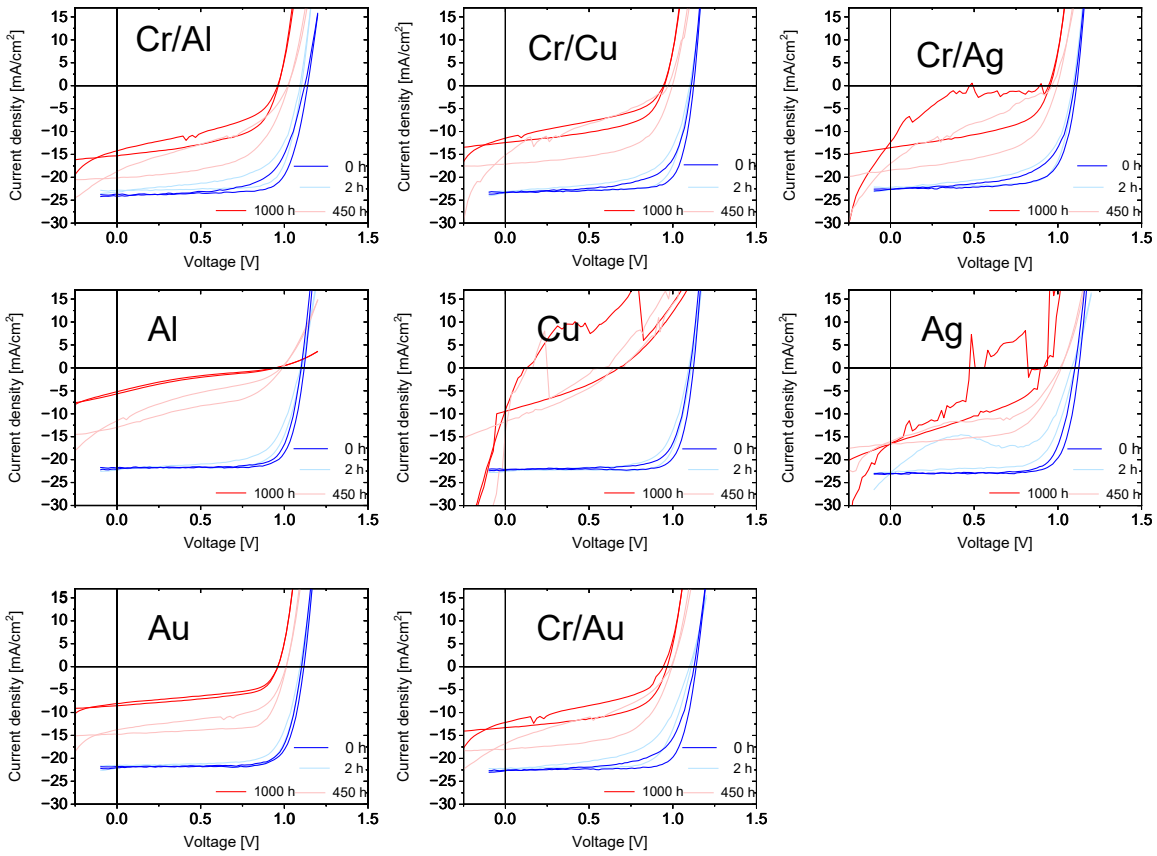



**Figure 6.5 *JV* scans Cr/metal ageing**

Current-voltage (JV) sweeps for the devices performing best at the start of the ageing are shown for all eight back electrode variations. The scans for 0 h, 2 h, 450 h, and 1000 h of ageing are coloured in dark blue, light blue, light red, and dark red in this order. The two lines of the same colour represent forward and reverse scan on the same device

Because PSCs show a hysteresis between different sweep directions for current-voltage scans on a device, this needs to be taken into account when working with PCE data from such scans. When PCE values from scans were used, I took an average of all scans, including both scan directions to get a value closer to the steady-state efficiency of the devices in each group. To assess the extent of hysteresis in a device a hysteresis index can be used.[225] I calculated the hysteresis index as the ratio of the PCE of the up to down sweep:

$$hysteresis\ index = \frac{PCE_{up}}{PCE_{down}} = \frac{PCE_{forward}}{PCE_{reverse}} \qquad 6.1$$

with a value of 1.00 indicating no hysteresis between the scan directions. For devices without a Cr layer, the hysteresis index was 0.97, indicating minimal hysteresis in those devices (Figure 6.6). On

the other hand, devices with a Cr layer displayed a much larger hysteresis exemplified by a lower hysteresis index of 0.85. Devices without a Cr layer showed much more frequent connection issues during the measurement than devices with Cr devices. For approximately 27% of the devices without Cr, one or two scans needed to be excluded due to contact issues, shunting, or device failures that led to inconsistent or non-representative measurements. This occurred in only 15% of devices with the Cr interlayer.

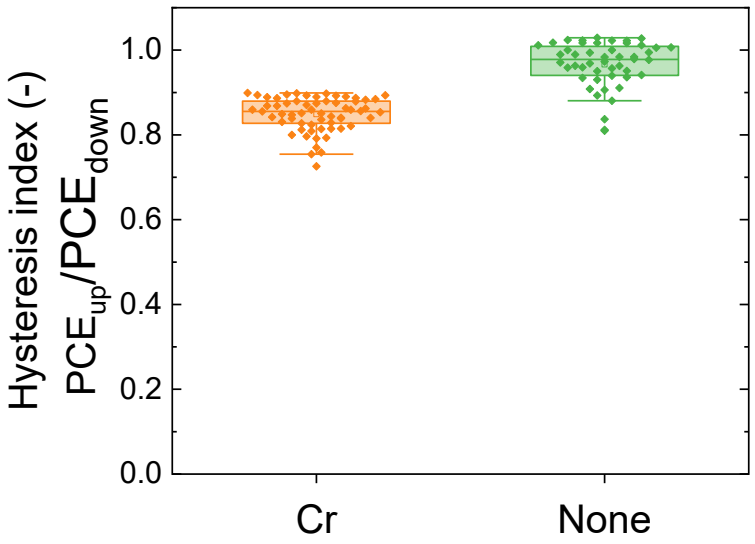



**Figure 6.6 Hysteresis Index**

The fraction of PCEs derived from current voltage scans in different directions (PCE up sweep/ PCE down sweep) is shown for devices with a 5 nm Cr layer and without any such interlayer ("None").

When preparing devices in this configuration (Figure 6.2a) I observed more frequent shunting issues in devices with Cr layers that were deposited from a chrome-coated tungsten wire, whereas there was no such issue when the Cr layer was deposited via e-beam evaporation (see Figure 6.7). When using a chrome-coated tungsten wire 82 out of 120 devices (38%) were shunted. Out of 64 devices with e-beam Cr evaporation none displayed a shunt. The shunts would disappear upon ageing (Figure 6.8). Overall, there are more processing issues when using the Cr layer.

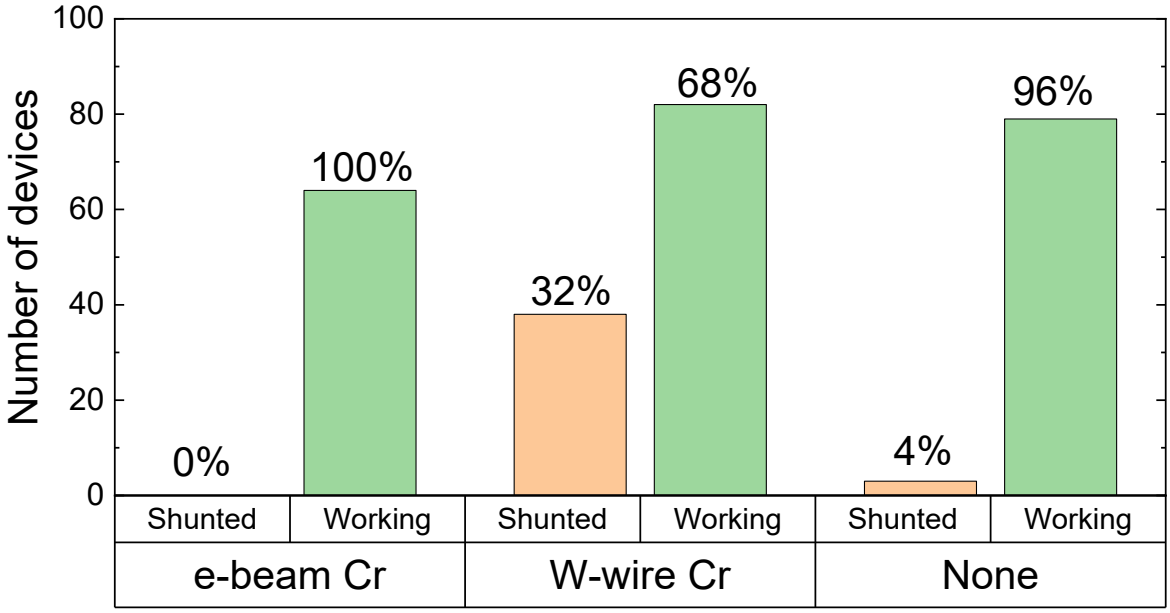



**Figure 6.7 Shunting Statistics**

Statistics on the number of shunted devices (FF between 0.24 and 0.30). Devices data from five different batches of devices with metal electrodes fabricated in four different evaporators and four different metals besides Cr are used in the calculation. Of 120 devices fabricated with a chrome layer deposited from a chrome-coated tungsten wire (W-wire), 32% or 38 devices were shunted. Fabricating the chrome layer with e-beam deposition resulted in a 0% shunting rate for 64 devices. Within 82 reference devices without a Cr layer, 4% were shunted (3 devices).

We assume that when a Cr-coated tungsten wire is used, clusters of Cr or $Cr_2O_3$ get impinged into the sample, causing damage to the ETL. When Cr is in contact with the perovskite it can thermally or bias-activated diffuse into the perovskite causing dendrites that shunt the entire devices. Upon ageing (or repeated measuring) the shunts can “burn out” turning the Cr filaments into less conductive chromium halides or oxides.

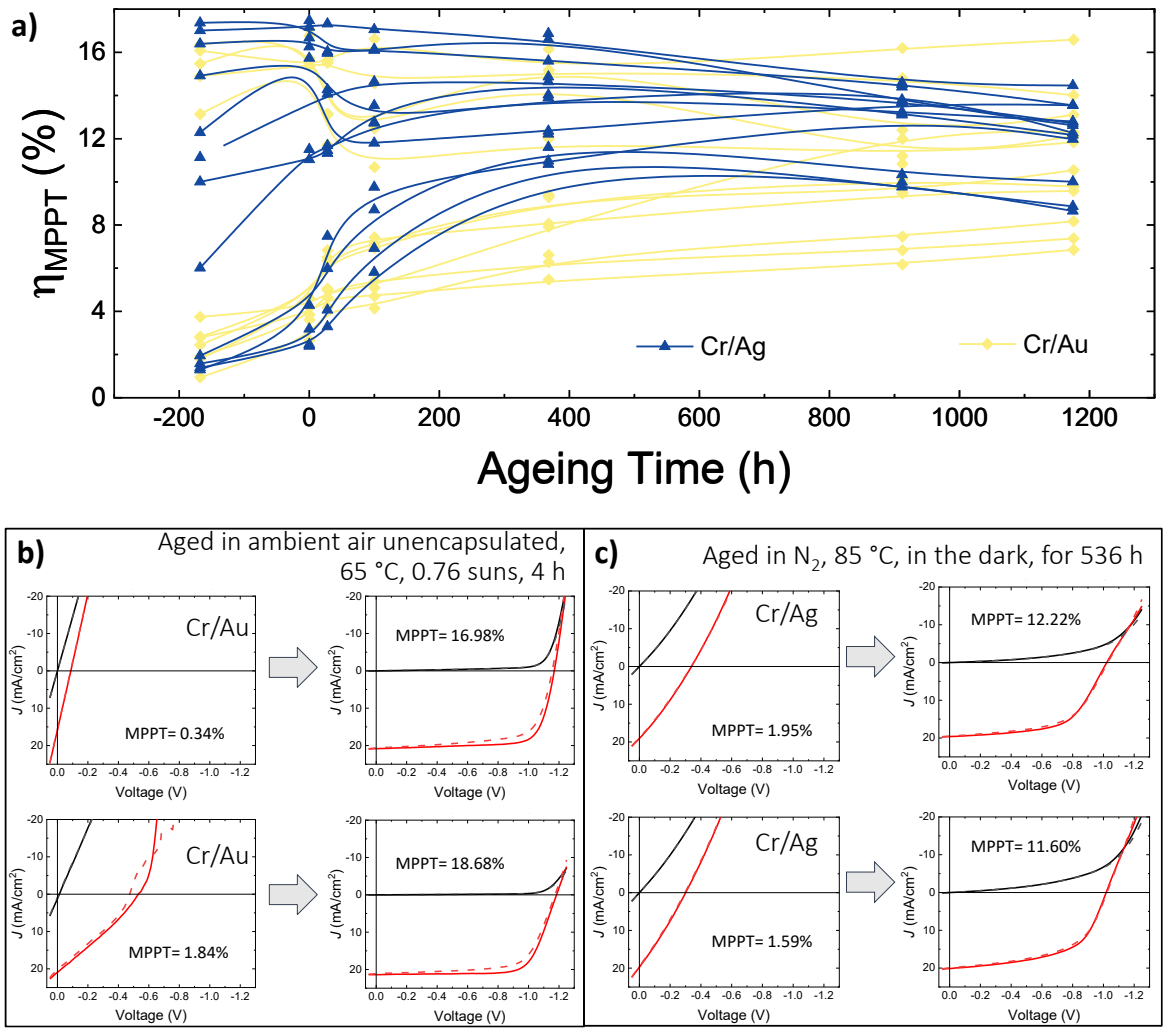



**Figure 6.8 Cr Shunt Ageing**

(a) The ageing behaviour of Cr/Ag and Cr/Au devices at 85°C in $N_2$. The maximum power point tracked (MPPT) efficiencies is plotted against the ageing time. The devices were fabricated, stored for 200 h and then transferred into the ageing chamber. Several devices performed low (below 6%) before the ageing was started (-200 h to 0 h). These devices improved by over 7abs% to around 13% MPPT efficiency upon ageing. This was generally observed for shunts in devices of Cr layers disappearing upon ageing and performance drastically increasing. (b) Examples of this behaviour for two devices aged 4 h unencapsulated at 65 °C 0.76 sun in air. The stabilised efficiencies improved from below 2% to 17% and higher. (c) The same behaviour as in (b) but slower under 85 °C in the dark in an $N_2$ atmosphere. In (b) and (c) The solid and dashed lines represent forward and reverse scan of a device. Red lines represent a *JV* measurment under AM1.5g illumination and black lines a measurment in the dark.

To be able to compare devices with and without Cr, all devices were glass-glass encapsulated with a UV-cured epoxy and then aged at elevated temperatures above 50 °C, under one sun equivalent illumination, and in ambient air. The resulting *JV* curves throughout the ageing can be seen in Figure 6.5. In Figure 6.9b I show the median PCE stability of all scans in both scan directions as a function

of ageing time. We acquired the MPPT efficiency stability for the first 450 h of ageing, confirming the same trend as shown in the median PCE data (Figure 6.9c - d).

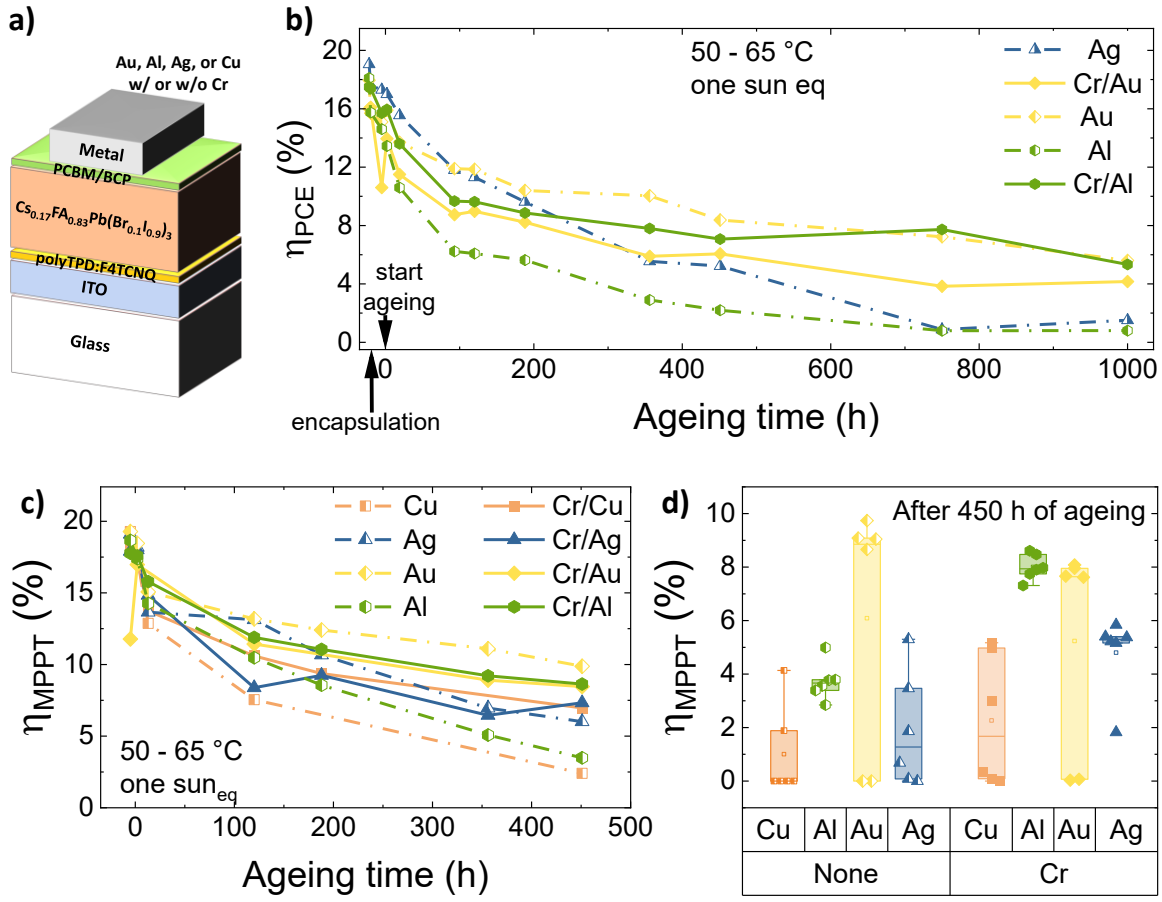



**Figure 6.9 Cr/metal Ageing Study**

(a) The used device stack. (b) The change of PCEs upon ageing of devices completed with an Ag, Au, Cr/Au, an Al, and a Cr/Al electrode. The PCEs were obtained via JV-sweeps and devices were aged under one sun-equivalent illumination at elevated temperatures. The lines indicate the median of all PCEs of both sweep directions of 18 devices per parameter. Yellow rhomboids, green octoids, blue triangles, and orange squares display Au, Al, Ag, and Cu electrode data. Electrodes without chrome are symbolised by half-filled symbols and dashed lines and electrons with a chrome interlayer are displayed with a filled symbol and continuous lines. At the beginning of the study, one well-performing device of each parameter was chosen and one-minute maximum power point tracking (MPPT) efficiencies were performed on these devices after the JVs for all devices were collected. The results of these MPPT efficiencies over time are shown in (c). After 450 h of ageing a 30 s MPPT efficiency was performed on all six devices on the best-performing substrate. (d) The statistical distribution of these measurements. Because of a measurement mistake, the MPP data was not acquired past 450 h of ageing.

After 13 h of ageing a thick layer of silver paste was added onto the electrode pad that served as contact to the measurement pins. No obvious change was present before and after applying the paste (see Figure 6.10).

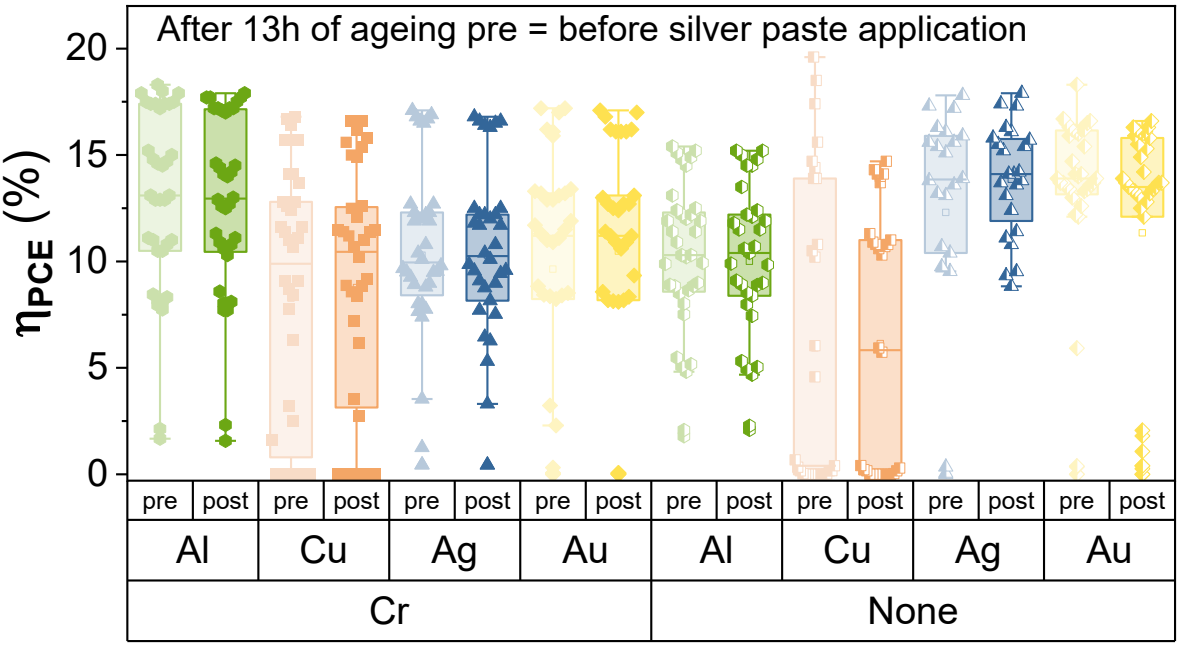



**Figure 6.10 Silver Paste Application**

After 13 h of ageing on all devices, the metal electrode outside the encapsulation was partly scratched off the ITO backing contact pads where the measurement pins connect to it. A thick layer of silver paste was applied to each pad. The PCE results from before this procedure are above labelled as "pre" and the results afterwards as "post". As opposed to other analyses, non-working devices were included in this plot to analyse if any "dead" devices become operational upon silver paste application.

For devices with less noble metal electrodes like Ag, Cu, and Al, I observed a strongly slowed-down degradation in device performance when a Cr layer was deposited between the ETL and the metal (see Figure 6.9b-c, Figure 6.12, and Figure 6.11). Especially Cu and Al devices without a Cr layer showed rapid initial degradation in MPPT efficiency and PCE. This decay in Al and Cu devices was even quicker than for devices with Ag. The champion Cu device dropped from around 20% to below their $T_{50}$ of 10% PCE after 157 h of ageing and the Al device after 325 h (Figure 6.11). Conversely, the Cr/Cu and Cr/Al champions fell below 10% after 440 h and 882 h respectively. The nano-layer of Cr improved the stability of Al and Cu significantly more than doubling the time before devices dropped below their $T_{50}$.

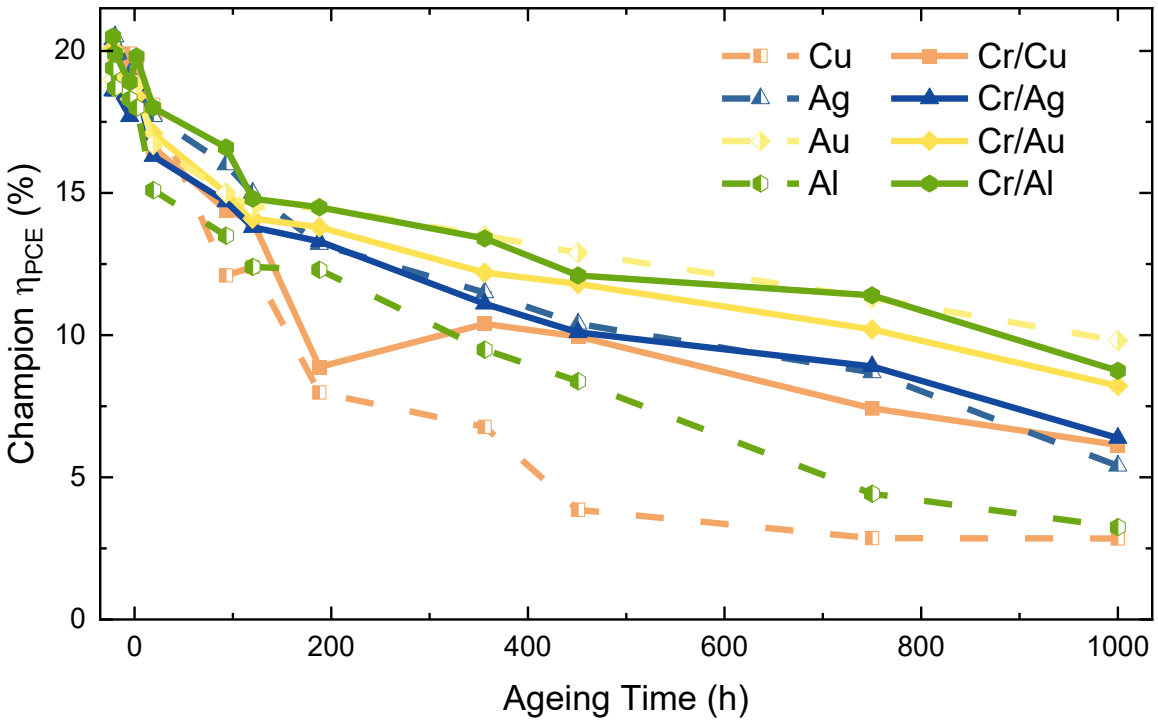



**Figure 6.11 Champion PCEs**

The best *JV* scan obtained PCE values for each electrode configuration over ageing time.

The same trend is confirmed by MPPT efficiency values (Figure 6.9c and d) with the Cr layer roughly doubling the stability of devices with Cu and Al electrodes. In this second study, the effect of the Cr layer was smaller for Ag devices leading only to a small improvement after long ageing times of 1000 h. Overall the median and champion PCE and $J_{SC}$ values before and after 1000 h of ageing clearly show a strong stability enhancement of the Cr layer for all metals but Au (Table 6). While a back electrode with just Al is the second-worst option in a stability comparison, the Cr/Al combination shows the close second highest stability, very similar to the stability of Au devices and notably higher than the one of Cr/Au devices (Figure 6.9a and b).

**Table 6 PCE and $J_{SC}$ ageing data**

Columns 2 and 3 show the median PCE out of all scans in both directions and the champion PCE out of the single best scan right after fabrication and after ageing for 1000 h under 1.0 suns at > 50 °C.

| Electrode | Median (Champion) PCE initial | Median (Champion) PCE after 1000 h | Median Jsc initial | Median Jsc after 1000 h |
|---|---|---|---|---|
| Materials | % | % | mA/cm^2 | mA/cm^2 |
| Al | 18.1 (19.4) | 0.8 (3.2) | 21.8 | 4.9 |
| Cr/Al | 16.0 (20.5) | 5.33 (8.8) | 23.2 | 12.2 |
| Au | 17.5 (19) | 4.16 (9.8) | 21.9 | 13.2 |
| Cr/Au | 18.1 (20.1) | 5.61 (8.2) | 21.7 | 10.1 |
| Ag | 19.5 (20.4) | 1.5 (5.4) | 22.5 | 3.8 |
| Cr/Ag | 10.8 (18.6) | 3.25 (6.4) | 21.6 | 9.5 |
| Cu | 18.3 (20.2) | 0.0 (2.9) | 22.2 | 0.0 |
| Cr/Cu | 16.8 (20.4) | 0.3 (6.1) | 22.3 | 3.2 |

All types of devices but the ones with Cu showed a slow uniform decay in $V_{OC}$ from around 1.10 V to around 0.95 V median $V_{OC}$ (Figure 6.12b). Devices with Cu and Cr/Cu degraded to a median $V_{OC}$ of around 0.8 and 0.9 V respectively. The slower degradation in devices with a 5 nm Cr below the metal electrodes was mainly due to better retention of $J_{SC}$ (Figure 6.12d and Table 6). This trend is shown in the change in *JV* behaviour displayed in Figure 6.5. Devices with the Cr buffer layer maintained generally higher current densities than their counterparts without such a layer. Cu devices without Cr dropped to a median $J_{SC}$ of 0 mA/cm$^2$ after around 450 h of ageing explaining their low performance. While the Cr/Cu devices maintained around 12 mA/cm$^2$ after 450 h their median $J_{SC}$ also dropped significantly down to less than 4 mA/cm$^2$ after 1000 h (Figure 6.12 and Table 6).

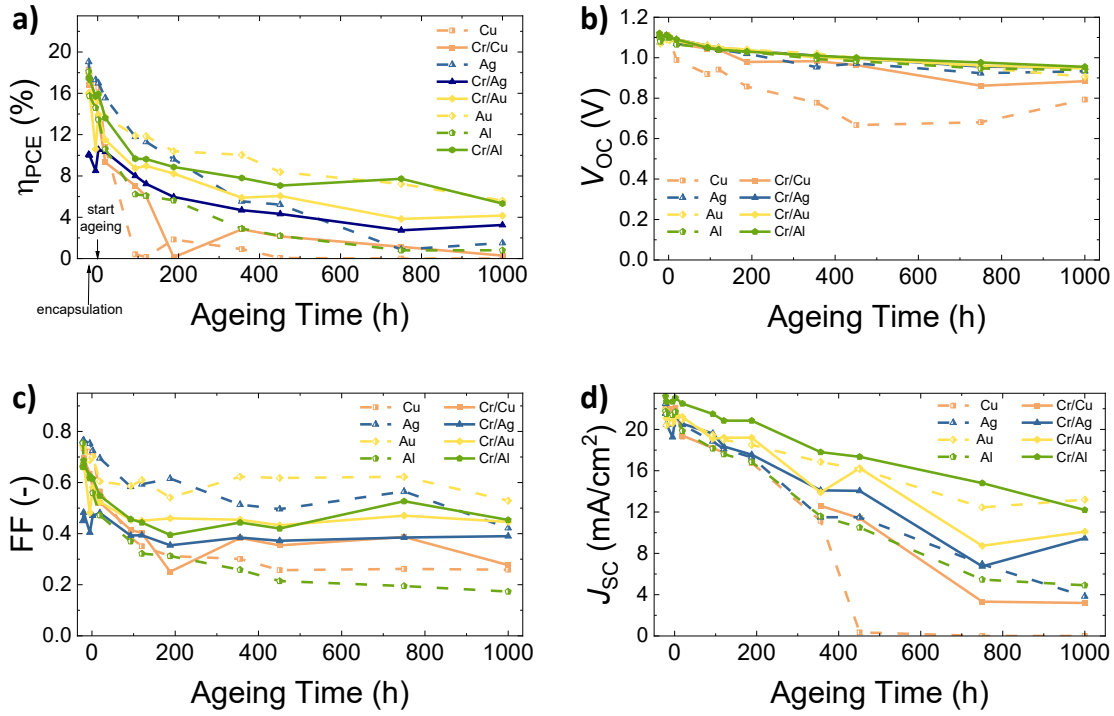



**Figure 6.12 Overview Cr/metal PCE**

Statistical development of device parameters for different metal back electrodes is shown. All parameters were obtained via *JV* sweeps on 18 devices per parameter (12 for Ag). Data for both sweep directions was included in the statistics. Therefore, 36 data points per electrode configuration were obtained. Faulty devices with connection errors were excluded. Symbols and lines present the median values of each of the electrode configurations. (a) - (d) show the PCE, $V_{OC}$, FF, and $J_{SC}$ in that order.

After 1000 h Al devices dropped to a median $J_{SC}$ of 4.9 and Cr/Al devices to 12.2 mA/cm$^2$. A similar trend was visible with a median $J_{SC}$ of around 3.8 mA/cm$^2$ for Ag and 9.5 mA/cm$^2$ for Cr/Ag devices after 1000 h. This significantly higher retention of current density led to them performing higher at the end of the ageing study. In the case of Ag and Cr/Ag devices, this higher current density overcompensates for the lower fill factors of Cr/Ag devices. This results in the Cr/Ag devices on median outperforming Ag devices at the end of the ageing study. Notably the median starting efficiency of Cr/Ag devices was with ~10% much lower than the one of Ag devices with ~19% (Figure 6.12a and c).

### 6.3.3 ITO and FTO Transparent Electrodes

We observed a lower stability in devices of the metal electrode comparison shown in Figure 6.9 compared to the high light-heat stability in Figure 6.2. Since the transparent electrode used was a major difference between the two studies (FTO in Figure 6.2a and ITO for devices in Figure 6.9), I

investigated the stability of FTO and ITO-based devices in a direct comparison with the most stable electrode in the second study (Au). Devices of the same device stack on ITO and FTO substrates were aged and in-depth characterised post-mortem.

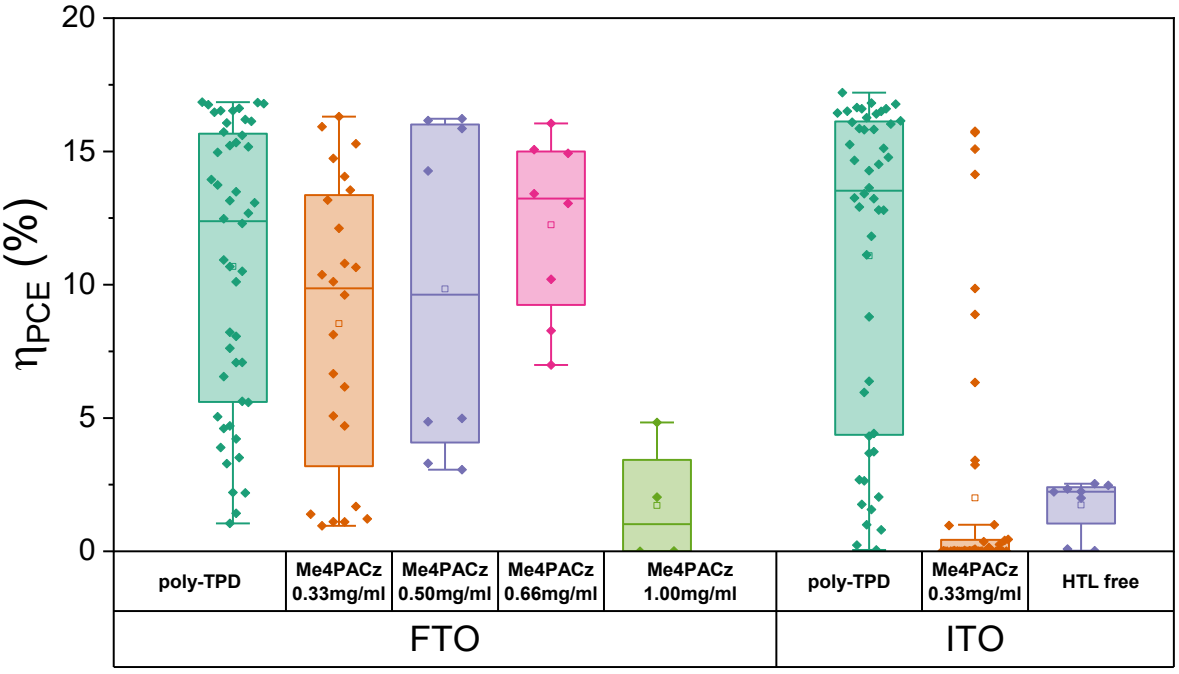



**Figure 6.13 Hole Transport Layers for FTO and ITO**

The performance of solar cells on FTO and ITO with different hole transport materials is shown. All devices were completed with $FA_{0.83}Cs_{0.17}Pb_{1.00}I_{2.7}Br_{0.3}$/PCBM/BCP/Au stack. Because of reproducibility issues with the self-assembled monolayer formation of Me4PACz the stability studies were conducted with polyTPD as the hole transporter.

To have a fair comparison between ITO-based and FTO-based devices I aimed to have the same hole transport material deposited with the same process parameters. Only with an identical device stacks besides the used TCOs, do I expect to see just the differences between the transparent conductive oxides. Initially, I aimed to use the state-of-the-art self-assembled monolayer (SAM) fabricated of 4-(3,6-Dimethyl-9H-carbazol-9-yl)butyl]phosphonic acid (Me4PACz) as a hole transporter. I achieved however a poor device yield with a few good and a large number of shunted and badly working devices for both FTO and ITO substrates as shown in Figure 6.13. The yield was particularly low with ITO. I assume the low yield is due to an incompatibility of the bulk passivation used inside the perovskite layer (BMP $BF_4^-$) and the SAMs. Devices with Me4PACz on FTO showed good stability as displayed in Figure 6.14, but an unusably low initial performance, which was hence excluded from the study. This highlights the need to plot absolute performance values in ageing studies and not

relative. On a relative performance plot the Me4PACz on FTO would have given a promising impression. Further, Lin et al.[63] show that using polyTPD results a higher heat and light stability compared to using $NiO_X$ as bottom HTL. This is not surprising given the mentioned photocatalytic activity of $NiO_x$ (see 2.5.2.3 Metal Oxide Instabilities). Because of this and the low reproducibility of other bottom HTL on least one of the used TCO substrates, only polyTPD devices were used for all stability studies presented in all chapters of this thesis.

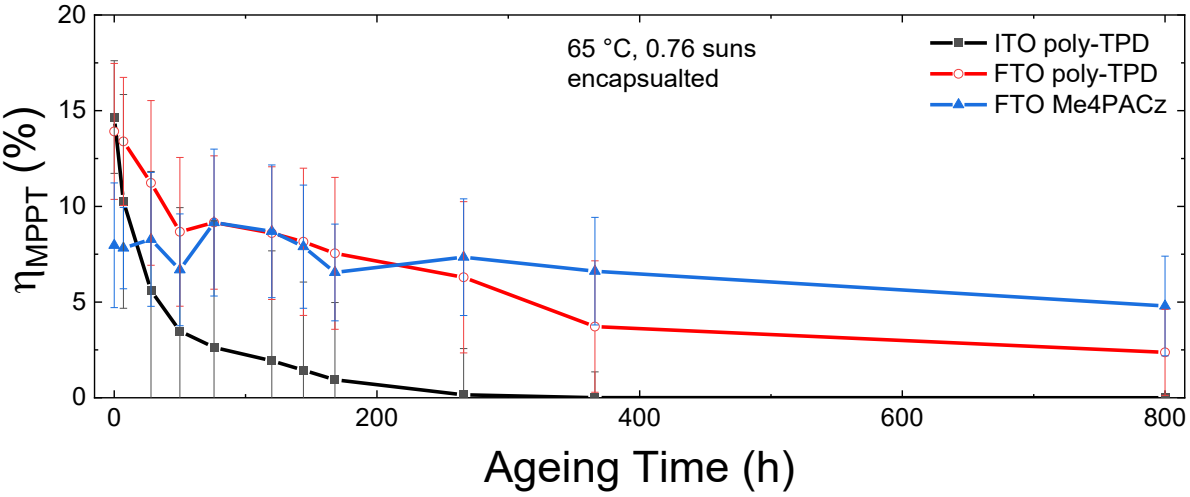



**Figure 6.14 Hole transport layer ageing comparison**

Ageing behaviour for ITO-based devices with polyTPD and FTO-based devices with polyTPD and Me4PACz at 65 °C, under continuous 0.76 suns illumination, in ambient air, and encapsulated.

Both ITO- and FTO-based devices show a decay of their stabilised performance measured via maximum power point tracking (MPPT efficiency) visible in Figure 6.19a. The ITO champion before the start of the ageing experiment started with a stabilised efficiency of 18.1%, which is 1% higher than of the highest performing FTO device at that time, with 17.1%. This confirms the general advantage of ITO-based devices showing slightly higher efficiencies than FTO-based PSC because of the higher transparency of ITO for the same sheet resistance. After 800 h of ageing, all 14 ITO devices in the ageing study performed with less than 0.01%, while the best-performing FTO device still stabilised at 7.0% efficiency. The development of different ageing parameters as well as representative Current Density-voltage (JV) curves are shown in Figure 6.15. ITO-based devices showed a strong exponential drop in all performance parameters for a large majority of devices within the first 400 h. A small number of devices showed initially a stability comparable to the stability of FTO-based devices, but started at much quicker linear degradation after about 200 h. Most ITO-

based devices developed “s-kink” current voltage scan shapes whereas the devices on FTO substrates did not.

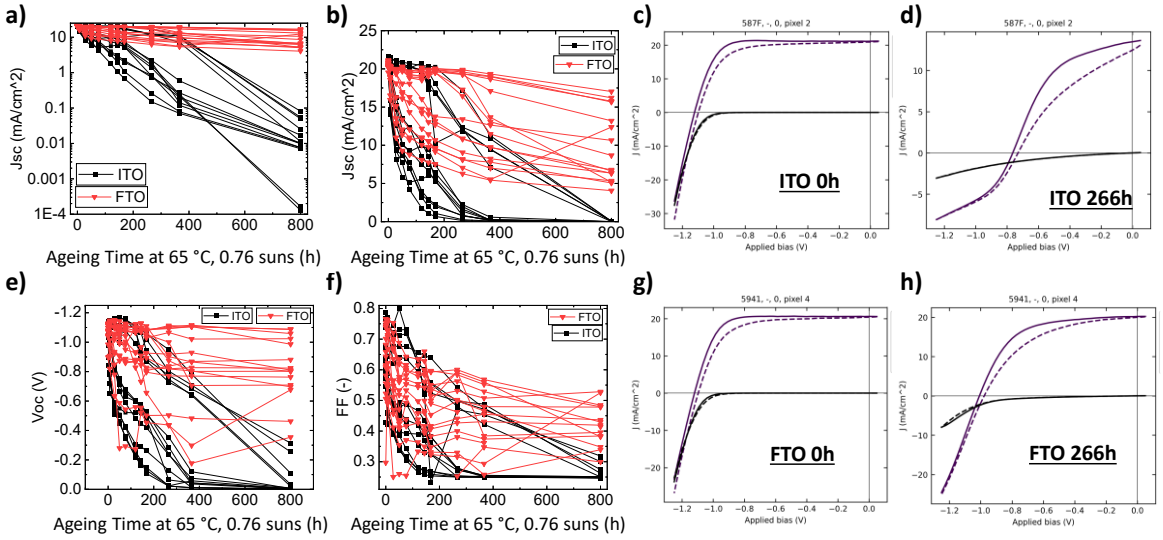



**Figure 6.15 Ageing Behaviour Transparent Electrodes at 65 °C**

The development of the performance parameters of devices with fluorine-doped tin oxide (FTO) are displayed with red triangles and indium tin oxide (ITO) based devices are shown with black squares. The short circuit current density ($J_{SC}$) on a log scale (a) and on a linear scale (b) against ageing time. Current density voltage (JV) scans of ITO-based devices at the beginning of the ageing (c) and after 266 h (d). (e) The open circuit voltage ($V_{OC}$) and (f) fill factor (FF) of the devices over the ageing time. *JV* scans of FTO-based devices at the beginning of the ageing (g) and after 266 h (h). For the *JV* scans the solid and dashed lines represent forward and reverse scans of a device, respectively.

To understand why the ITO samples degraded much more, time-of-flight secondary ion mass spectrometry (TOF-SIMS) was performed on one of the aged ITO-based devices and a just-fabricated device with an identical layer stack. I observed indium in the pristine well-performing ITO devices as well as in devices aged for 800 h under 0.76 sun illumination at 65 °C (Figure 6.18). In the fresh device, the indium was largely concentrated on the top surface of the perovskite, while in aged devices it was distributed more uniformly throughout the entire perovskite layer.

As mentioned before, ageing tests at one sun and 25°C are not sufficient stress tests for PSCs, as they do not replicate real-world conditions where a combination of light and heat contribute to degradation. However, a test at these conditions was performed to determine whether degradation in ITO-based devices occurs only at high temperatures or also just under illumination. Under one sun, at 25 °C, and $V_{OC}$, ITO-based PSCs exhibited a much quicker and abrupt drop in MPPT efficiency

after 200-400 hours, with nearly all devices falling below 4% efficiency after 250 h (Figure 6.16). In contrast, FTO-based devices showed a more gradual decline, maintaining MPPT efficiencies above 4% for all devices until 250 h. The primary losses in ITO-based cells were due to reductions in fill factor (FF) and $V_{OC}$ due to the development of "s-kinks" similar to those observed in high-temperature ageing trials presented above.

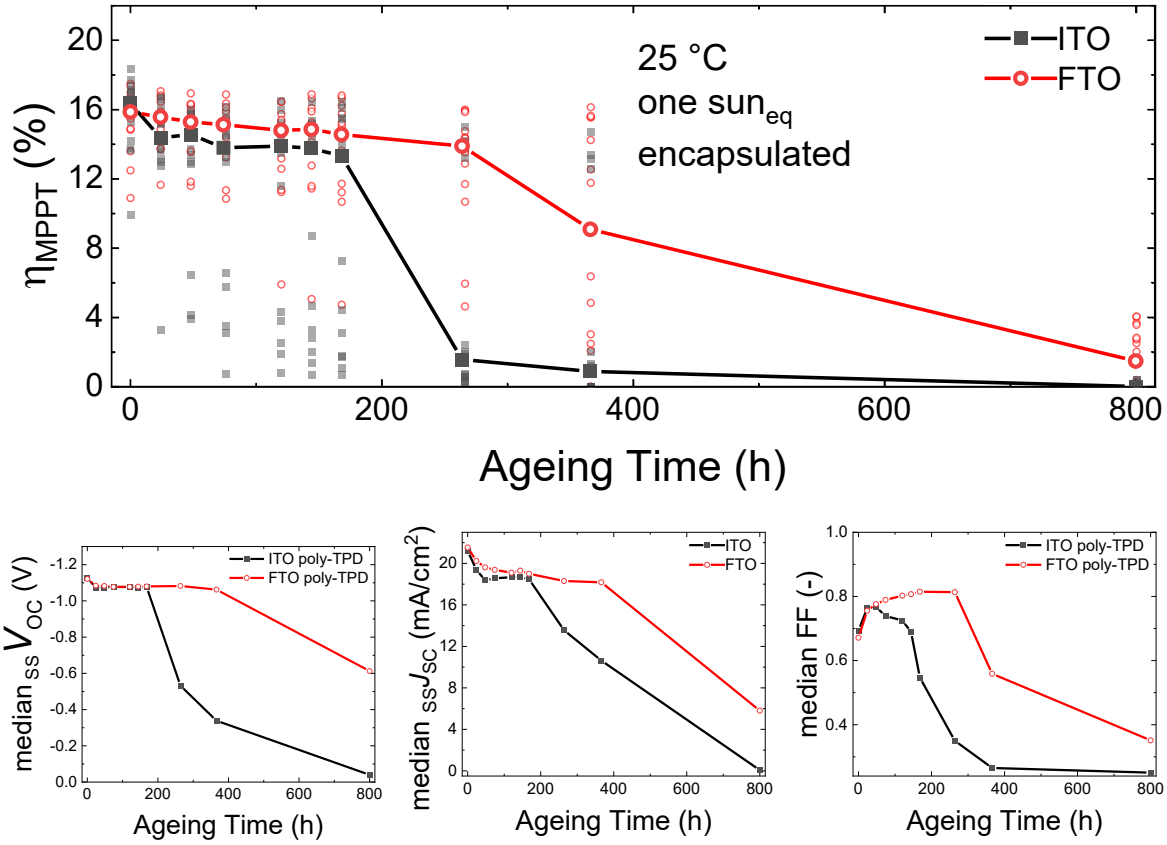



**Figure 6.16 ITO vs FTO Ageing Study at 25 °C**

The ageing behaviour of 14 FTO-based and 15 ITO-based devices is shown. All devices were encapsulated with a glass cover slip sealed at the edge with UV-cured epoxy in an $N_2$ environment. Devices were illuminated with a three-colour plant-growing LED array and cooled with a Peltier cooler to 25 °C. This is not comparable to operation or standard ageing conditions for photovoltaic devices. This experiment was conducted to decouple the effect of light and temperature on ITO ageing. At this temperature, the experiment could be more prone to encapsulation breakdown because of the potential condensation of water inside the encapsulation.

Post-mortem all devices aged at 25 °C were analysed via XRD. There were clearly visible ITO and FTO peaks on all the respective devices (Figure 6.17a). Further, all devices showed reflections I assigned to perovskite degradation products (Figure 6.17b). There were no clear differences of these degradation products between different substrates.

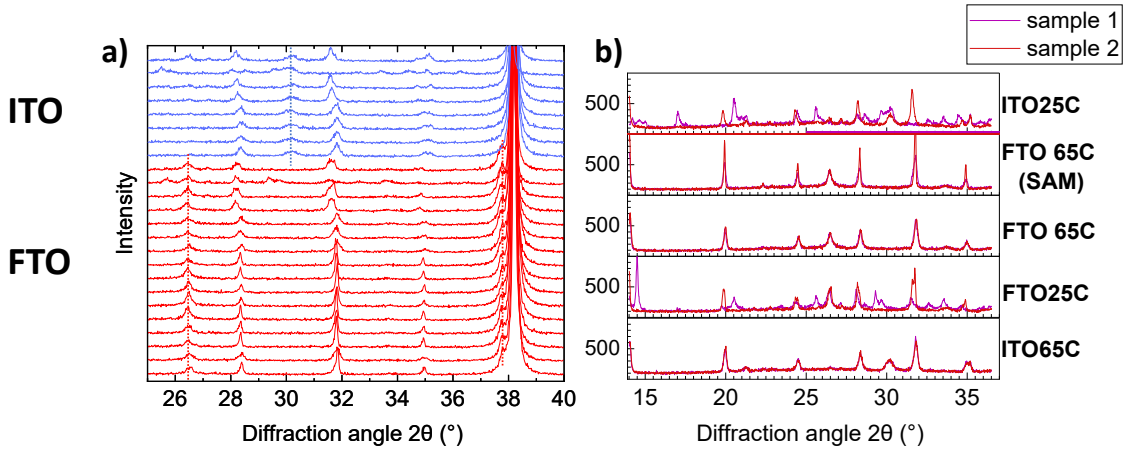



**Figure 6.17 X-ray Diffraction Spectra of Aged Devices on ITO and FTO**

(a) The differences in the X-ray Diffraction (XRD) pattern of ITO with a peak at about 30° and FTO having peaks at about 26.5 and 37.9°. Note that the latter one is only visible as a shoulder in the much stronger peak of the gold electrode at 38.1°. (b) XRD pattern of aged perovskite solar cell devices. There were signs of degradation as the formation of the unwanted $FAPbI_3$ δ-phase in some of the samples aged in the 25°C setups. However, there were no obvious differences between the spectra of ITO and FTO-containing devices.

Time of flight secondary ion mass spectrometry (TOF-SIMS) was performed on a pristine ITO/polyTPD/$FA_{0.83}Cs_{0.17}PbI_{2.7}Br_{0.3}$/PCBM/BCP/Cr/Au sample that was only measured once to be > 18% MPPT efficiency and then kept at RT in the dark in an $N_2$ atmosphere until TOF-SIMS was performed. A second TOF-SIMS was performed on an ITO PSC aged 800 h under 0.76 suns illumination at 65 °C. The encapsulation glass was mechanically removed before the measurement. Both samples show significant amounts of $Na^+$, $Au^+$, and $In^+$ ions in the perovskite film. The distribution of ions is higher and more uniform throughout the entire film for the aged device. In contrast, it looks like ions are located more at interfaces for the pristine sample. An exception is $Pb^{2+}$, which seems to accumulate at the ETL/perovskite interface for the aged device. The aged devices showed a 46% lower count in $In^+$, a 42% lower count in $C_2H_3^+$, and a 1,886% higher count in $C_3H_3^+$ ions compared to the pristine sample.

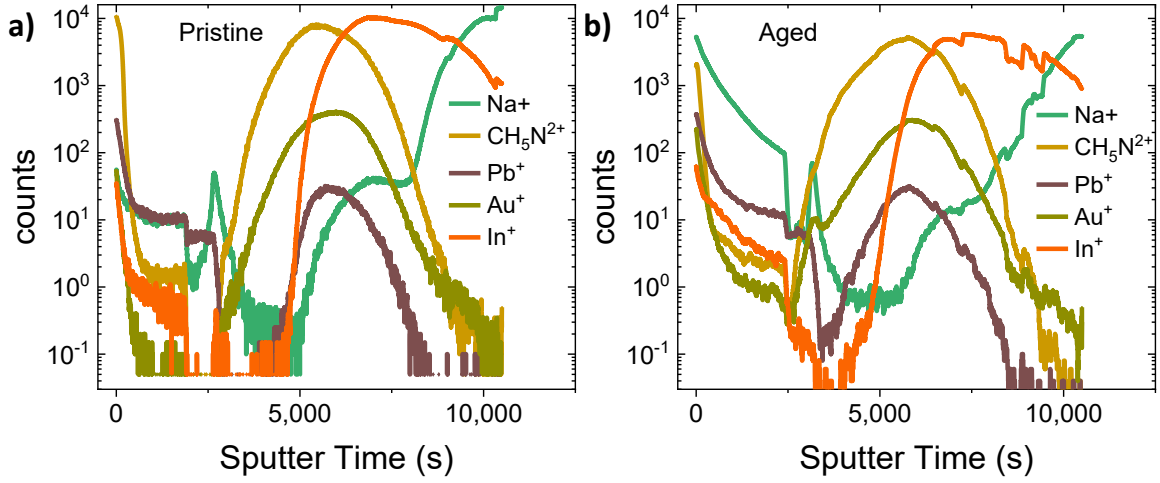



**Figure 6.18 Time of flight secondary ion mass spectrometry results**

TOF-SIMS results for a pristine and an aged ITO perovskite solar cell are shown in (a) and (b) respectively. All TOF-SIMS were performed by ION-TOF GmbH in Münster, Germany.

Scanning electron microscopy (SEM) cross-sections of aged devices on ITO and FTO show a different morphology of the perovskite layer. Aged ITO-based devices show several tens of nanometres large cavities, especially at the ITO/perovskite interface as well as around grain boundaries throughout the whole film thickness (Figure 6.19d). These cavities are not visible in devices on FTO (Figure 6.19e). This phenomenon was observed over the whole length of cross-sections on multiple different substrates.

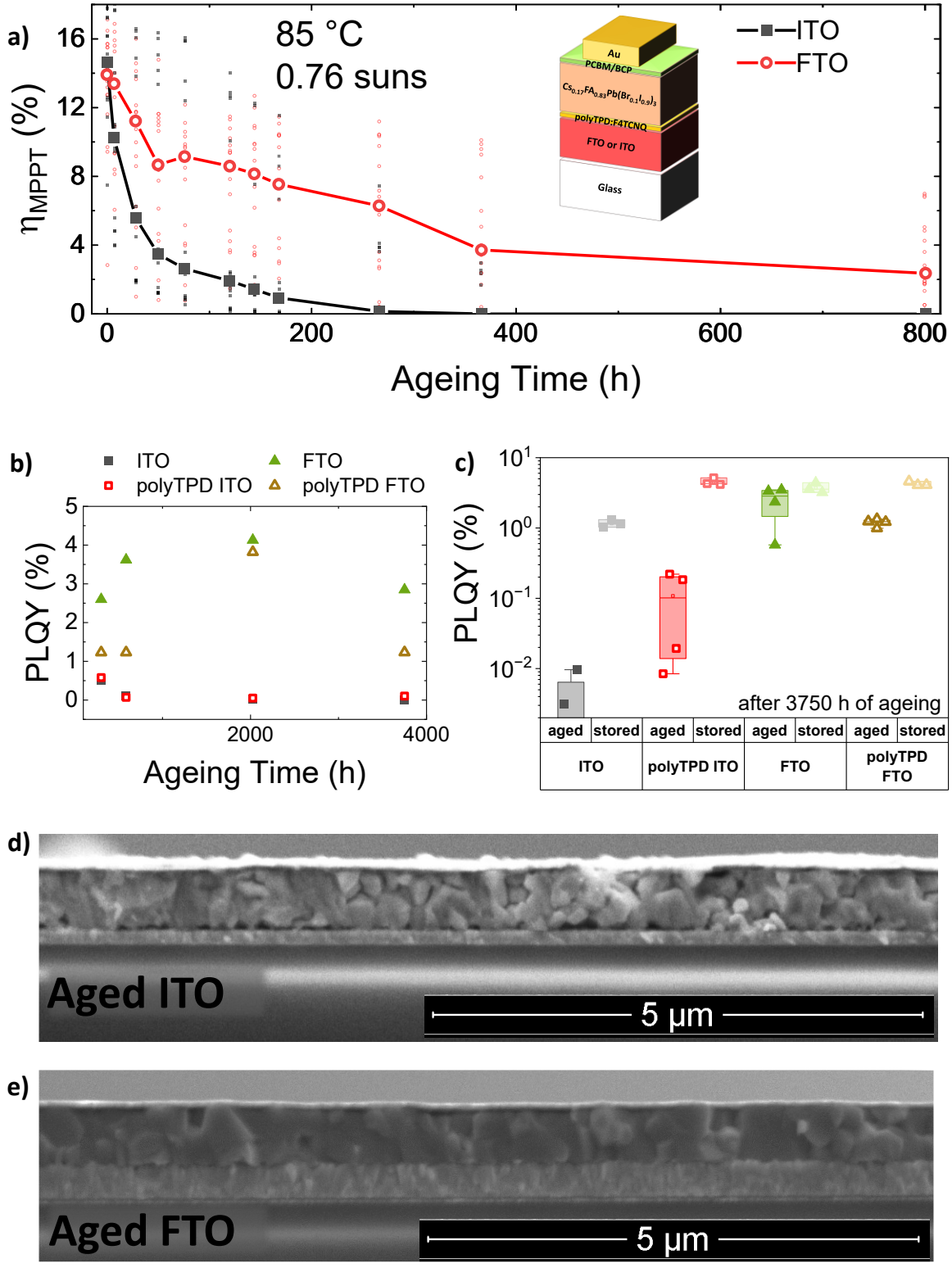



**Figure 6.19 Stability of Devices on ITO and FTO**

(a) The average MPPT efficiency performance of full PSC devices on FTO (in red line and circles) and ITO substrates (black line and squares) when the devices were aged under 65°C and 0.76 sun illumination in ambient air. The data of all individual devices of each category are shown with the same symbol. The device stack is shown in the inset. All devices were completed with an Au electrode. The ageing behaviour of PLQY of perovskite film on ITO and FTO is shown in (b) and (c). Perovskite films were aged under 0.76 sun equivalent illumination and at temperatures between 65 and 70 °C in an $N_2$ atmosphere for 3750 h. The perovskite films were deposited either directly on FTO or ITO substrates or as half-stacks on top of the HTL

polyTPD on top of ITO or FTO. PLQY and TRPL of the films were periodically measured throughout the ageing. The development of the PLQY is shown in (b) and statistics of the PLQY of aged films and films stored in the dark at room temperature in $N_2$ are displayed in (c). SEM cross-sections of ITO and FTO devices after being aged under one sun equivalent illumination at room temperature for 800 h are shown in (d) and (e), respectively.

To investigate the isolated effect of the ITO substrate on perovskite material upon the ageing conditions, I aged perovskite films identical to the active layer in our solar cell devices on different substrates including ITO, ITO/polyTPD, FTO, and FTO/polyTPD. The ageing was conducted at temperatures of 65-70 °C under an LED growing lamp with close to one sun illumination in an $N_2$ atmosphere for 3750 h. Reference devices were kept in the dark in an $N_2$ atmosphere at room temperature. Time-resolved photoluminescence (TRPL) and photoluminescence quantum yield (PLQY) measurements were conducted periodically throughout the ageing period to monitor the quality of the perovskite layer.

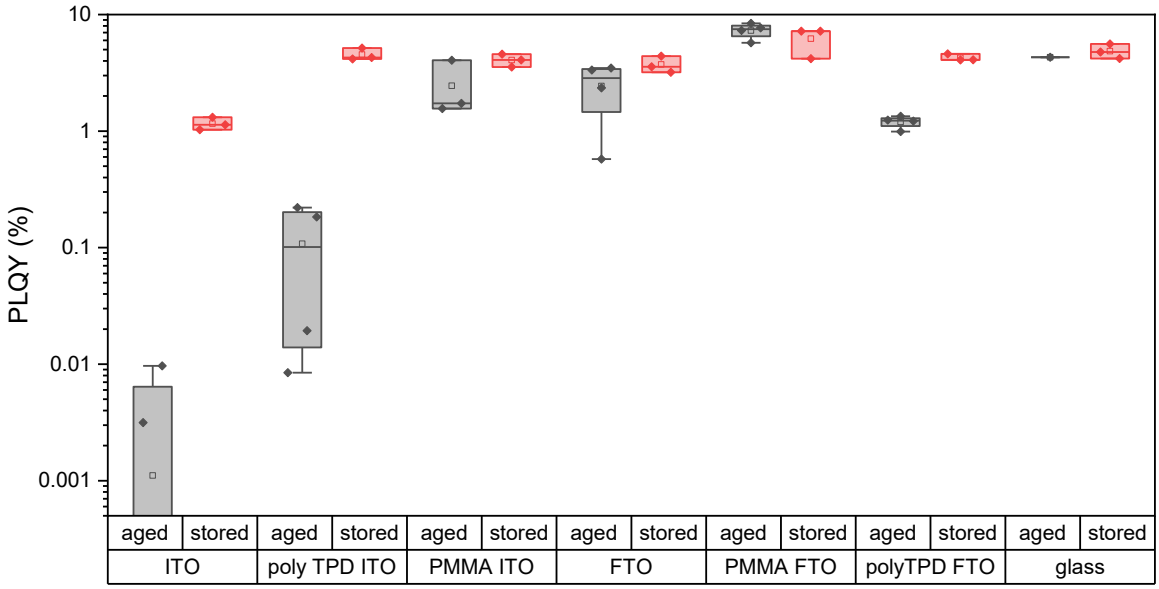



**Figure 6.20 Full Data Photoluminescence Quantum Yield Ageing Study**

Photoluminescence Quantum Yield (PLQY) data for different substrate types is shown. Stored films (in red) were kept in an $N_2$ glove box and aged samples in (black) were exposed to one sun equivalent illumination and 65°C temperature for 3750 h. All stored films showed an average PLQY of around 4% (3.7 - 6.2%). Only the sample on an ITO substrate showed a reduced PLQY of around 1.2% when stored. The perovskite aged on an ITO substrate also showed no PLQY signal exceeding the noise level (< 0.01%). The aged polyTPD ITO substrate showed a very low PLQY with an average of about 0.1%. The polyTPD FTO sample in contrast maintained 1.2% PLQY upon ageing. All other substrate types showed little difference between aged and stored samples.

The PLQY results are shown in Figure 6.19b-c (full results in Figure 6.20). The photoluminescence signal of films on an ITO or ITO/polyTPD substrate dropped immediately to below 1% upon ageing (Figure 6.19b). In contrast, perovskite on FTO or FTO/polyTPD substrates kept PLQY signals between 1 and 5% throughout the ageing time. All reference devices kept at room temperature besides the ones on ITO kept strong PLQY signals of above 3%. The ITO sample dropped to below 1% even when stored without exposure to any light or heat stress.

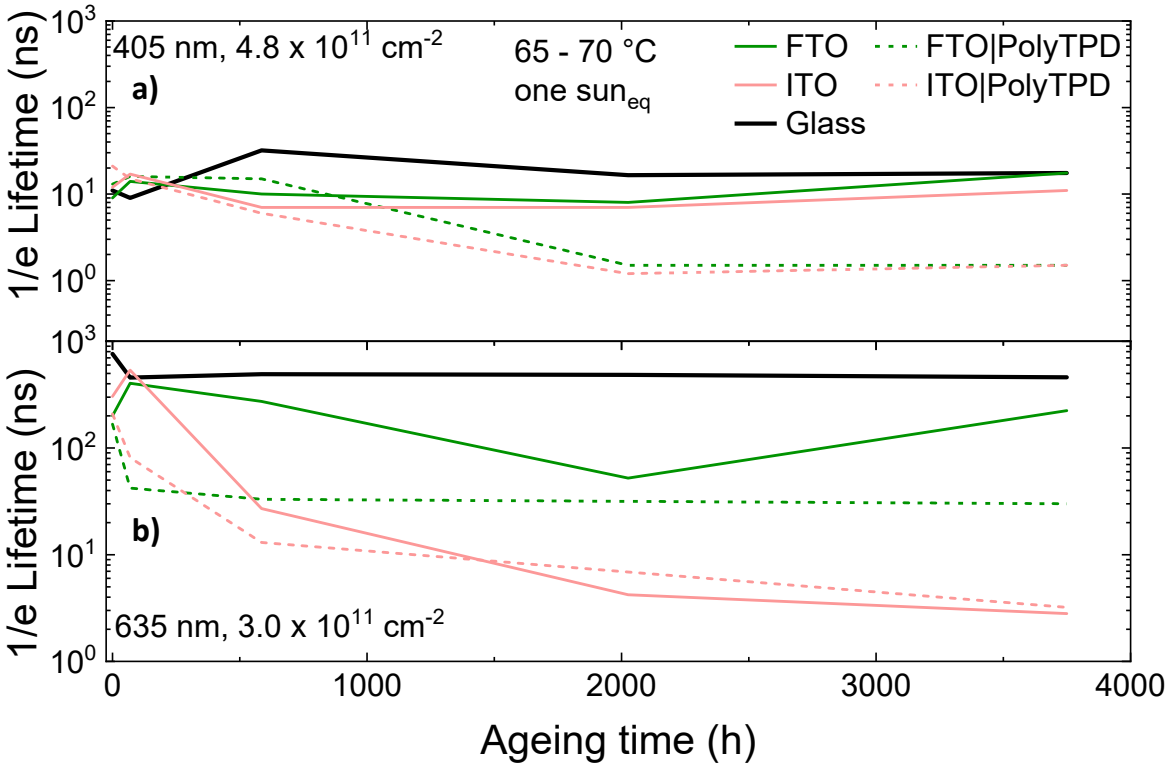



**Figure 6.21 Time-Resolved Photoluminescence of Transparent Electrodes**

Perovskite films were aged under one sun equivalent illumination and at temperatures between 65 and 70 °C in an $N_2$ atmosphere for 3750 h. The perovskite films were deposited either directly on FTO or ITO substrates or as half-stacks on top of the HTL polyTPD on top of ITO or FTO. On the films PLQY and TRPL were periodically measured during the ageing. The development of the TRPL with a 405 nm and a 635 nm laser excitation is shown in (a) and (b) respectively. When excited with a 405 nm laser both samples without a polyTPD layer stayed relatively stable while the ones with showed a reduction in lifetime of about one order of magnitude. When excited with a 635 nm laser the lifetime in both samples on an ITO substrate degraded by over two orders of magnitude while the lifetimes of both FTO samples stayed relatively constant. The lifetimes were calculated by Dr Manuel Kober-Czerny as the time when the PL intensity had reached 1/e of its initial value.

Time-resolved photoluminescence (TRPL) was performed throughout the ageing study on the same devices. Charge carrier lifetimes for each perovskite sample were calculated by Dr Manuel Kober-

Czerny from the photoluminescence decay signal as the time where the intensity had dropped to 1/e (approx. 36.8%) of its initial value. When excited with a 405 nm laser, there was no significant difference in TRPL lifetimes upon ageing between thin films deposited on FTO and ITO (Figure 6.21a). However, lifetimes based on TRPL measurements differed significantly when a 635 nm excitation laser was used. Over the ageing time, all samples fabricated on an ITO substrate showed a strong drop in lifetime by over two orders of magnitude from several hundred nanoseconds to about just two nanoseconds (Figure 6.21b). FTO-based samples, on the other hand, maintained similar lifetimes throughout the 3750 hours of ageing lifetimes of between 30 and 404 ns. Perovskite films deposited on a microscope slide were stable throughout the ageing, independently of the excitation laser used.

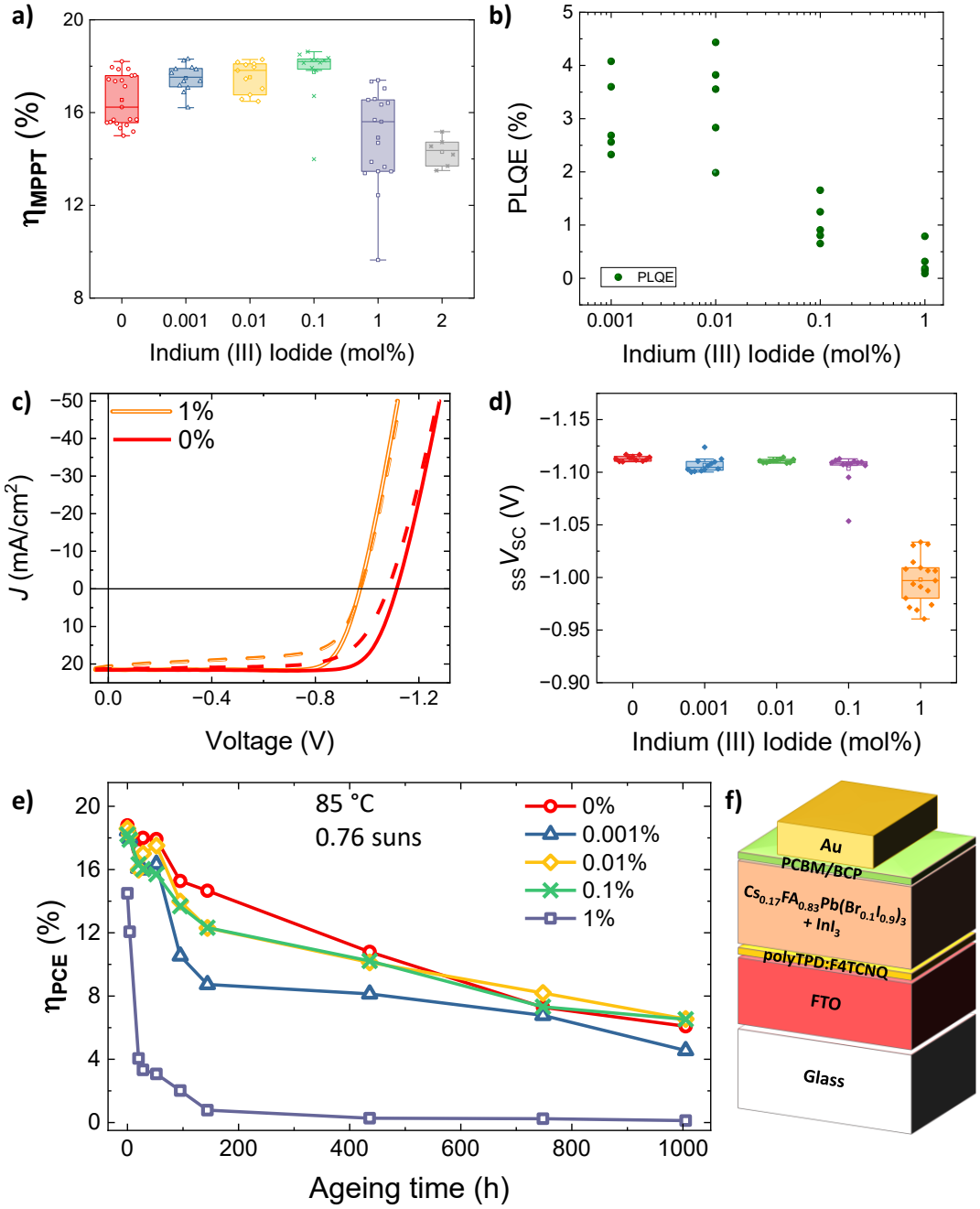



**Figure 6.22 Influence of added Indium (III) Iodide**

(a) The stabilised performance of devices with different percentages of excess Indium (III) Iodide added into the bulk perovskite of FTO-based devices. For devices with 1% and 2% added indium the performance drops while it increases slightly for smaller amounts. (b) The Photoluminescence Quantum Yield (PLQY) for films with the same amount of added Indium (III). There are signs of reduction in PLQY for 0.1% of indium excess in perovskite films. (c) The *JV* curves of the champion cells with 0 and 1% added indium. The solid and dashed lines represent forward and reverse scan of a device. (d) The stabilised open circuit voltage of devices with different percentages of excess Indium (III) iodide added into the bulk perovskite. For devices with 1% added indium the performance and open circuit voltage drop. The ageing behaviour of the same devices depicted in (a) is shown in (e) for an ageing conditions of 0.76 suns, 85 °C, encapsulated, and in ambient air. Devices with 1% added indium show a strongly accelerated decrease in efficiency while smaller amounts show a behaviour similar to devices without added indium. (f) The used device stack.

Based on our TOF-SIMS results, I investigated the influence of indium ions present in the perovskite layer by fabricating solar cell devices and thin films with a range of added indium ions from 2% excess relative to lead down to 0.001% on FTO substrates. Upon fabrication, there was no strong difference in performance between no added $In^{3+}$ (0%) and small amounts of added indium ions (0.001% - 0.1%) with 0.1% even showing slightly improved efficiency (Figure 6.22a). I, however, detected a reduced PLQY for In concentrations as low as 0.1% (Figure 6.22b).

For large amounts of added indium excess (1 - 2%), there was a sharp drop in median performance from around 18% down to around 14% largely due to a voltage drop (see Figure 6.22c and d). To probe the effect of indium in the perovskite layer on device stability I aged these devices at 85 °C under 0.76 suns illumination. The devices with large amounts of indium (1%) degraded to 4% median performance within 20 h of ageing (Figure 6.22e). The ageing behaviour of the devices on FTO substrates with 1% added indium was very similar to the ITO-based devices. Both ITO-based devices and FTO-based devices with 1% added indium iodide showed the same characteristics in a strong initial decrease of current density and development of "s-kinks". On the other hand, lower $In^{3+}$ concentrations maintained more than 15% median efficiency for the first day of ageing. The smaller indium concentrations showed a comparable rate of degradation to devices without added indium (0%). Surprisingly, 0.001% of excess $In^{3+}$ showed the second highest degradation rate while 0.01 and 0.1% aged almost identical to 0% (Figure 6.22e).

### 6.3.4 Perovskite Devices with Improved Long-term Stability

Because of the shown instability of ITO, I repeated the metal electrode comparison with the two most stable electrodes Au and Cr/Al on FTO instead of ITO substrates. This final study was performed in a different laboratory to also test lab-to-lab reproducibility and at an increased ageing temperature of 85 °C (as opposed to 50 - 67 °C for the previous study). ITO devices with Cr/Au electrodes were added for a repeated comparison of the stability influence of the transparent electrodes. The Cr/Al devices again showed strong stability (Figure 6.24) even exceeding the stability of devices with Au electrodes (FTO devices with Au electrodes are the 0% references of Figure 6.22). Interestingly, we were not able to fabricate working devices with an Al electrode without any Cr layer in the second lab because the devices degraded during the encapsulation process (see Figure 6.23).

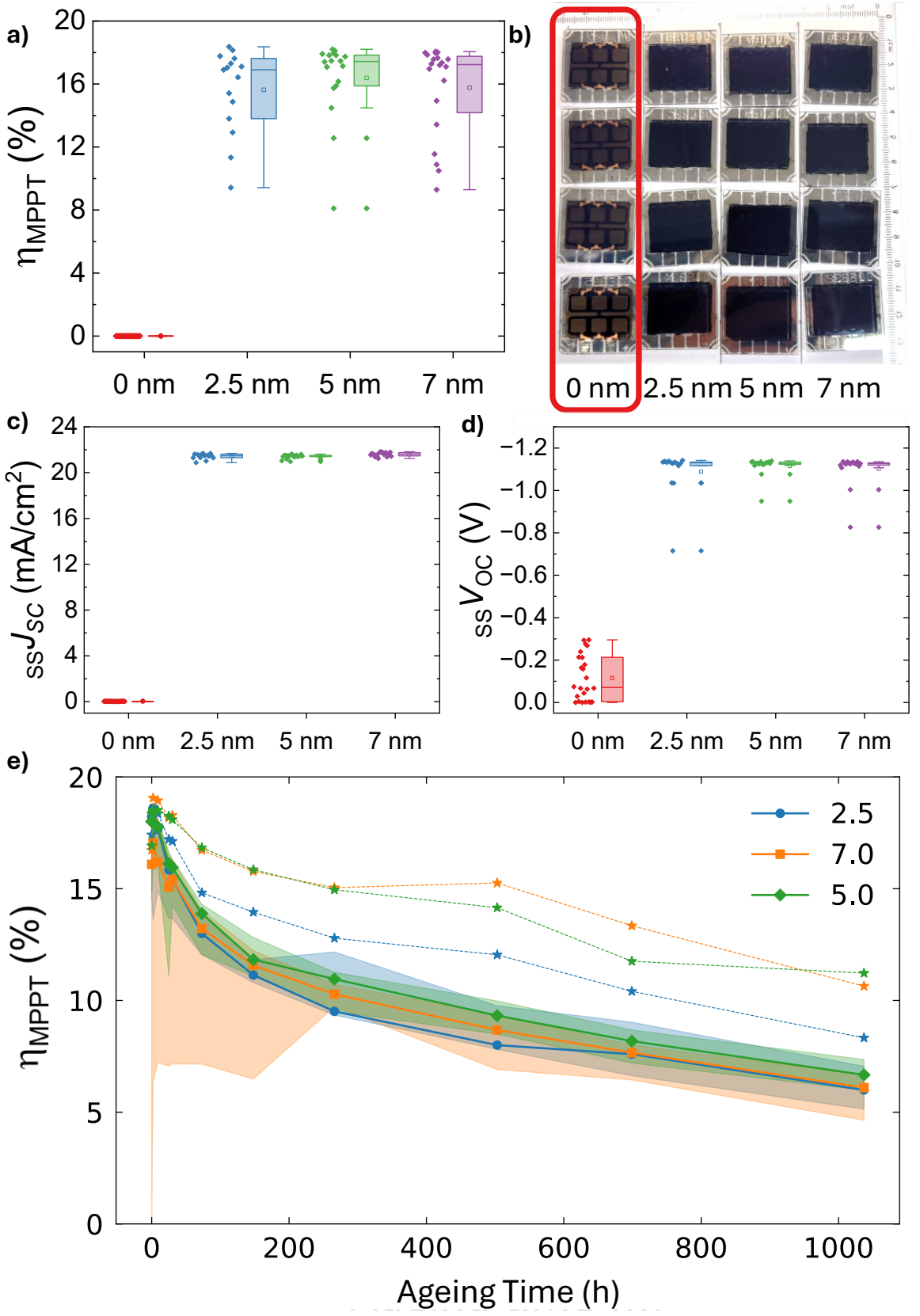



**Figure 6.23 Cr/Al Trial in a Different Evaporator**

(a) Maximum power point tracking results for p-i-n devices with different thicknesses of a Cr layer below a 100 nm Al electrode. The Cr and Al were deposited with the help by Dr Jin Yao at the EPSRC National Thin Film Facility for Advanced Functional Materials. All devices have an active area of 0.25 cm$^2$ and were measured right after fabrication and encapsulation were completed. All devices without a Cr layer (0 nm, red) show 0% stabilised efficiency. On the other hand, devices with different Cr layer thicknesses (2.5, 5, and 7 nm)

all show similar efficiencies with medians of around 18%. (b) The optical appearance of the devices before encapsulation (~16 h after fabrication). Devices without the Cr layer (0 nm, highlighted in red) show signs of perovskite decolouration and the Al electrode pattern is visible through the perovskite layer. Devices with Cr layers still appear uniformly dark. The damage to the perovskite layer is consistent with devices without a Cr layer producing 0 mA/cm$^2$ of stabilised current density ($_{SS}J_{SC}$) as shown in (c). The stabilised voltage is shown in (d). (e) Development of efficiency decay in ageing Cr/Al devices for different Cr layer thicknesses. Blue circles, orange squares, and green rhomboids represent a Cr layer thickness of 2.5, 7.0, and 5.0 nm below the 100 nm Al electrode. The stars of the same colours represent the champion device within each category.

After 1037 h at 85°C light the best-performing Cr/Al device performed at 11.2% MPPT efficiency (66% of its initial performance). The median for devices with 5nm Cr followed by 100 nm Al was 6.7% MPPT efficiency after 1037 h down from the initial 18%. We also compared different thicknesses of the Cr layer below the Al of 2.5, 5.0, and 7.5 nm. The result confirmed that the chosen thickness of 5 nm is the best in terms of long-term stability as shown in Figure 6.23e.

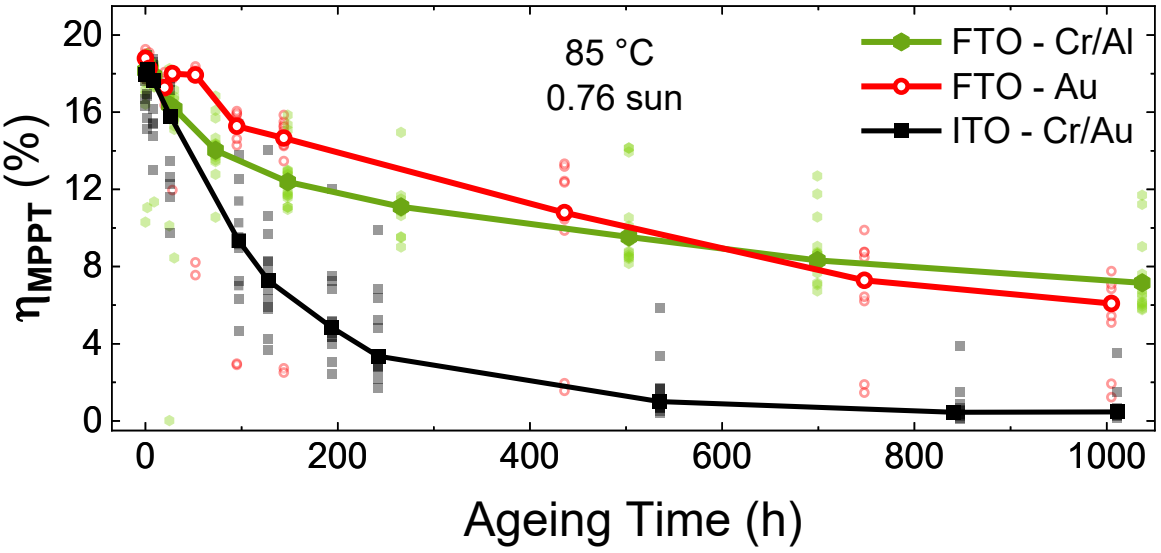



**Figure 6.24 Ageing Behaviour of Different Metal Electrodes on Different Transparent Conductive Oxides**

The ageing behaviour of 24 devices with Cr/Al electrodes on FTO substrates was compared to 12 devices with Au electrodes on FTO and 12 Cr/Au on ITO substrates. The efficiencies were obtained via maximum power point tracking and devices were aged under 0.76 sun equivalent illumination at 85 °C. The three categories were aged in the same ageing box in overlapping intervals. The bold continuous lines and large symbols indicate the median of efficiencies. Smaller semi-transparent symbols show the performance of all devices of each category. Red circles represent the device data of FTO-based devices with Au electrodes, green octagons of FTO devices with Cr/Al and black squares represent the data of ITO-based Cr/Au devices.

## 6.4 Discussion

The diverse range of ageing conditions and electrode materials investigated in this study reveals several important insights. Firstly, the stability of Cr/Au-based devices under different ageing conditions shows notable differences. While the champion device maintains a $T_{85}$ of 20,000 h at 85 °C in the dark, its lifetime is drastically reduced to about 90 h under 0.76 sun illumination at the same temperature (Figure 6.2b and Figure 6.24). This demonstrates the critical role of light exposure in degradation pathways. The high thermal stability highlights the need for combined heat and light stability testing. This stressed the need for sufficiently high temperatures in light-heat ageing tests to fully reveal real-world degradation pathways.

It is frequently discussed in the literature that the work function of the chosen electrode material matters for device performance (choosing deeper work function electrodes like Au for n-i-p and shallower ones like Cu for p-i-n).[226,227] We, however, did not observe this as all tested metals, even though varying widely in terms of their respective work functions, showed very similar device performance (Figure 6.4a). This indicates that metals can be used interchangeably as electrodes for PSC almost independently of their work function in vacuum if good charge selectivity is achieved with the transport layers.

The chrome-coated tungsten wire as a Cr source always showed a green rough surface after being used for evaporation. Like Kaltenbrunner et al.,[48] I assume this green layer to be $Cr_2O_3$. This layer even forms in evaporators in a very low oxygen environment (single-digit ppm $O_2$ in $N_2$). I attribute the high rate of shunted devices in Cr devices fabricated with these Cr sources to small pieces or clusters of chrome oxide being shut out of the source into the devices. Wiping the Cr wire would reduce the rate of shunting but not fully solve it.

The use of non-noble metals like Cu and Al could cause degradation of the contacts outside the actual solar cell device. This could happen for example by metal oxide formation on the contacts outside the encapsulated active area of the device which are needed to contact the device inside the encapsulation. This oxidation could negatively influence the connection to the measurement equipment resulting in an artificially lower device performance being measured. Because device performance remained unchanged when the silver paste was applied to the contact area outside the

encapsulation glass, we understand this as a minor or no issue. Further, four-wire measurements were conducted on Cr/Al devices throughout the third device ageing study (Figure 6.24). In each ageing step, the conductivity of the pad between the two measurement pins was obtained and no connection anomalies were discovered. This hints towards the degradation in Al and Cu devices lying within the device and not the connection strips outside of it.

The main difference in stability between devices with and without 5 nm Cr is a slower reduction in current density (see Figure 6.12d). Therefore, I assume damage to the perovskite layer itself to be a major part of the degradation of devices without a Cr layer. Less noble metals would react with halides leaving the perovskite layer and forming metal halides. This provides a sink for the degradation product of the perovskite layers shifting the reaction equilibrium and accelerating the decomposition reaction. The forming metal halide layer would display a low conductivity and form an interlayer shifting the energetics, explaining the faster reduction in the fill factor of devices without the Cr layer.

The Cr layer prevents the reaction between the metal back electrode and halides leaving the perovskite and this way slows down the perovskite degradation significantly. This effect is visible across all three less noble metals tested. I assume, therefore, that Cr can be used as a universal stability-enhancing buffer layer beneath metals prone to reaction with halides. I observed no stability improvement over Au with Cr/Au electrodes, which contradicts previous literature suggesting a positive effect of this material combination.

We assume the Cr layer to form a very thin oxide layer. This oxide layer provides an impermeable and inert barrier preventing halides from reaching the none-noble metals. I assume, based on the colouration of the Cr sources, that we deposit a $Cr_2O_3$/Cr. The chrome oxide could perform the described barrier function or serve as an oxidation source for the Al:

$$Cr_2O_3 + 2\,Al \rightarrow 2\,Cr + Al_2O_3 \qquad 6.2$$

Both chrome and aluminium oxide are known for their passivating properties towards acids and halides and $Al_2O_3$ has been used as a stable passivation layer in silicon solar cells.[251-255] Further, it has been reported by Xu et al.[233] that the thermal and chemical stability of $(Al_{1-X}Cr_X)_2O_3$ is much higher than that of $Cr_2O_3$. They found that in the $(Al_{1-X}Cr_X)_2O_3$ solid-state solution, the Al fraction

suppressed the formation of Cr(IV) species. The corundum-type solid-state solution $(Al_{1-X}Cr_X)_2O_3$ is frequently used for its excellent structural and thermal stability, including in processes like steel production.[256-258] This could explain the exceptionally high stability of Cr/Al electrodes, comparable to the five orders of magnitude more expensive Au electrodes. The reproducibility of the strong stability within different laboratories and ageing conditions underlines the validity of the finding of the extraordinary stability of this bilayer.

ITO is known to exhibit instability in acidic environments, undergoing degradation through acid-driven etching reactions.[124,125,236] In the context of PSCs, this instability is particularly relevant due to the presence of weak Brønsted acid salts, such as formamidinium-based compounds. Additionally, metal species within the device stack can act as catalysts to etching reactions, potentially accelerating ITO degradation over time. This highlights the susceptibility of ITO to chemical instability in PSC devices in particular.[127]

Kerner et al.[127] showed that when ITO films are in direct contact with a methylammonium lead triiodide ($MAPbI_3$) or a formamidinium lead triiodide ($FAPbI_3$) perovskite layer. A solid-state reaction between the materials can be triggered upon exposure to temperatures of 85 °C or -0.8 V of applied bias. Kerner et al. were able to detect 1 at.% of $InI_3$ on the top surface of a 200 nm thick $MAPbI_3$ film via X-ray photo spectroscopy (XPS) when aged on top of an ITO substrate at 100 °C for one hour. This shows that relatively large amounts of $In^{3+}$ get leached out of the ITO and diffuse throughout the perovskite layer. These results also agree well with our analysis of TOF-SIMS on aged and pristine PSC devices (see Figure 6.18). When normalising the respective counts of indium and lead irons at the top surface of the prospect layer I calculated 1% indium to lead for aged and 3% indium to lead ratio for pristine devices. This shows that one can find significant amounts of indium in the perovskite layer throughout the perovskite layer of as-fabricated PSC on ITO substrates.

Kerner et al.[127] further showed irreversible damage to an ITO/$MAPbI_3$/Au device when cycled once to -0.8 V. Since I age all devices at $V_{OC}$ they were kept for hundreds of hours at voltages higher than -1.0 V which is significantly above the threshold for irreversible damage reported by Kerner et al.[127] via cyclic voltammetry. This allows us to reasonably argue for a voltage-induced degradation reaction of the ITO layer. The results presented in the light-only ageing at 25 °C show that ITO-

based devices show even without heat exposure a quicker degradation than FTO-based devices (Figure 6.16). This ageing condition is, however, difficult to analyse because of possible encapsulation failure due to of thermal cycling causing delamination of the epoxy encapsulation on the much smoother ITO while the encapsulation might stay more intact on the rougher FTO. Encapsulation failure could explain the relatively abrupt device failure observed in ITO-based devices. When kept at 25 °C there might be moisture ingress and condensation taking place on the device. The development of "s-kinks" similar to the behaviour observed in 65 °C and 0.76 suns aged devices, however, indicates at least some degree of intrinsic degradation within the ITO-based devices, independent of encapsulation issues. This suggests that, while encapsulation failure may accelerate degradation, there is an underlying instability of the ITO layer under prolonged illumination and voltage bias.

Zhou et al.[128] studied the effect of indium doping on methylammonium lead triiodide perovskites. They showed that replacing as much as 1% of the lead stoichiometry with indium could negatively influence the photoluminescence of resulting perovskite films. The authors further showed that $In^{3+}$ doping into $MAPbI_3$ causes mid-band-gap states to form, which is consistent with reduced photoluminescence.

We only observed a negative effect of Indium ions on device stability for larger amounts of 1%. While this seems relatively large for impurities, our TOF-SIMS results as well as results by Kerner et al.[127] indicate Indium ions are in fact present in this order of magnitude if not higher inside the perovskite film deposited on ITO. The presence of indium in pristine devices indicates that $In^{3+}$ can etch out of the ITO into the perovskite during device fabrication. I assume that the perovskite annealing at 100 °C provides sufficient thermal energy for this to happen. The indium in the perovskite layer at the start of the ageing is expected to trigger an accelerated photoinduced degradation of the perovskite material in the device. Because of the neglectable difference in indium content in TOF-SIMS of aged and pristine devices, I assume that 65 °C ageing temperature does not cause significant further indium leaching. This ageing temperature can however be considered relatively low.

Possible mechanical issues could contribute to the degradation of PSC devices. It would be possible for these mechanical issues to be more pronounced on the smoother ITO substrates than on the rougher FTO substrates. This explanation is however unlikely to be the only factor because of reduced PLQY of perovskite films aged on ITO substrates. Further, the degradation in charge carrier lifetimes when measuring TRPL using a 635 nm laser cannot be explained by delamination. I expect to probe the bulk perovskite layer with this measurement based on the expected penetration depth of a laser with this wavelength. The faster degradation in lifetime for ITO substrates can only be explained by a degradation of the bulk perovskite layer and not simply by degradation of the interface. The cavities in the SEM cross-sections could be explained by mechanical delamination for example due to thermal cycling during measuring the devices. Another possible explanation could be the perovskite layer being much richer in $In^{3+}$ ions at the bottom interface which in turn could accelerate the degradation and material loss there and cause the cavities. This would be more consistent with the cavities, while being more pronounced at the interface, spreading throughout the entire perovskite film thickness.

In our TOF-SIMS results (see Figure 6.18) there are also significant amounts of sodium ions detected in the perovskite device. It has been suggested that $Na^+$ could substitute for lead in the perovskite lattice, resulting in a negatively charged $Na'_{Pb}$ defect.[237] This defect has, however, been proposed to have a positive and not a negative effect on the optoelectronic properties of the perovskite, increasing conductivity and stability to heat and light-induced degradation.[260-263] Further, as shown in Figure 6.20 and Figure 6.21, films were more stable on a microscope glass slide than on any other substrate. These slides are made of soda lime glass and contain 13 - 15% NaO.[241–244] If $Na^+$ were a problem, I would expect films on this glass to be less stable.

## 6.5 Conclusion

In conclusion, we show that a wide range of metals can be used on identical device stacks without major differences in resulting device performance. However, using cheap industrial metals Cu and Al, results in prohibitively low device stability when aged in light and heat. Using a Cr layer stabilising an Al electrode, we present an electrode configuration with comparable stability with Au

electrodes. I further demonstrate that instabilities caused by indium ions leaching out of ITO through the transport layers can be overcome by replacing it with FTO.

Finally, we show devices with much-improved stability using FTO as the transparent electrode and Cr/Al as the metal electrode. The champion device with Cr/Al and FTO maintained 61% of the maximum MPPT efficiency compared to 40% for the best Au device with FTO. Our findings address a critical gap in PSC technology, where no current electrode solution combines low-cost, resource accessibility, and stability. The Cr/Al bilayer and FTO electrode combination fulfils these requirements by delivering higher stability than Au electrodes while reducing raw material costs by five orders of magnitude and avoiding scarce elements like indium. This result offers a viable path forward for stable, sustainable, and scalable PSC deployment.

# 7 CONCLUSION AND OUTLOOK

In conclusion, this thesis improves the understanding of electrode-related degradation mechanisms in perovskite solar cells. Investigations include different transparent and opaque electrode materials. In Chapter 4 I investigate the electronic contact behaviour of carbon and metal electrodes in p-i-n devices. I find a semiconducting behaviour of the top few nanometres of the carbon electrode material and demonstrate the implications of different processing routes of carbon electrodes for the stability of the resulting devices. These differences between metal and carbon electrodes have been largely overlooked, which may have hindered progress with graphite-based electrode materials in this architecture. This thesis further provides an in-depth analysis of the differences in processing and interface energetics, elucidating why carbon electrodes are easier to implement in n-i-p compared to p-i-n structures. I demonstrate that a dense atomic layer-deposited (ALD) $SnO_2$ layer prevents damage to the underlying PCBM layer by acting as a continuous barrier. When combined with a conductive PH1000 interlayer, it enables ohmic contact with carbon electrodes by preventing the formation of energetic barriers. I achieve this way the first p-i-n perovskite solar cell without any evaporated layer. This approach paves the way for the integration of carbon electrodes into high-throughput perovskite solar cells, including all-perovskite tandem devices, which predominantly utilise p-i-n architecture for tandem applications.

Despite the potential of this structure, I found inadequate stability under light and heat ageing, with the $SnO_2$/electrode interface identified as the primary point of degradation. These results are presented in the first half of Chapter 5.1. While introducing a PH1000 layer improves the stability of this interface, blade-coated carbon electrodes with the $SnO_2$/PH1000/C architecture still display poor long-term stability. In the second half of Chapter 5.1 I present results showing that the long-term stability during heat-light ageing can be further enhanced using laminated instead of blade-coated carbon electrodes. This shows the importance of optimising electrode deposition methods to interface stabilisation and long-term efficiency.

In Chapter 5.2 I show that uniform graphene lamination on perovskite films on a cm-scale is possible. Such a graphene layer can enhance the retention of perovskite film crystallinity and absorption by

orders of magnitude as shown via XRD and optical imaging. However, more research is needed to achieve reliable integration of the laminated graphene into p-i-n PSC devices to achieve a comparable stability advantage to the one observed on thin films.

Besides the implementation and stability assessment, I also present comprehensive results on the influence of transparent and metal electrode materials in Chapter 6. There, I investigate the stability of perovskite solar cells with different metal back electrodes including Au, Ag, Cu, and Al electrodes with and without a Cr nanolayer below them. I demonstrate that a Cr layer universally stabilises all metal non-noble electrodes in the tested devices. Contradicting previous literature, I did not observe an enhancement combined with Au electrodes. The Cr layer resulted in the largest stability enhancement in combination with Al electrodes. I show in multiple ageing studies that the stability of Cr/Al electrodes exceeds the stability of Cr/Au electrodes while reducing material costs by five orders of magnitude.

Additionally, I investigate the comparative stability of the two most commonly used transparent electrode materials for perovskite solar cells: ITO and FTO. Also in Chapter 6 I present a largely improved stability when using FTO instead of ITO electrodes. My results suggest that indium ions leach from ITO into the rest of the device and cause the instability of ITO-based perovskite solar cells. At the end of Chapter 6 I present a stable device architecture using the Cr/Al bilayer in combination with a transparent FTO electrode. The champion device featuring Cr/Al bilayer electrodes and FTO maintained 61% of the maximum MPPT efficiency after over 1,000 h under light ageing at 85 °C, compared to only 40% for the best Au-based device with FTO. These results enable low-cost, highly stable, and scalable electrode alternatives to high-cost Au and unstable non-noble metals.

Further research is needed on the $SnO_2$/electrode interface and the formation of an energetic barrier at that interface to improve the stability of devices using this material. The interface's behaviour must be understood in more detail to prevent degradation and improve the long-term efficiency of p-i-n devices.

The use of laminated carbon electrodes in place of blade-coated electrodes shows promising results at laboratory scale. However, upscaling to industrial processes is necessary to make this technology

commercially viable. The integration of laminated graphene layers into p-i-n perovskite solar cells presents another approach for stability improvement. More research is required to enhance and integrate the lamination technique into devices, ensuring the stability advantages observed at the thin-film level are replicated.

Especially the Cr/Al combination could be easily implemented in industrial processes due to its similarity with other metal deposition techniques already in use. The scalability and industrial viability of the Cr/Al bilayer and FTO electrode combination should be further explored. The low material cost and stability of this configuration offer a significant advantage in both sustainability and performance. However, the practical implementation of this electrode structure requires further optimisation to achieve consistent performance addressing the larger spread in devices using Cr layers. Additionally, alternatives to ITO should be considered, particularly in light of the instability caused by indium leaching and the scarcity of indium as a raw material. The solution of replacing ITO with FTO here presented might not be feasible for all applications because of the lack of some processing routes for FTO including via sputtering and with lower temperatures. These challenges should be addressed in future work.

In summary, this thesis advances the understanding of electrode-induced degradation mechanisms in perovskite solar cells, particularly in p-i-n architectures. The findings on carbon electrodes, ALD $SnO_2$/PH1000, and Cr/Al bilayers provide pathways for improved stability and cost-effectiveness. However, key challenges in interface engineering remain, especially for carbon electrodes and the $SnO_2$ interface, as well as for the perovskite graphene interface. This work serves as a foundation for integrating carbon electrodes into multijunction and p-i-n devices, aligning with the broader trends in perovskite solar cell research and presenting a competitive, stable, and cost-effective metal electrode solution.

# 8 REFERENCES


1. Morgera, E. Promotion and protection of human rights in the context of climate change. https://doi.org/10.1163/9789004322714_cclc_2023-0165-0781 (2024).
2. UNESCO. *The World in 2030: Public Survey Report*. (2021).
3. Copernicus: 2024 is the first year to exceed 1.5°C above pre-industrial level | Copernicus. https://climate.copernicus.eu/copernicus-2024-first-year-exceed-15degc-above-pre-industrial-level (2025).
4. Calvin, K. *et al. IPCC, 2023: Climate Change 2023: Synthesis Report. Contribution of Working Groups I, II and III to the Sixth Assessment Report of the Intergovernmental Panel on Climate Change [Core Writing Team, H. Lee and J. Romero (Eds.)]. IPCC, Geneva, Switzerland.* https://www.ipcc.ch/report/ar6/syr/ (2023) doi:10.59327/IPCC/AR6-9789291691647.
5. Keeling, R. F., Morgan, E. J. & Keeling, C. D. Atmospheric Monthly In Situ CO2 Data - Mauna Loa Observatory, Hawaii (Archive 2024-11-13). In *Scripps CO2 Program Data. UC San Diego Library Digital Collections*. (2017).
6. Bazin, L. *et al.* NOAA/WDS Paleoclimatology - AICC2012 800KYr Antarctic Ice Core Chronology. NOAA National Centers for Environmental Information https://doi.org/10.25921/MSPS-9989.
7. Bereiter, B. *et al.* NOAA/WDS Paleoclimatology - Antarctic Ice Cores Revised 800KYr CO2 Data. NOAA National Centers for Environmental Information https://doi.org/10.25921/N8Y4-BP27.
8. Bereiter, B. *et al.* NOAA/WDS Paleoclimatology - EDML-Talos Dome Antarctic Ice Core 38-115KYrBP CO2 Data. NOAA National Centers for Environmental Information https://doi.org/10.25921/4VKS-EX31.
9. MacFarling Meure, C. *et al.* NOAA/WDS Paleoclimatology - Law Dome Ice Core 2000-Year CO2, CH4, and N2O Data. NOAA National Centers for Environmental Information https://doi.org/10.25921/G6KD-K189.

10. Lüthi, D. *et al.* High-resolution carbon dioxide concentration record 650,000–800,000 years before present. *Nature* **453**, 379–382 (2008).

11. Petit, J. R. *et al.* Climate and atmospheric history of the past 420,000 years from the Vostok ice core, Antarctica. *Nature* **399**, 429–436 (1999).

12. Freyer, H. D. & Wiesberg, L. Dendrochronology and 13C content in atmospheric CO2. *Nature* **252**, 757–757 (1974).

13. Graven, H., Keeling, R. F. & Rogelj, J. Changes to Carbon Isotopes in Atmospheric CO2 Over the Industrial Era and Into the Future. *Glob. Biogeochem. Cycles* **34**, e2019GB006170 (2020).

14. Ikeda, S., Shirakawa, H. & Hattori, I. The Relationship between the Atmospheric Carbon Dioxide Concentration and the Carbon-14 Activity in Tokyo. *Bull. Chem. Soc. Jpn.* **49**, 3697–3698 (1976).

15. Zhong, W. & Haigh, J. D. The greenhouse effect and carbon dioxide. *Weather* **68**, 100–105 (2013).

16. Durand, G. *et al.* Sea-Level Rise: From Global Perspectives to Local Services. *Front. Mar. Sci.* **8**, (2022).

17. Intergovernmental Panel On Climate Change (Ipcc). *The Ocean and Cryosphere in a Changing Climate: Special Report of the Intergovernmental Panel on Climate Change*. (Cambridge University Press, 2022). doi:10.1017/9781009157964.

18. Ngcamu, B. S. Climate change effects on vulnerable populations in the Global South: a systematic review. *Nat. Hazards* **118**, 977–991 (2023).

19. Hallegatte, S., Fay, M. & Barbier, E. B. Poverty and climate change: introduction. *Environ. Dev. Econ.* **23**, 217–233 (2018).

20. Ritchie, H., Rosado, P. & Roser, M. Sector by sector: where do global greenhouse gas emissions come from? (2024).

21. Moomaw, W. F. Introduction. in *IPCC Special Report on Renewable Energy Sources and Climate Change Mitigation* (2011).

22. Masson-Delmotte, V. P.-O.-O. *IPCC, 2018: Summary for Policymakers. In: Global Warming of 1.5°C. An IPCC Special Report on the Impacts of Global Warming of 1.5°C above Pre-*

*Industrial Levels and Related Global Greenhouse Gas Emission Pathways, in the Context of Strengthening the Global*. (2018).

23. Hossain, M. F. Estimation of Global Solar Energy to Mitigate World Energy and Environmental Vulnerability. in *Renewable Energy for Mitigating Climate Change* (CRC Press, 2021).
24. Dale, S. *BP Statistical Review of World Energy*. (BP Plc, London, UK, 2021).
25. Perez, R. & Perez, M. A fundamental look at energy reserves for the planet. *IEA SHC Sol. Update* **50**, (2009).
26. Perez, M. & Perez, R. Update 2022 – A fundamental look at supply side energy reserves for the planet. *Sol. Energy Adv.* **2**, 100014 (2022).
27. Singh, G. K. Solar power generation by PV (photovoltaic) technology: A review. *Energy* **53**, 1–13 (2013).
28. Best Research-Cell Efficiency Chart | Photovoltaic Research | NREL. https://www.nrel.gov/pv/cell-efficiency.
29. Green, M. A. The path to 25% silicon solar cell efficiency: History of silicon cell evolution. *Prog. Photovolt. Res. Appl.* **17**, 183–189 (2009).
30. Dr. Simon Philipps and Werner Warmuth. *Photovoltaics Report - Fraunhofer ISE*. https://www.ise.fraunhofer.de/en/publications/studies/photovoltaics-report.html (2024).
31. Ballif, C., Haug, F.-J., Boccard, M., Verlinden, P. J. & Hahn, G. Status and perspectives of crystalline silicon photovoltaics in research and industry. *Nat. Rev. Mater.* **7**, 597–616 (2022).
32. Lazard. Levelized Cost of Energy. *https://www.lazard.com* https://www.lazard.com/research-insights/levelized-cost-of-energyplus/ (2025).
33. International Energy Agency. *An Updated Roadmap to Net Zero Emissions by 2050 – World Energy Outlook 2022 – Analysis*. https://www.iea.org/reports/world-energy-outlook-2022/an-updated-roadmap-to-net-zero-emissions-by-2050 (2022).
34. Panasonic Corporation of North America. AllGuard Warranty. https://solar.na.panasonic.com/warranty/allguard (2025).
35. Schinke, C. *et al.* Uncertainty analysis for the coefficient of band-to-band absorption of crystalline silicon. *AIP Adv.* **5**, 067168 (2015).

36. Yu, X. & Yang, D. Growth of Crystalline Silicon for Solar Cells: Czochralski Si. in *Handbook of Photovoltaic Silicon* (ed. Yang, D.) 129–174 (Springer Berlin Heidelberg, Berlin, Heidelberg, 2019). doi:10.1007/978-3-662-56472-1_12.

37. Jiao, Y. *et al.* Siemens and siemens-like processes for producing photovoltaics: Energy payback time and lifetime carbon emissions. *JOM* **63**, 28–31 (2011).

38. Green, M. A. Thin-film solar cells: review of materials, technologies and commercial status. *J. Mater. Sci. Mater. Electron.* **18**, 15–19 (2007).

39. Diethelm, M. *et al.* Probing ionic conductivity and electric field screening in perovskite solar cells: a novel exploration through ion drift currents. *Energy Environ. Sci.* **18**, 1385–1397 (2025).

40. Snaith, H. J. *et al.* Anomalous Hysteresis in Perovskite Solar Cells. *J. Phys. Chem. Lett.* **5**, 1511–1515 (2014).

41. Bulloch, A., Wang, S., Ghosh, P. & Jagadamma, L. K. Hysteresis in hybrid perovskite indoor photovoltaics. *Philos. Trans. R. Soc. Math. Phys. Eng. Sci.* **380**, 20210144 (2022).

42. Yin, M. *et al.* Accurate and fast evaluation of perovskite solar cells with least hysteresis. *Appl. Phys. Express* **10**, 076601 (2017).

43. Chen, B., Yang, M., Priya, S. & Zhu, K. Origin of J – V Hysteresis in Perovskite Solar Cells. *J. Phys. Chem. Lett.* **7**, 905–917 (2016).

44. Zhang, W., Eperon, G. E. & Snaith, H. J. Metal halide perovskites for energy applications. *Nat. Energy* **1**, 1–8 (2016).

45. Grätzel, M. The light and shade of perovskite solar cells. *Nat. Mater.* **13**, 838–842 (2014).

46. Wehrenfennig, C., Eperon, G. E., Johnston, M. B., Snaith, H. J. & Herz, L. M. High charge carrier mobilities and lifetimes in organolead trihalide perovskites. *Adv. Mater. Deerfield Beach Fla* **26**, 1584 (2013).

47. Sutherland, L. J. *et al.* Vacuum-Free and Solvent-Free Deposition of Electrodes for Roll-to-Roll Fabricated Perovskite Solar Cells. *Adv. Energy Mater.* **12**, 2202142 (2022).

48. Kaltenbrunner, M. *et al.* Flexible high power-per-weight perovskite solar cells with chromium oxide–metal contacts for improved stability in air. *Nat. Mater.* **14**, 1032–1039 (2015).

49. Liu, D., Yang, C. & Lunt, R. R. Halide Perovskites for Selective Ultraviolet-Harvesting Transparent Photovoltaics. *Joule* **2**, 1827–1837 (2018).

50. Navrotsky, A. *Energetics and Crystal Chemical Systematics among Ilmenite, Lithium Niobate, and Perovskite Structures*. (Chemistry of Materials, 1998).

51. Kilner, J. Perovskites. in *Concise Encyclopedia of Advanced Ceramic Materials* 349–351 (Pergamon Press plc, 1991). doi:10.1016/B978-0-08-034720-2.50096-4.

52. Giovanni, D. Optical-Spin Dynamics In Organic-Inorganic Hybrid Lead Halide Perovskites. (Nanyang Technological University, Singapore, 2017).

53. Park, B. *et al.* Stabilization of formamidinium lead triiodide α-phase with isopropylammonium chloride for perovskite solar cells. *Nat. Energy* **6**, 419–428 (2021).

54. Kojima, A., Teshima, K., Shirai, Y. & Miyasaka, T. Organometal Halide Perovskites as Visible-Light Sensitizers for Photovoltaic Cells. *J. Am. Chem. Soc.* **131**, 6050–6051 (2009).

55. Bermúdez-García, J. M. *et al.* Multiple phase and dielectric transitions on a novel multi-sensitive [TPrA][M (dca) 3](M: Fe 2+, Co 2+ and Ni 2+) hybrid inorganic–organic perovskite family. *J. Mater. Chem. C* **4**, 4889–4898 (2016).

56. Tonui, P., Oseni, S. O., Sharma, G., Yan, Q. & Mola, G. T. Perovskites photovoltaic solar cells: An overview of current status. *Renew. Sustain. Energy Rev.* **91**, 1025–1044 (2018).

57. Gholipour, S. *et al.* Globularity-Selected Large Molecules for a New Generation of Multication Perovskites. *Adv. Mater.* **29**, 1702005 (2017).

58. Saliba, M. *et al.* Cesium-containing triple cation perovskite solar cells: improved stability, reproducibility and high efficiency. *Energy Environ. Sci.* **9**, 1989–1997 (2016).

59. Saliba, M. *et al.* Incorporation of rubidium cations into perovskite solar cells improves photovoltaic performance. *Science* **354**, 206–209 (2016).

60. Eperon, G. E. *et al.* Perovskite-perovskite tandem photovoltaics with optimized band gaps. *Science* **354**, 861–865 (2016).

61. Forgács, D. *et al.* Efficient wide band gap double cation – double halide perovskite solar cells. *J. Mater. Chem. A* **5**, 3203–3207 (2017).

62. McMeekin, D. P. *et al.* A mixed-cation lead mixed-halide perovskite absorber for tandem solar cells. *Science* **351**, 151–155 (2016).

63. Lin, Y.-H. *et al.* A piperidinium salt stabilizes efficient metal-halide perovskite solar cells. *Science* **369**, 96–102 (2020).

64. Yin, W.-J., Shi, T. & Yan, Y. Unique Properties of Halide Perovskites as Possible Origins of the Superior Solar Cell Performance. *Adv. Mater.* **26**, 4653–4658 (2014).

65. Kim, G.-W. & Petrozza, A. Defect Tolerance and Intolerance in Metal-Halide Perovskites. *Adv. Energy Mater.* **10**, 2001959 (2020).

66. Wang, F., Bai, S., Tress, W., Hagfeldt, A. & Gao, F. Defects engineering for high-performance perovskite solar cells. *Npj Flex. Electron.* **2**, 1–14 (2018).

67. Cho, S. H. *et al.* Investigation of Defect-Tolerant Perovskite Solar Cells with Long-Term Stability via Controlling the Self-Doping Effect. *Adv. Energy Mater.* **11**, 2100555 (2021).

68. Park, B. *et al.* Chemical engineering of methylammonium lead iodide/bromide perovskites: tuning of opto-electronic properties and photovoltaic performance. *J. Mater. Chem. A* **3**, 21760–21771 (2015).

69. Grancini, G. *et al.* One-Year stable perovskite solar cells by 2D/3D interface engineering. *Nat. Commun.* **8**, 15684 (2017).

70. Boyd, C. C., Cheacharoen, R., Leijtens, T. & McGehee, M. D. Understanding Degradation Mechanisms and Improving Stability of Perovskite Photovoltaics. *Chem. Rev.* **119**, 3418–3451 (2019).

71. Domanski, K. *et al.* Not All That Glitters Is Gold: Metal-Migration-Induced Degradation in Perovskite Solar Cells. *ACS Nano* **10**, 6306–6314 (2016).

72. Zhang, C. *et al.* A Review on Recent Development of Cooling Technologies for Photovoltaic Modules. *J. Therm. Sci.* **29**, 1410–1430 (2020).

73. Yuan, H. *et al.* Degradation of Methylammonium Lead Iodide Perovskite Structures through Light and Electron Beam Driven Ion Migration. *J. Phys. Chem. Lett.* **7**, 561–566 (2016).

74. Misra, R. K. *et al.* Temperature- and Component-Dependent Degradation of Perovskite Photovoltaic Materials under Concentrated Sunlight. *J. Phys. Chem. Lett.* **6**, 326–330 (2015).

75. Conings, B. *et al.* Intrinsic Thermal Instability of Methylammonium Lead Trihalide Perovskite. *Adv. Energy Mater.* **5**, 1500477 (2015).

76. Shi, L. *et al.* Gas chromatography–mass spectrometry analyses of encapsulated stable perovskite solar cells. *Science* **368**, eaba2412 (2020).

77. Niu, G., Li, W., Li, J., Liang, X. & Wang, L. Enhancement of thermal stability for perovskite solar cells through cesium doping. *RSC Adv.* **7**, 17473–17479 (2017).

78. Habisreutinger, S. N., McMeekin, D. P., Snaith, H. J. & Nicholas, R. J. Research Update: Strategies for improving the stability of perovskite solar cells. *APL Mater.* **4**, 091503 (2016).

79. Zhao, J. *et al.* Strained hybrid perovskite thin films and their impact on the intrinsic stability of perovskite solar cells. *Sci. Adv.* **3**, eaao5616 (2017).

80. Rolston, N. *et al.* Engineering Stress in Perovskite Solar Cells to Improve Stability. *Adv. Energy Mater.* **8**, 1802139 (2018).

81. Erdil, U. *et al.* Delamination of Perovskite Solar Cells in Thermal Cycling and Outdoor Tests. *Energy Technol.* **13**, 2401280 (2025).

82. Guha, S., Kazi, I., Nandy, A. & Sekar, G. Role of Lewis-Base-Coordinated Halogen(I) Intermediates in Organic Synthesis: The Journey from Unstable Intermediates to Versatile Reagents. *Eur. J. Org. Chem.* **2017**, 5497–5518 (2017).

83. Lancaster, N. L., Welton, T. & Young, G. B. A study of halide nucleophilicity in ionic liquids. *J. Chem. Soc. Perkin Trans. 2* 2267–2270 (2001) doi:10.1039/B107381H.

84. Kato, Y. *et al.* Silver Iodide Formation in Methyl Ammonium Lead Iodide Perovskite Solar Cells with Silver Top Electrodes. *Adv. Mater. Interfaces* **2**, 1500195 (2015).

85. Meng, H. *et al.* Inhibition of halide oxidation and deprotonation of organic cations with dimethylammonium formate for air-processed p–i–n perovskite solar cells. *Nat. Energy* **9**, 536–547 (2024).

86. Zhao, L. *et al.* Redox Chemistry Dominates the Degradation and Decomposition of Metal Halide Perovskite Optoelectronic Devices. *ACS Energy Lett.* **1**, 595–602 (2016).

87. Wang, S., Jiang, Y., Juarez-Perez, E. J., Ono, L. K. & Qi, Y. Accelerated degradation of methylammonium lead iodide perovskites induced by exposure to iodine vapour. *Nat. Energy* **2**, 1–8 (2016).

88. Motti, S. G. *et al.* Controlling competing photochemical reactions stabilizes perovskite solar cells. *Nat. Photonics* **13**, 532–539 (2019).

89. Rehman, W. *et al.* Photovoltaic mixed-cation lead mixed-halide perovskites: links between crystallinity, photo-stability and electronic properties. *Energy Environ. Sci.* **10**, 361–369 (2017).

90. Ming, W., Yang, D., Li, T., Zhang, L. & Du, M.-H. Formation and Diffusion of Metal Impurities in Perovskite Solar Cell Material CH3NH3PbI3: Implications on Solar Cell Degradation and Choice of Electrode. *Adv. Sci.* **5**, 1700662 (2018).

91. Wu, S. *et al.* A chemically inert bismuth interlayer enhances long-term stability of inverted perovskite solar cells. *Nat. Commun.* **10**, 1161 (2019).

92. Lim, J. *et al.* Revealing the Dynamics of the Thermal Reaction between Copper and Mixed Halide Perovskite Solar Cells. *ACS Appl. Mater. Interfaces* **14**, 20866–20874 (2022).

93. Deng, Y., Dong, Q., Bi, C., Yuan, Y. & Huang, J. Air-Stable, Efficient Mixed-Cation Perovskite Solar Cells with Cu Electrode by Scalable Fabrication of Active Layer. *Adv. Energy Mater.* **6**, 1600372 (2016).

94. Xu, Z. *et al.* Halogen Redox Shuttle Explains Voltage-Induced Halide Redistribution in Mixed-Halide Perovskite Devices. *ACS Energy Lett.* **8**, 513–520 (2023).

95. Seo, S., Jeong, S., Bae, C., Park, N. & Shin, H. Perovskite Solar Cells with Inorganic Electron- and Hole-Transport Layers Exhibiting Long-Term (≈500 h) Stability at 85 °C under Continuous 1 Sun Illumination in Ambient Air. *Adv. Mater.* **30**, 1801010 (2018).

96. Boyd, C. C. *et al.* Barrier Design to Prevent Metal-Induced Degradation and Improve Thermal Stability in Perovskite Solar Cells. *ACS Energy Lett.* **3**, 1772–1778 (2018).

97. Lang, D. V., Grimmeiss, H. G., Meijer, E. & Jaros, M. Complex nature of gold-related deep levels in silicon. *Phys. Rev. B* **22**, 3917–3934 (1980).

98. Bulowski, W. *et al.* Optimization of the ETL titanium dioxide layer for inorganic perovskite solar cells. *J. Mater. Sci.* **59**, 7283–7298 (2024).

99. Li, T., Yang, P., Wang, Y. & Yan, T. Research Progress on Modified-Titanium Dioxide Electron Transport Layers in Perovskite Solar Cells. *Mod. Phys. Chem. Res.* **4**, 88–92 (2024).

100. Zhu, Z. *et al.* High-Performance Hole-Extraction Layer of Sol–Gel-Processed NiO Nanocrystals for Inverted Planar Perovskite Solar Cells. *Angew. Chem. Int. Ed.* **53**, 12571–12575 (2014).

101. Seo, S. *et al.* An ultra-thin, un-doped NiO hole transporting layer of highly efficient (16.4%) organic–inorganic hybrid perovskite solar cells. *Nanoscale* **8**, 11403–11412 (2016).

102. Marley, F. A. *et al.* First-Principles Approach to Finite Element Simulation of Flexible Photovoltaics. *Energies* **17**, 4064 (2024).

103. Al-Mamun, M. R., Kader, S., Islam, M. S. & Khan, M. Z. H. Photocatalytic activity improvement and application of UV-TiO2 photocatalysis in textile wastewater treatment: A review. *J. Environ. Chem. Eng.* **7**, 103248 (2019).

104. Nakata, K. & Fujishima, A. TiO2 photocatalysis: Design and applications. *J. Photochem. Photobiol. C Photochem. Rev.* **13**, 169–189 (2012).

105. Shayegan, Z., Lee, C.-S. & Haghighat, F. TiO2 photocatalyst for removal of volatile organic compounds in gas phase – A review. *Chem. Eng. J.* **334**, 2408–2439 (2018).

106. Bhattu, M., Acevedo, R. & Alhadrawi, M. NiO as a promising photocatalyst for wastewater purification: A review. *E3S Web Conf.* **588**, 02013 (2024).

107. Motahari, F., Reza Mozdianfard, M., Soofivand, F. & Salavati-Niasari, M. NiO nanostructures: synthesis, characterization and photocatalyst application in dye wastewater treatment. *RSC Adv.* **4**, 27654–27660 (2014).

108. Leijtens, T. *et al.* Overcoming ultraviolet light instability of sensitized TiO2 with meso-superstructured organometal tri-halide perovskite solar cells. *Nat. Commun.* **4**, 2885 (2013).

109. Choi, J., Song, S., Hörantner, M. T., Snaith, H. J. & Park, T. Well-Defined Nanostructured, Single-Crystalline TiO2 Electron Transport Layer for Efficient Planar Perovskite Solar Cells. *ACS Nano* **10**, 6029–6036 (2016).

110. Wang, K.-P. *et al.* Detrimental Defect Cooperativity at TiO2/CH3NH3PbI3 Interface: Decreased Stability, Enhanced Ion Diffusion, and Reduced Charge Lifetime and Transport. *ACS Energy Lett.* **9**, 5888–5897 (2024).

111. Mohanraj, J. *et al.* NiOx Passivation in Perovskite Solar Cells: From Surface Reactivity to Device Performance. *ACS Appl. Mater. Interfaces* **16**, 42835–42850 (2024).

112. Xu, Z. *et al.* Self-Assembled Monolayer Suppresses Interfacial Reaction between NiOx and Perovskite for Efficient and Stable Inverted Inorganic Perovskite Solar Cells. *ACS Appl. Mater. Interfaces* **16**, 53811–53821 (2024).

113. Tiwari, N. *et al.* Advances and Potentials of NiO Surface Treatments for p−i−n Perovskite Solar Cells. *Sol. RRL* **6**, 2100700 (2022).

114. Peng, J. *et al.* Interface passivation using ultrathin polymer–fullerene films for high-efficiency perovskite solar cells with negligible hysteresis. *Energy Environ. Sci.* **10**, 1792–1800 (2017).

115. Liu, J. *et al.* Electron injection and defect passivation for high-efficiency mesoporous perovskite solar cells. *Science* **383**, 1198–1204 (2024).

116. Ke, W. *et al.* Low-Temperature Solution-Processed Tin Oxide as an Alternative Electron Transporting Layer for Efficient Perovskite Solar Cells. *J. Am. Chem. Soc.* **137**, 6730–6733 (2015).

117. Jiang, Q., Zhang, X. & You, J. SnO2: A Wonderful Electron Transport Layer for Perovskite Solar Cells. *Small* **14**, 1801154 (2018).

118. Girolamo, D. D. *et al.* Progress, highlights and perspectives on NiO in perovskite photovoltaics. *Chem. Sci.* **11**, 7746–7759 (2020).

119. Nath, B., Ramamurthy, P. C., Hegde, G. & Roy Mahapatra, D. Role of electrodes on perovskite solar cells performance: A review. *ISSS J. Micro Smart Syst.* **11**, 61–79 (2022).

120. Sittinger, V. *et al.* Indium-based transparent conductive oxides developed for perovskite and perovskite-silicon tandem solar cell applications. *Surf. Coat. Technol.* **457**, 129286 (2023).

121. Zhu, H. *et al.* In situ energetics modulation enables high-efficiency and stable inverted perovskite solar cells. *Nat. Photonics* **19**, 28–35 (2025).

122. Hou, F. *et al.* Monolithic perovskite/silicon tandem solar cells: A review of the present status and solutions toward commercial application. *Nano Energy* **124**, 109476 (2024).

123. Mariotti, S. *et al.* Interface engineering for high-performance, triple-halide perovskite–silicon tandem solar cells. *Science* **381**, 63–69 (2023).

124. Afre, R. A., Sharma, N., Sharon, M. & Sharon, M. Transparent Conducting Oxide Films for Various Applications: A Review. *Rev. Adv. Mater. Sci.* **53**, 79–89 (2018).

125. Choi, J.-H., Kim, S.-O., Hilton, D. L. & Cho, N.-J. Acid-catalyzed kinetics of indium tin oxide etching. *Thin Solid Films* **565**, 179–185 (2014).

126. Park, S. M. *et al.* Engineering ligand reactivity enables high-temperature operation of stable perovskite solar cells. *Science* **381**, 209–215 (2023).

127. Kerner, R. A. & Rand, B. P. Electrochemical and Thermal Etching of Indium Tin Oxide by Solid-State Hybrid Organic–Inorganic Perovskites. *ACS Appl. Energy Mater.* **2**, 6097–6101 (2019).

128. Zhou, L. *et al.* Theoretical and Experimental Investigation of Mixed Pb–In Halide Perovskites. *J. Phys. Chem. C* **122**, 15945–15953 (2018).

129. Chung, D. D. L. Review graphite. *J. Mater. Sci.* **37**, 1475–1489 (2002).

130. Jiang, P. *et al.* Fully printable perovskite solar cells with highly-conductive, low-temperature, perovskite-compatible carbon electrode. *Carbon* **129**, 830–836 (2018).

131. Bogachuk, D. *et al.* Low-temperature carbon-based electrodes in perovskite solar cells. *Energy Environ. Sci.* **13**, 3880–3916 (2020).

132. Wang, Q., Phung, N., Girolamo, D. D., Vivo, P. & Abate, A. Enhancement in lifespan of halide perovskite solar cells. *Energy Environ. Sci.* **12**, 865–886 (2019).

133. Meng, F. *et al.* Current progress in interfacial engineering of carbon-based perovskite solar cells. *J. Mater. Chem. A* **7**, 8690–8699 (2019).

134. Hadadian, M., Smått, J.-H. & Correa-Baena, J.-P. The role of carbon-based materials in enhancing the stability of perovskite solar cells. *Energy Environ. Sci.* **13**, 1377–1407 (2020).

135. Chang, N. L. *et al.* A manufacturing cost estimation method with uncertainty analysis and its application to perovskite on glass photovoltaic modules. *Prog. Photovolt. Res. Appl.* **25**, 390–405 (2017).

136. Fagiolari, L. & Bella, F. Carbon-based materials for stable, cheaper and large-scale processable perovskite solar cells. *Energy Environ. Sci.* **12**, 3437–3472 (2019).

137. Dera, B. Preismonitor März 2024. https://www.deutsche-rohstoffagentur.de/DERA/DE/Produkte/Rohstoffpreise/Preismonitor/preismonitor_node.html (2024).

138. Su, H. *et al.* Carbon film electrode based square-centimeter scale planar perovskite solar cells exceeding 17% efficiency. *Mater. Sci. Semicond. Process.* **107**, 104809 (2020).

139. Zhou, C. & Lin, S. Carbon-Electrode Based Perovskite Solar Cells: Effect of Bulk Engineering and Interface Engineering on the Power Conversion Properties. *Sol. RRL* **4**, 1900190 (2020).

140. Tian, C. *et al.* Oxygen management in carbon electrode for high-performance printable perovskite solar cells. *Nano Energy* **53**, 160–167 (2018).

141. Duan, M. *et al.* Boron-Doped Graphite for High Work Function Carbon Electrode in Printable Hole-Conductor-Free Mesoscopic Perovskite Solar Cells. *ACS Appl. Mater. Interfaces* **9**, 31721–31727 (2017).

142. Bi, E. *et al.* Diffusion engineering of ions and charge carriers for stable efficient perovskite solar cells. *Nat. Commun.* **8**, 15330 (2017).

143. Gholipour, S. *et al.* Highly Efficient and Stable Perovskite Solar Cells based on a Low-Cost Carbon Cloth. *Adv. Energy Mater.* **6**, (2016).

144. Baranwal, A. K. *et al.* 100 °C Thermal Stability of Printable Perovskite Solar Cells Using Porous Carbon Counter Electrodes. *ChemSusChem* **9**, 2604–2608 (2016).

145. Li, X. *et al.* Outdoor Performance and Stability under Elevated Temperatures and Long-Term Light Soaking of Triple-Layer Mesoporous Perovskite Photovoltaics. *Energy Technol.* **3**, 551–555 (2015).

146. Wu, Z. *et al.* Highly Efficient and Stable Perovskite Solar Cells via Modification of Energy Levels at the Perovskite/Carbon Electrode Interface. *Adv. Mater.* **31**, 1804284 (2019).

147. Tan, W., Bowring, A. R., Meng, A. C., McGehee, M. D. & McIntyre, P. C. Thermal Stability of Mixed Cation Metal Halide Perovskites in Air. *ACS Appl. Mater. Interfaces* **10**, 5485–5491 (2018).

148. Kay, A. & Grätzel, M. Low cost photovoltaic modules based on dye sensitized nanocrystalline titanium dioxide and carbon powder. *Sol. Energy Mater. Sol. Cells* **44**, 99–117 (1996).

149. Ku, Z., Rong, Y., Xu, M., Liu, T. & Han, H. Full Printable Processed Mesoscopic CH3NH3PbI3/TiO2 Heterojunction Solar Cells with Carbon Counter Electrode. *Sci. Rep.* **3**, 3132 (2013).

150. Bogachuk, D. *et al.* Perovskite Solar Cells with Carbon-Based Electrodes – Quantification of Losses and Strategies to Overcome Them. *Adv. Energy Mater.* **12**, 2103128 (2022).

151. Pockett, A. *et al.* Origin of Exceptionally Slow Light Soaking Effect in Mesoporous Carbon Perovskite Solar Cells with AVA Additive. *J. Phys. Chem. C* **123**, 11414–11421 (2019).

152. Lu, X. *et al.* Efficient carbon electrode perovskite solar cells with robust buffer interfaces. *J. Mater. Res. Technol.* **24**, 8162–8170 (2023).

153. Li, Y. *et al.* Blade-Coated Carbon Electrode Perovskite Solar Cells to Exceed 20% Efficiency Through Protective Buffer Layers. *Adv. Funct. Mater.* **33**, 2301920 (2023).

154. Beynon, D. *et al.* All-Printed Roll-to-Roll Perovskite Photovoltaics Enabled by Solution-Processed Carbon Electrode. *Adv. Mater.* **35**, 2208561 (2023).

155. Zouhair, S. *et al.* Employing 2D-Perovskite as an Electron Blocking Layer in Highly Efficient (18.5%) Perovskite Solar Cells with Printable Low Temperature Carbon Electrode. *Adv. Energy Mater.* **12**, 2200837 (2022).

156. Ahn, N. *et al.* Trapped charge-driven degradation of perovskite solar cells. *Nat. Commun.* **7**, 13422 (2016).

157. Elmolla, E. S. & Chaudhuri, M. Photocatalytic degradation of amoxicillin, ampicillin and cloxacillin antibiotics in aqueous solution using UV/TiO2 and UV/H2O2/TiO2 photocatalysis. *Desalination* **252**, 46–52 (2010).

158. Babu, V. *et al.* Improved Stability of Inverted and Flexible Perovskite Solar Cells with Carbon Electrode. *ACS Appl. Energy Mater.* **3**, 5126–5134 (2020).

159. Zhang, X. *et al.* Efficient and carbon-based hole transport layer-free CsPbI 2 Br planar perovskite solar cells using PMMA modification. *J. Mater. Chem. C* **7**, 3852–3861 (2019).

160. Zouhair, S. *et al.* Fill Factor Assessment in Hole Selective Layer Free Carbon Electrode-Based Perovskite Solar Cells with 15.5% Certified Power Conversion Efficiency. *Sol. RRL* **6**, 2100745 (2022).

161. Zhang, H. *et al.* High-efficiency (>20%) planar carbon-based perovskite solar cells through device configuration engineering. *J. Colloid Interface Sci.* **608**, 3151–3158 (2022).

162. Sutherland, L. J. *et al.* A high-pressure isostatic lamination technique to fabricate versatile carbon electrode-based perovskite solar cells. *Commun. Mater.* **5**, 1–9 (2024).

163. Zhang, H. *et al.* Self-Adhesive Macroporous Carbon Electrodes for Efficient and Stable Perovskite Solar Cells. *Adv. Funct. Mater.* **28**, 1802985 (2018).

164. Sepalage, G. A. *et al.* Can Laminated Carbon Challenge Gold? Toward Universal, Scalable, and Low-Cost Carbon Electrodes for Perovskite Solar Cells. *Adv. Mater. Technol.* **7**, 2101148 (2022).

165. Jeon, N. J. *et al.* Solvent engineering for high-performance inorganic–organic hybrid perovskite solar cells. *Nat. Mater.* **13**, 897–903 (2014).

166. Taylor, A. D. *et al.* A general approach to high-efficiency perovskite solar cells by any antisolvent. *Nat. Commun.* **12**, 1878 (2021).

167. Mohammadzadeh, H. Post-Deposition Treatment of Laminated Carbon Top-Electrodes for Fabrication of Efficient Perovskite Solar Cells. *Adv. Energy Mater. Manuscr. Prep.* (2025).

168. de Mello, J. C., Wittmann, H. F. & Friend, R. H. An improved experimental determination of external photoluminescence quantum efficiency. *Adv. Mater.* **9**, 230–232 (1997).

169. Carron, R. *et al.* Bandgap of thin film solar cell absorbers: A comparison of various determination methods. *Thin Solid Films* **669**, 482–486 (2019).

170. Lyu, B., Yang, L., Luo, Y., Zhang, X. & Zhang, J. Counter electrodes for perovskite solar cells: materials, interfaces and device stability. *J. Mater. Chem. C* **10**, 10775–10798 (2022).

171. Kerner, R. A. *et al.* Reactions at noble metal contacts with methylammonium lead triiodide perovskites: Role of underpotential deposition and electrochemistry. *APL Mater.* **7**, 041103 (2019).

172. Wagner, L. *et al.* The resource demands of multi-terawatt-scale perovskite tandem photovoltaics. *Joule* **8**, 1142–1160 (2024).

173. Rehman, A. ur *et al.* Electrode metallization for scaled perovskite/silicon tandem solar cells: Challenges and opportunities. *Prog. Photovolt. Res. Appl.* **31**, 429–442 (2023).

174. Einspruch, N. G., Cohen, S. S. & Gildenblat, G. S. *VLSI Metallization*. (Academic Press, 2014).

175. Fu, F. *et al.* Monolithic Perovskite-Silicon Tandem Solar Cells: From the Lab to Fab? *Adv. Mater.* **34**, 2106540 (2022).

176. Kern, D. M. Preismonitor Juli 2023. (Deutsche Rohstoffagentur (DERA) in der Bundesanstalt für Geowissenschaften und Rohstoffe (BGR), 2023).

177. Chen, H. *et al.* Improved charge extraction in inverted perovskite solar cells with dual-site-binding ligands. *Science* **384**, 189–193 (2024).

178. Jiang, Q. & Zhu, K. Rapid advances enabling high-performance inverted perovskite solar cells. *Nat. Rev. Mater.* **9**, 399–419 (2024).

179. Min, H. *et al.* Perovskite solar cells with atomically coherent interlayers on SnO2 electrodes. *Nature* **598**, 444–450 (2021).

180. Yoo, J. J. *et al.* Efficient perovskite solar cells via improved carrier management. *Nature* **590**, 587–593 (2021).

181. Xiong, L. *et al.* Review on the Application of SnO2 in Perovskite Solar Cells. *Adv. Funct. Mater.* **28**, 1802757 (2018).

182. Park, S. Y. & Zhu, K. Advances in SnO2 for Efficient and Stable n–i–p Perovskite Solar Cells. *Adv. Mater.* **34**, 2110438 (2022).

183. Lemercier, T., Perrin, L., Berson, S., Flandin, L. & Planes, E. Innovative PIN-type perovskite solar cells with 17% efficiency: processing and characterization. *Mater. Adv.* **2**, 7907–7921 (2021).

184. Dong, H. *et al.* Improving electron extraction ability and device stability of perovskite solar cells using a compatible PCBM/AZO electron transporting bilayer. *Nanomaterials* **8**, 720 (2018).

185. Zhou, Y. *et al.* Efficiently Improving the Stability of Inverted Perovskite Solar Cells by Employing Polyethylenimine-Modified Carbon Nanotubes as Electrodes. *ACS Appl. Mater. Interfaces* **10**, 31384–31393 (2018).

186. Wei, J. *et al.* Highly Stable Hybrid Perovskite Solar Cells Modified with Polyethylenimine via Ionic Bonding. *ChemNanoMat* **4**, 649–655 (2018).

187. Yerramilli, A. S. *et al.* Improved performance of inverted perovskite solar cells due to the incorporation of zirconium acetylacetonate buffer layer. *Sol. Energy Mater. Sol. Cells* **200**, 109927 (2019).

188. Zhang, C. *et al.* Enhancing performance of organic-inorganic perovskite solar cells using super halogen additive. *Org. Electron.* **108**, 106548 (2022).

189. Chen, C. *et al.* Effect of BCP buffer layer on eliminating charge accumulation for high performance of inverted perovskite solar cells. *RSC Adv.* **7**, 35819–35826 (2017).

190. Tremblay, M.-H. *et al.* Benzocyclobutene polymer as an additive for a benzocyclobutene-fullerene: application in stable p–i–n perovskite solar cells. *J. Mater. Chem. A* **9**, 9347–9353 (2021).

191. Bai, Y. *et al.* Enhancing stability and efficiency of perovskite solar cells with crosslinkable silane-functionalized and doped fullerene. *Nat. Commun.* **7**, 12806 (2016).

192. Dingemans, G. & Kessels, W. M. M. Status and prospects of Al2O3-based surface passivation schemes for silicon solar cells. *J. Vac. Sci. Technol. A* **30**, 040802 (2012).

193. Musselman, K. P., Uzoma, C. F. & Miller, M. S. Nanomanufacturing: High-Throughput, Cost-Effective Deposition of Atomic Scale Thin Films via Atmospheric Pressure Spatial Atomic Layer Deposition. *Chem. Mater.* **28**, 8443–8452 (2016).

194. Raninga, R. D. *et al.* Strong performance enhancement in lead-halide perovskite solar cells through rapid, atmospheric deposition of n-type buffer layer oxides. *Nano Energy* **75**, 104946 (2020).

195. Bush, K. A. *et al.* 23.6%-efficient monolithic perovskite/silicon tandem solar cells with improved stability. *Nat. Energy* **2**, 1–7 (2017).

196. Groenendaal, L., Jonas, F., Freitag, D., Pielartzik, H. & Reynolds, J. R. Poly(3,4-ethylenedioxythiophene) and Its Derivatives: Past, Present, and Future. *Adv. Mater.* **12**, 481–494 (2000).

197. Kim, K. M. *et al.* Work function optimization of vacuum free top-electrode by PEDOT:PSS/PEI interaction for efficient semi-transparent perovskite solar cells. *Sol. Energy Mater. Sol. Cells* **176**, 435–440 (2018).

198. Yu, Y., Hoang, M. T., Yang, Y. & Wang, H. Critical assessment of carbon pastes for carbon electrode-based perovskite solar cells. *Carbon* **205**, 270–293 (2023).

199. Jin, J. *et al.* Highly efficient and stable carbon-based perovskite solar cells with the polymer hole transport layer. *Sol. Energy* **220**, 491–497 (2021).

200. Henderson, C. *et al.* Charge transfer complex formation between organic interlayers drives light-soaking in large area perovskite solar cells. *Energy Environ. Sci.* **16**, 5891–5903 (2023).

201. Matsuo, Y., Son, D., Shimoi, Y. & Marumoto, K. Direct observation of spins at bathocuproine (BCP) interfaces: An electron spin resonance study on BCP/metal (Al or Au) thin films. *Chem. Phys. Lett.* **607**, 29–33 (2014).

202. Chen, K. *et al.* A Lumped-Parameter Equivalent Circuit Model for Perovskite Solar Cells' S-Shaped I-V Kinks. *IEEE Electron Device Lett.* **42**, 379–382 (2021).

203. Tress, W. *et al.* Imbalanced mobilities causing S-shaped IV curves in planar heterojunction organic solar cells. *Appl. Phys. Lett.* **98**, 063301 (2011).

204. Tress, W., Corvers, S., Leo, K. & Riede, M. Investigation of Driving Forces for Charge Extraction in Organic Solar Cells: Transient Photocurrent Measurements on Solar Cells Showing S-Shaped Current–Voltage Characteristics. *Adv. Energy Mater.* **3**, 873–880 (2013).

205. Sundqvist, A., Sandberg, O. J., Nyman, M., Smått, J.-H. & Österbacka, R. Origin of the S-Shaped JV Curve and the Light-Soaking Issue in Inverted Organic Solar Cells. *Adv. Energy Mater.* **6**, 1502265 (2016).

206. Li, D.-B. *et al.* Eliminating S-Kink To Maximize the Performance of MgZnO/CdTe Solar Cells. *ACS Appl. Energy Mater.* **2**, 2896–2903 (2019).

207. Prabu, R. T. *et al.* CsPbI3 perovskite solar cell and decoding its skink feature in J-V curve. *Mater. Sci. Semicond. Process.* **162**, 107539 (2023).

208. Jacobs, D. A. *et al.* Hysteresis phenomena in perovskite solar cells: the many and varied effects of ionic accumulation. *Phys. Chem. Chem. Phys.* **19**, 3094–3103 (2017).

209. Park, B. *et al.* Long-Term Chemical Aging of Hybrid Halide Perovskites. *Nano Lett.* **19**, 5604–5611 (2019).

210. Minussi, F. B., Bertoletti, E. M., Eiras, J. A. & Araújo, E. B. Intrinsic aging in mixed-cation lead halide perovskites. *Sustain. Energy Fuels* **6**, 4925–4937 (2022).

211. Zhao, Q. *et al.* Oxygen Vacancy Mediation in SnO2 Electron Transport Layers Enables Efficient, Stable, and Scalable Perovskite Solar Cells. *J. Am. Chem. Soc.* **146**, 19108–19117 (2024).

212. Jewell, E., Philip, B. & Greenwood, P. Improved Manufacturing Performance of Screen Printed Carbon Electrodes through Material Formulation. *Biosensors* **6**, 30 (2016).

213. Lee, H. & Lee, C. Analysis of Ion-Diffusion-Induced Interface Degradation in Inverted Perovskite Solar Cells via Restoration of the Ag Electrode. *Adv. Energy Mater.* **8**, 1702197 (2018).

214. Sun, P. Z. *et al.* Limits on gas impermeability of graphene. *Nature* **579**, 229–232 (2020).

215. Senthilkumar, V., Vickraman, P., Jayachandran, M. & Sanjeeviraja, C. Structural and optical properties of indium tin oxide (ITO) thin films with different compositions prepared by electron beam evaporation. *Vacuum* **84**, 864–869 (2010).

216. Jacobsson, T. J. *et al.* Exploration of the compositional space for mixed lead halogen perovskites for high efficiency solar cells. *Energy Environ. Sci.* **9**, 1706–1724 (2016).

217. Vegard, L. Die Konstitution der Mischkristalle und die Raumfüllung der Atome. *Z. Für Phys.* **5**, 17–26 (1921).

218. Slimi, B. *et al.* Synthesis and characterization of perovskite FAPbBr3−xIxthin films for solar cells. *Monatshefte Für Chem. - Chem. Mon.* **148**, 835–844 (2017).

219. Zhou, L. *et al.* Enhanced planar perovskite solar cell efficiency and stability using a perovskite/PCBM heterojunction formed in one step. *Nanoscale* **10**, 3053–3059 (2018).

220. Song, T. *et al.* Enhancing Performance and Stability of Sn–Pb Perovskite Solar Cells with Oriented Phenyl-C61-Butyric Acid Methyl Ester Layer via High-Temperature Annealing. *ACS Nano* **18**, 2992–3001 (2024).

221. Jain, A. *et al.* Minimizing residues and strain in 2D materials transferred from PDMS. *Nanotechnology* **29**, 265203 (2018).

222. Choi, W. *et al.* Effect of Annealing in Ar/H2 Environment on Chemical Vapor Deposition-Grown Graphene Transferred With Poly (Methyl Methacrylate). *IEEE Trans. Nanotechnol.* **14**, 70–74 (2015).

223. Liu, W., Sun, Q., Zhang, J., Huang, X. & Yue, Y. Annealing-induced one order of magnitude enhancement in heat dissipation at graphene/SiO2 interface. *Mater. Today Nano* **24**, 100383 (2023).

224. Marcus, P. *Corrosion Mechanisms in Theory and Practice, Third Edition*. (CRC Press, 2011).

225. Habisreutinger, S. N., Noel, N. K. & Snaith, H. J. Hysteresis Index: A Figure without Merit for Quantifying Hysteresis in Perovskite Solar Cells. *ACS Energy Lett.* **3**, 2472–2476 (2018).

226. Hossain, M. I. & Aïssa, B. Effect of Structure, Temperature, and Metal Work Function on Performance of Organometallic Perovskite Solar Cells. *J. Electron. Mater.* **46**, 1806–1810 (2017).

227. Rong, X. *et al.* Impact of metal electrode work function of CH3NH3PbI3/p-Si planar heterojunction perovskite solar cells. *Sol. Energy* **158**, 424–431 (2017).

228. Ohmi, T. *et al.* The Technology of Chromium Oxide Passivation on Stainless Steel Surface. *J. Electrochem. Soc.* **140**, 1691 (1993).

229. Koudelkova, M., Augustynski, J. & Berthou, H. On the Composition of the Passivating Films Formed on Aluminum in Chromate Solutions. *J. Electrochem. Soc.* **124**, 1165 (1977).

230. Wagner, J. B., Lawless, K. R. & Gwathmey, A. T. Passivation of Aluminum by Chromate Solutions. **114**, (1967).

231. Niewelt, T., Kwapil, W., Selinger, M., Richter, A. & Schubert, M. C. Long-Term Stability of Aluminum Oxide Based Surface Passivation Schemes Under Illumination at Elevated Temperatures. *IEEE J. Photovolt.* **7**, 1197–1202 (2017).

232. Kotipalli, R. *et al.* Passivation effects of atomic-layer-deposited aluminum oxide. *EPJ Photovolt.* **4**, 45107 (2013).

233. Xu, T., Xu, Y., Liao, N., Li, Y. & Nath, M. High-Temperature Chemical Stability of Cr(III) Oxide Refractories in the Presence of Calcium Aluminate Cement. *Materials* **14**, 6590 (2021).

234. Ramm, J. *et al.* Thermal Stability of Thin Film Corundum-Type Solid Solutions of (Al1–xCrx)2O3 Synthesized Under Low-Temperature Non-Equilibrium Conditions. *Adv. Eng. Mater.* **9**, 604–608 (2007).

235. Gozzi, D., Cignini, P. L., Stampa, E., Alfonsi, B. & Petrucci, M. Some evidences on the instability of Cr-Cr2O3 electrode in the electrochemical oxygen sensors at steelmaking temperatures. *Trans. Iron Steel Inst. Jpn.* **23**, 205–212 (1983).

236. Mammana, S. S. *et al.* Study of wet etching thin films of indium tin oxide in oxalic acid by monitoring the resistance. *Thin Solid Films* **567**, 20–31 (2014).

237. Senocrate, A. *et al.* Charge carrier chemistry in methylammonium lead iodide. *Solid State Ion.* **321**, 69–74 (2018).

238. Bang, S.-M. *et al.* Defect-Tolerant Sodium-Based Dopant in Charge Transport Layers for Highly Efficient and Stable Perovskite Solar Cells. *ACS Energy Lett.* **5**, 1198–1205 (2020).

239. Li, N. *et al.* Cation and anion immobilization through chemical bonding enhancement with fluorides for stable halide perovskite solar cells. *Nat. Energy* **4**, 408–415 (2019).

240. Zhao, W., Yao, Z., Yu, F., Yang, D. & Liu, S. (Frank). Alkali Metal Doping for Improved CH3NH3PbI3 Perovskite Solar Cells. *Adv. Sci.* **5**, 1700131 (2018).

241. Th. Greyer GmbH & Co. KG. Labsolute® Microscope Slides made from Soda-lime Glass. https://www.humeau.com/media/blfa_files/TC_Lames-microscope_82707695001_FR_120320.pdf

242. Knittel Glass. Microscope Slides – Data Sheet. https://knittel-glaeser.com/Download/data-sheet_OT_eng.pdf (2012)

243. In vitro diagnostic – medical device. Data Sheet Microscope glass slides. https://bio-optica.it/ftp/Sito/technical_datasheet/VetriniMicroscopia_en.pdf

244. Tichane, R. M. & Carrier, G. B. Microstructure of a Soda-Lime Glass Surface. *J. Am. Ceram. Soc.* **44**, 606–610 (1961).